Continuous Wet-Chemical Synthesis and Pyrolysis of Inorganic-Organic Hybrid Materials based on Polyoxomolybdates and their Electrochemical Performance as Anode Materials in Lithium-Ion Batteries

Dissertation

Zur Erlangung des Grades
des Doktors der Naturwissenschaften
der Naturwissenschaftlichen-Technischen Fakultät
der Universität des Saarlandes

von

Mana Abdirahman Mohamed

Saarbrücken

2025

Tag des Kolloquiums:	08.08.2025
Dekan:	Prof. Dr.-Ing. Dirk Bähre
Berichterstatter:	Prof. Dr. Guido Kickelbick
	Priv.-Doz. Dr.-Ing. Guido Falk
Vorsitz:	Prof. Dr.-Ing. Markus Gallei
Akademischer Mitarbeiter:	Dr. Christoph Zollitsch

Die vorliegende Dissertation wurde in der Zeit von November 2018 bis August 2022 an der Universität des Saarlandes in der der Naturwissenschaftlich-Technischen Fakultät am Institut für Anorganische Festkörperchemie im Arbeitskreis von Herrn Prof. Dr. Guido Kickelbick angefertigt.

Danksagung

An dieser Stelle möchte ich mich ganz herzlich bei allen bedanken, die mich während meiner Promotionszeit stets ermutigt, fachlich beraten, tatkräftig unterstützt und mir immer zur Seite gestanden haben.

An erster Stelle möchte ich mich bei Prof. Dr. Guido Kickelbick für die Möglichkeit bedanken, meine Doktorarbeit zu diesem interessanten Thema in seiner Arbeitsgruppe durchführen zu können. Ich danke ihm dafür, dass er mich immer wieder zu neuen Forschungsfragen angeregt hat. Die regelmäßigen wissenschaftlichen Diskussionen haben immer wieder interessante Ideen hervorgebracht.

Herrn Dr. Guido Falk danke ich für die wissenschaftliche Betreuung und Begutachtung meiner Dissertation.

Darüber hinaus möchte ich mich bei der gesamten Arbeitsgruppe Kickelbick für die freundliche Aufnahme, das gute Arbeitsklima und die große Unterstützung jedes Einzelnen bedanken. Vielen Dank an Max, Bastian, Thomas, Svenja, Tobias, Lucas, Anna, Kristina, Sandra, Kimia, Aylin, Jan-Falk, Stefan Engel, Elias, Aaron, Dennis, Achim, Nadja, Nils, Jessica und Ralf für die tolle Zusammenarbeit. Ich habe sowohl die gemeinsame Arbeitszeit als auch die gemeinsame Zeit außerhalb des Labors sehr geschätzt. Ich freue mich darauf, mit Euch verbunden zu bleiben.

Mein herzlicher Dank geht insbesondere an Christina, sowohl für die Einarbeitung in das Thema als auch für die tolle Unterstützung während meiner Schreibphase und darüber hinaus. Besonders bedanken möchte ich mich bei Oliver für die vielen Tipps und Ratschläge, die stetige Unterstützung in allen Belangen und die vielen konstruktiven Diskussionen. Ich möchte mich auch bei Robert für die hilfreichen Diskussionen und Ratschläge bezüglich der Rietveld-Verfeinerung bedanken. Ich danke auch Michael für die Festkörper-NMR-Messungen. Ich danke auch Bernd für die Durchführung der Röntgen-Einkristallstrukturanalyse, für die Verfeinerung der Kristallstruktur und für die pH-Messungen. Vielen Dank auch an Jörg Schmauch für die Einarbeitung und Unterstützung bei der Rasterelektronenmikroskopie und auch für die Aufnahme von HR-TEM und TEM Bildern. Susanne Harling danke ich für die Durchführung der Elementaranalysen und für ihre tatkräftige Unterstützung bei den präparativen Arbeiten. Ich danke auch Ajda für ihre große Hilfe im Labor.

Weiterhin danke ich den technischen Mitarbeitern, insbesondere unserer Feinmechanikerin Sylvia und unserem Elektriker Stefan Blank sowie Rudolf Richter aus der Konstruktion für die technische Unterstützung beim Aufbau der zahlreichen Spezialanfertigungen und für die schnelle und unkomplizierte Hilfe bei Reparaturen und Wartungen.

Susanne Limbach danke ich herzlich für die freundliche und unkomplizierte Unterstützung bei organisatorischen Fragen. Traudel und Christel danke ich für ihren wertvollen Einsatz bei der Praktikumsbetreuung.

Mein besonderer Dank gilt meinen Kooperationspartnern. Vom Leibniz-Institut INM (Institut für Neue Materialien) danke ich Herrn Prof. Dr. Volker Presser und Frau Dr. Stefanie Arnold für die gute Kooperation, die vielen Anregungen sowie die rasche Revision der Manuskripte. Dr. Antje Quade danke ich für XPS-Messungen und hilfreiche Diskussionen.

Mein herzlicher Dank gilt auch meinen neuen Kollegen und Freunden in meiner neuen Heimat auf der Ostalb für die tolle Aufnahme und die Unterstützung und Motivation während der Schreibphase.

Ein großer Dank gilt meiner Familie und meinen Freunden, die mir den nötigen Rückhalt und Ansporn gegeben haben und immer ein offenes Ohr für mich hatten. Ich danke meinen Freunden Jule und Philipp sowie Maike, die mir das Einleben in Saarbrücken besonders erleichtert haben. Durch euch und unsere gemeinsamen Ausflüge habe ich viel außerhalb des Laboralltags erlebt. Ein besonderer Dank gilt meinem Bruder Mo, der immer für mich da war. Mo danke ich für seine persönliche Unterstützung und für seine ständige Motivation. Trotz der großen Entfernung konnte ich mich durch unsere gemeinsamen Gespräche und die vielen gemeinsamen Reisen immer verbunden fühlen.

Zum Schluss möchte ich mich bei meinem Partner Chris für seine Expertise im grafischen Bereich sowie bei IT- und technischen Problemen bedanken. Ganz besonders möchte ich mich bei Chris dafür bedanken, dass er mich immer unterstützt hat und mir jederzeit zur Seite stand.

Tausend Dank an euch alle!

Table of Contents

List of abbreviations

1,8-DAN	1,8-diaminonaphthalene
AHM	ammonium heptamolybdate
CB	conduction band
CC	carbon cloth
CIJR	confined impinging jet reactor
CNT	carbon nanotube
CVD	chemical vapor deposition
DMSO	dimethyl sulfoxide
DTO	dithiooxamide
en	ethylenediamine
GO	graphene oxide
H_2BDC	1,4-benzenedicarboxylic acid
HMD	hexamethylenediamine
IUPAC	international union of pure and applied chemistry
LIB	lithium-ion batterie
LTO	lithium titanate ($Li_4Ti_5O_{12}$)
MOF	metal-organic framework
NMR	nuclear magnetic resonance spectroscopy
ORMOSIL	organically modified silica
PANI	polyaniline
PEDOT	poly(3,4-ethylenedioxythiophene)
PLGA	poly(lactic-co-glycolic acid)
POM	polyoxometalate
POMOF	POM-based metal-organic frameworks
RGO	reduced graphene oxide
SBU	structural building block
SEM	scanning electron microscopy
SWNT	single-walled carbon nanotube
TEM	transmission electron microscope
TET	titanium tetraethylate
TG	thermogravimetric analysis
TPT	tris-(4-pyridyl)triazine

VB	valence band
XPS	X-ray photoelectron spectroscopy
XRD	X-ray powder diffraction

Kurzzusammenfassung

Die kontinuierliche nasschemische Synthese von Partikeln mit skalierter Oberfläche im Mikro- bis Nanometerbereich ist mit dem Mikrojetreaktor möglich. Die Synthese mit dem Mikrojetreaktor ist ein nachhaltiges, energiearmes Verfahren, mit dem sich hohe Durchsätze bei hoher Reproduzierbarkeit erzielen lassen. Diese Faktoren sind für industrielle Anwendungen besonders wichtig. In dieser Dissertation wurden anorganisch-organische Hybridmaterialien durch die wässrige Fällungsreaktion mit Ammoniumheptamolybdat (AHM) und verschiedenen organischen Spezies, nämlich para-Phenylendiamin (PPD), 1,8-Diaminonaphthalin (1,8-DAN) oder Hexamethylendiamin (HMD), synthetisiert. Es wurden systematische Studien durchgeführt, indem die Verhältnisse der Reaktanten variiert wurden. Unterschiedliche molare Verhältnisse von Molybdaten zu organischen Spezies und der pH-Wert führten zu verschiedenen kristallinen Hybridverbindungen. Durch Pyrolyse dieser anorganisch-organischen Hybridvorläufer können Mischungen aus Molybdäncarbid, -nitrid, -oxid, elementarem Mo und gemischten anionischen Verbindungen wie $Mo(C,N,O)_x$-Verbindungen, die in eine kohlenstoffhaltige Matrix eingebettet sind, erhalten werden. Die Morphologie der Ausgangsmaterialien bleibt auch nach der Pyrolyse erhalten. Da die Morphologie eine Schlüsseleigenschaft für die Leistung von Lithium-Ionen-Batterien ist, eignet sich dieses Verfahren besonders gut für die Materialsynthese von Lithium-Ionen-Batterien.

Abstract

Continuous wet-chemical synthesis of scale surface area particles in the micro- to nanometer range is possible with the microjet reactor. Synthesis involving the microjet reactor is a sustainable, low-energy process that can be used to achieve high throughputs with high reproducibility. These factors are especially important for industrial applications. In this dissertation, inorganic-organic hybrid materials were synthesized through the aqueous precipitation reaction with ammonium heptamolybdate (AHM) and different organic species, namely para-phenylenediamine (PPD), 1,8-diaminonaphthalene (1,8-DAN) or hexamethylenediamine (HMD). Systematic studies were performed by varying the ratios of the reactants. Varying molar ratios of molybdates to organic species and pH resulted in different crystalline hybrid compounds. By pyrolyzing these inorganic-organic hybrid precursors, mixtures of molybdenum carbide, nitride, oxide, elemental Mo and mixed anionic compounds such as $Mo(C,N,O)_x$ composites embedded in a carbonaceous matrix can be obtained. The morphology of the starting materials is also preserved after pyrolysis. Since morphology is a key property for Li-ion battery performance, this process is particularly suitable for Li-ion battery material synthesis.

1 Introduction

1.1 Lithium Ion Battery

The ever-increasing scarcity of fossil fuels and the ever-increasing CO_2 emissions resulting from global warming pose serious problems for the planet. In order to overcome the energy and environmental crisis, research is constantly being conducted into environmentally friendly renewable energy generation, including wind, solar, and hydroelectric power plants. Because these energy sources depend on unpredictable environmental factors, high-efficiency energy conversion and storage technologies are critical. Lithium-ion batteries (LIBs), with their high specific energy, high power density and stable performance, are considered the most suitable candidates for electrochemical energy storage. Global research efforts are focused on the improvement of the current shortcomings of LIBs, including safety, energy density, battery life and performance.[1–4]

LIBs use electrochemical processes to convert chemical energy into electrical energy. The mechanism and schematic setup of a LIB is shown in **Figure 1**. A microporous membrane (separator) separates two electrodes - a positive electrode (cathode) and negative electrode (anode). There is also an electrolyte (containing a lithium salt) between the two electrodes. The separator prevents a short circuit because it is permeable to the electrolyte and the Li^+ ions. Transition metal oxides or phosphates (e.g. $LiCoO_2$ or $LiFePO_4$) are typically used as the cathode material. The anode material is usually graphite. Li^+ ions migrate from the anode to the cathode through the electrolyte and separator during the discharge process. Simultaneously, an equal number of electrons flow to the cathode via the external circuit. During charging, the process is reversed. Li^+ ions migrate via the electrolyte and separator from the cathode to the anode.[2–6]

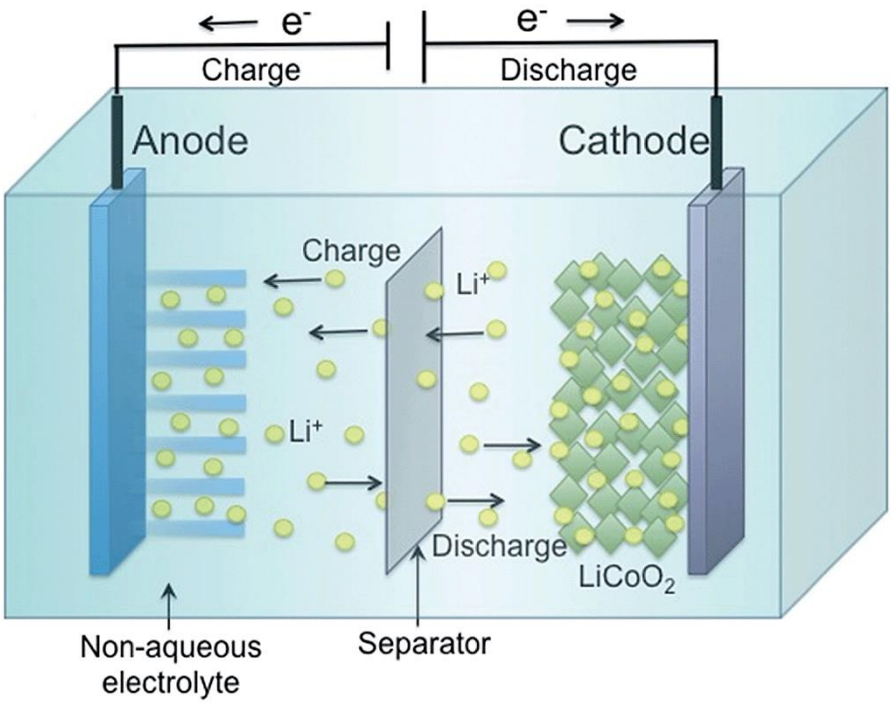

Figure 1: Graphic illustration of the discharge and charge processes in LIBs, showing lithium intercalation and deintercalation. Reproduced from Ref.[2] Used with permission of Royal Society of Chemistry (RSC), from Roy, P.; Srivastava, S. K. Nanostructured Anode Materials for Lithium Ion Batteries. *J. Mater. Chem. A* 2015, *3*, 2454–2484. https://doi.org/10.1039/c4ta04980b; permission conveyed through Copyright Clearance Center, Inc. Copyright © 2015.

LIBs utilize redox chemistry, which involves simultaneous reduction and oxidation reactions between two redox pairs.[7]

The following chemical reactions occur at the anode and cathode in LIBs, resulting in the production of Li^+ ions and electrons:[2–4,6]

Anode: $6\ C + x\ Li^+ + xe^- \leftrightarrow Li_xC_6$ (**Eq. 1**)

Cathode: $LiCoO_2 \leftrightarrow Li_{1-x}CoO_2 + x\ Li^+ + x\ e^-$ (**Eq. 2**)

Total reaction: $6\ C + LiCoO_2 \leftrightarrow Li_xC_6 + Li_{1-x}CoO_2$ (**Eq. 3**)

LIBs with improved power and energy densities for future smaller and lighter batteries, suitable electrode materials must fulfill the demands for long cycle life, superior ionic and electrical conductivity, and reversible capacity. Environmental and economic

factors such as cost, availability and safety are also critical. Ideally, cathode materials should have a high voltage, while a low potential would be advantageous for anode materials. The layered oxide $LiCoO_2$[8] represents the first industrially available cathode material. Among cathode materials, $LiCoO_2$ enables reversible and stable lithiation and delithiation. Other common cathode materials include $LiFePO_4$[9] with an olivine structure and $LiMn_2O_4$[10] with a spinel structure.[1,6,11,12]

There are three different lithiation processes for electrode materials for LIBs. These three different reaction mechanisms are intercalation, alloying, and conversion (**Figure 2**). Each of the three mechanisms has advantages and disadvantages. Electrode materials must therefore be developed in such a way that the disadvantages are kept to a minimum and the storage benefits are maximized.[13,14]

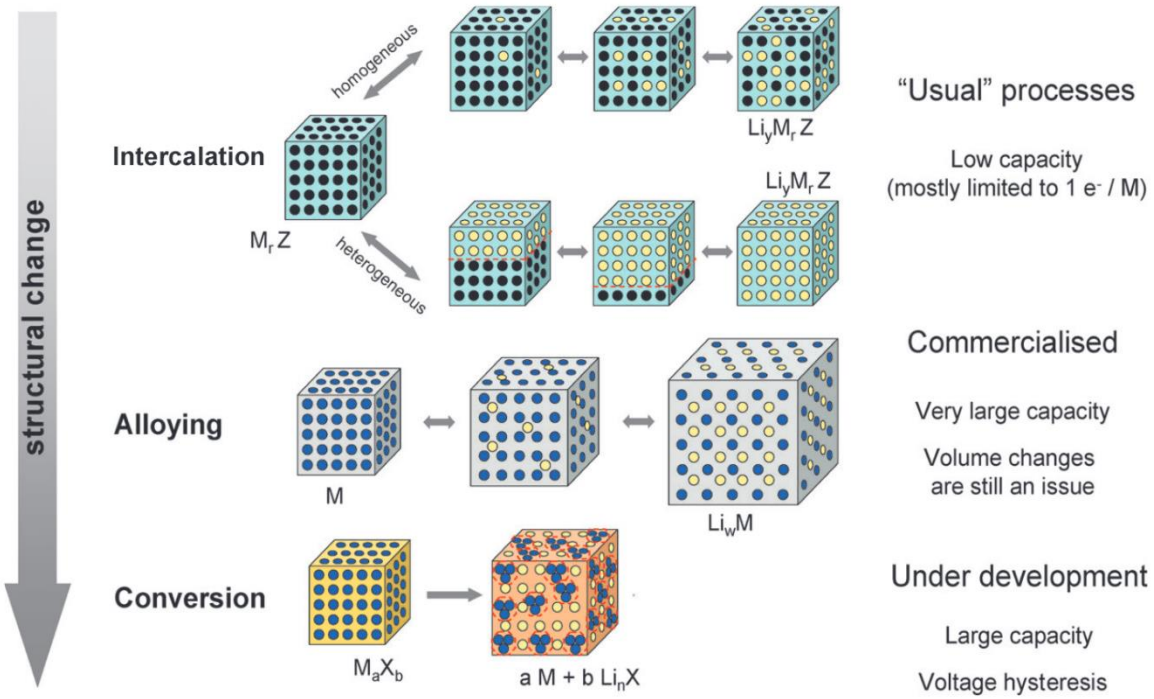

Figure 2: Illustration of the different reaction mechanisms found in electrode materials for LIBs. The black circles represent: Cavities in the crystal structure, blue circles: metals, yellow circles: Lithium. Adapted from Ref.[13] Used with permission of Chemical Society, from Palacín, M. R. Recent Advances in Rechargeable Battery Materials: A Chemist's Perspective. *Chem. Soc. Rev.* 2009, *38*, 2565–2575. https://doi.org/10.1039/b820555h; permission conveyed through Copyright Clearance Center, Inc. Copyright © 2009.

Electrode materials based on intercalation mechanisms proceed without significant structural changes. Li^+ ions enter a host material through topotactic and reversible insertion between free lattice sites or layers. Due to their high reversibility and simplicity, electrode materials based on intercalation mechanisms are widely used. However, this type of electrode does not provide high energy densities. This is because the specific charge is limited by both the mass and volume of the host material. Due to limited storage sites in the host material, which can only store one electron per ion center, the capacities of the electrode materials are limited. The smallest cations that can easily penetrate solids through intercalation reactions are Li^+ ions and protons. A major advantage of the intercalating mechanisms is the stable structure of electrode materials, as little or no volumetric expansion occurs. As a result, higher performance, longer cyclic life and safer battery operation are possible.[13–15]

The next lithiation mechanism for electrode material is the alloying mechanism. Electrochemical alloying can occur between lithium and metals or semiconducting materials at room temperature in non-aqueous electrolytes. Such alloyed electrode materials are suitable as anode materials because of their low operating potentials. Elements selected from Si, Ge and Sn can alloy with Li to achieve very high theoretical capacities. The alloying process between Li and Si, Ge and Sn results in the formation of $Li_{22}Si_5/Li_{15}Si_4$ (4212 mA h g^{-1}, 3579 mA h g^{-1})[16], $Li_{22}Ge_5/Li_{15}Ge_4$ (1625 mA h g^{-1}, 1384 mA h g^{-1})[17] and $Li_{22}Sn_5$ (994 mA h g^{-1})[18]. Despite the numerous advantages of alloy-based anode materials, the very high achievable capacities, low costs and large quantities, their practical application is hampered by major problems. During the lithiation mechanism of alloy-based anode materials, large volume changes occur, which lead to significant capacity losses and poor cyclic lifetimes.[1,13,14]

The third mechanism involves the electrode materials based on the conversion reaction. This involves a phase change of the electrode materials during the electrochemical process. During the cycle, the electrode material is completely transformed. This causes the formation of novel compounds having new properties. Binary transition metals including metal oxides, fluorides, phosphides, and sulfides are among the materials that undergo conversion reactions. The conversion reaction of transition metal compounds with lithium results in metallic nanoparticles embedded in a matrix. This leads to very high capacities because the reaction results in the complete reduction of the transition metal to the metallic form. The redox potential increases with the ionicity of the metal-oxide, fluoride, phosphide and sulfide bonds. This results in

low redox potentials for these materials, making them suitable anode materials. Fluorides are an exception, achieving high redox potentials, which makes them suitable for application as cathode material. In the case of electrode materials based on the conversation reaction, a large voltage hysteresis is obtained during discharge and charge. This causes a lack of energy efficiency. For these reasons, the commercial application of electrode materials relying on the conversion reaction has remained limited.[13,14,19]

Pure lithium as an anode material in LIBs has the highest theoretical capacity of 3861 mA h g^{-1} and the lowest potential of 0 V. Pure lithium used as an anode material has enormous safety risks. Increased dendrite formation occurs during cycling, potentially causing short circuits. In the worst case, this can cause a fire or explosion. The high reactivity as well as the infinite volume change and the reduced lifetime of lithium electrodes are further aspects that hinder the application.[1,3,20] The safety risks can be significantly minimized or prevented by using intercalation compounds such as lithium titanate ($Li_4Ti_5O_{12}$, LTO). However, LTO has drawbacks as an anodic material because the material has a low theoretical capacity of 175 mA h g^{-1} and a high redox potential of 1.55 V.[21,22] Graphite is extensively used commercially for anode materials. The reasons are the natural occurrence, the low costs, the long cycle stability and the low redox potential of less than 0.3 V of graphite electrodes. However, the disadvantages are its low theoretical capacity of 372 mA h g^{-1}, the low rate and the limited space for ion storage.[23–26] For widespread commercial application, cost-effective anode materials with long lifetimes and high power and energy densities are required to address the rapidly growing requirements of the battery industry. Therefore, extensive research into new anode materials is needed.[1,27–29]

1.1.1 POM-based Inorganic-Organic Materials for Lithium-Ion Batteries

Searching novel electrode materials for LIBs, inorganic-organic hybrid materials based on polyoxometalates have emerged in recent years. Polyoxometalates (POMs) consist of extraordinary redox-active metal oxide clusters with tunable structures and high charge storage capacities. By integrating POMs into an organic matrix, it is possible to engineer electrode materials with enhanced electrochemical behavior. Synergistic effects can be utilized through the combined effect of inorganic and organic compounds. This results in advantages such as attenuation of the volume change

during cyclization, increased electronic conductivity and improved ion diffusion. This eliminates the problems associated with conventional electrode materials. Precise control over surface properties, composition and morphology results from the adjustability and structural flexibility of the POM-based hybrid materials. The resulting diversity provides a huge range for the creation of future electrode systems.[30–32]

1.2 Inorganic organic hybrid materials

Inorganic-organic hybrid materials are derived from the combination of inorganic and organic components. Based on the IUPAC (International Union of Pure and Applied Chemistry) definition, hybrid materials are a close mixture of inorganic or organic components or both. Typically, the interpenetration of the components is on the order of less than 1 µm.[33] Due to the synergy of the inorganic and organic components, hybrid materials exhibit added and/or improved functionalities and properties. Inorganic-organic hybrid materials thus form interfaces between two chemical worlds with important contributions in and from materials science. Many efforts have been made recently to develop multifunctional inorganic-organic hybrid materials by combining the chemical activities of their building blocks.[33–38]

Two types of classifications are widely found in the literature to categorize hybrid materials (**Figure 3**). One is based on the nature of the interactions among the organic and inorganic compounds, which is the most common classification. The second classification takes into account which component acts as the dominant matrix and which one acts as a guest.[37,38]

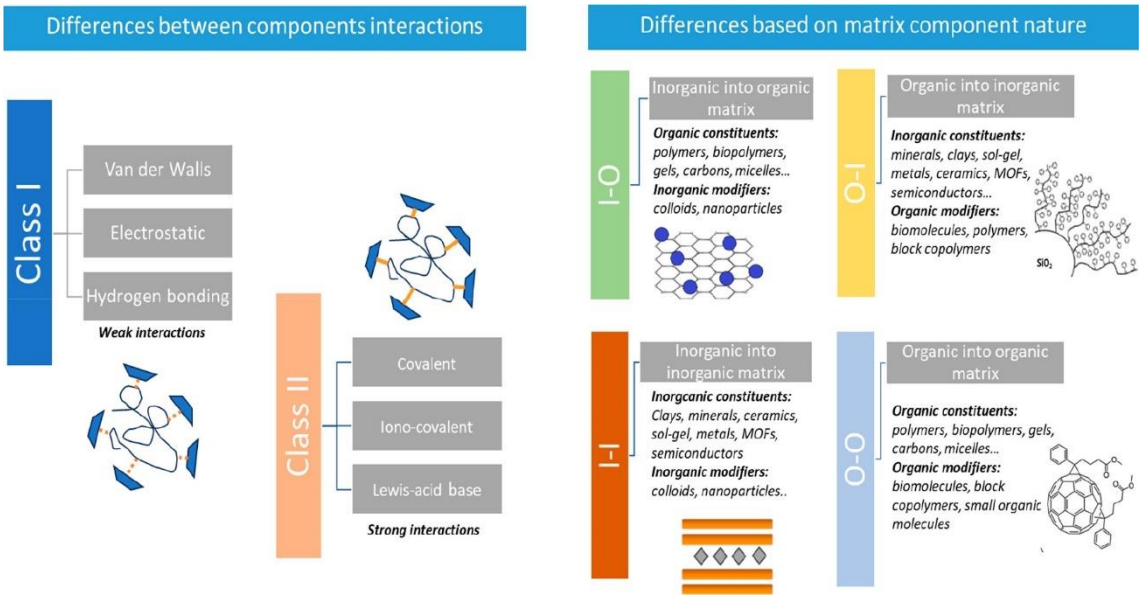

Figure 3: General categorization of hybrid materials. Classification according to the type of interaction between the components (left). Categorization based on the type of matrix and guest component (right).Reproduced from Ref.[38] This figure is published and licensed under CC BY 4.0. Copyright © 2024 The Authors. Published by American Chemical Society.

According to the first classification, class I hybrids are defined as ones that result from weak interactions within the organic and inorganic building blocks. These weak interactions include electrostatic, hydrogen bonds, and/or van der Waals interactions. In contrast, class II hybrids involve strong chemically based interactions. For example, the inorganic and organic units are linked by strong covalent bonds. Due to the fact that both stronger and weaker interactions can occur in the same hybrid material, this classification is sometimes ambiguous.[34–38]

The second categorization of hybrid materials emphasizes the nature of the predominant structural matrix component versus that which is accommodated. Accordingly, hybrid materials can be separated into two major groups: inorganic-organic (IO) hybrids, when there is an inorganic host into which organic guests are integrated and organic-inorganic (OI), in which the matrix forms an organic phase. This classification is particularly important regarding nanocomposites (**Figure 4**), in which one of the two building blocks determines the structure.[34,38]

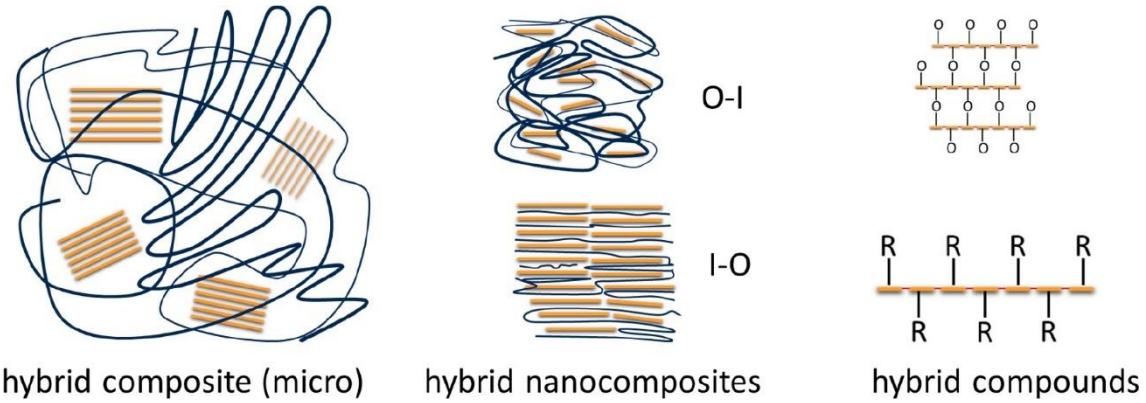

Figure 4: Schematic illustration of various types of hybrid materials in which the dispersion of organic and inorganic components occurs at different stages (black lines show organic units representing a polymer and orange lines show inorganic units corresponding to a layered phase or aggregated rods). Reproduced from Ref.[38] This figure is published and licensed under CC BY 4.0. Copyright © 2024 The Authors. Published by American Chemical Society.

The concepts of composite or nanocomposite are used to describe the formation of new materials by combining different phases. According to this, hybrid materials and nanocomposite could appear as synonyms. However, the classification criteria are different. While hybrids refer to the combination of different components, composites and nanocomposites relate to their dispersion degree.[38] According to the IUPAC definition, a composite is a material composed of several distinct (non-gaseous) phase domains, including not less than one domain that appears to be continuous. The term nanocomposite is used when the dimension of one phase is in the nanometer range.[33] The schematic representation in **Figure 4** illustrates this clearly. In the case of a hybrid composite material (**Figure 4, left**), there is a combination of organic and inorganic phases that goes further than a physical mixture. The integrity of the phases is maintained. In this way, the material retains areas of the individual phases. In a hybrid nanocomposite (**Figure 4, middle**), further increasing the degree of dispersion causes the domains of the single components to blur or disappear. In this particular case, the IO or OI classification discussed before makes sense. Last but not least, in hybrid materials (**Figure 4, right**), polysiloxanes or metal-organic frameworks (MOF), the organic and inorganic compounds are linked on the molecular levels and form porous structures.[38] According to IUPAC, such porous materials can be divided among three classes, depending on their pores size. Microporous materials have pore sizes down

to 2 nm, mesoporous materials have pore sizes from 2 to 50 nm, and macroporous materials have pore sizes greater than 50 nm.[39,40]

All possible combinations of inorganic and organic components result in a wide variety of compositions and chemical structures. This results in a broad field of applications for hybrid materials, including energy storages, sensor technology, catalytic applications, photonics and biomedicine. The focus of this dissertation is on the application of energy storage. This area will be discussed in more detail in the following.[38]

Hybrid materials are gaining importance in the field of energy storage. For example, the limitations of pseudocapacitive materials (metal-transition oxides or conductive polymers), such as changes in crystal structure, volume growth during cycling, and limited capacity, may be resolved by combination to carbon materials, thereby increasing the performance of supercapacitors.[41] Furthermore, in order to produce electrodes with a hybrid electrochemical reaction, faradaic can also be integrated into the networks of capacitive-like materials. This would make it possible to eliminate the gap between supercapacitors and batteries in regard to performance and energy densities.[42] The structure of the materials plays an enormously important role in energy storage for the performance of the end devices. However, faradaic materials are often not very conductive, so they are optimally embedded in the conductive carbon matrix and the volume change can also be compensated for, for example downsizing to the nanometer scale. There are countless possible combinations. Multiple hybridizations (carbon/metal oxide/conductive polymer) are also being explored. There are many specialized reviews on this topic in the literature.[42] Reddy et al.[43], for example, focused on CNT-based hybrids for applications in energy storages in their review. Gómez-Romero et al.[44,45], on the other hand, focused on polymer-metal oxide hybrids (including polyoxometalates).[38]

1.2.1 Polyoxometalate

Polyoxometalates (POMs) are commonly used components in inorganic-organic hybrid materials. POMs represent a special group of chemical compounds with the formula $[M_xO_y]^{n-}$, which consist of consisting of early transition metals (e.g. Mo^{VI}, W^{VI}, V^{V}, Nb^{V}, and Ta^{V}) that form anionic molecular metal oxide clusters linked by common oxygen atoms, forming defined cluster frameworks with extremely diverse functional properties. Thus, POMs are ideally suited as inorganic components in inorganic-

organic hybrid materials. In addition to isopolyoxometalates, which contain one type of metal atom in their metal-oxygen skeleton, the so-called addenda atom (M), there are heteropolyoxometalates with a further heteroatom (X) (e.g. B, Si, P, Mn, Co, Gd).[31,46–51] This results in many possible variations for the POMs. In the POM cluster anion, both addenda and possibly hetero-metal can be varied, which leads to a structural diversity of POM cluster anions. Some of the best known such POM cluster anion representatives are the Keggin anion $[XM_{12}O_{40}]^{n-}$, Dawson anion $[X_2M_{18}O_{62}]^{n-}$, Lindqvist anion $[Mo_6O_{19}]^{2-}$ and Anderson anion $[XM_6O_{24}]^{n-}$ (**Figure 5**). The clusters are distinguished by their different topological structures.[44,48]

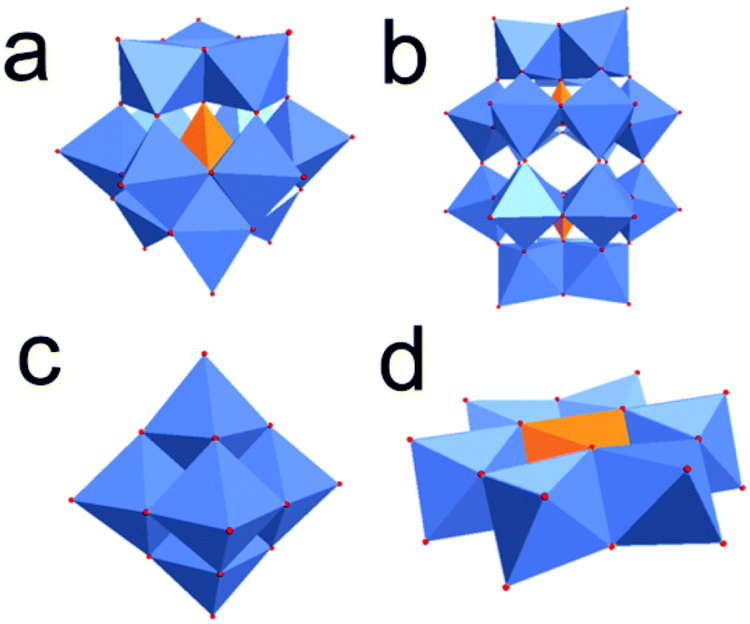

Figure 5: Typical representatives of the POM cluster anions (a) Keggin anion; (b) Dawson anion; (c) Lindqvist anion and (d) Anderson anion. Addenda atoms (M) are shown in blue, O atoms in red and heteroatoms (X) e.g. B, Si, P in orange. Reproduced from Ref.[48] and licensed under a Creative Commons Attribution-NonCommercial 3.0 Unported Licence. Copyright © 2015. Published by Royal Society of Chemistry (RSC).

The redox properties of the POM cluster anions can be adjusted by varying the heteroatoms and/or addenda atoms. According to decreasing oxidizability, the addenda atoms can be ordered as listed below: $V^{(V)} > Mo^{(VI)} > W^{(VI)}$.[46,52]
Due to the large number of different POM clusters, synthetic difficulties arise. The formation of POM clusters depends strongly on the pH value, the concentration, the reactant ratios, the order in which the various reagents are added, the temperature and

the pressure. Different POM clusters of vanadates, molybdates and tungstates as a function of the pH values are shown in **Figure 6**.[53–55]

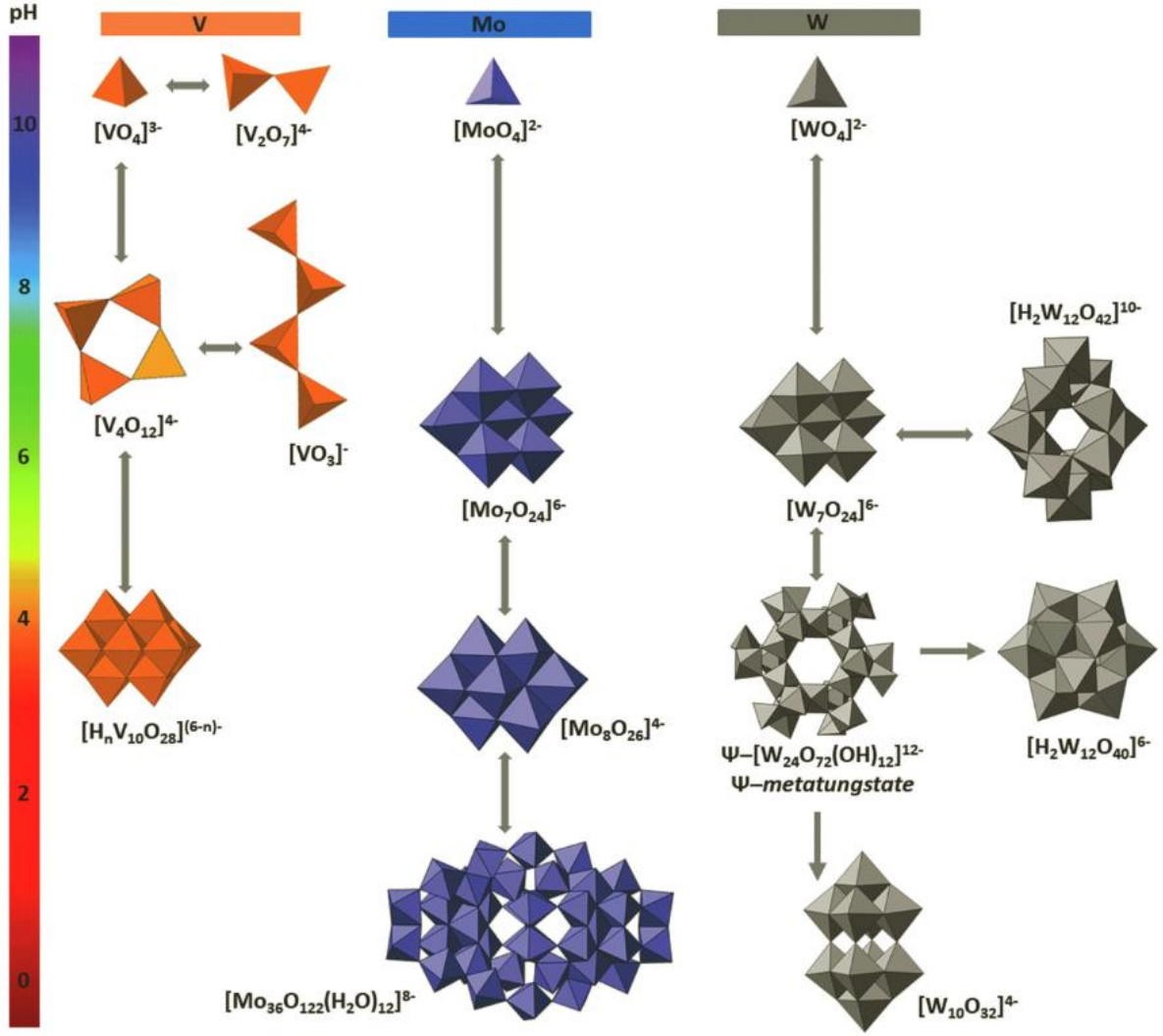

Figure 6: Structure of the main POM clusters ({VO_x}, orange polyhedra; {MoO_x}, blue polyhedra; {WO_x}, gray polyhedra (x = 4-7)) in aqueous solution as a function of pH. Reproduced from Ref.[53] Copyright © 2023. Published and using under permission by Jenny Stanford Publishing Pte Ltd.

In order to produce POM clusters, the simplest synthesis method involves adjusting the pH value of an aqueous solution of $[MO_x]^{n-}$ anions. This leads to complex self-organization of larger structures via condensation of the $\{MO_6\}$ units. The clusters can then be precipitated by adding counterions (e.g. alkali metals or organic cations).[53–55] POMs are very good contenders for energy storage applications owing to their unique electrochemical redox properties. They can engage in fast reversible electron

exchange reactions, as the compounds are highly stable in different oxidation and reduction state. For this reason, POMs are referred to in the literature as electron storage devices or sponges. The Keggin anion $[PMo_{12}O_{40}]^{3-}$ as the most well-known representative can undergo reversible multivalent reduction and oxidation reactions. If all Mo^{VI} ions are reduced to Mo^{IV} ions, 24 electrons are reversibly transferred (**Figure 7**). Furthermore, the main structure remains intact during the redox reaction without changing its molecular geometry. This makes them ideal for use as electrode materials, as no major volume changes occur during redox processes.[46,48–50] The hollow sphere structure of POMs enables a large space and surface area for lithium-ion storage. The diffusion of lithium ions is also facilitated by the large cavities on the molecule. The Li ions fit into the real 3D spaces in the outer edge of the molecular POM clusters.[30,56,57] In this context, the more electrons are absorbed by the POM cluster, the more negative the reduction potential becomes. The cluster is destroyed when a maximum quantity of electrons has been exceeded. The maximum quantity of electrons a cluster can accept is dependent on the type of cluster, the type of metal atoms in the cluster, the electrochemical stability and the operating conditions of the battery.[58,59]

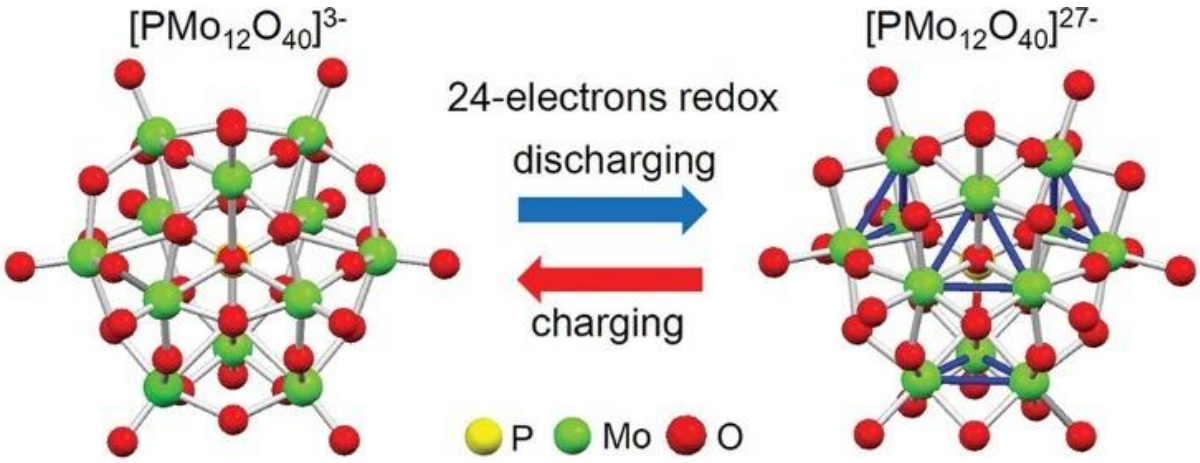

Figure 7: Charging and discharging processes of the Keggin anion $[PMo_{12}O_{40}]^{3-}$ - reversible transfer of 24 electrons. Reprinted with permission from Wang, H.; Hamanaka, S.; Nishimoto, Y.; Irle, S.; Yokoyama, T.; Yoshikawa, H.; Awaga, K. In Operando X-Ray Absorption Fine Structure Studies of Polyoxometalate Molecular Cluster Batteries: Polyoxometalates as Electron Sponges. *J. Am. Chem. Soc.* 2012, *134*, 4918–4924. https://doi.org/10.1021/ja2117206.[51] Copyright © 2012. Published by American Chemical Society.

Various POM clusters with different transition metals have been used for rechargeable batteries. In 2011, the heteropolyoxomolybdate of the Keggin type $K_3[PMo_{12}O_{40}]$ was first investigated for use in LIBs as a cathodic material. The material demonstrated a capacity of above 200 mAh g^{-1} in the range of potentials from 4.2 V to 1.5 V.[60] In further studies, theoretical and experimental investigations were performed to better comprehend the structure and redox characteristics during the charging and discharging processes. Through a reversible 24 electron redox reaction, the total of 12 Mo^{6+} ions will be reduced to Mo^{4+}. In a voltage range of 4.0 V and 1.5 V, this results in a high capacity of about 270 Ah kg^{-1}. Further investigations showed that there is a slight shrinkage of the molecular structure in the reductive phase $[PMo^{12}O^{40}]^{27-}$ relative to $[PMo^{12}O^{40}]^{3-}$.[31,51,61] A vanadium-based POM ($Li_7[V_{15}O_{36}(CO_3)]$) showed outstanding properties as cathodic material for LIBs having a specific capacity of 250 mA g^{-1}, energy densities and power densities of 1.5 kWh L^{-1} and 55 kW L^{-1}, accordingly. The $\{V_{15}O_{36}\}$ clusters contain eight V^{IV} centers and seven V^{V} centers, which exhibit multi-electron redox properties.[31,62] Zhang *et al.* presented a highly stabilized crystalline microporous metal oxide containing Mo, V, and Bi with a large capacity of 380 Ah kg^{-1}, which is an excellent cathode for LIBs. The strategic incorporation of a third metal ion into the crystal Mo-V complex oxides (orth-MoVO) has been successful in increasing the stabilizing properties of the material.[31,63]

1.2.2 Polyoxometalate-Based Inorganic-Organic Hybrid Materials

Although POMs are effective electrode materials owing to their highly defined structure and excellent redox characteristics, their low specific surface area due to agglomeration in the electrolyte and increased solubility in the electrolyte causes shorter lifetimes, reduced capacities, and poorer stability of battery performance.[61,64] In addition, poor cycle and rate performance occurs due to non-uniform and non-nanoscale distribution of POM clusters, which hampers electron transfer among the electrode and the material. The disadvantages can be compensated by forming hybrid or composite materials using different materials with a large surface area or a porous structure. A combination of POM with carbon materials or redox-active organic compounds would improve the functionality, stability and electrical conductivity in combination.[31,32]

Various carbon materials, such as carbon nanotubes (CNTs), single-walled carbon nanotubes (SWNTs), and multi-walled carbon nanotubes (MWNTs), as well as graphene and their derivatives, such as reduced graphene oxide (RGO) or graphene oxide (GO), were reported to enhance the energy storage capacity of LIBs.[31,65] Several approaches have been developed for combining POMs with carbon materials. These include non-covalent functionalization by means of intermolecular interactions, including electrostatic interactions and π-π interactions among POMs and organic materials, and covalent functionalization by covalently grafting POMs onto organic materials. To increase electron transfer and lithium-ion diffusion, a nanohybrid system with POM clusters and nanotubes (SWNTs) was developed. A POM $TBA_3[PMo_{12}O_{40}]$ (where TBA = $[N(CH_2CH_2CH_2CH_3)_4]^+$) has been coated on the surfaces of the SWNTs through electrostatic interactions. The large surface area of the POM/SWNT hybrid system results in a capacity of 320 Ah kg^{-1} (**Figure 8a, c**).[31,65,66] By using graphene in such hybrid systems, the capacitive effect can be improved as graphene has a higher specific surface area than CNTs. As cathode material for application in LIB, $TBA_3[PMo_{12}O_{40}]$/rGO hybrid systems were realized by grafting the POM molecules onto the surfaces of rGO. The POM/rGO hybrid system shows a capacity of approx. 140 Ah kg^{-1} (**Figure 8b, c**).[31,32,65,67]

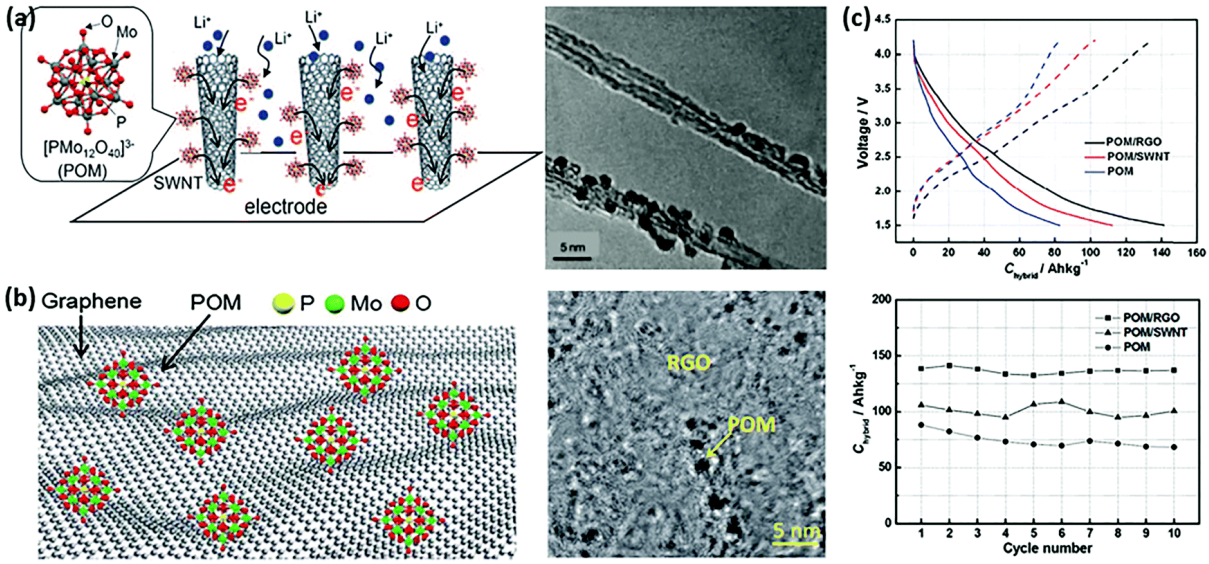

Figure 8: (a) Visualization andTEM image of POM/SWNT hybrids with possible interaction of lithium, Used with permission of John Wiley and Sons, from Kawasaki, N.; Wang, H.; Nakanishi, R.; Hamanaka, S.; Kitaura, R.; Shinohara, H.; Yokoyama, T.; Yoshikawa, H.; Awaga, K. Nanohybridization of Polyoxometalate Clusters and Single-Wall Carbon Nanotubes: Applications in Molecular Cluster Batteries. *Angew. Chem.* 2011, *123*, 3533–3536. https://doi.org/10.1002/ange.201007264; permission conveyed through Copyright Clearance Center, Inc. Copyright © 2011. (b) Visualization and TEM image of $TBA_3[PMo_{12}O_{40}]$/rGO hybrid. Used with permission of Royal Society of Chemistry (RSC), Kume, K.; Kawasaki, N.; Wang, H.; Yamada, T.; Yoshikawa, H.; Awaga, K. Enhanced Capacitor Effects in Polyoxometalate/ Graphene Nanohybrid Materials: A Synergetic Approach to High Performance Energy Storage. J. Mater. Chem. A 2014, 2, 3801–3807. https://doi.org/10.1039/c3ta14569g; permission conveyed through Copyright Clearance Center, Inc. Copyright © 2014. (c) Comparison of electrochemical performances in a LIB. Reproduced from Ref.[65–67] Used with permission of Royal Society of Chemistry (RSC), from Horn, M. R.; Singh, A.; Alomari, S.; Goberna-Ferrón, S.; Benages-Vilau, R.; Chodankar, N.; Motta, N.; Ostrikov, K.; Macleod, J.; Sonar, P.; Gomez-Romero, P.; Dubal, D. Polyoxometalates (POMs): From Electroactive Clusters to Energy Materials. *Energy Environ. Sci.* 2021, *14*, 1652–1700. https://doi.org/10.1039/d0ee03407j; permission conveyed through Copyright Clearance Center, Inc. Copyright © 2021.

The use of conductive redox-active organic molecules and polymers is another strategy for improving the material properties. Due to their excellent conductivity, they improve the transfer of electrons to the POMs.[31] A polyaniline/polyoxometalate hybrid nanofiber was developed as a cathodic material for LIBs, consisting of the phosphomolybdic acid polyanion $[PMo_{12}O_{40}]^{3-}$ and a polyaniline matrix. This compound showed significantly improved electrochemical performance. The polyaniline/polyoxometalate hybrid nanofiber has a high specific capacity (183.4 mA h g^{-1} at 0.1 C), excellent rate capability (94.2 mA h g^{-1} at a rate of 2 C), and stable cycling behavior (80.7% capacity retention after 50 cycles).[49] Based on molybdovanadophosphoric acid heteropolyacid $H_5PMo_{10}V_2O_{40}$ ($PMo_{10}V_2$) and polydopamine, a $PMo_{10}V_2$/PDA microsphere composite is obtained. The material is produced by hydrothermal in-situ polymerization in a strongly acidic medium. The $PMo_{10}V_2$/PDA microsphere composite showed a specific capacity of 915 mA h g^{-1} under a current density of 100 mA g^{-1}, a rate capability of 559.6 mA h g^{-1} under a high current density of 2000 mA g^{-1}, and excellent cycling stability. After 65 cycles, no capacity loss was observed for a current density of 100 mA g^{-1}, and at a high current density of 1000 mA g^{-1}, capacity was maintained even after approximately 93%.[68]

In the literature, all three components POM, carbon material and conductive polymer are often combined. Currently, there is little knowledge about the characteristics of the charge transfer among the conductive carriers and the POMs. This needs to be better understood to enable the commercial applications of this triple combination in LIBs. A graphene/polyaniline/polyoxotungstate cathode material for LIBs (rGO@PANI/PW_{12}) was successfully designed. The rGO@PANI/PW_{12} shows a specific capacity of 285 mA h g^{-1} at 50 mA g^{-1}, a good cycling stability with a capacity loss of only 0.028% per cycle at over 1000 cycles and a rate capability of 140 mA h g^{-1} at 2 A g^{-1}. The good electrochemical properties of rGO@PANI/PW_{12} are explained by the quick electron migration from the reduced PANI polycation to the PW_{12} polyanion along with the strong redox properties of PW_{12}.[65,69] Furthermore, an anode material of PANI, $H_3PMo_{12}O_{40}$ (PMo_{12}) and carbon cloth (CC) ((PANi)-PMo_{12}/CC composite) was developed. The (PANi)-PMo_{12}/CC composite achieves a capacity of 1092 mA h g^{-1} at 1 A g^{-1} for 200 cycles. On the basis of both experimental measurements and theoretical calculations, the possibility of electron migration from PANI to neighboring POM clusters affects the electronic conductivity of the material. The data also show a strong electrostatic interaction between PANI and $[PMo_{12}O_{40}]^{3-}$. Furthermore, the calculations

show that when the adsorption point on the POM cluster is close to a PANI chain, the adsorption energy of Li^+ is lower. This can be explained by the interactions between these units.[31,32,61,65]

POM-based metal-organic frameworks (POMOFs) are attracting much attentions owing to their synergistic and functionally integrated effects. As alternatives to metal ions in MOFs, POMs are ideal building blocks. To prevent the solubilization of POMs in organic electrolytes, MOFs are also investigated as carriers for the immobilization of POMs. POMOFs are suitable for potential applications in LIBs. This is due to their unique combination of POM and MOF properties, including open pore architecture and redox-rich chemistry.[31,65] The first POMOF was designed to enhance the cycling performance of the anodes in LIBs. POMOF-1 consists of an advanced 3D network architecture of flexibly redox-active POM clusters with redox-active organic ligands. POMOF-1 was hydrothermally prepared and consists of $\{Ni_6PW_9\}$ structured building blocks (SBUs) and stiff carboxylate linkers, $\{[Ni_6(OH)_3(H_2O)(en)_3(PW_9O_{34})][Ni_6(OH)_3(H_2O)_4(en)_3(PW_9O_{34})](BDC)_{1.5}\}[Ni(en)(H_2O)_4]\cdot H_3O$ (en = ethylenediamine, H_2BDC = 1,4-benzenedicarboxylic acid). When applied as an anodic material in LIBs, POMOF-1 shows very good electrochemical properties. The intrinsic pore structure allows absorption of major volumetric changes and ion diffusion at comparatively large current rates during cycling. As a result, exceptional cycle stability is observed. During lithiation and delithiation, the local structure and the components remain intact. A discharging capacity of 1421 mA h g^{-1} at a current of 1.25 C with a reversible capacity of about 350 mA h g^{-1} after 500 cycles was achieved.[70] Shortly afterwards, a new POMOF $[PMo_8^{V}Mo_4^{VI}O_{37}(OH)_3Zn_4]$ $[TPT]_5\cdot 2TPT\cdot 2H_2O$ (NNU-11, TPT = tris-(4-pyridyl)triazine) was introduced. The structure of POMOF NNU-11 is ultra-stable due to the directed bonding of Zn-ε-Keggin fragments with the TPT ligands, resulting in 2D layers. The 2D layers are interconnected by π-π stacking effects to form a 3D arrangement. For application in LIBs as an anodic material, NNU-11 shows a discharging capacity of 1322.3 mA h g^{-1} at a current density of 50 mA g^{-1} with a stable reversible capacity of 750 mA h g^{-1} after 200 cycles. This is due to the good redox properties of the POMs and the functionality of the MOFs. NNU-11 shows very good chemical stability owing to the support of π-π stacking effects.NNU-11 was stable in air, aqueous solution from pH 1 to 11, and various solvents.[31,32,65,71]

POM clusters can be integrated into a matrix or onto a substrate by forming a hybrid or composite material. For this purpose, either the POM can be mixed with the

monomer and then polymerized or the prefabricated polymer can be mixed with the POM. These are the options for incorporating the POMs into the polymers.[68,72] Class I POM-based hybrid materials are based on non-covalent interactions, while class II materials are based on covalent interactions. Due to the more stable bonds between the two units, the POM-based hybrid materials are more advantageous but come with synthetic challenges.[73,74] By using conductive and redox-active polymers, it is possible to optimize material properties and electrical conductivity. This results in enormous advantages for electrochemical applications. In particular, polypyrrole, polyaniline, and poly(3,4-ethylenedioxythiophene) (PEDOT) have been as conductive polymers in hybrid materials for LIBs.[45,75–77] Nevertheless, a variety of monomers may be polymerized to electroactive polymers by electropolymerization.[78] These include ortho/para-phenylenediamine[79–81], 1,5-diaminonaphthalene[82] or 1,8-diaminonaphthalene[83]. Combining these materials with POMs results in hybrid materials with superior electrochemical properties.

1.2.3 Composite materials derived from POM-based inorganic-organic hybrid materials

Due to the abundance of transition metal species, POM-based inorganic-organic hybrid materials are also promising source materials. By combining POM [$PMo_{12}O_{40}$] with the subsequent chelating ligands dithiooxamide (DTO) or L-cysteine, POM chelates are obtained. These POM-DTO or POM-L-cysteine chelates are used in the next step to produce D- or L-MoS_2-C composites in the next step via concurrent self-sulfurization and self-carbonization via pyrolysis. The architecture of the MoS_2-C composite material consists of dense Mo_2S bubbles enclosed by thin P- and N-doped carbon layers. The carbon coating and the encapsulating wider carbon substrate are seamlessly welded together, which prevents the active MoS_2 species from detaching and breaking up the conductive network. The composite D-MoS_2-C, which was produced by pyrolysis of POM-DTO chelates, profits from the robustness, elasticity and conductivity of the DTO-derivative carbon network. This material is used as an anodic material in LIBs and has a reversibility capacity after 700 cycles of 1500-2000 mA h g^{-1} at 0.5-1 A g^{-1}.[84] MoO_2 nanoparticles encapsulated in a porous octahedron carbon network were prepared by directly calcining of the POMOF (NENU-5) precursor and subsequent etching step. This synthesis strategy of the MoO_2@C nano-octahedron via precursor treatment enables in-situ generation of a porous carbon

matrices. This increases the ion diffusion of the enclosed MoO_2 nanoparticles and the active centers for the storage of redox ions. For application as an anodic material for LIBs, the MoO_2@C nano-octahedral composites provide a reversible specific capacity of 1442 mA h g^{-1} after 50 cycles at 100 mA g^{-1} and 443.8 mA h g^{-1} after 850 cycles at 1000 mA g^{-1}.[31,85]

1.3 Molybdenum oxide carbide composite materials

Transition metal carbides, oxides and sulfides have been investigated due to their superior theoretical capacity as alternative electrode materials to graphite for LIBs. Molybdenum oxides, such as MoO_3[86–88] and MoO_2[89–91], are considered as potential anode materials for LIBs based on their large theoretical capacitance, high stability, lower electrical resistance, and high electrochemical activity. Compared to molybdenum oxides, molybdenum carbides such as Mo_2C or MoC_x show favorable lithium storage properties on account of the mechanical and chemical stability and the better electrical conductivity.[92–94] The combination of molybdenum oxides and carbides provides promising properties for the possible appliance of these materials in electrodes of LIBs. A single-phase molybdenum oxide carbide was obtained from this combination. This material could be very promising as it has a higher electrical conductivity (than molybdenum oxides) and a higher specific capacitance (than molybdenum carbides). Due to drastic volume changes and strong particle agglomeration that occur during the charge/discharge process. This results in the problems of rapid capacity drop and limited performance of molybdenum carbide, oxide and oxide carbide electrodes. These disadvantages can be overcome by combining molybdenum carbide, oxide and oxide carbides with carbonaceous materials.[94,95]

In general, the conventional industrial production of molybdenum carbides is carried out using powder metallurgical processes. In this process, molybdenum oxides are reduced to elemental molybdenum using hydrogen. The elemental molybdenum is then carburized with carbon powders at temperatures of 1500-2000 °C. The major drawbacks of this process are the high energy consumption and the fact that the Mo2C formed does not exhibit a high specific surface area. This means that the Mo_2C formed is not suitable for the employment in LIBs. Chemical vapor deposition (CVD) is another potential production method. In this process, carbon-containing gases including CO, CH_4 and C_2H_6 are used with Mo-containing precursors such as $Mo(CO)_6$, $MoCl_5$ and

MoF_6 to deposit the materials on various substrates. This method has some problems, the resulting Mo_2C does not show satisfactory purity and pore structure. Furthermore, the equipment for CVD systems is quite complex, the reagents to be used are expensive and the operation is costly. The gaseous Mo precursors are harmful to the environment and living organisms.[96,97]

The production of molybdenum carbides and molybdenum oxide carbides using precursor methods is one of the most promising alternative synthesis strategies. Moderate reaction conditions and a versatile precursor composition allow for a greater flexibility in the size and morphology of the final product. In addition, these methods do not require high energy consumption. Suitable precursors can be produced by precipitation reaction. Subsequent pyrolysis enables the production of the target compound. Several examples of the precursor route are listed below. Mixtures of various molybdates with hexamethylenediamines[98], aniline[99], para-phenylenediamine[100], melamine[101], dicyandiamide[102] and 2-methylimidazole[95]. A new process based on $MoCl_5$ and urea was developed to synthesize Mo_2C and Mo_2N nanoparticles. A polymeric, glassy phase is formed by dissolving $MoCl_5$ in ethanol and adding urea. This is followed by pyrolysis under nitrogen gas flow. Molybdenum carbide or nitride could be produced by varying the molar proportion of metal to urea.[103,104]

Ammonium heptamolybdate $(NH_4)_6Mo_6O_{24}$ (AHM) is a popular source of molybdenum in the precursors. AHM is often used in precipitation reactions with cationic organic compounds.[103] Another potential source of molybdenum is $MoCl_5$[103], but compounds such as MoO_3 and H_2MoO_4 are less commonly used due to their low solubility.[96]

1.3.1 Mechanisms of pyrolysis

Several phases can be formed from the pyrolysis reaction of such precursors. These include orthorhombic high-temperature Mo_4O_{11}[105,106], monoclinic MoO_2[106], orthorhombic Mo_2C[107] and cubic Mo[108]. The dominance area diagram for carbothermic reduction of MoO_2 (**Figure 9**), which illustrates the carbothermic reaction in the Mo-O-C system, shows that MoO_2, MoC and C are in equilibrium at around 600 °C. At this temperature, molybdenum oxide carbides can be obtained. Above 650 °C, Mo_2C is the most stable phase.[109] Further molybdenum carbide products like cubic or hexagonal MoC_x (x = 0.46-0.75) can also be formed. Molybdenum nitrides such as Mo_2N can be produced by the incorporation of amine ligands.[103,109]

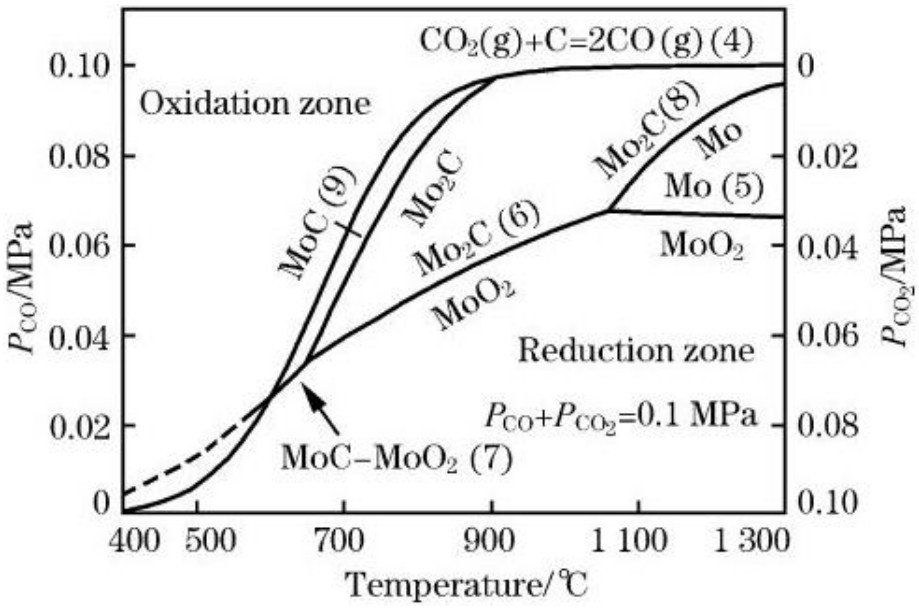

Figure 9: Dominance area diagram for carbothermic reduction of MoO_2. Reproduced from Ref.[109] by permission of Springer Nature and Copyright Clearance Center. Copyright © 2013. Published by Journal of Iron and Steel Research International.

Molybdenum carbide is formed out of the precursor during pyrolysis in a two-stage process. Starting from ammonium heptamolybdate, MoO_3 is formed in the first stage by splitting off H_2O and NH_3 (**Eq. 4**). In the next step, the MoO_3 formed reacts with a carbon source in a carbothermal reduction and forms carbides such as Mo_2C (**Eq. 5**).[97,109,110]

$$(NH_4)_6Mo_7O_{24} \cdot 4\,H_2O \xrightarrow[-\,6\,NH_3]{-\,7\,H_2O} 7\,MoO_3 \qquad \textbf{(Eq. 4)}$$

$$MoO_3 \xrightarrow[-\,1/4\,CO]{+\,1/4\,C} 1/4\,Mo_4O_{11} \xrightarrow[-\,3/4\,CO]{+\,3/4\,C} MoO_2 \xrightarrow[-\,2\,CO]{+\,2.5\,C} 1/2\,Mo_2C \xrightarrow[-\,x\,1/2\,CO_2]{+\,x\,CO} MoC_x \qquad \textbf{(Eq. 5)}$$

$$MoO_2 \xrightarrow[-\,2\,CO]{+\,2\,C} Mo \xrightarrow[-\,1/2\,CO_2]{+\,CO} Mo_2C$$

An excess or lack of carbon leads to unwanted by-products such as elemental Mo or residual oxides. Therefore, the proportion from MoO_3 to the carbon source is decisive.[110]

1.3.2 Crystal chemistry of molybdenum carbides

A brief digression to understand the formation of the respective molybdenum carbide phases with the general composition MoC_x. Various molybdenum carbides can be found in the binary Mo-C phase diagram.[111] Listed according to their carbon content, the structurally characterized modifications are shown in **Table 1**. The hexagonal γ-/γ' MoC (x = 1) has the highest carbon content here. It crystallizes dimorphously in the WC or TiP type structure.[112] At a lower carbon content, a defective cubic NaCl-type structure is formed. This is visible as the carbon content is reduced from x = 0.67 to x = 0.75.[113] A defective hexagonal NiAs-type structure is found at a carbon proportion between x = 0.46 and x = 0.64.[114] Due to the lack of carbon, these phases are stabilized by the corresponding carbon content, suggesting electronic reasons.[115] The orthorhombic phase Mo_2C appears at x = 0.5 and crystallizes in $Fe_2N_{0.94}$ structure type.[107,116] However, the latter phase shows reduced electrochemical activity.[95,117–119] Consequently, the defects in the cubic and hexagonal MoC_x phases could be important in electrochemical intercalation chemistry.[110,120]

Table 1: Crystal chemistry of MoC_x phases.

Composition	**Mo_2C**	**$MoC_{0.46}$ – $MoC_{0.64}$**	**$MoC_{0.67}$ – $MoC_{0.75}$**	**γ-MoC**	**γ'-MoC**
Space group	*Pbcn*	*P*6$_3$/*mmc*	*Fm*$\bar{3}$*m*	*P*$\bar{6}$*m*2	*P*6$_3$/*mmc*
Structure type	$Fe_2N_{0.94}$	defective NiAs	defective NaCl	WC	TiP
Stacking sequence	AB	AB	ABC	AA	AABB

C amount

In addition to the pure carbides MoC_x, it is also possible that oxide carbides $Mo(C,O)_x$, nitride carbides $Mo(C,N)_x$ and oxide nitride carbides $Mo(C,N,O)_x$ are formed. It is not possible to differentiate between these phases using X-ray diffraction due to the small differences between C, N and O.[110]

1.4 Nanoparticles

Among the most important tasks in today's research is to find (create) new materials with better properties. During the last decades nanoparticles are gaining more interest. These classes of materials offer a broad potential range of applications, from catalysis, electronics, energy and textiles to biotechnology and medicine.[121–125] Nanoparticles are characterized by the fact that their size is between 1 and 100 nm. The characteristics of nanoparticles are strongly influenced by their size. The fact that smaller particles have a high surface area is one of the reasons.[124–127] The so called surface effect is induced by the larger surface-to-volume ratio in nanomaterials (**Figure 10**). The reduction of the particle size results in an increase in the number of atoms on the surface. In comparison to bulk atoms, surface atoms tend to be more chemically active due to coordinatively unsaturated surface atoms. This results in a higher surface energy with decreasing the particles sizes.[128,129]

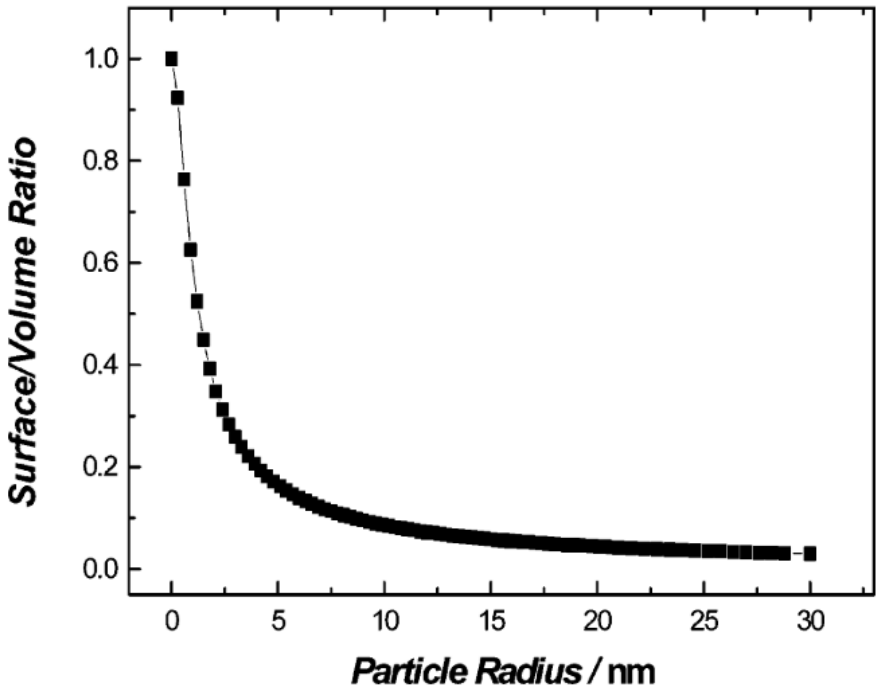

Figure 10: Surface/volume ratio as a relation of the particle size. Reprinted with permission from Burda, C.; Chen, X.; Narayanan, R.; El-Sayed, M. A. Chemistry and Properties of Nanocrystals of Different Shapes. *Chem. Rev.* 2005, *105*, 1025–1102. https://doi.org/10.1021/cr030063a.[128] Copyright © 2005. Published by American Chemical Society.

Another reason for the dependence of particle size on properties is the quantum size effect. Since the electronic wave functions of the conduction electrons in metals and semiconductors delocalize within the particle, the electrons are defined by "particles in a box". In addition, there is a size dependence, since the density of states and the particle energies decisively depend on the size of the box. This changes both the position of the energy states and the distribution of electrons in the energy states, which leads to effects such as a larger band gap in semiconductors. Consequently, the HOMO-LUMO band gaps of semiconductor particles, and thus their absorbance and fluorescence wavelengths, are size related. Thus, as the particle size reduces, the energy difference between the top valence band (VB) and the bottom conduction band (CB) rises Therefore, excitation of the nuclei requires higher energy, which becomes free as the crystal returns to its ground state by a color shift of the emitted light from long-wave (red color) to short-wave (blue color) (**Figure 11**).[128–131]

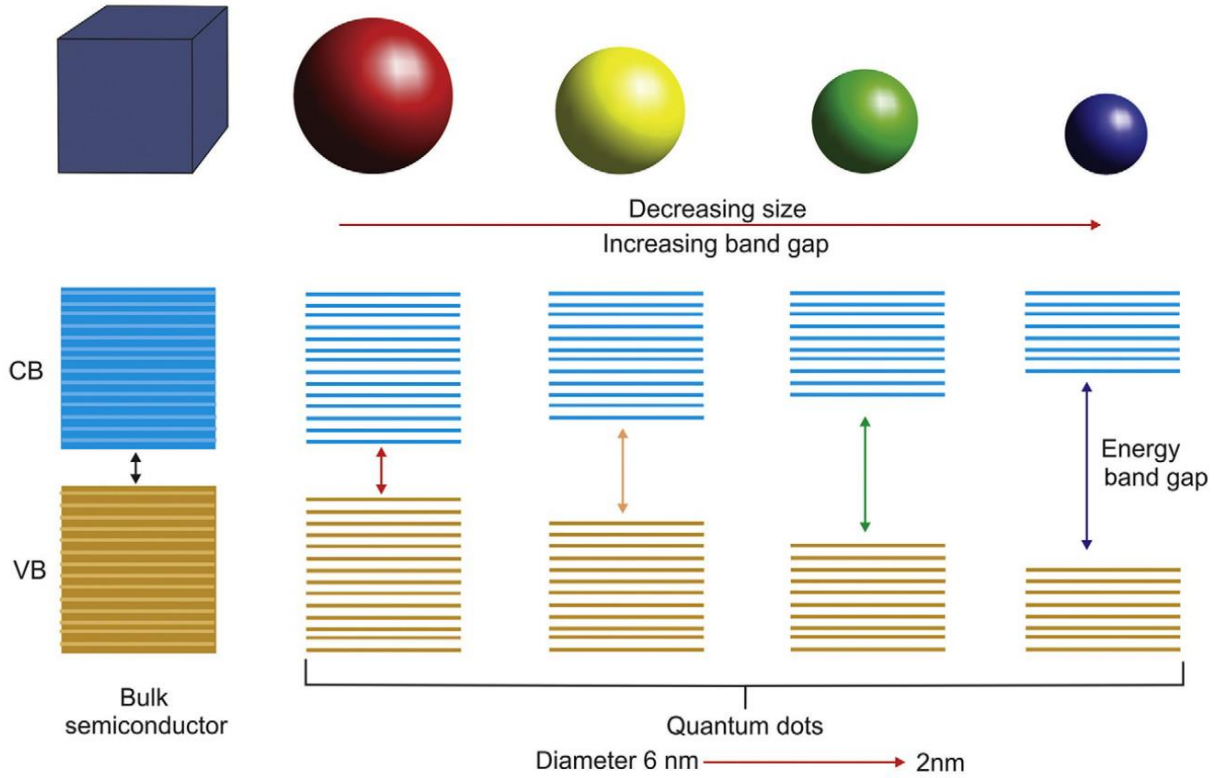

Figure 11: Quantum size effects: Increase in band gap and blue shift as particle size decreases (CB: conductive band; VB: valence band). Reproduced from Ref.[130] by permission of Elsevier and Copyright Clearance Center. Copyright © 2018.

These two effects are mainly responsible for the fact that the chemical and physical characteristics of nanoparticles differ enormously from corresponding bulk materials of the identical compound. It leads, for example, to the melting point decreasing with decreasing particle size. The melting point for bulk tin is 232 °C it can reduced of about 70 °C by decreasing the size of tin nanoparticles.[124,128,132]

CdSe semiconductors usually luminesce in a characteristic red color. It is possible to tune this continuously from red to blue in the length range below 10 nm.[126,133]

1.4.1 Synthesis of Nanoparticles

There are two main strategies for the production of nanoparticles: “top-down” and “bottom-up” method. The “top-down” method starts from a bulk solid, which is reduced to nanoparticles, e.g. by milling. The “bottom-up method, on the other hand, works in the opposite direction, synthesizing nanoparticles from atomic or molecular compounds in a gas or liquid phase. The "bottom-up" technique is more commonly used.[134]

One of the simplest ways to produce nanoparticles is the precipitation reaction. In general, the precipitation reaction proceeds from dissolved reactants in which a new solid is formed. The addition of excess dissolved solids leads to precipitation. In order for nucleation to take place, the solution requires supersaturation. This is either accomplished by dissolving the substance immediately at higher temperatures and then cooling it, or by the addition of a reactant that creates a supersaturated solution as the reaction proceeds. During the precipitation processes the following steps are passed: nucleation, growth, ripening and recrystallization (aging). However, these different steps can also overlap.[128,135]

In the case of first nucleation, a differentiation can be made between homogeneous and heterogeneous nucleation. Homogeneous nucleation occurs without the involvement of other substances by combining dissolved molecules or ions to form nuclei. In contrast, heterogeneous nucleation occurs at structural inhomogeneities (nuclei, impurities, vessel surfaces) to which ions or molecules can attach, e.g., by adsorption, until a nucleus is formed.[128,135–137]

In homogeneous nucleation, the supersaturated solution is not energetically stable from therefore, according to thermodynamics, the process can be considered as a change in the total energy of the particle. This consists of the sum of the surface energy (ΔG_s) and bulk volumetric energy (ΔG_v) (**Figure 12**).[128,135–138]

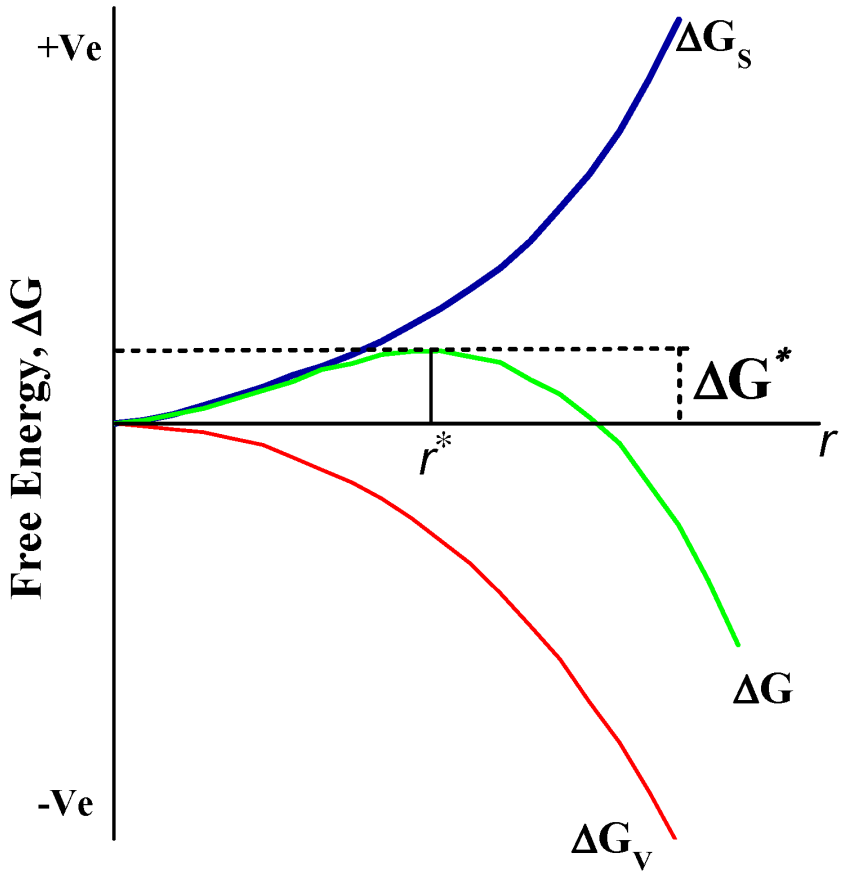

Figure 12: Schematic illustration of the change in Gibb's free energy during nucleation and the growth process. Reproduced from Ref.[138] This figure is published and licensed under an open access Creative Common CC BY license. Copyright © 2021. Published by MDPI.

The total free energy ΔG for a globular particle of radius r is given by the surface energy γ and the free energy of the crystal volume ΔG_v (**Eq. 6**).[128,135–138]

$$\Delta G = 4\pi r^2 \gamma + \frac{4}{3}\pi r^3 \Delta G_V \qquad \textbf{(Eq. 6)}$$

As a consequence, the energy of the crystal (ΔGv) varies depending on the temperature T, the Boltzmann constant kB, the supersaturation of the solution S and its molar volume v (**Eq. 7**).[128,135–138]

$$\Delta G_V = \frac{-k_B T \ln(S)}{v} \qquad \textbf{(Eq. 7)}$$

∆G exhibits a positive maximum for a critical size (r*) when S>1. The activation energy for nucleation is the maximum of the free energy. Stable nuclei form and grow into particles as soon as the nuclei are higher than the critical size and their free energy for growth continues to reduce. If one sets d∆G/dr = 0, one obtains the critical nucleus size r*. The critical radius defines the minimum size that is necessary without the particles dissolving again. Thus, all particles with r > r* will grow and all particles with r < r* will dissolve for a given value of S. The lower the critical nucleus size r*, the lager the saturation ratio S. (**Eq. 8**).[128,135–138]

$$r^* = \frac{2\,\gamma v}{k_B T \ln(S)} \qquad \textbf{(Eq. 8)}$$

Nucleation is a static process because the energy barrier represents the activation energy, so the nucleation rate is represented by the Arrhenius equation (**Eq. 9**). The equation allows three parameters to be varied: Surface free energy, supersaturation and temperature. Where supersaturation has the largest influence on the nucleation rate.[128,135–138]

$$J(T, \Delta G^*) = A\, exp\left(-\frac{\Delta G^*}{k_B T}\right) \qquad \textbf{(Eq. 9)}$$

Heterogeneous nucleation occurs at preferred locations on the surfaces, such as phase boundaries or contamination. At these locations, the effective surface energy is reduced, and consequently the activation energy (energy barrier to nucleation) decreases. Thus, this nucleation is more likely to occur at preferred locations. Therefore, heterogeneous nucleation is more frequent compared to homogeneous nucleation, which is considered to be the driving forces behind successful nucleus-directed grown nanoparticles. However, it is assumed in nanoparticle synthesis that both types of nucleation occur sequentially and also in parallel.[136,137]

After nucleation is complete and a nucleus is formed, these can grow in various ways to form a crystal. The next step of the growth process begins. Growth can occur via molecular additions. This involves the deposition of soluble species onto the solid surface. It is also possible that particles be grown through aggregation with other

particles. Finally, ripening occurs. According to Ostwald ripening, bigger particles further grow while the ones that are smaller decrease in size and dissolve.[128,135]
In the 1950s, LaMer and his colleagues developed another nucleation theory.[139,140] In their mechanism, they conceptually divided nucleation and growth into two stages. This nucleation theory relied on LaMer's studies of the synthetic formation of sulfur sols obtained from the degradation of sodium thiosulfate. First, free sulfur was formed out of the thiosulfate, then sulfur sols were formed in the solution. In three sections, the procedure of nucleation and growth, based on LaMer's process, can be classified: (I) Rapid increasing of the monomer concentration of the solution. Starting from a specific point, a supersaturation level (C_s) is reached. Here homogeneous nucleation can be achieved, but "practically infinitely". (II) An increase in saturation occurs. A level (C_{min}) is reached, here the energy barrier (activation energy) for nucleation may be exceeded. This leads towards fast self-nucleation. (III) Due to this, the supersaturation level decreases and the nucleation period is terminated. Growth is controlled by the diffusion of the monomers across the solvent. The LaMer mechanism is illustrated in **Figure 13**. Here the concentration is represented graphically as a function of time.[136,137,139,140]

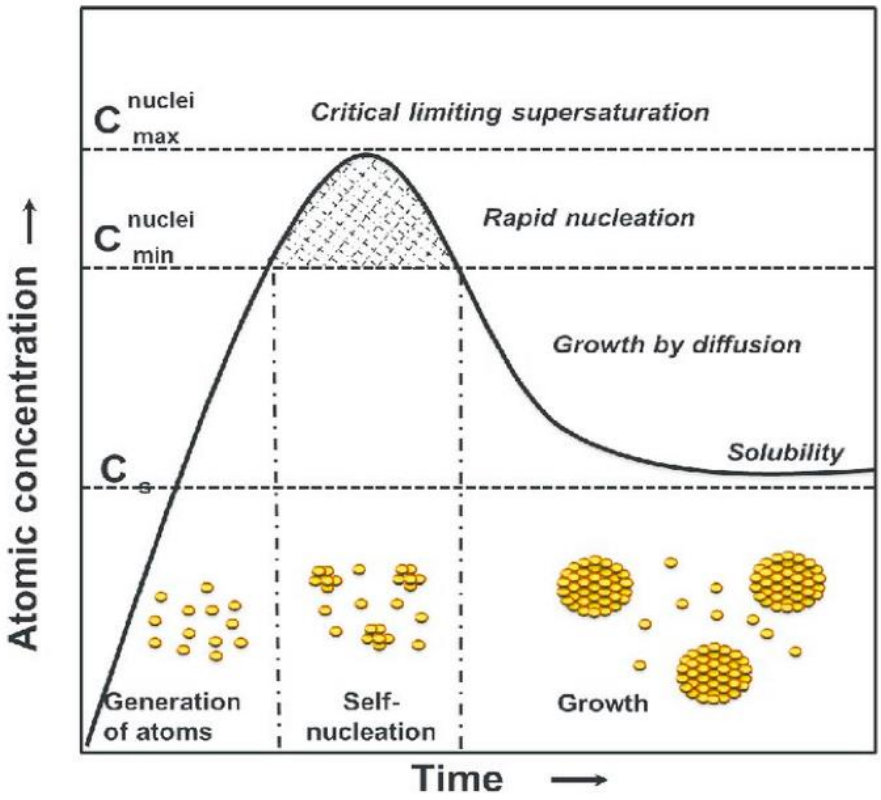

Figure 13: LaMer model the mechanism of nucleation. Reproduced from Ref.[141] This figure is published and licensed under an open access Creative Common CC BY license. Copyright © 2021. Published by MDPI.

Nanoparticle synthesis by bottom-up methods usually follows the nucleation of growth. Traditionally batch processes are then used. Several methods for such wet chemical synthesis are known in literature. The simplest ways to produce nanoparticles is the precipitation reaction. Further strategies are exchange reaction, redox reaction, hydrolysis and sol-gel processing.[134]

The following parameters are important for precipitation reactions in the microjet reactor. A high supersaturation in a short time interval is required. To achieve this, the solubility products of the products must be very low and the solid-forming reaction must take place very quickly. This results in a large number of nuclei promoting the formation of small amorphous or nanocrystalline particles.[142] In addition, precise temperature control and the use of high initial concentrations are beneficial. By avoiding secondary nucleation, narrow particle size distributions can be achieved. This is made possible by quickly reducing the supersaturation as a consequence of the high speed of the surface reaction kinetics. For homogeneous particles, an even supersaturation with no

major local variations is also crucial. A prerequisite for the reduction of locally occurring concentration gradients is very rapid mixing, preferably quicker with respect to the nucleation time.[143]

1.5 Methods for the Continuous Production Particles

Although batch processes are commonly used by default, they have several drawbacks. In batch reactors, inadequate mixing results in a heterogeneous distribution of reactants and temperatures. This results in a wide particle size distribution and poor reproducibility. In addition, scaling up is difficult because larger batches make it more challenging to control reaction parameters and produce inconsistent particles.[134,144,145]

In order to overcome these disadvantages, continuous synthesis comes to fore in science. The last 20 years researcher in these fields developed many approaches for continuous synthesis.[134,146] Two different methods of continuous synthesis of particles can be distinguished: gas-phase continuous synthesis and liquid-phase continuous synthesis. The disadvantages of gas-phase syntheses are that the use of high temperatures leads to highly agglomerated or aggregated particles. In the following, the focus is on continuous synthesis methods in liquid phases.[147–151] Here we have a promising process for consisting and controlled production of particles. Microreactor/microfluidic synthesis allows better control of reaction parameters that affect particle size distribution. This results in more homogeneous particles.[134,146] The large surface area to volume ratio of the microreactor causes an improved heat and mass transfer.[134,152] These methods also allow the scaling-up.[146,153] It is important to reach a high flow rate in order to enable high throughputs.[154] Furthermore, increasing the size of the reactor tubes up to the millimeter range can lead to up-scaling.[155] If an expansion of the reaction chamber proves challenging or for further scale-up, the number of tubes or channels can be paralleled / numbering-up.[156] The massively reduced reaction time at the micrometer length scale offer the possibility to accomplish reaction which would be too fast for conventional methods. Overall through efficient mixing these techniques provide potential for an automated approach which make the use for industrial processes attractive.[134,152] Moreover the microreactors have the advantage of implementing high-throughput screening experiments in optimizing the synthesis condition, determining nucleation and growth kinetics and evaluating material preparation method. This could be achieved equipping the microreactors with

automated sampling and feeding machines[157], online detectors[158], and programmed cooling and heating systems[159]. However, the transformation from batch to continuous processes is not straightforward. The essential parameters - mixing, heat transfer and reaction time - must remain the same when switching from a batch to a continuous process in order to achieve consistent results.[146]

Continuous flow microreactors along with segmented flow microreactors are two main categories into which microreactors can be classified **(Figure 14)**. Several advantages are known for the continuous flow microreactors including facile control, high throughput, large temperature adaptability and easy operation. There are also some disadvantages which are limiting their application such as cross-contamination or clogging from direct contact with the channel walls[160], which urge researchers to develop new strategies.[134]

The simplest continuous flow microreactor is the capillary or tubular microfluidic reactors which has a flow cross sectional area in the micrometer range **(Figure 14a)**. Robust materials such as silica glass[161], stainless steel[162] and polymers (PVC and PEEK)[163] are used for this type of microreactors. The main challenges in the synthesis of semiconductor nanocrystals are high temperatures, corrosive starting materials and fast kinetics.[164] These can be overcome with capillary or tubular microfluidic reactors, which possess special features including ease of use, robust materials and high temperature adaptability.[134]

Segmented flow microreactors still can be categorized into two subgroups. These include gas-liquid (bubble) microfluidic reactors and liquid-liquid or droplet-based microfluidic reactors **(Figure 14b)**. The methods can resolve the problems of continuous flow reactors and additionally provide several advantages like efficient mixing, rapid mass transfer and large interfacial area However, they also present several problems, including the challenge of realizing multi-step reactions, inaccurate controlling the coalescence of droplets with specific reactants to induce the reaction, and droplet instabilities.[134]

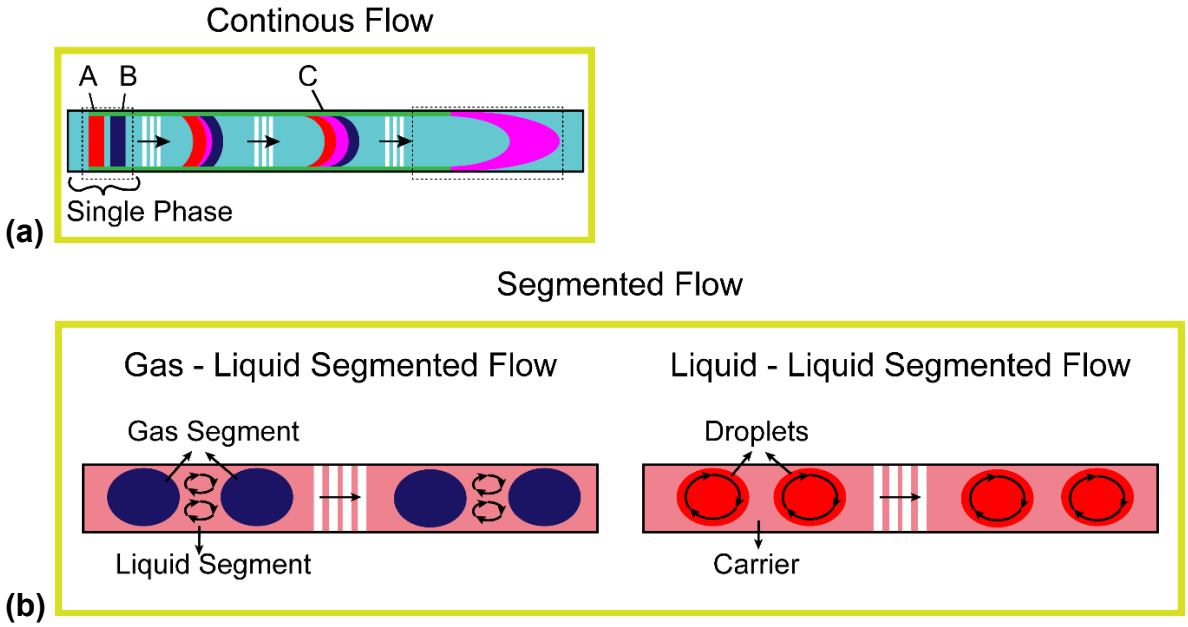

Figure 14: Comparison between the two main synthesis strategies in microreactors (a) continuous flow, and (b) segmented flow.

Inert gas bubbles are created in a segmented gas-liquid reactor to improve the mixture via generating a circulation inside a liquid droplet, while reducing axial dispersion through separation of the liquid droplets among one another. The size distribution is clearly narrowed through the reduced residence time distribution.[165] Although this gas-liquid approach provides a distinct benefit, such as simple isolation from gas and liquid, as the generated particles may contact the channel wall, fluid flow is affected by deposition or clogging. On the other hand, in liquid-liquid segment flow method, the precursor solvent is encapsulated in the liquid droplet. Which prevents contamination or clogging because the liquid droplet does not interact with the channel walls. Moreover, such droplets are accurately controllable and can be influenced in microfluidic reactors, e.g., by droplet formation, droplet separation and droplet fusion.[134]

1.5.1 T-Mixers

In the precipitation of particles, turbulent mixing is a crucial parameter. Reactor design is critical to achieving maximum mixing efficiency. By adjusting parameters such as reactor geometry, channel structure and flow conditions, mixing efficiency can be optimize.[166,167]

The most common geometries are the T- and Y-shaped mixers, which achieve very short mixing times in the range of milliseconds.[168] In the T-shaped mixer (**Figure 15a**), two liquid streams flowing perpendicular to each other mix via a connected straight outlet channel. Similarly, the Y-shaped mixer (**Figure 15b**) also contains a long straight outlet channel, which is connected by two angled inlet channels.[166] Another reactor with a similar geometry is the confined impinging jet reactor (CIJR) (**Figure 15c**). Here, two linear jets of liquid meet and flow into a small cylindrical chamber with a conical head, in which the liquids mix. The liquids leave the reactor through a connected outlet channel.[168,169]

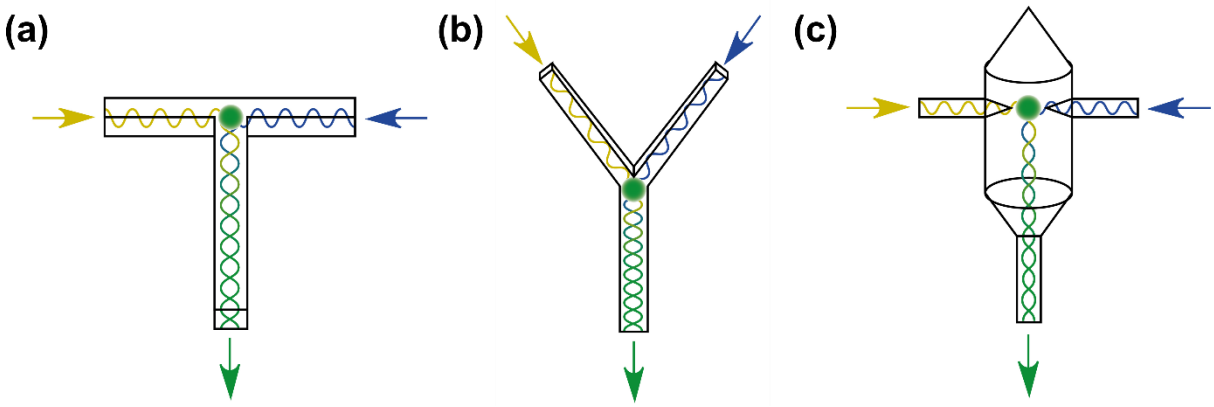

Figure 15: Illustration of the reactor geometries of a) T-shaped, b) Y-shaped and c) confined impinging jets. Educt streams (yellow and blue arrow), product stream (green arrow) and gas stream (orange arrow).

The effectiveness of CIJRs and T-mixers for particle formation during turbulent precipitation for the manufacturing of polymer nanoparticles was investigated by Marchisio *et al.*[169] In addition, researchers created a mathematical model for the optimization, scaling up and design of the reactors for polymer synthesis.[169] The investigations by Marchiso et al.[169] showed that the mixing chambers of CIJRs significantly improved the mixing capability. Smaller particle sizes were achieved with CIJRs. In addition, the CIJRs were highly capable of transforming pressure drop to turbulent kinetic energy. It was also found that reducing the inlet jet diameter resulted in increasing the jet velocity and providing a quicker and more effective mixing (**Figure 16**).[169]

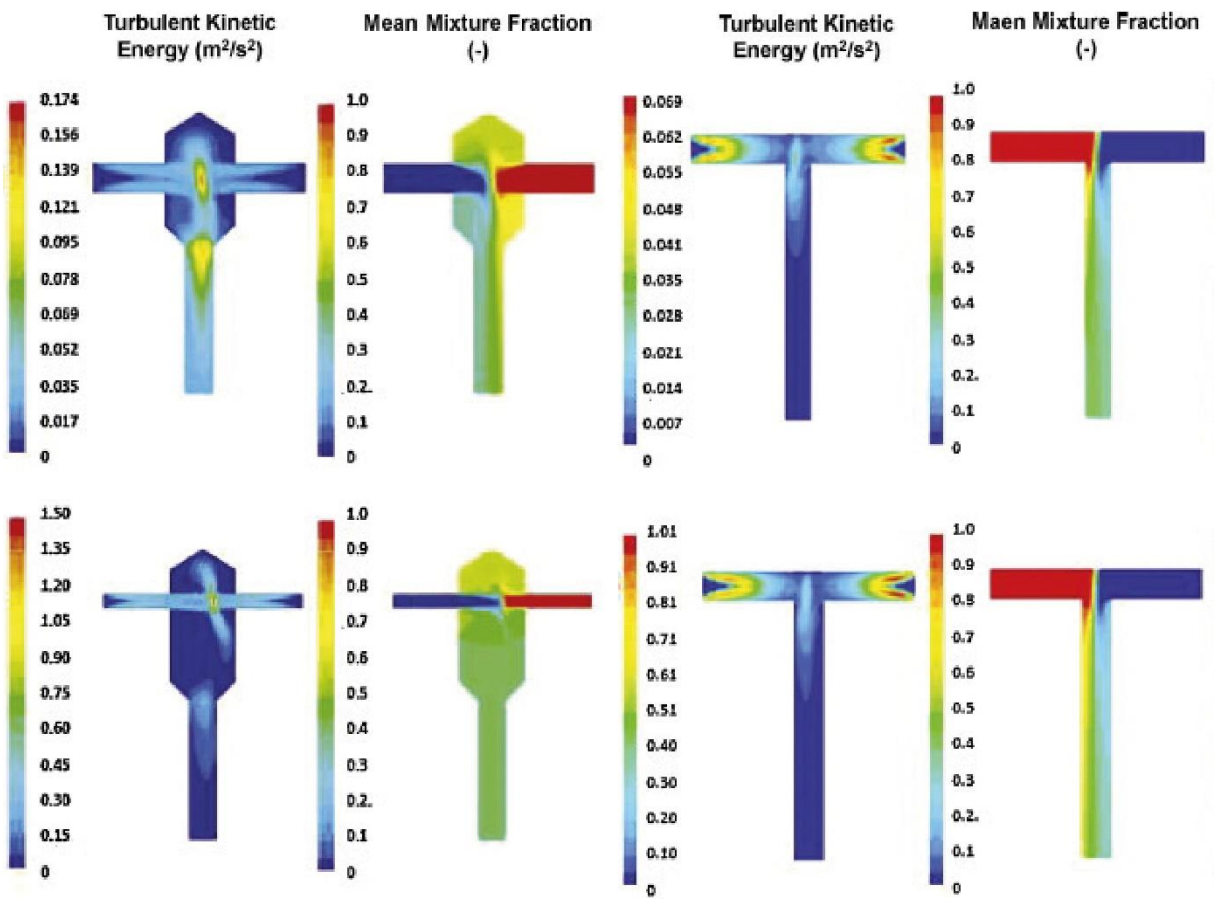

Figure 16: Contour plots for CIJRs and T-mixers of the turbulent kinetic energy (m^2/s^2) and variance of the mixing fraction at a flow rate of 120 ml/min and inlet jet diameters of d = 2 mm (above) and d = 1 mm (bellow). Reproduced from Ref.[169] by permission of Elsevier and Copyright Clearance Center. Copyright © 2011.

1.5.2 Microjet reactor

The microjet reactor was created and patented by Bernd Penth.[170,171] The microjet reactor represents an evolution in comparison to the CIJR. An additional inlet for gases (vertical to the liquid inlets) represents the enhanced improvement (**Figure 17**). This extension makes the reactor extremely suitable for solid particle synthesis, as the additional gas flow carries the product away from the reactor and thus prevents clogging. In the microjet reactor, the liquids are pressed into two inlets through tight nozzles (in the size region of a few hundred micrometers in diameter). As a result, the liquids collide as impinging jet, which leads to high jet velocities and fast mixing conditions.[172,173] New flow conditions result from the additional gas flow and the modified reactor geometry, which leads to new possibilities for particle synthesis.

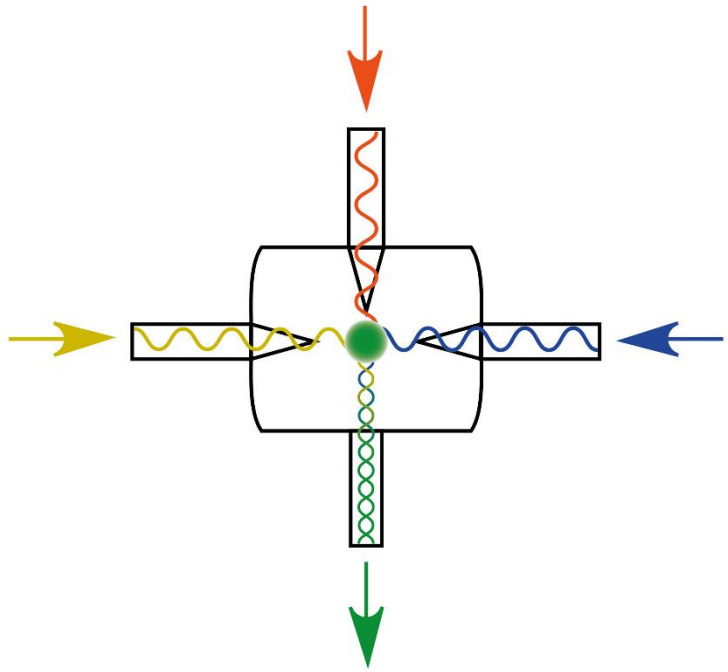

Figure 17: Illustration of the reactor geometries of Microjet reactor.

In research, the microjet reactor has been investigated over the last 20 years for the production of various inorganic, hybrid and pharmaceutical particles. In 2004, Wille *et al.*[174] (Clariant GmbH) investigated the microjet reactor for the synthesis of model azo pigments as part of a screening study of various microdevices with a number of different options. Essentially, the process proved to be suitable for pigment syntheses. However, the limitation to just two reactant flows and the restriction regarding the maximum flow ratio were criticized by the authors. Due to the fact that the collision point shifts once the flow rate ratio reaches a particular value of 1:1.5, which leads to clogging, the reactor was impractical for the special azo coupling reaction (**Eq. 10**).[174]

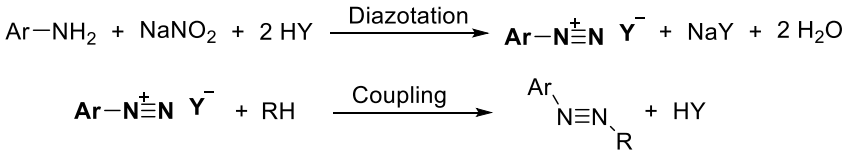

(Eq. 10)

Ar: (hetero-) aromatic group
R: coupling component residue
Y: Cl, Br, NO_2, HSO_4

Rüfer *et al.*[175] studied the capability of the microjet for solid-state synthesis using a precipitation reaction of barium sulphate from barium chloride and potassium sulphate.

The focus of the investigation was on the effect of various variables (reactant and stabilizer concentration, volume flows, supporting gas pressure) on particle size and stabilization against agglomeration. Particle sizes between 60 and 150 nm could be reproducibly adjusted. Similar batch experiments were able to yield particles down to a minimal size of 300 nm. According to the researchers, clogging was completely prevented or reduced by the impinging jet principle, and the rapid and intensive stirring in the microjet reactor had a favorable impact on nucleation. Briefly afterwards, Dittert *et al.*[176] succeeded in synthesizing titanium dioxide nanoparticles with various phase compositions (anatase, brookite, rutile, amorphous) by continuous synthesis via hydrolysis of titanium tetraethylate (TET). The phase content could be influenced most strongly by changing the temperature of the reactant solution. In 2014, Betke *et al.*[172] published a continuous wet-chemical precipitation of zinc oxide (ZnO), magnetite (Fe_3O_4) and brushite ($CaHPO_4 \cdot 2\ H_2O$) particles. The effects of various process variables, including process temperature and flow rate, were methodically analyzed. The particle sizes could be varied between 44 – 102 nm for zinc oxide, 46 – 132 nm for magnetite and 100 – 500 nm for brushite. The polymeric nanoparticles temoporfin loaded with Eudragit®RS 100 (copolymers of methyl methacrylate and ethyl acrylate/ methacrylic acid) was developed for powerful application in the gastrointestinal tract using continuous flow technology with a microjet mixer by Beyer *et al.*[177] These technologies enable the adjustment of a wide range of physicochemical factors, including particle size, size distribution, particle yields, and encapsulation effectiveness. Finally, optimized process parameters allowed the fabrication of 4.5 g of polymeric nanoparticles per hour. Both iron oxides ferrihydrite ($Fe_5O_7OH \cdot 4\ H_2O$) and schwertmannite ($Fe_8O_8(OH)_{4.5\text{-}6}(SO_4)_{1.75\text{-}4}$) were continuously synthesized by the rapid precipitation of iron sulfate and ammonium solutions as published by Reichelt *et al.*[178] In this study, particle sizes ranging from 8.5 up to 53 µm were achieved. The authors investigated the impact of various variables on the chemical product properties, including pH, reactant concentration, and aging behavior. Technical parameters such as the use of a gas stream and the jet diameter were also investigated. A higher jet velocity and increased mixture were achieved by reducing the nozzle and jet diameter. In contrast, a reduction of the nozzle diameter from 100 to 50 resulted in no change in the primary particle size and only a slight reduction in the agglomerate diameter. The authors explained this by saying that the speed was already sufficient with the larger nozzle diameter. This meant that the mixing process could already be completed

before nucleation. Only Brownian agglomeration would be reduced by further increasing the jet speed. Better product homogeneity and a reduction in agglomerate size could be achieved by using a gas stream.

The continuous production of pharmaceutical nanoparticles on the basis of solvent/non-solvent precipitations using microjet reactor technology was described by A. K. Türeli.[179] The efficient control of particle characteristics (size, polydispersity index and drug loading) was investigated as a function of different active ingredients, matrix materials and influences of various parameters such as capillary and nozzle parameters, flow rate, temperature, pressure and solvent type. This made it possible to develop a novel system with improved *in-vitro* properties for the oral administration of drugs. Türeli *et al.*[180] (MJR PharmJet GmbH) utilized the enhanced control of the process variables of the microjet reactor technology. This enabled them to synthesize nanocarriers having increased drug loading through the generation of counter-ion complexes. The authors published a further study[181] on a systematic design of experiments on the characteristics of ciprofloxacin poly(lactic-co-glycolic acid) nanoparticles (PLGA) investigating the influence of the process variables gas pressure, flow rate and temperature. Unlike the known properties of small viscosity systems, a reduction in particle size was observed at low flow rates. This is caused by the large interfacial tension and the large viscosity of dimethyl sulfoxide (DMSO). The low flow rate reduces the solvent and non-solvent volumes in the mixing chamber, which can result in increased diffusion of DMSO toward the water phase.

Additional inorganic compounds prepared using the microjet reactor include yttrium orthovanadate particles by Volk *et al.*[182] and metal chalcogenides by Hieme[152]. Volk *et al.*[182] succeeded in synthesizing high-purity, nanoscale yttrium orthovanadate particles having a mean grain size of 100 nm using microjet reactor technology through a wet chemical precipitation reaction. In a feasibility study, Hiemer *et al.*[152] investigated the preparation of doped metal particles. They succeeded in synthesizing Ta-doped nanocrystalline tin dioxides and cadmium sulfide particles.

Lohmann-Richters and Odenwald *et al.*[183] published a synthetic preparation of cesium hydrogen phosphate particles (CsH_2PO_4). The use of microjet reactor technologies, a scalable, simple and robust method for the production of cesium hydrogen phosphate (CsH_2PO_4) particles below 200 nm was developed. In addition, Odenwald *et al.* published several papers on the use of microjet reactor technologies to synthesize functional organically modified silica (ORMOSIL)[173,184–186] and tin(IV) oxide particles[187]

by sol-gel synthesis. Modl *et al.* carried out a continuous synthesis for surfactant-free platinum nanoparticles using microjet reactor technology.[188]

Corresponding publications from this dissertation extend the list of the above work to include the continuous manufacture of inorganic-organic hybrid materials based on ammonium heptamolybdate as the inorganic unit and para-phenylenediamine (PPD)[189], 1,8-diaminonapthalene (1,8-DAN)[190] or hexamethylenediamine (HMD)[190] as the organic unit. By pyrolysis, these inorganic-organic hybrid materials were used as precursors for composite materials. This made it possible to produce the corresponding metal carbides, nitrides and oxides embedded in a carbon matrix.[110,190]

1.5.3 Flow conditions – Reynolds number

The Reynolds number (*Re*) represents one of the major non-dimensional quantities used to characterize flow conditions in microfluidics. It is determined to be the ratio of the inertial force to the viscous force (**Eq. 11**), wherein u is the mean flow velocity [m/s], d is the hydraulic diameter [m], ρ is the density of the fluid [kg/m^3] and η is its dynamic viscosity [kg/m·s].[166,168,191–194]

$$Re = \frac{u \cdot d \cdot \rho}{\eta} \qquad \textbf{(Eq. 11)}$$

As soon as the decisive Reynolds number is exceeded, the previously laminar flow becomes susceptible towards small disturbances. Once the critical value is reached, a change from a laminarly to a turbulent flow is to be expected. Within the range from 2300 to 4000, the critical Reynolds number can vary.[191,193,195] In macroscopic large pipes, higher Reynolds numbers of more than 4000 can be achieved for the fluid flows. Since the characteristic length for calculating the Reynolds number is an order of magnitude smaller, such high Reynolds numbers cannot be achieved for microreactors operating at low pressures and low flow rates. Under moderate pressures of 1-10 bar, the Reynolds numbers of flows in microreactors rarely reach 2000, so rapid mixing by turbulence in microreactors cannot be achieved at these pressures.[193] Contrary to this, turbulent conditions are achieved in microjet reactors due to high pressures.[170,175] The movement of liquids at low Reynolds numbers is mainly based on molecular diffusion under laminar flow conditions. Difficulties arise in the rapid and efficient mixing of liquids in microreactors due to the drawback of laminar flow.[166] Reynolds number

increases and the micromixing time is shortened due to higher volume flows. The correlation which exists within the Reynolds number or micromixing time and particle size distribution has been investigated in several studies.[168,196]

Barium sulphate precipitates are used as a model system for these investigations. A higher supersaturation was obtained due to rapid mixing and consequently to faster nucleation and growth rates. As a result, more and smaller particles are formed by increasing Reynolds numbersIncreasing the Reynolds number further has little effect on the particle size distribution when the reactant solution is thoroughly mixed prior to particle formation (**Figure 18**).[168]

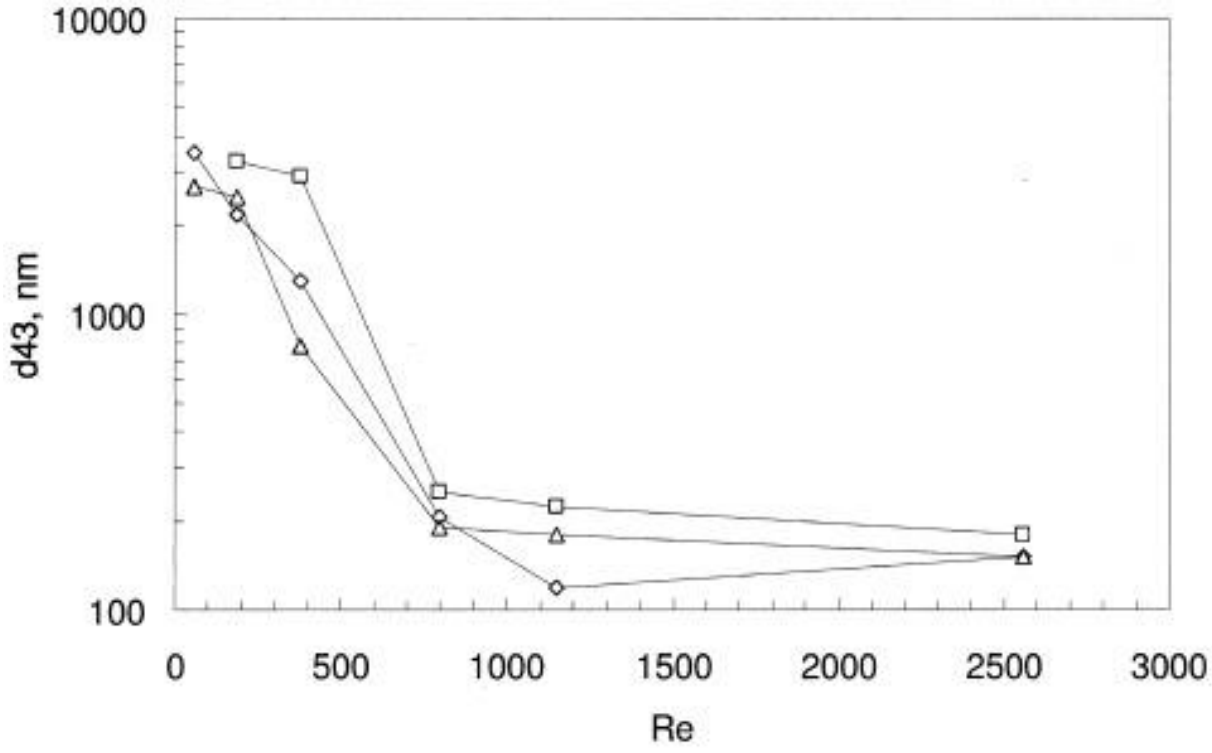

Figure 18: Influence of Reynolds number and average particle size on volume distribution. Reproduced from Ref.[168] by permission of John Wiley and Sons and Copyright Clearance Center. Copyright © 2015.

1.5.4 Mixing efficiency and mixing time

In general, micromixers have shorter mixing times than conventional systems. Usually, micromixer mixing times lie within the region of one second to a couple of milliseconds. The effect of mass transfer on the reaction rate can be clearly reduced on account of the very short diffusion times resulting from the small dimensions.[168,193,197]

In many chemical reactions with liquids, the efficiency depends on the quality of the mixture. By adjusting parameters such as the geometry of the micromixer, the channel structure and the flow conditions, scientists improve the mixing performance. Beyond this, consideration must be given to the influence of the flow behavior of the liquid, diffusion effects and inertia and surface effects on the mixing properties. The only effective variable is the specific power input. That is, improvements in mixing efficiency through geometric optimization are associated with increased energy output.[154,166,198]
One of the common approaches to determine the mixing efficiency is the Villermaux-Dushman reaction, which is based on subsequent concurrent reactions:[199–203]

$$H_2BO_3^- + H^+ \rightarrow H_3BO_3 \qquad \textbf{(Eq. 12)}$$

$$5\,I^- + IO_3^- + 6\,H^+ \rightarrow 3\,I_2 + 3\,H_2O \qquad \textbf{(Eq. 13)}$$

$$I_2 + I^- \leftrightarrow I_3^- \qquad \textbf{(Eq. 14)}$$

In this reaction, the neutralization of boric acid (**Eq. 12**) and the redox reaction (**Eq. 13**) compete for the H^+ ions. The redox reaction (**Eq. 13**) occurs rapidly, but much more slowly compared to the neutralization reaction (**Eq. 12**).[204–206] The iodine generated in the redox reaction undergoes a quasi-instantaneous reaction with iodide ions and forms an equilibrium with triiodide ions (**Eq. 14**).[207,208] The concentration of the triiodide ions formed is detected spectroscopically at 353 nm and are calculated using the Beer-Lambert law. The more I_3^- ions present, the worse the micromixture[196,198,202]
Applying the Villermaux-Dushman test reaction, the mixing efficiency of microjet reactor was analyzed for the setup of 300 µm nozzles and a flow rate of 250 ml/min. A mixing time of 10 ms was determined.[186]

2 Research Goals

The goal of this work is the development of a continuous wet-chemical synthesis of inorganic-organic hybrid materials in a microjet reactor. In addition to the simple and sustainable synthesis of new materials, the analysis and characterization of the products is an essential component.

Continuous wet chemical synthesis in a microjet reactor is a particularly efficient method that generates a high throughput. In addition, the method proves to be particularly advantageous producing particles with a narrow particle size distribution. As a result, this synthesis method is interesting for the production of materials for lithium-ion batteries (LIBs).

The focus is on the synthesis and characterization of new materials for the application as anodic materials in LIBs. In collaboration with the working group of Prof. Dr. Volker Presser from the Leibniz Institute INM (Institute for New Materials), the electrochemical performance the materials produced for their electrochemical performance is being examined.

Several steps are necessary to achieve these goals. The first stage is the preparation and optimization of POM-based inorganic-organic hybrid materials in the microjet reactor. The structure of the resulting compounds will be characterized using X-ray powder diffraction, single crystal structure analysis, thermogravimetric analysis, elemental analysis, IR spectroscopy, solid-state magnetic resonance spectroscopy (NMR) and scanning electron microscopy.

In the next step, composite materials derived from the POM-based inorganic-organic hybrid materials produced above are synthesized via pyrolysis. For structural analysis, these materials are analyzed using X-ray powder diffraction, elemental analysis, Raman spectroscopy, scanning electron microscopy and transmission electron microscopy.

Next, the two classes of materials produced above will be tested for their application as anode materials in LIBs and their electrochemical properties will also be investigated.

The final step is to break down the electrochemical performance of the anode materials with the help of post-mortem examinations and model studies. The following analytical methods are used for this purpose: X-ray powder diffraction, IR spectroscopy, Raman spectroscopy, X-ray photoelectron spectroscopy (XPS), solid-state magnetic resonance spectroscopy (NMR) and scanning electron microscopy.

3 Results and Discussion

This dissertation includes the following peer-reviewed research papers as subsections of the following Results and Discussion chapter.

List of publications:

- Abdirahman Mohamed, M.; Arnold, S.; Janka, O.; Quade, A.; Presser, V.; Kickelbick, G. ***Self-Activation of Inorganic-Organic Hybrids Derived through Continuous Synthesis of Polyoxomolybdate and Para-Phenylenediamine Enables Very High Lithium-Ion Storage Capacity.*** *ChemSusChem* **2023**, *16*, 1–15. https://doi.org/10.1002/cssc.202202213.
- Abdirahman Mohamed, M.; Arnold, S.; Janka, O.; Quade, A.; Schmauch, J.; Presser, V.; Kickelbick, G. ***Continuous Wet Chemical Synthesis of Mo(C,N,O)$_x$ as Anode Materials for Li-Ion Batteries.*** *J. Mater. Chem. A* **2023**, *11*, 19936–19954. https://doi.org/10.1039/d3ta03340f.
- Abdirahman Mohamed, M.; Janka, O.; Harling, S.; Kickelbick, G. ***Precursor-Based Syntheses of Mo(C,N,O)x, Molybdenum Carbide, Nitride, and Oxide Applying a Microjet Reactor.*** *Solids* **2024**, *5*, 443–459. https://doi.org/10.3390/solids5030030.

3.1 Self-Activation of Inorganic-Organic Hybrids Derived through Continuous Synthesis of Polyoxomolybdate and para-Phenylenediamine Enables Very High Lithium-Ion Storage Capacity

This chapter presents the first continuous synthesis of inorganic-organic hybrid materials using the Microjet reactor. The redox-active reactant ammonium heptamolybdate (AHM) was used as the inorganic component and para-phenylenediamine (PPD) as the organic component. These materials are therefore potential contenders as anode materials in LIBs.

The development of low-energy, sustainable processes and high scalability with high reproducibility are particularly important for upscaling the production of battery materials. For applications in LIBs, the production of large surface areas of the materials is crucial. Both particle size and morphology contribute significantly to the electrochemical performance. Furthermore, inorganic-organic hybrid materials offer great adjustability of properties by skillfully combining suitable inorganic and organic components.

Systematic studies showed that depending on the ratio between AHM and PPD and the pH value, two different crystalline hybrid compounds are obtained. The hybrid materials were produced under simple acidic aqueous precipitation reaction in the microjet reactor.

Besides synthesis, the focus is on detailed characterizations of the materials and the study of the electrochemical lithiation of the materials.

Author Contributions:

Mana Abdirahman Mohamed: Conceptualization, materials synthesis, measurements, data analysis, writing, plotting, discussion, and manuscript revision.

Stefanie Arnold: Electrochemical measurements, writing, plotting, discussion, Raman measurements, and manuscript revision.

Oliver Janka: Discussion and manuscript revision.

Antje Quade: XPS measurement, plotting, discussion, and manuscript revision.

Volker Presser: Supervision, discussion, and manuscript revision.

Guido Kickelbick: Conceptualization, supervision, project administration, discussion, and manuscript revision.

Check for updates

ChemSusChem

Research Article
doi.org/10.1002/cssc.202202213

Chemistry Europe
European Chemical Societies Publishing

www.chemsuschem.org

Self-Activation of Inorganic-Organic Hybrids Derived through Continuous Synthesis of Polyoxomolybdate and *para*-Phenylenediamine Enables Very High Lithium-Ion Storage Capacity

Mana Abdirahman Mohamed,[a] Stefanie Arnold,[b, c] Oliver Janka,[a] Antje Quade,[e] Volker Presser,*[b, c, d] and Guido Kickelbick*[a]

Inorganic-organic hybrid materials with redox-active components were prepared by an aqueous precipitation reaction of ammonium heptamolybdate (AHM) with *para*-phenylenediamine (PPD). A scalable and low-energy continuous wet chemical synthesis process, known as the microjet process, was used to prepare particles with large surface area in the submicrometer range with high purity and reproducibility on a large scale. Two different crystalline hybrid products were formed depending on the ratio of molybdate to organic ligand and pH. A ratio of *para*-phenylenediamine to ammonium heptamolybdate from 1:1 to 5:1 resulted in the compound $[C_6H_{10}N_2]_2[Mo_8O_{26}]\cdot 6\ H_2O$, while higher PPD ratios from 9:1 to 30:1 yielded a composition of $[C_6H_9N_2]_4[NH_4]_2[Mo_7O_{24}]\cdot 3\ H_2O$. The electrochemical behavior of the two products was tested in a battery cell environment. Only the second of the two hybrid materials showed an exceptionally high capacity of 1084 mAh g^{-1} at 100 mA g^{-1} after 150 cycles. The maximum capacity was reached after an induction phase, which can be explained by a combination of a conversion reaction with lithium to Li_2MoO_4 and an additional in situ polymerization of PPD. The final hybrid material is a promising material for lithium-ion battery (LIB) applications.

Introduction

The ever-growing demand for portable electronic devices and larger energy storage systems requires optimization and continuous expansion of lithium-ion battery (LIB) technology. The success of this technology is based on its superior energy density, long cycle life, and reliable stability, explaining the dominance of LIB among present-day electrochemical energy storage devices. The most often used anode material in LIBs is graphite, which is limited to a delithiation capacity of 372 mAh g^{-1} (with a stoichiometry of LiC_6).[1] Therefore, other materials, such as mixed metal oxides e.g. $Li_4Ti_5O_{12}$ (LTO),[2] or nanoparticles of transition metal oxides, such as CoO, CuO, and Fe_2O_3, are currently under investigation for an improved battery performance.[3–5] One of the major problems with some new electrode materials is the significant volume change during lithiation and delithiation, which can lead to fractures in the electrode and often results in capacity fading.[6]

Inorganic-organic hybrid materials exhibiting redox activity are promising candidates for simultaneously solving several problems, for example, lower energy consumption during production or lower volume expansion during intercalation compared to traditional pure inorganic materials. Polyoxometalates (POMs), with their unique electrochemical redox properties and high stability with distinct oxidation and reduction states, are ideally suited as the inorganic component in such materials.[7] One of the most prominent examples is the phosphomolybdate anion, especially $[PMo_{12}O_{40}]^{3-}$ with a Keggin structure that shows fast and reversible electron transfer reactions without changing its molecular geometry.[7,8] Pure polyoxomolybdates $[Mo_7O_{24}]^{6-}$ and $[Mo_8O_{26}]^{4-}$ show redox activity and are readily available through acidifying an aqueous molybdate solution.[9] Particularly, the heptamolybdate anion $[Mo_7O_{24}]^{6-}$ is an exceptionally redox-active polycounterion showing metal-centered redox processes.[10–12] One strategy to increase capacity is to blend POMs with redox-active organic

[a] *M. A. Mohamed, Dr. O. Janka, Prof. Dr. G. Kickelbick*
Inorganic Solid-State Chemistry, Saarland University
Campus C4 1, 66123 Saarbrücken (Germany)
E-mail: guido.kickelbick@uni-saarland.de
Homepage: https://www.uni-saarland.de/en/chair/kickelbick.html
[b] *S. Arnold, Prof. Dr. V. Presser*
INM—Leibniz Institute for New Materials
66123 Saarbrücken (Germany)
E-mail: volker.presser@leibniz-inm.de
Homepage: http://www.leibniz-inm.de/en/research/interface-materials/energy-materials/
[c] *S. Arnold, Prof. Dr. V. Presser*
Department of Materials Science and Engineering, Saarland University
66123 Saarbrücken (Germany)
[d] *Prof. Dr. V. Presser*
Saarene—Saarland Center for Energy Materials and Sustainability
66123 Saarbrücken (Germany)
Homepage: http://saarene.de
[e] *Dr. A. Quade*
Leibniz Institute for Plasma Science and Technology
Felix-Hausdorff-Straße 2, 17489 Greifswald (Germany)
Homepage: https://www.inp-greifswald.de/en/

Supporting information for this article is available on the WWW under https://doi.org/10.1002/cssc.202202213

This publication is part of a Special Collection highlighting "The Latest Research from our Board Members". Please visit the Special Collection at chemsuschem.org/collections.

ChemSusChem
Research Article
doi.org/10.1002/cssc.202202213
Chemistry Europe
European Chemical Societies Publishing

molecules to yield inorganic-organic hybrid materials. *para*-Phenylenediamine (PPD) represents an excellent redox mediator through a two-electron oxidation-reduction reaction. Moreover, PPD can polymerize under electrochemical conditions.[13–16] Furthermore, the two nitrogen atoms provide a possible coordination site for Li^+ during the lithiation-delithiation process. Therefore, they can improve the Li mobility of hybrid materials made of this organic compound. An example of a redox-active inorganic-organic hybrid system is the combination of phosphomolybdate polyanion $[PMo_{12}O_{40}]^{3-}$ and a polyaniline matrix, which was applied as cathode materials for LIBs.[8] Also, POM-based metal–organic frameworks (POMOFs) materials,[17] a POM-incorporated metallapillararene metal–organic framework (MOF),[18] and metallacalixarene MOFs with different Keggin type polyoxometalates showed already promising electrochemical performance as LIB anode materials.[18] Porous POMOF anode materials revealed high chemical stability and reached a capacity of 710 mAh g^{-1} after 50 cycles with a specific current of 100 mA g^{-1}. The likewise promising capacity retention of 82% at a high rate of 800 mA g^{-1} after 500 cycles complement these findings.[19] A stable chiral three-dimensional POM-based MOF built by achiral 1,3-bis-(4-pyridyl)propane (BPP) and Zn-ε-Keggin showed an enhanced electrochemical activity as an anode of LIBs reaching a highly reversible capacity of 1004 mAh g^{-1} at 100 mAh g^{-1} after 100 cycles.[20] Finally, Zhang et al. presented a new redox-active poly-counterion doping concept that improves the capacity performance of conducting polymers.[11]

To further advance LIB technology, improved performance of electrode materials must be combined with the possibility of large-scale production processes. Our previous studies have shown that precipitation methods, usually carried out in batch processes, can be converted into a continuous process by using a so-called microjet reactor.[21,22] This opens up the possibility for large-scale and low-energy-consuming production of well-defined (nano)particles. In this process, two reactant solutions are fed under high pressure into a reaction chamber where rapid mixing takes place and the nucleation process is initiated. A gas jet then removes the product from the mixing chamber, and particle growth takes place on the way to the collection vessel. The separation of nucleation and growth allows good control of particle properties and has already been used in the production of silicon oxycarbides for LIB applications.[23–25] The main advantages of this process in the production of energy materials are its scalability, low energy consumption, and avoidance of additional additives.[26]

In this work, we present a systematic study of the formation of an inorganic-organic hybrid material precipitated from *para*-phenylenediamine (PPD) and ammonium heptamolybdate (AHM). PPD fulfills two roles here, firstly it can be protonated during the acid precipitation process and replaces the charge balancing ammonium ions, secondly it can support the electrochemical activity of the hybrid materials formed by its own redox activity. Hybrid materials with similar composition were known from literature as precursors for pyrolytic preparation of Mo_2C.[27] In contrast to previously published work in which the hybrid materials were thermally decomposed, we asked ourselves whether the thermally untreated materials could already be used as potential electrode materials. It was important to find out whether the ratio between organic and inorganic components in the precipitation reaction also has an effect on the composition of the precipitated product and its electrochemical activity.

Results and Discussion

Precipitation reaction of inorganic-organic hybrid material

Inorganic-organic hybrid materials are formed by a precipitation reaction in an aqueous solution by mixing AHM as a molybdenum source with PPD under acidic conditions (Figure 1).

For the precipitation of the hybrid material, the organic molecules must have Lewis-basic functional groups that allow the formation of cations under acidic conditions and allow a full or partial exchange of the ammonium ions in the starting material. The resulting precipitate forms a salt between the molybdate anions and PPD cations.

Prior to the use of the microjet, various molar ratios between the organic compounds and the molybdenum source (1:1 to 30:1) were applied in initial batch reactions to investigate the correlation between the formation of inorganic-organic hybrid materials and the reactants used. These studies were transferred to the continuous production of the inorganic-organic hybrid materials with a microjet reactor, which allows the continuous formation of these precipitates.[21,22] Reactant

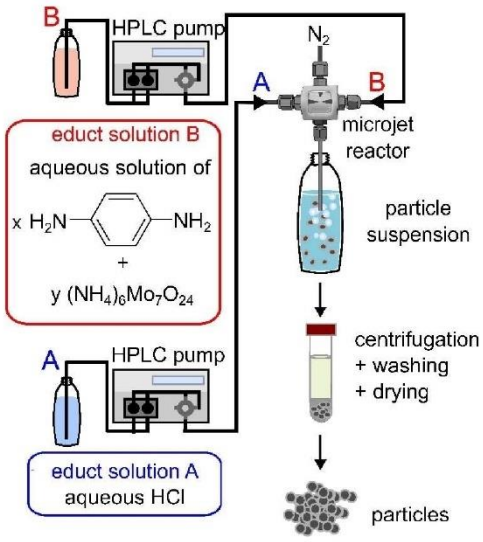

Figure 1. General reaction scheme for the production of the PPD/molybdate products.

ChemSusChem
Research Article
doi.org/10.1002/cssc.202202213
Chemistry Europe
European Chemical Societies Publishing

solutions 1 contained AHM and PPD in addition to a diluted solution of HCl (reactant solution 2, see experimental section).

Various analytical methods were used to characterize the product formed. For example, FTIR spectroscopy detected a broad band at 3550–3350 cm^{-1}, which can be assigned to the stretching vibration of the N–H group of PPD.[28] In addition, a broad band at 3600–3200 cm^{-1} indicates the presence of water.[29] The vibrations at 1650–1550 cm^{-1} are based on the bands of N–H deformation vibrations. In addition, there are C=C stretching vibrations at 1500–1480 cm^{-1}. Moreover, the typical bands of molybdate entities are found between 935 cm^{-1} and 810 cm^{-1} (Figure 2a). These observations confirm the incorporation of the organic and the inorganic components in the precipitates.[30–33] A comparison of the FTIR spectra of the

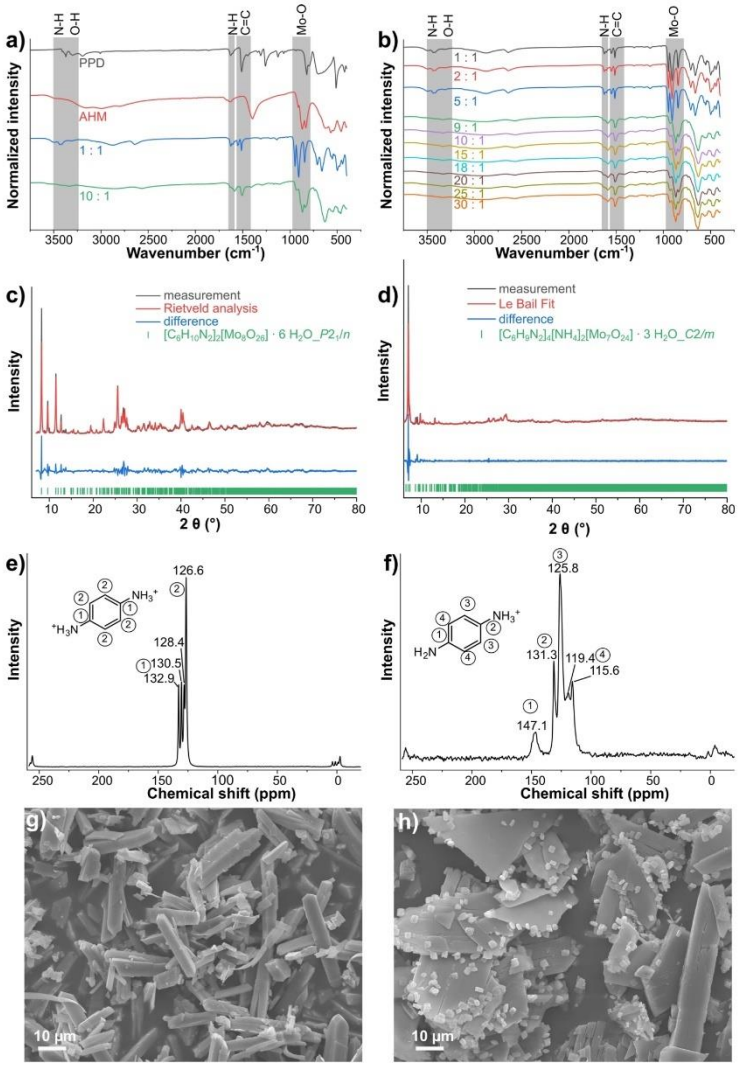

Figure 2. Material characterization: (a) FTIR spectra of PPD/molybdate precipitates in different ratios compared to their reactants. (b) FTIR spectra of PPD/molybdate in different ratios. (c,d): X-ray diffractograms of two different PPD/molybdate precipitates (ratios 10:1 and 1:1). (c) Rietveld refinement of PPD/molybdate (1:1). (d) Le Bail fit of PPD/molybdate (10:1). Differences in the intensities can be attributed to texture problems or preferred orientation. (e,f): ^{13}C CP-MAS NMR spectra. (g) Scanning electron micrograph of PPD/molybdate (1:1). (h) Scanning electron micrograph of PPD/molybdate (10:1).

ChemSusChem
Research Article
doi.org/10.1002/cssc.202202213
Chemistry Europe
European Chemical Societies Publishing

PPD/molybdate precipitates revealed that the samples with the ratios 1:1, 2:1, and 5:1 containing low amounts of PPD differ from those with higher organic ligand content (Figure 2b).

Elemental analyses for the precipitates (see Supporting Information, Table S1) reveal two regions with different compositions depending on the mixing ratio, indicating the formation of at least two different compounds. The samples with ratios of 1:1, 2:1, and 5:1 correspond to the composition $[C_6H_{10}N_2]_2[Mo_8O_{26}]\cdot 6\,H_2O$. In contrast, the samples with a mixing ratio from 9:1 to 30:1 indicate a composition in line with $[C_6H_9N_2]_4[NH_4]_2[Mo_7O_{24}]\cdot 3\,H_2O$.

Powder X-ray diffraction confirmed the existence of the literature known product $[C_6H_{10}N_2]_2[Mo_8O_{26}]\cdot 6\,H_2O$ in the precipitate of the PPD to AHM ratios 1:1 up to 5:1 (Figure S2a). No other phases corresponding to side products were observed in all those diffractograms. $[C_6H_{10}N_2]_2[Mo_8O_{26}]\cdot 6\,H_2O$ crystallizes in the monoclinic crystal system with the space group $P2_1/n$ and lattice parameters $a=834.31(9)$, $b=2145.8(3)$, $c=1027.6(1)$ pm, and $\beta=99.415(2)$.[34] The structure of the compound, which was previously characterized by single-crystal X-ray analysis, showed the existence of two octamolybdate anions, $[Mo_8O_{26}]^{4-}$, four double-protonated PPD cations, and twelve water molecules per unit cell. The octamolybdate clusters $[Mo_8O_{26}]^{4-}$ are surrounded by H_2PPD^{2+} cations with an open channel structure and octamolybdate clusters as guests (Figure S1).[34] Larger amounts of PPD (mixing ratio from 9:1 to 30:1) lead to different diffraction patterns (Figure S2a) and significantly different composition, based on the data from elemental analysis. Structural investigations on single crystals of this compound are extremely difficult since it crystallizes as very thin hexagonal platelets (Figure S3), which are very fragile and show a high degree of stacking faults. From the obtained dataset, a monoclinic structure with a space group C2/m and lattice parameters of $a=2029.9(1)$ pm, $b=1819.6(1)$ pm, $c=2521.2(1)$ pm, and $\beta=90.6(1)^\circ$ and the presence of four $HPPD^+$ and one $[Mo_7O_{24}]^{6-}$ anion per formula unit can be deduced (Figure S4). The monoprotonated PPD cations can be unambiguously deduced when measuring the pH value of the supernatant from which the crystals were obtained. The measured pH was 4.4, therefore, when using the pK_a values from the literature ($pK_{a1}=2.67$, $pK_{a2}=6.2$),[35] only the first protonation can take place. For reasons of electroneutrality, two NH_4^+ cations must be present in the crystal structure. From the difference Fourier maps, the remaining electron density was attributed to these two ammonium cations and water molecules with the NH_4^+ cations being arbitrarily located. A total of 3 H_2O molecules could be derived, however, severe disorder of these is present. This results in a sum formula of $[C_6H_9N_2]_4[NH_4]_2[Mo_7O_{24}]\cdot 3\,H_2O$. Details on the structural determination can be found in the Supporting Information (Tables S2 and S3).

The information obtained from the structural analysis agrees well with combination of the previously discussed CHN (Table S1), X-ray data (Figure S2a), and TGA-FTIR data (thermogravimetric analysis coupled with Fourier-transform infrared spectroscopy; Figure S7).

The transition range 5:1 to 9:1 between the observed formation of the two compounds was studied in more detail. For this purpose, the mixing ratios 6:1, 7:1, and 8:1 were investigated. At the mixing ratio of 6:1, the formation of $[C_6H_{10}N_2]_2[Mo_8O_{26}]\cdot 6\,H_2O$ occurs, but there are also new reflections indicating the formation of a new component. At a mixing ratio of 7:1, the reflections of $[C_6H_9N_2]_4[NH_4]_2[Mo_7O_{24}]\cdot 3\,H_2O$ are observed, along with some new reflections that were also visible at 6:1. Finally, at a mixing ratio of 8:1, only $[C_6H_9N_2]_4[NH_4]_2[Mo_7O_{24}]\cdot 3\,H_2O$ appears to form (Figure S2b). Rietveld refinement based on the single-crystal data from the literature was performed for the PPD/molybdate precipitate with mixing ratios from 1:1 to 5:1 (Figure 2c). For mixing ratios of 9:1 to 30:1, Le Bail refinements were performed using the structural information obtained from the single crystal investigations (Figure 2d).

Since the reaction conditions (temperature, total volume, amount of hydrochloric acid) were kept constant and only the AHM to PPD ratio was varied, the synthesis of the inorganic-organic hybrid material seems to depend mainly on two parameters: (I) the content of organic components and thus (II) the pH of the solution. It is known that an acidic reaction leads to the condensation of ortho-molybdates enabling the formation of larger molybdate clusters [Eq. (1)].[9,34,36,37] An increasing PPD content results in an increase of the pH, thus removing protons from the system, and subsequently hampering the formation of the octa-molybdate cluster, underlining the observation of a hepta-molybdate cluster in the precipitate of the reactions containing a high PPD to molybdate ratio.

$$7\,[MoO_4]^{2-} \underset{-\,4\,H_2O}{\overset{+\,8\,H^+}{\rightleftharpoons}} [Mo_7O_{24}]^{6-} \underset{-\,2\,H_2O}{\overset{+\,MoO_4^{2-},\,4\,H^+}{\rightleftharpoons}} [Mo_8O_{26}]^{4-} \qquad (1)$$

^{13}C CP-MAS NMR spectra (cross polarization-magic angle spinning nuclear magnetic resonance spectra) of the PPD/molybdate (Figure 2e,f) confirm the presence of double protonated diamines in PPD/molybdate (1:1) (H_2PPD^{2+}) (Figure 2e) and mono-protonated diamines in PPD/molybdate (10:1) ($HPPD^+$) (Figure 2f). The presence of two different compounds forming in the respective precipitates is supported by scanning electron microscopy (SEM; Figure 2g,h). Variations of morphologies of the crystals were observed for different precipitates (Figure S3). Smaller amounts of PPD lead to anisotropic rod-shaped morphologies. In comparison, larger PPD amounts lead to sheet-like morphologies, which underpins the formation of different compositions depending on the AHM:PPD ratio obtained by CHN analysis. The temperature in the microjet synthesis influences the particle size. Thus, increasing temperature leads to smaller particle sizes (Figure S5).

Thermogravimetric analysis (TGA) provides valuable information on the synthesized inorganic-organic hybrid material (Figure S6). Pristine AHM shows three mass loss events up to 300 °C, based on the loss of water and ammonia.[38] According to the literature, after the decomposition of the precipitate, MoO_3 has formed, which sublimes and leads to the observed mass loss.[38] The sublimation of MoO_3 starting at 600 °C can be explained by its relatively high vapor pressure.[39–42] For the

ChemSusChem
Research Article
doi.org/10.1002/cssc.202202213
Chemistry Europe
European Chemical Societies Publishing

PPD/molybdate precipitates, two different trends of the TGA curves are visible. At low PPD concentration (exemplarily shown for the 1:1 ratio), the TGA curve show three mass losses, while at higher concentrations (10:1) only two mass losses were observed. For the 1:1 ratio, the first mass loss originates from the desorption of adsorbed surface water and the second from the loss of crystal water. The decompositions of the precipitates show similar thermal behavior to carbon-supported ammonium molybdate decomposition.[34] These conclusions are supported by TGA-FTIR measurements (Figure S7). According to the chemical composition $[C_6H_{10}N_2]_2[Mo_8O_{26}] \cdot 6\,H_2O$ the loss of six water molecules fits the value of the second mass loss. The third mass loss at around 700 °C shows the loss of CO and CO_2, leading to carbide phase formation. In contrast, the first mass loss observed at higher PPD concentrations results from the release of water and ammonia at around 192 °C, and the second mass loss is again the decomposition of the organic component, proven by the detection of CO and CO_2.

Electrochemical characterization of PPD/molybdate as LIB anode

The various synthesized hybrid materials were investigated for their suitability for energy storage systems. The materials were subjected to conventional LIB processing, namely, casting after compounding with carbon black conductive additive and polyvinylidene fluoride binder. Cyclic voltammetry was performed at different scan rates (0.1–10 $mV\,s^{-1}$) in the voltage range from 0.01 V to 3.00 V vs. Li^+/Li to evaluate the underlying lithium-storage mechanism in the obtained electrodes (Figures 3a,b and S8). For both hybrid systems (PPD/molybdate (1:1) and PPD/molybdate (10:1)), one clear reduction/oxidation peak couple is found at 1.3 V and 1.5 V vs. Li^+/Li, respectively. The transformation reaction, involving the formation of amorphous Li_2O and complete reduction of the molybdates, can be attributed to the obtained region when the lithiation potential decreases from 1.5 V to 0.05 V vs. Li^+/Li.[43]

The pseudocapacitive feature can be further investigated by a kinetic analysis that includes an analysis of the rate-dependent current signal. The relationship between the current (i) and scan rate (v) is given by $i = av^b$, where a and b characterize the fitting parameters. Thereby obtained b-values of 0.5 correspond to an ideal diffusion-limited charge storage process typical for battery-like behavior. At the same time, a b-value of 1 indicates a perfect surface-limited charge storage process typical for electrosorption processes/capacitive processes.[44–46] The b-value analysis conducted on cyclic voltammetry is shown in Figure S9. The pronounced lithiation-delithiation peak of PPD/molybdate (1:1) shows a b-value of 0.82 and 0.79, respectively. The more pseudocapacitive regions at 0.62 V and 2.75 V vs. Li^+/Li exhibit slightly enhanced b-values of 0.94 and 0.82 for delithiation, respectively. For the same regions in the lithiation curve, however, we obtain lower values of 0.71 and especially 0.56, which are closer to the values for the ideal diffusion-limited charge storage process. The b-value analysis of PPD/molybdate (10:1) provides for the pronounced lithiation-delithiation peak of PPD/molybdate (10:1) a b-value of 0.63 and 0.74. The additional values obtained at 0.62 V and 2.75 V vs. Li^+/Li characterize significantly more pseudocapacitive regions with much higher b-values of 0.91 and 0.93 for delithiation and 0.73 as 0.86 for lithiation, respectively.

To further investigate the electrochemical performance and associated conversion reaction of the different hybrid samples, galvanostatic charge and discharge experiments were performed. The obtained reduction and oxidation peaks from cyclic voltammetry are consistent with the galvanostatic discharge and charge curves (Figure 3c,d). No clear plateaus can be detected for the PPD/molybdate (1:1) sample, which cannot be assigned to associated (redox) reactions. In the sample with a higher insertion of PPD, there is no pronounced plateau in the first cycles, but after a while, there are two clear plateaus at 1.35 V and 0.8 V vs. Li^+/Li. This indicates that different reactions occur during cycling, supported by continuously increased capacity observed during the first cycles. In general, an increase in capacity is attributed to pre-activation of the material.[47,48] However, this cannot explain the persistent increase during more than 120 cycles, which started with a delithiation capacity of 195 $mAh\,g^{-1}$ and reached a very high value of 1084 $mAh\,g^{-1}$ in the 150th cycle (Figure 3e). This 556% increase must be related to a change in the electrode material. This behavior can be confirmed by post-mortem analysis, which shows a complete degradation of the material and the formation of crystalline Li_2MoO_4, as shown by the powder X-ray diffraction pattern in Figure 4b.

It is difficult to separate the theoretical specific capacity of the two components and infer the hybrid materials, because the capacity is not simply the combination of the two components, but depends on many different factors, such as the particle size, the morphology, the homogeneous distribution of the different components and on the interaction of the different components. This is a principle that is often observed in hybrid materials.

Our data suggests a mechanism characterized initially by ion intercalation and a gradual transition to a process dominated by the transformation reaction. This can be confirmed in the plateaus in the later cycle curves. This trend is seen to a lesser extent in the PPD/molybdate (1:1) sample and very pronounced in the PPD/molybdate (10:1) sample. Moreover, the galvanostatic lithiation-delithiation curves show a potential drift during the electrochemical measurement of the battery cell. The plateau of the lithiation curve shifts toward higher capacity, while the plateau of the delithiation curve also shifts slightly in that direction. The reasons for these shifts may be a change in kinetics, undesirable side reactions, and a change in the reaction mechanism. During cycling, the slope of the discharge curves of the PPD/molybdate (10:1) sample also changed, i.e., flattened. This may be associated with a reduction in the grain size of the electrode material during cycling.[45] Although the charge storage process is Faradaic, the charge transfer and storage are kinetically much faster than conventional battery materials with significantly different redox peaks.[49,50] The hybrid PPD/molybdate (10:1) material clearly indicates that the structure obtained directly after the reaction

ChemSusChem
Research Article
doi.org/10.1002/cssc.202202213
Chemistry Europe
European Chemical Societies Publishing

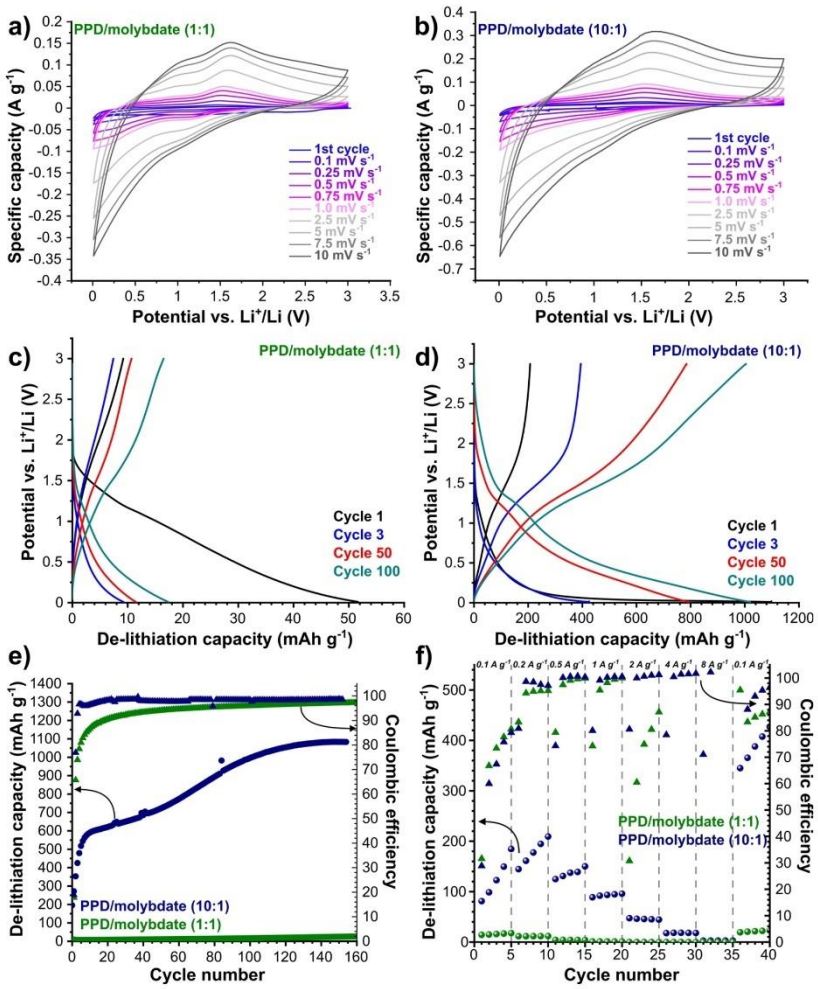

Figure 3. Electrochemical performance of PPD/molybdate hybrid materials: (a,b) Cyclic voltammograms at different scanning rates and potential range between 0.01 V and 3.00 V vs. Li^+/Li for (a) PPD/molybdate (1:1), and (b) PPD/molybdate (10:1). (c,d) Galvanostatic charge and discharge profiles at an applied specific current of 100 mA g^{-1} between 0.01 V and 3.00 V vs. Li^+/Li of (c) PPD/molybdate (1:1), and (d) PPD/molybdate (10:1). (e) Galvanostatic charge–discharge cycling performance showing the electrochemical stability with corresponding Coulombic efficiency values at a specific current of 100 mA g^{-1} for PPD/molybdate (1:1), PPD/molybdate (10:1). (f) Rate performance evaluated from galvanostatic charge-discharge cycling at different specific currents with corresponding Coulombic efficiencies for PPD/molybdate (1:1), PPD/molybdate (10:1).

in the microjet reactor is electrochemically very active and is further activated during cycling, making it a promising high capacity material for application in lithium-ion batteries. These observations can also be confirmed by the rate tests performed (Figure 3f), which show that the hybrid materials exhibit very unstable performances. This is especially true for the PPD/molybdate (10:1) sample, since pre-activation cannot occur and the capacities grow towards the fifth cycle of a rate. In contrast, the PPD/molybdate (1:1) sample shows poor Coulombic efficiency above a specific current of 2 A g^{-1}.

Compared to other hybrid and composite MoO_x systems (Table 1), the optimized inorganic-organic hybrid materials presented in this work provide very favorable electrochemical performance values (e.g., 1084 mAh g^{-1} after 150 cycles) for $[C_6H_9N_2]_4[NH_4]_2[Mo_7O_{24}]\cdot 3\,H_2O$ which can compete with results reported in "state-of-the-art" literature, with straightforward

ChemSusChem
Research Article
doi.org/10.1002/cssc.202202213
Chemistry Europe
European Chemical Societies Publishing

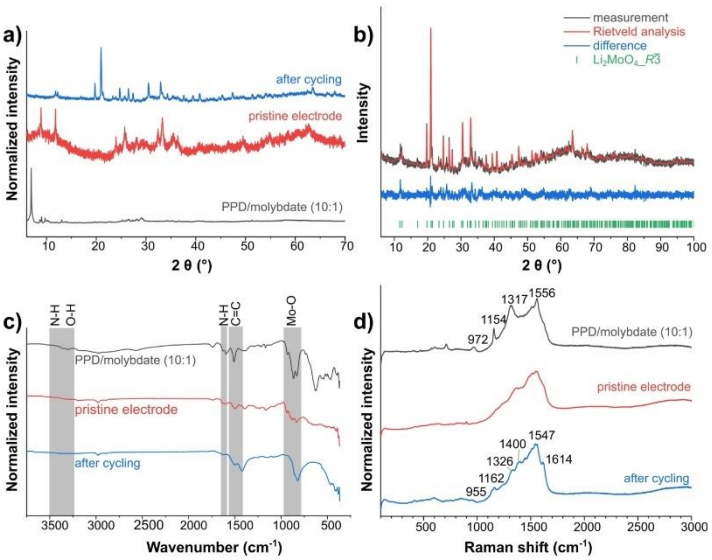

Figure 4. (a) X-ray diffractograms of PPD/molybdate (10:1), pristine electrode, and the electrode after cycling. (b) Rietveld analysis of the cycled PPD/molybdate (10:1). (c) FTIR spectra of PPD/molybdate (10:1), pristine electrode material, and the electrode after cycling. (d) Raman spectra of PPD/molybdate (10:1), pristine electrode material, and the electrode after cycling.

Table 1. Summary of the different electrochemical performances and properties of various molybdenum oxide hybrid or composite materials. Data from literature sources that are not available are indicated as "n.a.". EC = ethylene carbonate; DEC = diethyl carbonate; EMC = ethyl methyl carbonate; DMC = dimethyl carbonates; PVdF = polyvinylidene fluoride; $LiPF_6$ = lithium hexafluorophosphate; CMC = carboxymethyl cellulose; CNT = carbon nanotubes; rGO = reduced graphene oxide.

Ref.	Material	Total electrode composition	Potential [V]	Electrolyte	Normalization	Capacity [mAh g^{-1}]	Cycles
Han et al.[51]	MoO_3/CNT	MoOx/CNTs: Super P, PVdF 8:1:1	0.01–3.0	1 M $LiPF_6$ in EC/DEC (1:1 by volume)	n.a.	500 at 0.1 A g^{-1}	90
Chen et al.[54]	Amorphous MoO_x Thin Films	n.a.	0.01–3.0	1 M $LiPF_6$ in EC/EMC/DMC (1:1:1 by volume)	n.a.	845 at 90 μA cm^{-2}	100
Han et al.[55]	nanoporous graphene/molybdenum oxide	n.a.	0.01–3.0	1 M $LiPF_6$ in EC/DMC (1:1 by volume)	n.a.	710 at 1 A g^{-1}	150
Larson et al.[56]	Molybdenum oxide nanoporous asymmetric membranes	52% MoO_2 48% C	0.01-3.0	1 M $LiPF_6$ in EC/DMC/DEC (1:1:1 by volume)	n.a.	480 at 0.12 A g^{-1}	150
Naresh et al.[57]	MoO_3 /rGO	active material: Super P: PVdF 8:1:1	0.1–2.5	1 M $LiPF_6$ in EC/DMC (1:1 by volume)	n.a.	568 at 0.5 A g^{-1}	100
Xin et al.[53]	Mo_2C@C core-shell nanocrystals	active material: acetylene black: sodium alginate 7:2:1	0.01-3.0	1 M $LiPF_6$ in EC/EMC/DMC (1:1:1 by volume)	n.a.	1089 at 0.1 A g^{-1}	100
Yang et al.[52]	MoO_2–Mo_2C–C	MoO_2–Mo_2C–C: acetylene black: CMC 7:2:1	0.01–3.0	1 M $LiPF_6$ in EC/DC (1:1 by volume)	n.a.	1188 at 0.1 A g^{-1}	250
Gao et al.[58]	MoO_2/C hybrid	MoO_2/C hybrid: acetylene: PVdF 8:1:1	0.01–3.0	1 M $LiPF_6$ in EC/DEC (1:1 by volume)	n.a.	700 at 0.2 A g^{-1}	100
Our work	$[C_6H_9N_2]_4[NH_4]_2[Mo_7O_{24}]\cdot 3\,H_2O$ hybrid	Mo-hybrid: conductive carbon additive: PVdF 8:1:1	0.01–3.0	1 M $LiPF_6$ in EC/DMC (1:1 by volume)	Total hybrid	1084 at 0.1 A g^{-1}	150

processing. For example, the optimized MoO_2 and MoO_3/CNTs nanocomposites in the work of Han et al.[51] provide less than half of our capacity (500 mAh g^{-1}) with very low cycling stability (90 cycles). The MoO_2–Mo_2C–C microspheres in the work of Yang et al.[52] were based on a one-step annealing approach and provided an excellent reversible capacity of 1188 mAh g^{-1} after 250 cycles at a specific current of 100 mA g^{-1}. The electrochemical behavior is very similar to our hybrid material even with the persistent increase in capacity, which is likely related to a change in the material and/or reaction mechanism. While slightly higher delithiation capacity is obtained after 250 cycles compared to our system, the capacities are very similar

ChemSusChem
Research Article
doi.org/10.1002/cssc.202202213
Chemistry Europe
European Chemical Societies Publishing

after 150 cycles when comparing the two systems (~ 1000 mAh g^{-1}). The coupled Mo_2C@C core-shell nanocrystals on 3D graphene fabricated in the work of Xin et al.[53] also show very comparable capacity values (reversible capacity of 1090 mAh g^{-1} after 100 cycles at 0.1 A g^{-1}).

After continuous microjet reactor synthesis, the materials obtained can directly achieve high electrochemical performance without additional thermal or chemical processing. By fine-tuning the synthesis conditions, a characteristic electrochemical behavior similar to that described in the literature for molybdenum oxides could be achieved. The possibility to further modify these components makes this type of inorganic-organic hybrid synthesis very promising for electrochemical storage.

Material characterization of PPD/molybdate LIB anodes

To explain the unexpected improvement in electrochemical performance of PPD/molybdate (10:1) during cycling, the original electrode and the post-cycling electrode were characterized by powder X-ray diffraction, FTIR spectroscopy, and Raman spectroscopy (Figure 4a–d). These measurements were compared with the as-synthesized PPD/molybdate (10:1). For this purpose, the electrodes were prepared after cycling by stopping the cells in the delithiated state after 100 cycles, and the obtained electrode was rinsed with DMC to remove the residual salt. The X-ray diffractograms (Figure 4a) show a clear change comparing the PPD/molybdate and the electrode. The diffraction pattern of the electrode seems to shift and the reflections broaden considerably, as would be expected if a reduction is associated with a decrease in crystallite size (see above). The crystallite size of PPD/molybdate (10:1) is 48(1) nm and decreases to 40(10) nm (average over eight reflections) after electrode preparation. After cycling, the X-ray diffractograms change significantly, confirming the formation of lithium molybdate (Li_2MoO_4; Figure 4b), which crystallizes in the trigonal crystal system with space group $R\bar{3}$ ($a = 1433.0(2)$ pm, $c = 958.4(2)$ pm).[59]

In the FTIR spectra (Figure 4c), the observed bands in the as-prepared electrode are still at the same positions, indicating that the same structure must be present. However, the broad water band in the range 3600–3200 cm^{-1} has disappeared.[29] This indicates that solvent exchange occurred during the electrode preparation. The FTIR spectrum of the cycled sample shows that the N–H bands at 1650–1550 cm^{-1} are no longer present. One possible reason for this is the deprotonation of the amine groups. This would make the nitrogen atom a possible coordination site for Li^+ during the lithiation-delithiation process. It is possible that PPD is involved in a redox reaction. In this case, *p*-benzoquinone diimine may be formed by a two-electron redox reaction. PPD can also be electrochemically polymerized in situ.[13–16] The splitting of the C=C band in the cycled sample can be assigned to C=C and C=N vibrations. This is consistent with the work on polymerized PPD found in the literature.[16,60,61]

Comparison of the different Raman spectra (Figure 4d) shows a clear change in the PPD/molybdate (10:1) and the cycled sample, indicating a polymerization. In PPD/molybdate (10:1), a band at 1556 cm^{-1} is observed, assigned to C=C vibrations. After cycling, the band shifts to 1547 cm^{-1}, and a new band appears at the shoulder at 1614 cm^{-1} corresponding to C=C and C=N vibrations. Other additional peaks at 1511 cm^{-1}, 1400 cm^{-1}, 1326 cm^{-1}, and 1162 cm^{-1} correspond to C–C, C–N, C–N^+, and C–H vibrations of the quinoid ring, respectively. The equivalent bands of the C–H and C–N vibrations are shifted to 1317 cm^{-1} and 1154 cm^{-1} in the PPD/molybdate (10:1) sample.[16,61] The Mo–O vibrations are visible at 972 cm^{-1} in the PPD/molybdate (10:1) sample, and after cycling the band shifts to 955 cm^{-1}. That highlights the observed change of the molybdate unit. The band at 972 cm^{-1} is assigned to $Mo_7O_{24}^{6-}$ units, while the band at 955 cm^{-1} corresponds to MoO_4^{2-} units.[62]

X-ray photoelectron spectroscopy (XPS) measurements were performed to obtain information on the oxidation states of the Mo-species and the oxygen-bonding states. The Mo3d peaks were fitted with three components (Figure 5). The Mo^{6+} component has the highest binding energy with a binding energy of 232.6 eV. The signal caused by a reduced Mo^{m+} (presumably Mo^{5+}) species was fitted with a constant binding energy distance of −1.3 eV to Mo^{6+}, while Mo^{n+} (presumably Mo^{4+}) was fitted with a constant binding energy distance of −3 eV with respect to Mo^{6+}.[63]

The samples PPD/molybdate (1:1) (Figure 5a) and PPD/molybdate (10:1) (Figure 5b) were compared with the pristine electrode and the electrode after cycling to obtain further information about the redox processes taking place. Due to the high surface sensitivity of XPS spectroscopy, the information depth is about 10 nm. Therefore, only qualitative information is obtained. The precipitates PPD/molybdate (1:1) and PPD/molybdate (10:1) show the presence of Mo^{6+} (Figure 5a,b). In the pristine electrode of both samples, molybdenum species with lower oxidation numbers appear (Figure 5c,d). This indicates that the molybdenum has already been reduced during the electrode preparation step. After cycling, the content of Mo-species with a lower oxidation number increases in both samples. In addition, small contributions of even further reduced Mo^{4+} appear (Figure 5e,f). Thus, further reduction of the molybdenum species is observed, which can be attributed to electrochemical processes in the cell. A similar trend occurs for both samples PPD/molybdate (1:1) and PPD/molybdate (10:1), compared to their electrodes and the electrodes after cycling. These investigations show that both components the molybdenum species as well as the organic species contribute to the redox process.

The O1s peaks were fitted with four signals (Figure 6). The signal at 530.6 eV was used for calibration, which is due to the O–Mo^{6+} interaction. The O–Mo^{5+} contribution was observed at a binding energy of 531.2 eV. The binding energies assigned to O=C and O–Mo^{4+} bonds overlap at 532.0 eV, and the contribution originating from the O–C bond has a binding energy of 533.3 eV.[63] These binding energies agree well with the literature values. They can be explained by the higher electron

ChemSusChem
Research Article
doi.org/10.1002/cssc.202202213
Chemistry Europe
European Chemical Societies Publishing

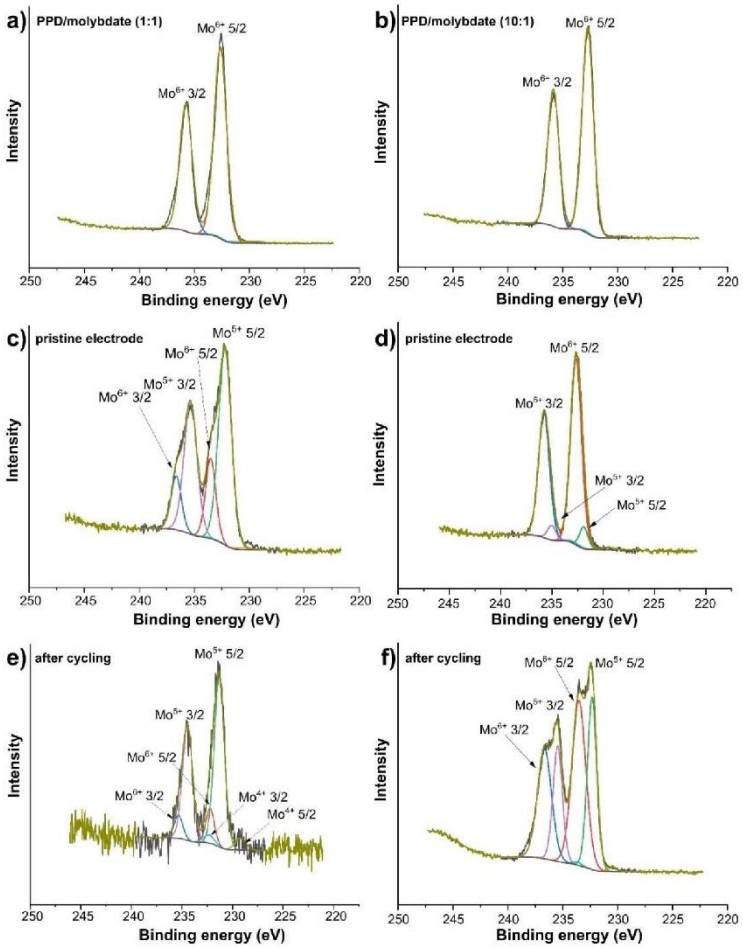

Figure 5. Fitted XPS Mo3d spectra: (a) PPD/molybdate (1:1); (b) PPD/molybdate (10:1); (c) pristine electrode PPD/molybdate (1:1); (d) pristine electrode of PPD/molybdate (10:1); (e) electrode after cycling of PPD/molybdate (1:1); (f) electrode after cycling of PPD/molybdate (10:1).

density of the more electronegative oxygen when the metal atom is more oxidized, leading to a decrease in binding energy.[64] PPD/molybdate (1:1) (Figure 6a) and PPD/molybdate (10:1) (Figure 6b) have mainly O–Mo^{6+} bonds. In the pristine electrodes (Figure 6c,d) the proportion of O–Mo^{5+} increases, which correlates with the results of the Mo3d peaks. The observed O=C and C–O bonds may originate from the conductive additive (carbon black) used for the electrode preparation.

The cycled electrode of PPD/molybdate (1:1) (Figure 6e) exhibits O–Mo^{4+} and C–O bonds. The O1s peak of the cycled electrode of PPD/molybdate (10:1) (Figure 6f) is broader. It shows less O–Mo^{6+} and more O=C and C–O bonds, which is due to the formation of lithium carbonate during the cycling process through the formation of a solid electrolyte interphase (SEI).[65] The original electrode of PPD/molybdate (1:1) contains the highest amount of O–Mo^{5+}, which correlates with the Mo bonds in Mo3d spectra. The amounts of O=C and O–C are comparable to those of other samples.

During electrode preparation, a change in the material is observed, as explained earlier. This change can be attributed to a chemical reaction of the material when treated with DMSO. The analyses (Figure S10) show that this leads to solvent exchange and a redox reaction. In the redox reaction induced this way, the PPD is partially oxidized and the DMSO and the

ChemSusChem
Research Article
doi.org/10.1002/cssc.202202213
Chemistry Europe
European Chemical Societies Publishing

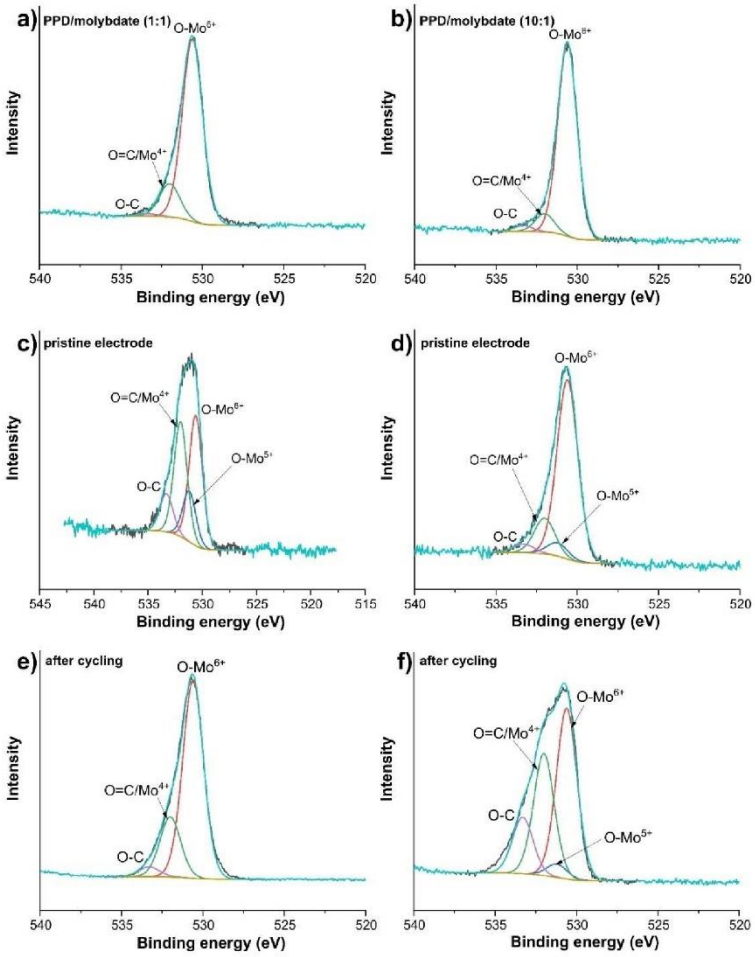

Figure 6. Fitted XPS O1s spectra: (a) PPD/molybdate (1:1); (b) PPD/molybdate (10:1); (c) pristine electrode PPD/molybdate (1:1); (d) pristine electrode of PPD/molybdate (10:1); (e) electrode after cycling of PPD/molybdate (1:1); (f) electrode after cycling of PPD/molybdate (10:1).

molybdenum are partially reduced. This shows that the material is very redox-active.

Post-mortem analyses of the product were difficult due to the limited amount of material and the high content of various components. Therefore, we decided to carry out a model study applying a chemical lithiation instead of an electrochemically driven process. In this way, we obtained evidence for the description of electrochemical lithiation. PPD/molybdate treated with DMSO was subsequently chemically lithiated with *n*-butyllithium (*n*-BuLi) to produce a sample as close as possible to electrochemical lithiation (Figure 7). The product was then characterized by powder X-ray diffraction, FTIR spectroscopy and ^{13}C CP-MAS NMR spectroscopy. It can be concluded that a redox-induced polymerization of the PPD takes place, resulting in a redox-active, positively charged poly(*p*-phenylenediamine) (Scheme 1). Composites of such polymers with metal species have proven to be highly conductive.[61]

Comparison of the X-ray diffraction patterns of DMSO-treated and chemically lithiated PPD/molybdate (10:1) after cycling, and PPD/molybdate (1:1) after cycling (Figure 7a) reveals the formation of the same phase. Using the structural data of trigonal Li_2MoO_4[59] the Rietveld analysis (Figure 7b) shows good agreement.

After chemical lithiation or electrochemical cycling, the molybdate component of the inorganic-organic hybrid material converts to Li_2MoO_4. This indicates that the electrochemical

ChemSusChem
Research Article
doi.org/10.1002/cssc.202202213
Chemistry Europe
European Chemical Societies Publishing

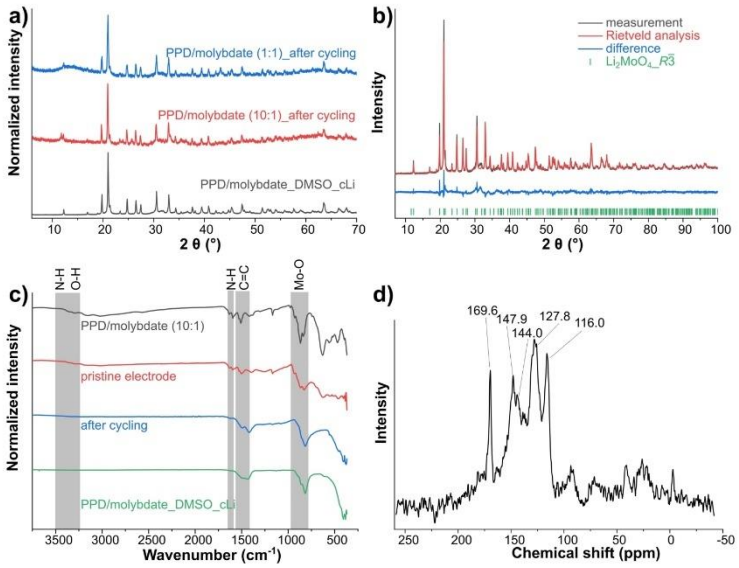

Figure 7. Results of chemical lithiation: (a) PXRD pattern of DMSO-treated and chemically lithiated PPD/molybdate, PPD/molybdate (10:1) after cycling and PPD/molybdate (1:1) after cycling. (b) Rietveld analysis of DMSO-treated and chemically lithiated PPD/molybdate. (c) FTIR spectra of PPD/molybdate (10:1), pristine electrode, after cycling and chemically lithiated PPD/molybdate_DMSO. (d) ^{13}C CP-MAS NMR spectrum of DMSO-treated and chemically lithiated PPD/molybdate.

cycling is reproducible by chemical lithiation with *n*-BuLi. It can be concluded that the molybdenum species contribute to the electrochemical activity, but the organic component seems to play a significant factor. Subsequently, the organic component was investigated in more detail by FTIR spectroscopy (Figure 7c) and ^{13}C CP-MAS NMR spectroscopy (Figure 7d). The FTIR spectra reveal that the bands of the DMSO-treated and chemically lithiated PPD/molybdate (10:1) and the PPD/molybdate (10:1) (Figure 7c) remain at the same position after cycling, indicating that the same organic species was formed. In the DMSO-treated PPD/molybdate (10:1) anode material used, a partial reduction of DMSO to DMS as well as Mo(VI) to Mo(V) takes place, which leads to partial oxidation of PPD to the corresponding benzoquinone diimine. The oxidative polymerization is activated during the electrochemical cycling. The ^{13}C CP-MAS NMR spectrum of DMSO-treated and chemically lithiated PPD/molybdate (Figure 7d) reveals the formation of a PPD trimer. The PPD dimer forms by recombination of the PPD cation radicals (Scheme 1). An N coupling of the PPD cation radical ($[HPPD]^{\bullet 2+}$) (**1**) is dominant upon dimerization. After dimerization, a new coupling with $[HPPD]^{\bullet 2+}$ and PPD dimer (**2**) occurs to form a PPD trimers (**3**). The peak at 169.6 ppm belongs to the carbon cation double-bonded to nitrogen ($C{=}NH^+$).[61]

Conclusions

In this work, a sustainable, continuous approach for the preparation of inorganic-organic hybrid materials with remarkable electrochemical properties using a microjet reactor is presented. Two inorganic-organic hybrid materials were synthesized from aqueous solutions of PPD and AHM at room temperature. The inorganic-organic hybrid material precipitated at low PPD:AHM ratios has the composition $[C_6H_{10}N_2]_2[Mo_8O_{26}]\cdot 6\,H_2O$, while the one at high PPD:AHM ratios contains a heptamolybdate anion and exhibits the composition $[C_6H_9N_2]_4[NH_4]_2[Mo_7O_{24}]\cdot 3\,H_2O$. The electrochemical measurements of PPD/molybdate (10:1) showed that an optimized electrode material could be produced by simply adjusting the synthesis parameters. Without further treatment, this material shows exceptional delithiation capacities through conversion reactions up to 1084 $mAh\,g^{-1}$. For reaching this high capacity the material requires an induction phase, which can be explained by several conversion reactions in the material during the redox processes. Both, the formation of Li_2MoO_4 and the polymerization of the PPD could be detected. The combination of inorganic and organic redox-active species in a hybrid material opens a large playground for the adjustment of specific properties. Moreover, the microjet approach represents a sustainable, energy-saving production method for such LIB materials.

ChemSusChem
Research Article
doi.org/10.1002/cssc.202202213
Chemistry Europe
European Chemical Societies Publishing

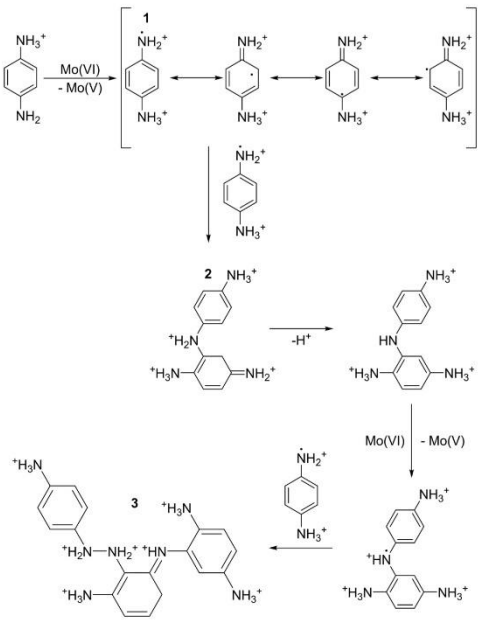

Scheme 1. Proposed polymerization mechanism of PPD. Reproduced and modified from reference [61] with permission from John Wiley and Sons.

Experimental Section

Materials

Ammonium heptamolybdate tetrahydrate (AHM; ≥99%) was obtained from Carl Roth. *Para*-phenylenediamine (PPD; 97%) and *n*-Butyllithium (*n*-BuLi; 2.5 M in hexane, packaged under nitrogen in resealable AcroSeal bottles) were purchased from Alfa Aesar. The concentration of *n*-butyllithium was determined by titration to 2.27 M. The hydrochloric acid (HCl; 37%) was obtained from Bernd Kraft GmbH. Ethanol (99% denatured with 1% PE) and 2-propanol (97%) were received from BCD Chemie GmbH. Dimethyl sulfoxide (DMSO; 99%) was supplied from Fisher Scientific GmbH. Conductive carbon additive (Type C65) was purchased from IMERYS Graphite&Carbon, polyvinylidene fluoride (PVdF, 99.5%), dimethyl sulfoxide (DMSO, anhydrous, ≥99.9%), and lithium hexafluorophosphate ($LiPF_6$) (LP30; 1 M in an ethylene carbonate (EC) and dimethyl carbonate (DMC) mixture in the ratio EC:DMC (1:1 by volume) as electrolyte from Sigma Aldrich. All chemicals were used without further purification. VWR International GmbH provided *n*-hexane (> 97%). It was dried in a solvent purifying system SPS 5 (MBraun).

Synthesis

Beaker synthesis of precipitates

The general procedure for the precipitation formation was that AHM was dissolved in water (500 mL). The amine (these were added in different ratios; Table S4) was then dissolved in water (500 mL) and the two solutions were mixed, then dilute HCl solution (1 L) was added, which led to the formation of a precipitate. Finally, the precipitates obtained from beaker synthesis were isolated by centrifugation (8000 rpm, 15 min). The products were washed with ethanol and dried at 80 °C.

Microjet synthesis

A diluted solution of HCl (solution A) and a mixture of AHM and the amines in water (solution B; Table S5) were used. AHM and the required amount of PPD were each dissolved in water (500 mL) to obtain solution B. For the microjet experiments, 1 L of each solution was used. Two high-performance liquid chromatography (HPLC) pumps (LaPrep P110 preparative HPLC pump, VWR) were used to transport the solutions with a flow rate of 250 mL min^{-1}. The reaction took place in the microjet reactor, where the solutions were forced through a nozzle with a diameter of 300 micrometers with high pressure into a reaction chamber. Nitrogen gas was used to remove the here-formed particles.[21] After the syntheses in the microjet reactor, the particles were isolated by centrifugation (8000 rpm, 15 min). The products were washed with ethanol and dried at 80 °C.

Chemical lithiation

For the chemical lithiation, PPD/molybdate (10:1)_DMSO (0.5 g) was first added to hexane (20 mL) under an argon atmosphere. To this was added 74 equivalents of *n*-butyllithium (2.27 M in *n*-hexane) with stirring. The reaction was stirred at 80 °C for 6 h. The reaction was terminated by the addition of 2-propanol to quench the remaining *n*-butyllithium. The product was separated by filtration. Finally, the product was washed with 2-propanol and dried at 80 °C.

Structural and chemical characterization

Fourier-transform infrared spectroscopy (FTIR) measurements of dried samples were recorded in attenuated total reflectance (ATR) mode using a Bruker Vertex 70 spectrometer. Each spectrum was performed in the wavenumber range 370–4500 cm^{-1} and by averaging 16 scans with a spectral resolution of 4 cm^{-1}. Thermogravimetric Analyses (TGA) were performed on a Netzsch TG F1 Iris under a constant flow of N_2 (40 mL min^{-1}) with a heating rate of 20 °C min^{-1} to a maximum of 900 °C. During the measurements, the samples were placed in an open alumina crucible. The TG-FTIR measurements were performed under the same conditions. The elemental analyses were conducted on an Elementar Vario Micro cube.

Powder X-ray diffraction (XRD) patterns of the pulverized samples were recorded at room temperature on a D8-A25-Advance diffractometer (Bruker) in Bragg-Brentano θ–θ geometry (goniometer radius 280 mm) with $Cu_{K\alpha}$-radiation ($\lambda = 154.0596$ pm). A 12 µm Ni foil working as K_β filter and a variable divergence slit were mounted at the primary beam side. An LYNXEYE detector with 192 channels was used at the secondary beam side. Experiments were carried out in a 2θ range of 6° to 130° with a step size of 0.013° and a total scan time of 1 or 4 h. The recorded data was evaluated using the Bruker TOPAS 5.1 software, with the observed reflections being treated via single-line fits.[66]

The single-crystal data set was collected using a Bruker D8 Venture diffractometer with a microfocus sealed tube and a Photon II detector. Monochromated $Cu_{K\alpha}$ radiation ($\lambda = 1.54178$ Å) was used. Data was collected at 133(2) K and corrected for absorption effects using the multi-scan method. The structure was solved by direct methods using SHELXT[67] and was refined by full matrix least

ChemSusChem
Research Article
doi.org/10.1002/cssc.202202213
Chemistry Europe
European Chemical Societies Publishing

squares calculations on F^2 (SHELXL2018[68]) in the graphical user interface Shelxle.[69] Details on the single-crystal X-ray diffraction experiments is given in the Supporting Information. Deposition Number 2226468 contains the supplementary crystallographic data for this paper. These data are provided free of charge by the joint Cambridge Crystallographic Data Centre and Fachinformationszentrum Karlsruhe Access Structures service.

SEM images were recorded using a JEOL JSM-7000 F microscope with a working distance of 10 mm and operating at 20 kV. For the sample preparation, a small amount was placed on a specimen stub covered with a carbon adhesive foil, followed by the deposition of a gold layer.

Solid-state CP-MAS NMR spectra were recorded using a Bruker AV400WB spectrometer. A resonance frequency of 100.65 MHz for ^{13}C NMR spectra was used. The spinning frequency for the MAS experiments was 13 kHz. X-ray photoelectron spectroscopy (XPS) was performed with an Axis Supra (Kratos Analytical) spectrometer. Wide and elemental scans were acquired employing $Al_{K\alpha}$ radiation with 150 W power with a pass energy of 160 eV and 80 eV, respectively, while for high-resolution measurements, 225 W with 10 eV were used. The data processing was done with CasaXPS (Casa Software, version 2.3.15).

Raman spectra were recorded with a Renishaw inVia Raman Microscope equipped with a neodymium-doped yttrium aluminum garnet laser with an excitation wavelength of 532 nm and a laser power of approximately 0.05 mW at the surface of the sample, a 2400 mm^{-1} grating, and a 50×objective lens with a numeric aperture of 0.75. Five different spots from each sample were recorded with five accumulations and 30 s acquisition time. All spectra were normalized to 100%.

Electrochemical characterization

Electrode materials and preparation

The hybrid material working electrodes were prepared by mixing 80 mass% $[C_6H_{10}N_2]_2[Mo_8O_{26}]\cdot 6\,H_2O$ or the $[C_6H_9N_2]_4[NH_4]_2[Mo_7O_{24}]\cdot 3\,H_2O$ powders, respectively, with 10 mass % conductive carbon additive (Type C65, IMERYS Graphite&Carbon) and 10 mass% polyvinylidene fluoride (PVdF, Sigma Aldrich), dissolved in dimethyl sulfoxide (DMSO, anhydrous, Sigma Aldrich), in a SpeedMixer DAC 150 SP from Hauschild. First, the active material and the conductive carbon were combined in a mortar and ground carefully. The dry powder mix was then dry-mixed for 5 min at 1000 rpm. Drop by drop, DMSO solvent was added to the mixture until the slurry reached the desired viscosity. This paste was again mixed at 1500 rpm for 5 min, following 2500 rpm for 5 min. Finally, the PVdF binder solution (10 mass% PVdF in DMSO) was added, and the viscous electrode past kept mixing for 10 min at 800 rpm. To obtain a homogenous electrode slurry, the suspension was agitated for 12 h using a magnetic stirrer. The obtained slurries were doctor-blade cast on copper foil with a wet thickness of 200 μm. The electrodes were initially dried at ambient conditions overnight. Then, a further vacuum drying step at 110 °C for 12 h was conducted to remove the remaining solvent. Dry-pressing in a rolling machine ((HR01 hot rolling machine, MTI) was used to regulate the electrode packing density. After that, utilizing press-punch (EL-CELL), 10 mm diameter discs were punched from the coating and used as the working electrode (WE). The resulting electrode thickness of the dried electrodes was 100 ± 10 μm with a material loading of 3.0 ± 0.5 mg cm^{-2}.

Cell preparation and electrochemical characterization

For electrochemical testing in an organic electrolyte, 2032-type coin cells were assembled in an argon-filled glove box (MBraun Labmaster 130; O_2 and $H_2O < 0.1$ ppm) using a hydraulic crimper (MSK-110, MTI corp.). Both the counter electrode (CE) and the reference electrode (RE) were made from a pressed and punched lithium metal disc (MTI corp.) with a diameter of 11 mm and a uniform thickness of 0.45 mm (RE). To separate the working and counter/reference electrodes, vacuum-dried glass-fiber separator (GF/F, Whatman) discs of 18 mm diameter were utilized. A stainless-steel spacer/-current collector was placed on the backside of each counter electrode. The cells were filled with 150 μL 1 M lithium hexafluorophosphate ($LiPF_6$) in an ethylene carbonate (EC) and dimethyl carbonate (DMC) mixture in the ratio EC:DMC (1:1 by volume) as electrolyte (LP30, Sigma Aldrich).

All electrochemical measurements were carried out at a climate chamber (Binder) with a constant temperature of 25 ± 1 °C. Cyclic voltammetry (CV) measurements were performed with a multi-channel potentiostat/galvanostat VMP300 (Bio-Logic Science Instrument), equipped with the EC-Lab software. All CV measurements were carried out with different scan rates of 0.10/0.25/0.50/0.75/1.00/2.50/5.00/7.50/10.00 mV s^{-1} in a potential window of 0.01–3.00 V vs. Li^+/Li. Galvanostatic charge-discharge cycling with potential limitation (GCPL) tests in the range of 0.01–3.00 V vs. Li^+/Li with a charge-discharge current of 100 mA g^{-1} were carried out using an Arbin system. The mass of active material was utilized to normalize the specific current and specific capacity calculations. Cells prepared for post-mortem analysis were stopped after 100 cycles in the de*-lithiated state, and the obtained electrode was rinsed with DMC to remove the remaining salt. Rate performance experiments were carried out in the same potential window at different currents to obtain more information about the half-cell rate capacity and higher currents. To get more information about the half-cell rate capability and higher currents, rate performance measurements were conducted by using the same potential window for different currents. The applied specific currents were 0.1 A g^{-1}, 0.2 A g^{-1}, 0.5 A g^{-1}, 1.0 A g^{-1}, 2.0 A g^{-1}, 4.0 A g^{-1}, 8.0 A g^{-1}, and (again) 0.1 A g^{-1}.

Author Contributions

Mana Abdirahman Mohamed: Materials synthesis, measurements, data analysis, writing, plotting, discussion, and manuscript revision. Stefanie Arnold: Electrochemical measurements, writing, plotting, discussion, Raman measurements, and manuscript revision. Oliver Janka: Discussion and manuscript revision. Antje Quade: XPS measurement, plotting, discussion, and manuscript revision. Volker Presser: Supervision, discussion, and manuscript revision. Guido Kickelbick: Conceptualization, supervision, project administration, discussion, and manuscript revision.

Acknowledgments

Instrumentation and technical assistance for this work were provided by the Service Center X-ray Diffraction, with financial support from Saarland University and German Science Foundation (project number INST 256/349-1 and project number INST 256/506-1). In addition, we thank Dr. Michael Zimmer for the CP-MAS

ChemSusChem | Research Article doi.org/10.1002/cssc.202202213 | Chemistry Europe European Chemical Societies Publishing

NMR measurements. We also thank Dr. Bernd Morgenstern for performing the X-ray single-crystal structure analysis, for the refinement of the crystal structure and for pH measurements. Many thanks also to Jörg Schmauch for assistance with scanning electron microscopy. We thank Susanne Harling for performing the elemental analyses and for her assistance with preparative work. The INM authors thank Prof. Dr. Eduard Arzt (INM) for his continued support. Open Access funding enabled and organized by Projekt DEAL.

Conflict of Interest

The authors declare no conflict of interest.

Data Availability Statement

The data that support the findings of this study are available in the supplementary material of this article.

Keywords: continuous synthesis · electrodes · inorganic-organic hybrid materials · lithium-ion batteries · polyoxometalates

[1] M. Yoshio, H. Wang, K. Fukuda, Y. Hara, Y. Adachi, *J. Electrochem. Soc.* **2000**, *147*, 1245.
[2] A. K. Boehm, S. Husmann, M. Besch, O. Janka, V. Presser, M. Gallei, *ACS Appl. Mater. Interfaces* **2021**, *13*, 61166–61179.
[3] Z. Xiu, D. Kim, M. H. Alfaruqi, J. Song, S. Kim, P. T. Duong, V. Mathew, J. P. Baboo, J. Kim, *J. Alloys Compd.* **2017**, *696*, 143–149.
[4] L. Lu, X. Han, J. Li, J. Hua, M. A. Ouyang, *J. Power Sources* **2013**, *226*, 272–288.
[5] V. Etacheri, R. Marom, R. Elazari, G. Salitra, D. Aurbach, *Energy Environ. Sci.* **2011**, *4*, 3243–3262.
[6] P. Poizot, S. Laruelle, S. Grugeon, L. Dupont, J.-M. Tarascon, *Nature* **2000**, *407*, 496–499.
[7] M. Genovese, K. Lian, *Curr. Opin. Solid State Mater. Sci.* **2015**, *19*, 126–137.
[8] H. Yang, T. Song, L. Liu, A. Devadoss, F. Xia, H. Han, H. Park, W. Sigmund, K. Kwon, U. Paik, *J. Phys. Chem. C* **2013**, *117*, 17376–17381.
[9] F. Li, L. Xu, *Dalton Trans.* **2011**, *40*, 4024–4034.
[10] S. S. Khandolkar, C. Näther, W. Bensch, B. R. Srinivasan, *J. Coord. Chem.* **2016**, *69*, 1166–1178.
[11] M. Y. Zhang, Y. Song, D. Yang, Z. Qin, D. Guo, L. J. Bian, X. G. Sang, X. Sun, X. X. Liu, *Adv. Funct. Mater.* **2021**, *31*, 1–10.
[12] S. S. Khandolkar, P. Raghavaiah, Srinivasan, B. R. Synthesis, *J. Chem. Sci.* **2015**, *127*, 1581–1588.
[13] K. B. Hatzell, M. Beidaghi, J. W. Campos, C. R. Dennison, E. C. Kumbur, Y. A. Gogotsi, *Electrochim. Acta* **2013**, *111*, 888–897.
[14] L. Xu, Y. Sun, B. Han, S. Chang, *J. Electrochem. Soc.* **2019**, *166*, A1363–A1369.
[15] E. Deunf, F. Dolhem, D. Guyomard, J. Simonet, P. Poizot, *Electrochim. Acta* **2018**, *262*, 276–281.
[16] D. Li, Y. Liu, B. Lin, C. Lai, Y. Sun, H. Yang, X. Zhang, *RSC Adv.* **2015**, *5*, 98278–98287.
[17] Q. Huang, T. Wei, M. Zhang, L. Z. Dong, A. M. Zhang, S. L. Li, W. J. Liu, J. Liu, Y. Q. Lan, *J. Mater. Chem. A* **2017**, *5*, 8477–8483.
[18] X. Y. Yang, T. Wei, J. Li, Sen, N. Sheng, P. P. Zhu, J. Q. Sha, T. Wang, Y. Q. Lan, *Inorg. Chem.* **2017**, *56*, 8311–8318.
[19] S. Xia, F. Li, X. Li, F. Cheng, C. Sun, J. J. Liu, H. Guo, *Dalton Trans.* **2018**, *47*, 5166–5170.
[20] W. Cheng, F.-C. Shen, Y.-S. Xue, X. Luo, M. Fang, Y.-Q. Lan, Y. A. Xu, *ACS Appl. Energ. Mater.* **2018**, *1*, 4931–4938.
[21] C. Odenwald, G. Kickelbick, *J. Sol-Gel Sci. Technol.* **2019**, *89*, 343–353.
[22] A. Betke, G. Kickelbick, *Inorganics* **2014**, *2*, 1–15.
[23] B. Krüner, C. Odenwald, A. Tolosa, A. Schreiber, M. Aslan, G. Kickelbick, V. Presser, *Sustain. Energy Fuels* **2017**, *1*, 1588–1600.
[24] B. Krüner, C. Odenwald, N. Jäckel, A. Tolosa, G. Kickelbick, V. Presser, *ACS Appl. Energ. Mater.* **2018**, *1*, 2961–2970.
[25] B. Krüner, C. Odenwald, A. Quade, G. Kickelbick, V. Presser, *Batteries & Supercaps* **2018**, *1*, 135–148.
[26] S. Fleischmann, A. Tolosa, V. Presser, *Chem. Eur. J.* **2018**, *24*, 12143–12153.
[27] C. Ge, P. Jiang, W. Cui, Z. Pu, Z. Xing, A. M. Asiri, A. Y. Obaid, X. Sun, J. Tian, *Electrochim. Acta* **2014**, *134*, 182–186.
[28] F. Cataldo, *Eur. Polym. J.* **1996**, *32*, 43–50.
[29] K. Ohno, M. Okimura, N. Akai, Y. Katsumoto, *Phys. Chem. Chem. Phys.* **2005**, *7*, 3005–3014.
[30] M. Pang, X. Wang, W. Xia, M. Muhler, C. Liang, *Ind. Eng. Chem. Res.* **2013**, *52*, 4564–4571.
[31] Z. Shi, B. Gao, Q. Mo, Z. J. Shao, K. Nie, B. Liu, H. Zhang, Y. Wang, Y. Zhang, Q. Gao, X. Sun, X. M. Cao, P. Hu, Y. Tang, *ChemNanoMat* **2018**, *4*, 194–202.
[32] Q. Gao, C. Zhang, S. Xie, W. Hua, Y. Zhang, N. Ren, H. Xu, Y. Tang, *Chem. Mater.* **2009**, *21*, 5560–5562.
[33] A. Davantès, G. Lefèvre, *J. Phys. Chem. A* **2013**, *117*, 12922–12929.
[34] S. Upreti, A. Ramanan, *Cryst. Growth Des.* **2005**, *5*, 1837–1843.
[35] *Handbook of Chemistry and Physics*, 98th Ed. (Eds.: J. R. Rumble, D. R. Lide, T. J. Bruno), CRC Press: Boca Raton **2017**.
[36] A. Müller, E. Krickemeyer, H. Bögge, M. Schmidtmann, F. Peters, C. Menke, J. Meyer, *Angew. Chem.* **1997**, *109*, 499–502; *Angew. Chem. Int. Ed.* **1997**, *36*, 484–486.
[37] J. Aveston, E. W. Anacker, J. S. Johnson, *Inorg. Chem.* **1964**, *3*, 735–746.
[38] W. F. Chen, C. H. Wang, K. Sasaki, N. Marinkovic, W. Xu, J. T. Muckerman, Y. Zhu, R. R. Adzic, *Energy Environ. Sci.* **2013**, *6*, 943–951.
[39] H. C. Zeng, *J. Cryst. Growth* **1998**, *186*, 393–402.
[40] H. C. Zeng, C. W. Sheu, H. C. Hia, *Chem. Mater.* **1998**, *10*, 974–979.
[41] S. Balakumar, H. C. Zeng, *J. Cryst. Growth* **1999**, *197*, 186–194.
[42] V. V. Atuchin, T. A. Gavrilova, T. I. Grigorieva, N. V. Kuratieva, K. A. Okotrub, N. V. Pervukhina, N. V. Surovtsev, *J. Cryst. Growth* **2011**, *318*, 987–990.
[43] J. S. Chen, Y. L. Cheah, S. Madhavi, X. W. Lou, *J. Phys. Chem. C* **2010**, *114*, 8675–8678.
[44] V. Augustyn, J. Come, M. A. Lowe, J. W. Kim, P. L. Taberna, S. H. Tolbert, H. D. Abruña, P. Simon, B. Dunn, *Nat. Mater.* **2013**, *12*, 518–522.
[45] S. Fleischmann, J. B. Mitchell, R. Wang, C. Zhan, D. E. Jiang, V. Presser, V. Augustyn, *Chem. Rev.* **2020**, *120*, 6738–6782.
[46] S. Ardizzone, G. Fregonara, S. Trasatti, *Electrochim. Acta* **2002**, *35*, 263–267.
[47] W. H. Ryu, D. H. Kim, S. H. Kang, H. S. Kwon, *RSC Adv.* **2013**, *3*, 8527–8534.
[48] J. Tang, C. E. Zavala Lugo, S. F. Acuña Guzmán, G. Daniel, V. G. Kessler, G. A. Seisenbaeva, V. G. Pol, *J. Mater. Chem. A* **2016**, *4*, 18107–18115.
[49] S. Fleischmann, Y. Zhang, X. Wang, P. T. Cummings, J. Wu, P. Simon, Y. Gogotsi, V. Presser, V. Augustyn, *Nat. Energy* **2022**, *7*, 222–228.
[50] H. S. Kim, J. B. Cook, H. Lin, J. S. Ko, S. H. Tolbert, V. Ozolins, B. Dunn, *Nat. Mater.* **2017**, *16*, 454–462.
[51] D. Han, S. Hwang, S. M. Bak, K. W. Nam, *Electrochim. Acta* **2021**, *388*, 1–10.
[52] X. Yang, Q. Li, H. Wang, J. Feng, M. Zhang, R. Yuan, Y. Chai, *Chem. Eng. J.* **2018**, *337*, 74–81.
[53] H. Xin, Y. Hai, D. Li, Z. Qiu, Y. Lin, B. Yang, H. Fan, C. Zhu, *Appl. Surf. Sci.* **2018**, *441*, 69–76.
[54] W. Chen, H. Zhang, Y. Wang, Z. Ma, Z. Li, *Electrochim. Acta* **2014**, *144*, 369–375.
[55] J. Han, P. Liu, Y. Ito, X. Guo, A. Hirata, T. Fujita, M. Chen, *Nano Energy* **2018**, *45*, 273–279.
[56] E. Larson, L. Williams, C. Jin, X. Chen, J. DiCesare, O. Shepperd, S. Xu, J. Wu, *J. Mater. Res.* **2021**, 1–12.
[57] N. Naresh, P. Jena, N. Satyanarayana, *J. Alloys Compd.* **2019**, *810*, 1–8.
[58] S. Gao, Y. Tang, H. Zhao, L. Liu, Y. Gu, R. Sheng, *Int. J. Energy Res.* **2021**, *45*, 6418–6425.
[59] U. Kolitsch, *Zeitschrift fuer Krist.* **2001**, *216*, 449–454.
[60] S. M. Sayyah, S. S. Abd El-Rehim, M. M. El-Deeb, S. M. Kamal, R. E. Azooz, *J. Appl. Polym. Sci.* **2010**, *117*, 943–952.
[61] G. Ciric-Marjanovic, B. Marjanović, P. Bober, Z. Rozlívková, J. Stejskal, M. Trchová, J. Prokeš, *J. Polym. Sci. Part A* **2011**, *49*, 3387–3403.
[62] E. Payen, J. Grimblot, S. Kasztelan, *J. Phys. Chem.* **1987**, *91*, 6642–6648.

ChemSusChem
Research Article
doi.org/10.1002/cssc.202202213
Chemistry Europe
European Chemical Societies Publishing

[63] L. Liu, W. Zhang, P. Guo, K. Wang, J. Wang, H. Qian, I. Kurash, C. H. Wang, Y. W. Yang, F. Xu, *Phys. Chem. Chem. Phys.* **2015**, *17*, 3463–3469.
[64] S. Ikari, Y. Sasaki, T. Ito, *Inorg. Chem.* **1989**, *28*, 447–451.
[65] X. Liu, Y. Lyu, Z. Zhang, H. Li, Y. S. Hu, Z. Wang, Y. Zhao, Q. Kuang, Y. Dong, Z. Liang, Q. Fan, L. Chen, *Nanoscale* **2014**, *6*, 13660–13667.
[66] Bruker AXS, Karlsruhe G 2014 Topas 5.1. General Profile and Structure Analysis Software for Powder Diffraction Data.
[67] Sheldrick, G. M. SHELXT – Integrated Space-Group and Crystal-Structure Determination. *Acta Crystallogr. Sect. A Found. Crystallogr.* **2015**, *A71*, 3–8.
[68] Sheldrick, G. M. Crystal Structure Refinement with SHELXL. *Acta Crystallogr. Sect. C Struct. Chem.* **2015**, *C71*, 3–8.
[69] Hübschle, C. B.; Sheldrick, G. M.; Dittrich, B. ShelXle: A Qt Graphical User Interface for SHELXL. *J. Appl. Crystallogr.* **2011**, *44*, 1281–1284.

Manuscript received: November 29, 2022
Revised manuscript received: December 16, 2022
Accepted manuscript online: December 21, 2022
Version of record online: February 3, 2023

ChemSusChem

Supporting Information

Self-Activation of Inorganic-Organic Hybrids Derived through Continuous Synthesis of Polyoxomolybdate and *para*-Phenylenediamine Enables Very High Lithium-Ion Storage Capacity

Mana Abdirahman Mohamed, Stefanie Arnold, Oliver Janka, Antje Quade, Volker Presser,* and Guido Kickelbick*

Supporting Information

Self-activation of Inorganic-Organic Hybrids derived via Continuous Synthesis of Polyoxomolybdate and para-Phenylenediamine enables very High Lithium Ion Storage Capacity

Mana Abdirahman Mohamed[a] (0000-0003-0708-7623),
Stefanie Arnold[b,c] (0000-0002-4954-4610), Dr. Oliver Janka[a] (0000-0002-9480-3888),
Dr. Antje Quade[e] (0000-0003-0814-4319), Prof. Dr. Volker Presser[b,c,d]* (0000-0003-2181-0590), and Prof. Dr. Guido Kickelbick[a]* (0000-0001-6813-9269)

[a] Saarland University, Inorganic Solid-State Chemistry, Campus C4 1, 66123 Saarbrücken, Germany, https://www.uni-saarland.de/en/chair/kickelbick.html

[b] INM – Leibniz Institute for New Materials, 66123 Saarbrücken, Germany, http://www.leibniz-inm.de/en/research/interface-materials/energy-materials/

[c] Saarland University, Department of Materials Science and Engineering, 66123 Saarbrücken, Germany

[d] Saarene - Saarland Center for Energy Materials and Sustainability, 66123 Saarbrücken, Germany, http://saarene.de/

[e] Leibniz Institute for Plasma Science and Technology, Felix-Hausdorff-Straße 2, 17489 Greifswald, Germany, https://www.inp-greifswald.de/en/

* Corresponding authors:

GK: guido.kickelbick@uni-saarland.de

VP: volker.presser@leibniz-inm.de

Table S1: Elemental analysis of the precipitated products PPD/molybdate.

	C / %	H / %	N / %
Theor. $[C_6H_{10}N_2]_2[Mo_8O_{26}] \cdot 6\ H_2O$	9.53	2.13	3.71
Theor. $[C_6H_9N_2]_4[NH_4]_2[Mo_7O_{24}] \cdot 3\ H_2O$	18.22	3.19	8.85
PPD/molybdate (1:1)	9.51	2.13	3.65
PPD/molybdate (2:1)	9.61	2.18	3.68
PPD/molybdate (5:1)	9.67	2.18	3.71
PPD/molybdate (9:1)	18.83	3.04	7.63
PPD/molybdate (10:1)	18.46	3.06	7.49
PPD/molybdate (15:1)	18.96	3.08	7.67
PPD/molybdate (18:1)	18.93	3.14	7.68
PPD/molybdate (20:1)	18.98	3.12	7.72
PPD/molybdate (25:1)	19.59	3.19	7.93
PPD/molybdate (30:1)	19.36	3.18	7.79

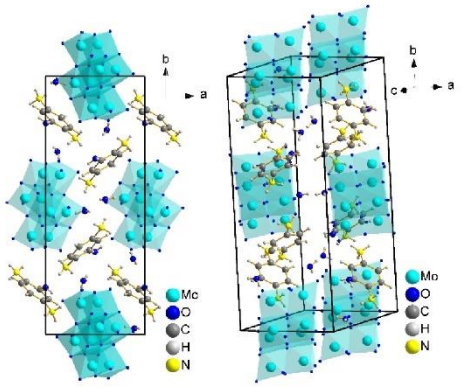

Figure S1: Unit cell of $[C_6H_{10}N_2]_2[Mo_8O_{26}] \cdot 6\ H_2O$.[1]

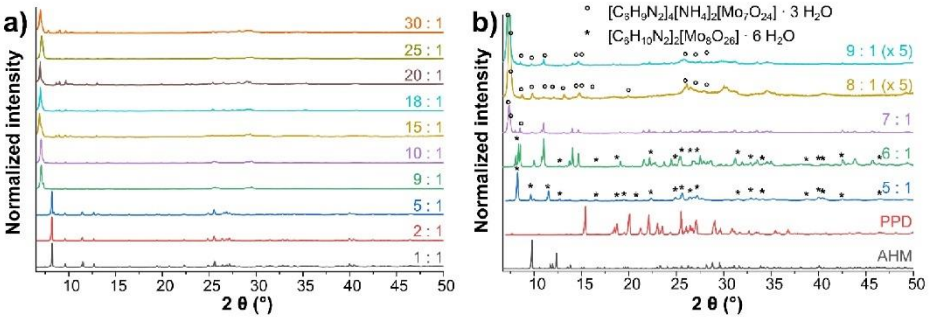

Figure S2: (a) X-ray diffractograms of PPD/molybdate precipitates with different ratios. (b) X-ray diffractograms of the PPD/molybdate precipitations with different mixing ratios are plotted alongside the diffraction patterns of pure PPD and AHM. The reflections of $[C_6H_{10}N_2]_2[Mo_8O_{26}] \cdot 6\ H_2O$(*) are marked with asterisks, and the reflections of $[C_6H_9N_2]_4[NH_4]_2[Mo_7O_{24}] \cdot 3\ H_2O$ (°) are marked with circles. Differences in the intensities can be attributed to texture problems or rather preferred orientation.

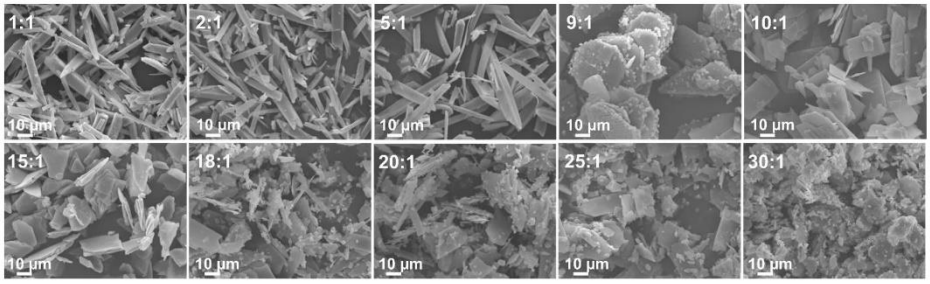

Figure S3: Scanning electron micrographs of PPD/molybdate products from microjet synthesis. The respective AHM to PPD ratios are given.

Refinement details for $[C_6H_9N_2]_4[NH_4]_2[Mo_7O_{24}] \cdot 3\ H_2O$

All non H-atoms were located in the electron density maps and refined anisotropically. C-bound H atoms were placed in positions of optimized geometry and treated as riding atoms. Their isotropic displacement parameters were coupled to the corresponding carrier atoms by a factor of 1.2 (CH). The N-bound hydrogen atoms of the phenylenediamine ligands were placed in positions of optimized geometry and treated as riging atoms, too. Their occupancy factors were adopted to a protonation degree of 1.5 for one phenylenediamine ligand (LH^+), which was determinded by potentiometric measurements. The occupation factors of some of the LH^+ units were constrained to some degree and added to four LH^+ per asymmetric unit. Acoordingly, two NH^{4+} ions were randomly occupied with three water molecules to ensure the electroneutrality in the structure.

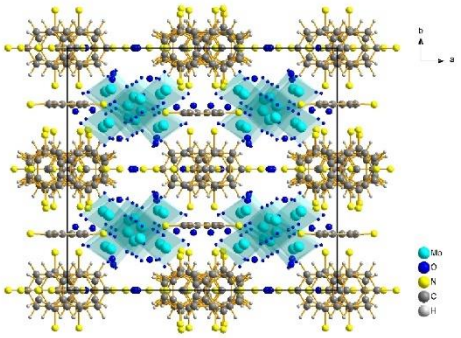

Figure S4: Unit cell of $[C_6H_9N_2]_4[NH_4]_2[Mo_7O_{24}] \cdot 3\ H_2O$.

Table S2: Crystal data and structure refinement for $[C_6H_9N_2]_4[NH_4]_2[Mo_7O_{24}] \cdot 3\ H_2O$.

Empirical formula	**$C_{24}H_{50}Mo_7N_{10}O_{27}$**
Formula weight	1582.32
Temperature	133(2) K
Wavelength	1.54178 Å
Crystal system	monoclinic
Space group	*C*2/*m*
Unit cell dimensions	a = 20.2993(11) Å, b = 18.1963(10) Å, c = 25.2122(14) Å, β = 90.622(2)°
Volume	9312.1 $Å^3$
Z	8
Density (calculated)	2.26 g/cm^3
Absorption coefficient	15.8 mm^{-1}
F(000)	6192
Crystal size	0.160 x 0.150 x 0.030 mm^3
Theta range for data collection	1.75 to 68.40°
Index ranges	$-24 \le h \le 23$, $-21 \le k \le 21$, $-30 \le l \le 30$
Reflections collected	84334
Independent reflections	8855 [R(int) = 0.0428]
Completeness to theta = 67.68°	100.0 %
Absorption correction	Semi-empirical from equivalents
Max. and min. transmission	0.7531 and 0.4433
Refinement method	Full-matrix least-squares on F^2
Data / restraints / parameters	8855 / 304 / 767
Goodness-of-fit on F^2	1.041
Final R indices [I>2sigma(I)]	R1 = 0.0385, wR2 = 0.1013
R indices (all data)	R1 = 0.0396, wR2 = 0.1020
Largest diff. peak and hole	2.325 and -1.568 e.$Å^{-3}$

Table S3: Atomic coordinates, Wyckoff positions, equivalent isotropic displacement parameters ($Å^2 x\ 10^3$) and site occupation factors for $[C_6H_9N_2]_4[NH_4]_2[Mo_7O_{24}] \cdot 3\ H_2O$. U_{eq} is defined as one third of the trace of the orthogonalized U_{ij} tensor.

	Wyck.	*x / a*	*y / b*	*z / c*	U_{eq}	s.o.f.
Mo(1)	8*j*	0.2748(1)	0.7396(1)	0.3868(1)	36(1)	1
Mo(2)	8*j*	0.3653(1)	0.8256(1)	0.3041(1)	24(1)	1
Mo(3)	8*j*	0.1621(1)	0.8297(1)	0.3238(1)	25(1)	1
Mo(4)	8*j*	0.2516(1)	0.7034(1)	0.2567(1)	21(1)	1
Mo(5)	8*j*	0.3457(1)	0.8093(1)	0.1760(1)	23(1)	1
Mo(6)	8*j*	0.1436(1)	0.8197(1)	0.1957(1)	24(1)	1
Mo(7)	8*j*	0.2295(1)	0.7120(1)	0.1238(1)	29(1)	1
O(1)	8*j*	0.2782(2)	0.6587(3)	0.4220(2)	54(1)	1
O(2)	8*j*	0.2836(2)	0.8078(3)	0.4333(2)	55(1)	1
O(3)	8*j*	0.3607(2)	0.7444(2)	0.3565(2)	34(1)	1
O(4)	8*j*	0.1810(2)	0.7507(2)	0.3750(2)	34(1)	1
O(5)	8*j*	0.4487(2)	0.8105(2)	0.2950(2)	32(1)	1
O(6)	8*j*	0.2630(2)	0.7982(2)	0.3128(1)	25(1)	1
O(7)	8*j*	0.0781(2)	0.8181(2)	0.3286(2)	35(1)	1
O(8)	8*j*	0.3610(2)	0.9013(2)	0.3444(2)	38(1)	1
O(9)	8*j*	0.1803(2)	0.9065(2)	0.3608(2)	40(1)	1
O(10)	8*j*	0.2587(2)	0.6495(2)	0.3134(2)	30(1)	1
O(11)	8*j*	0.3407(2)	0.7326(2)	0.2468(1)	23(1)	1
O(12)	8*j*	0.1644(2)	0.7397(2)	0.2624(1)	24(1)	1
O(13)	8*j*	0.3424(2)	0.8722(2)	0.2384(1)	25(1)	1
O(14)	8*j*	0.1673(2)	0.8792(2)	0.2554(1)	24(1)	1
O(15)	8*j*	0.4296(2)	0.7933(2)	0.1735(2)	33(1)	1
O(16)	8*j*	0.2439(1)	0.7853(2)	0.1899(1)	22(1)	1
O(17)	8*j*	0.0598(2)	0.8123(2)	0.2055(2)	34(1)	1
O(18)	8*j*	0.2428(2)	0.6399(2)	0.2053(2)	29(1)	1
O(19)	8*j*	0.3306(2)	0.8755(2)	0.1300(2)	41(1)	1
O(20)	8*j*	0.1521(2)	0.8838(2)	0.1456(2)	36(1)	1
O(21)	8*j*	0.3231(2)	0.7221(2)	0.1326(2)	30(1)	1
O(22)	8*j*	0.1439(2)	0.7277(2)	0.1527(2)	28(1)	1
O(23)	8*j*	0.2242(2)	0.6223(2)	0.0990(2)	42(1)	1
O(24)	8*j*	0.2217(2)	0.7655(3)	0.0688(2)	42(1)	1
N(1)	8*j*	0.0491(2)	0.6546(3)	0.2135(3)	45(1)	1
C(1)	8*j*	0.0482(2)	0.5745(3)	0.2120(2)	28(1)	1
C(2)	8*j*	0.1072(2)	0.5382(3)	0.2119(2)	29(1)	1

C(3)	8*j*	-0.0115(2)	0.5380(3)	0.2127(2)	27(1)	1
N(2)	4*i*	0.1439(3)	1/2	-0.0627(3)	36(2)	1
N(3)	4*i*	-0.1330(3)	1/2	-0.0739(3)	48(2)	1
C(4)	4*i*	0.0715(4)	1/2	-0.0687(3)	30(2)	1
C(5)	8*j*	0.0380(3)	0.4342(3)	-0.0704(2)	35(1)	1
C(6)	8*j*	-0.0299(3)	0.4343(3)	-0.0733(3)	39(1)	1
C(7)	4*i*	-0.0647(4)	1/2	-0.0744(3)	32(2)	1
N(4)	4*i*	0.2827(4)	1/2	0.1556(4)	52(2)	1
N(5)	4*i*	0.5565(4)	1/2	0.1234(4)	62(3)	1
C(8)	4*i*	0.3538(5)	1/2	0.1460(4)	41(2)	1
C(9)	8*j*	0.3873(3)	0.5656(4)	0.1427(3)	52(2)	1
C(10)	8*j*	0.4545(3)	0.5652(4)	0.1356(3)	53(2)	1
C(11)	4*i*	0.4887(4)	1/2	0.1323(4)	41(2)	1
N(6)	4*i*	0.3931(4)	1/2	0.5638(4)	75(3)	1
N(7)	4*i*	0.6695(4)	1/2	0.5910(4)	54(2)	1
C(12)	4*i*	0.4654(5)	1/2	0.5707(4)	53(3)	1
C(13)	8*j*	0.4988(4)	0.5651(5)	0.5744(3)	61(2)	1
C(14)	8*j*	0.5659(4)	0.5655(4)	0.5815(3)	55(2)	1
C(15)	4*i*	0.6010(4)	1/2	0.5852(4)	44(2)	1
N(8)	8*j*	-0.0443(2)	0.8445(3)	0.2730(3)	49(2)	1
C(16)	8*j*	-0.0448(3)	0.9253(3)	0.2757(2)	31(1)	1
C(17)	8*j*	-0.1036(2)	0.9616(3)	0.2817(2)	32(1)	1
C(18)	8*j*	0.0142(2)	0.9620(3)	0.2711(2)	27(1)	1
N(9)	8*j*	0.3650(3)	0.7325(5)	0.0266(2)	72(2)	1
C(19)	8*j*	0.4349(3)	0.7314(4)	0.0128(2)	42(2)	1
C(20)	8*j*	0.4525(3)	0.7322(4)	-0.0394(2)	41(1)	1
C(21)	8*j*	0.5186(3)	0.7323(4)	-0.0528(2)	38(1)	1
N(10)	4*i*	0.3132(8)	0	0.4255(6)	47(4)	0.5
N(11)	4*i*	0.5461(10)	0	0.5469(9)	111(9)	0.5
C(22)	4*i*	0.3724(7)	0	0.4563(5)	53(4)	0.5
C(23)	8*j*	0.3990(7)	0.9347(7)	0.4737(7)	70(3)	0.5
C(24)	8*j*	0.4576(7)	0.9344(7)	0.5024(7)	78(4)	0.5
C(25)	4*i*	0.4869(10)	0	0.5162(9)	75(5)	0.5
N11	8*j*	0.5814(4)	0.1394(5)	0.3339(4)	40(2)	0.5
N21	8*j*	0.5784(8)	0.8388(7)	0.3846(5)	105(5)	0.5
C11	8*j*	0.5811(5)	0.0642(6)	0.3467(2)	33(2)	0.5
C21	8*j*	0.5229(5)	0.0246(6)	0.3445(4)	42(3)	0.5
C31	8*j*	0.5223(6)	0.9515(6)	0.3569(4)	51(3)	0.5
C41	8*j*	0.5793(6)	0.9153(7)	0.3714(4)	58(3)	0.5

C51	8*j*	0.6371(7)	0.9541(7)	0.3741(4)	52(3)	0.5
C61	8*j*	0.6391(7)	0.0277(7)	0.3619(4)	48(3)	0.5
N(12)	8*j*	0.3744(10)	0.7256(9)	0.5203(7)	49(5)	0.25
C(26)	8*j*	0.4371(9)	0.7428(6)	0.5099(7)	28(3)	0.25
C(27)	8*j*	0.4571(10)	0.7539(10)	0.4554(8)	34(3)	0.25
C(28)	8*j*	0.5229(10)	0.7718(10)	0.4463(8)	39(4)	0.25
C(29)	8*j*	0.5697(10)	0.7788(8)	0.4878(8)	44(4)	0.25
C(30)	8*j*	0.5495(10)	0.7680(11)	0.5415(8)	40(4)	0.25
C(31)	8*j*	0.4842(9)	0.7501(10)	0.5517(8)	37(4)	0.25
N(13)	8*j*	0.6314(10)	0.7957(11)	0.4789(8)	54(5)	0.25
O(1W)	4*i*	0.2474(4)	1/2	0.2686(4)	76(2)	1
O(4W)	4*i*	0.2448(5)	0	0.1388(7)	149(7)	1
O(2WA)	8*j*	0.3349(6)	0.6310(10)	0.5206(3)	121(9)	0.71(2)
O(2WB)	8*j*	0.2850(20)	0.5550(20)	0.5096(12)	160(20)	0.29(2)
O(3W)	8*j*	0.1719(5)	0.8949(6)	0.0278(4)	142(4)	1
N(1A)	4*i*	0.2619(5)	0	0.2507(7)	109(6)	1
N(1B)	4*i*	0.0708(8)	0	0.0140(6)	130(6)	1
N(1C)	8*j*	0.1945(3)	0.6256(4)	-0.0092(2)	30(1)	1
N(1D)	4*i*	0.2848(9)	0	0.4090(9)	55(5)	1

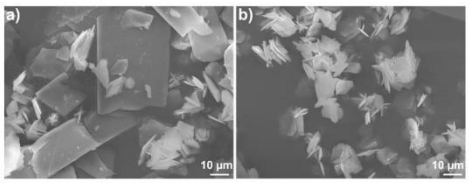

Figure S5: Scanning electron micrographs of PPD/molybdate products from microjet synthesis at room temperature (a) and 50 °C (b).

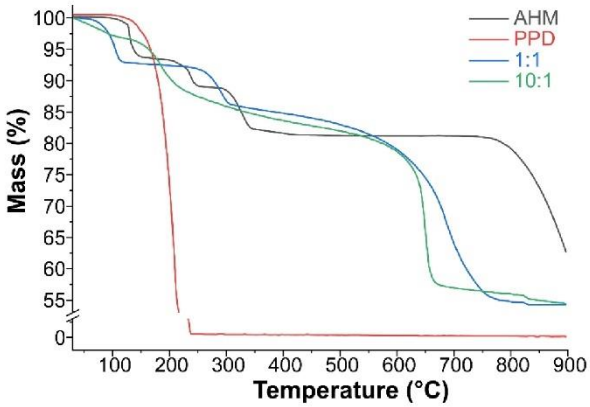

Figure S6: Comparisons of thermogravimetric curves of PPD/molybdate with their reactants; heating rate: 20 °C min^{-1}; nitrogen atmosphere.

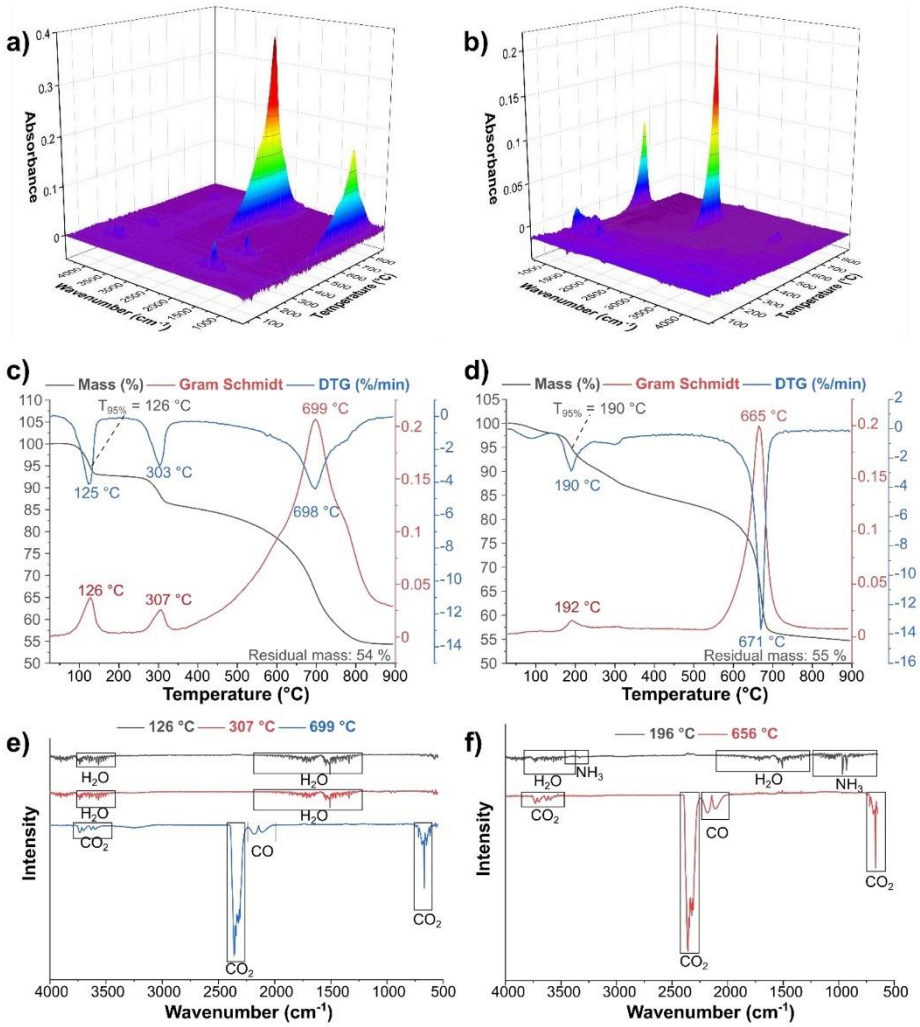

Figure S7: (a) TG-FTIR measurements of PPD/molybdate (1:1), (b) TG-FTIR measurements of PPD/molybdate (10:1), (c) thermogravimetric curve, with Gram-Schmidt and differential thermogravimetric curve of PPD/molybdate (1:1); heating rate: 20 °C min^{-1}; gas: Nitrogen; (d) thermogravimetric curve, with Gram-Schmidt and differential thermogravimetric curve of PPD/molybdate (10:1); heating rate: 20 °C min^{-1}; gas: nitrogen; (e) associated FTIR spectra of PPD/molybdate (1:1) and (f) associated FTIR spectra of PPD/molybdate (10:1).

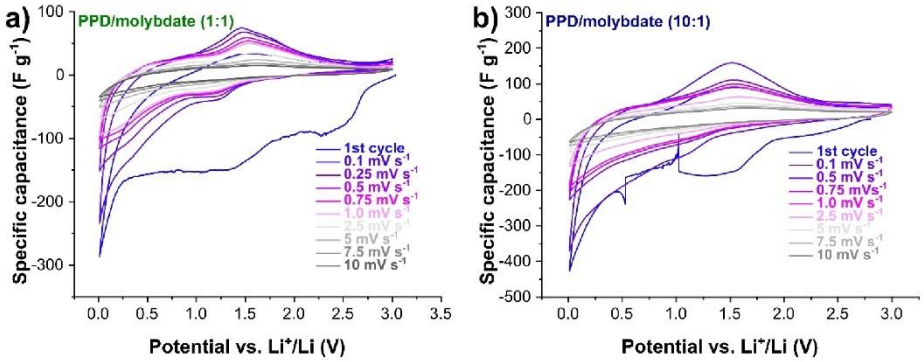

Figure S8: Electrochemical performance showing cyclic voltammogram at different scanning rates and a potential range between 0.01 V and 3.00 V vs. Li^+/Li for (a) PPD/molybdate (1:1); (b) PPD/molybdate (10:1).

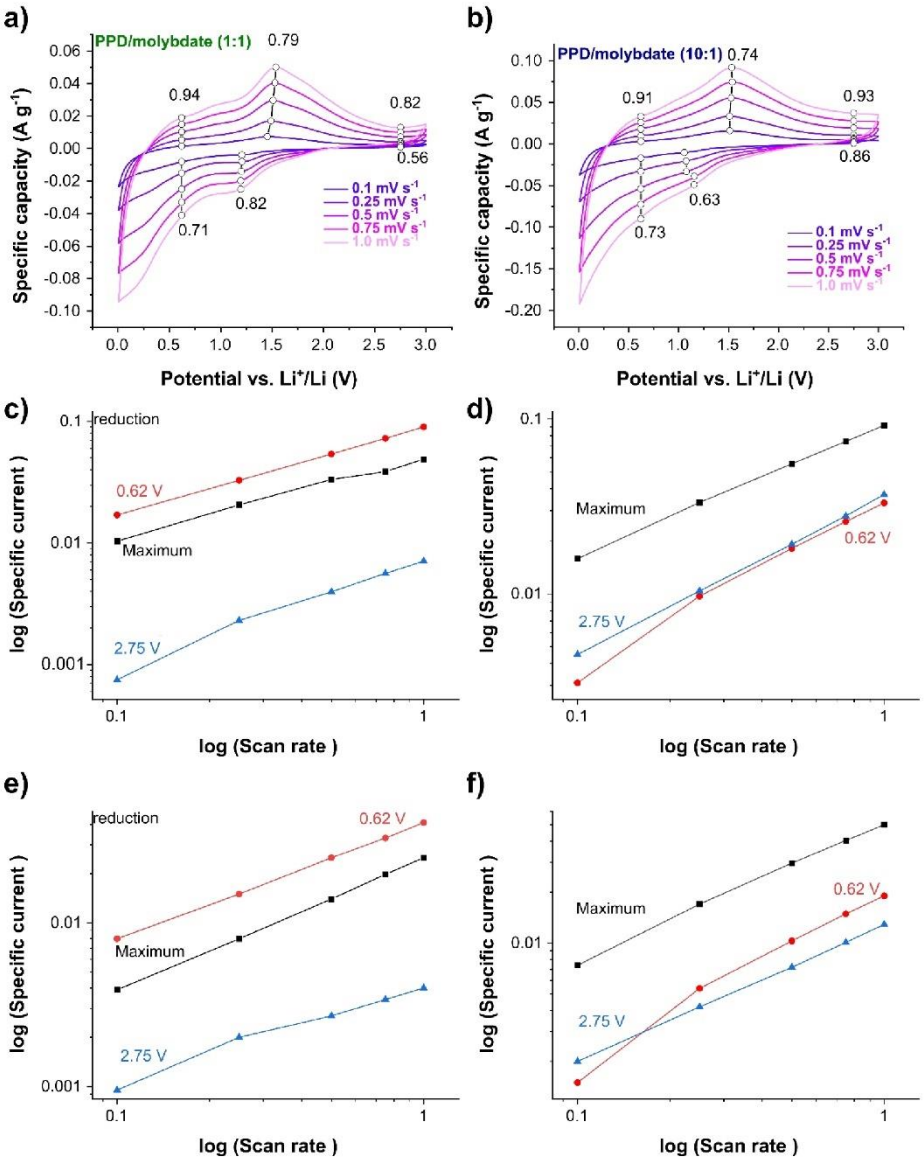

Figure S9: Cyclic voltammograms at different scanning rates and kinetic fitting to calculate b-Values for (a, c, e) PPD/molybdate (1:1); (b, d, f) PPD/molybdate (10:1).

Supporting discussion:

We have always observed a change in the pristine electrode when comparing PPD/molybdate (10:1) and the pristine material. This indicates that the material changes during electrode fabrication. To investigate the reason for the change and resulting product, the applied PPD/molybdate (10:1) was added with an excess of DMSO and stirred for 1 h. To remove the DMSO, the material was dried in analogy to the electrode preparation in a vacuum (6 mbar) at 80 °C. The hypothesis that in the electrode preparation used DMSO caused a change in the hybrid material aligns with a visible color change of the product (**Figure S10a-b**, **Figure S11**).

In addition, X-ray diffractograms, FTIR spectra, ^{13}C CP-MAS NMR spectra, TG-FTIR measurements, and XPS spectra were recorded from the PPD/molybdate (10:1) and the PPD/molybdate (10:1) treated with DMSO. A major phase change was well visible in the X-ray diffractograms (**Figure S10c**). The X-ray diffraction pattern remains similar, but the reflections are widened enormously, and the reflection positions are shifted to higher angles. That indicates the crystallite size becomes smaller, and the structure remains intact although the unit cell size decreases. The FTIR spectra (**Figure S10d**) remain unchanged (i.e., no bands shift) of the structure. At the same time, the broad water band in the 3600-3200 cm^{-1} range has disappeared.[2] As a result, a solvent exchange must have occurred during the electrode production.

These findings are consistent with those shown for the electrode material. The ^{13}C CP-MAS NMR spectra of PPD/molybdate (10:1) treated with DMSO reveal a slight change compared to the ^{13}C CP-MAS NMR spectra of PPD/molybdate (10:1) (**Figure S10e**). Although the main peaks remain the same, some additional peaks appear at 166.1 ppm, 94.6 ppm, 40.2 ppm, and 18.4 ppm. The peak at 166.1 ppm implies the formation of p-benzoquinone diamine because this peak belongs to the nitrogen double-bonded carbon (C=NH). The primary amine-bonded carbon (C-NH_2) shows a peak at 94.6 ppm.[3] Finally, at 40.2 ppm and 18.4 ppm, the peaks can be assigned to DMSO and dimethyl sulfide (DMS). These results suggest that after adding DMSO, a redox reaction is induced. Parts of the PPD are oxidized to p-benzoquinone diimine while, at the same time, DMSO is reduced to DMS. The presence of DMS and the solvent exchange from water to DMSO is confirmed by the TG-FTIR measurements (**Figure S10f**). Instead of the loss of water and ammonia visible at the measurements of PPD/molybdate (10:1), we see a loss of DMSO, DMS, and ammonia in the measurements of PPD/molybdate (10:1) treated with DMSO.

In **Figure S10g** the element composition obtained via XPS for PPD/molybdate (10:1) and PPD/molybdate (10:1) after the DMSO treatment is shown. It can be seen that after treatment with DMSO, there also are visible amounts of S and traces of F and Si. In addition, C content increases, as expected for a solvent exchange where DMSO is incorporated in the structure. The results of the high-resolution measured peaks are shown in **Figure S10h**. In the PPD/molybdate sample, Mo^{6+} is present, but after DMSO treatment, we determined a lower oxidation number Mo^{m+} (probably Mo^{5+}). PPD/molybdates have mainly O bound to Mo^{6+} and a lower ratio of O=C bonds (no Mo^{4+}). After DMSO treatment, more Mo^{5+} containing bonds are evident, which also correlates with the ratios in the Mo 3d peaks. These data show that during the treatment with DMSO, the molybdenum is also partially reduced.

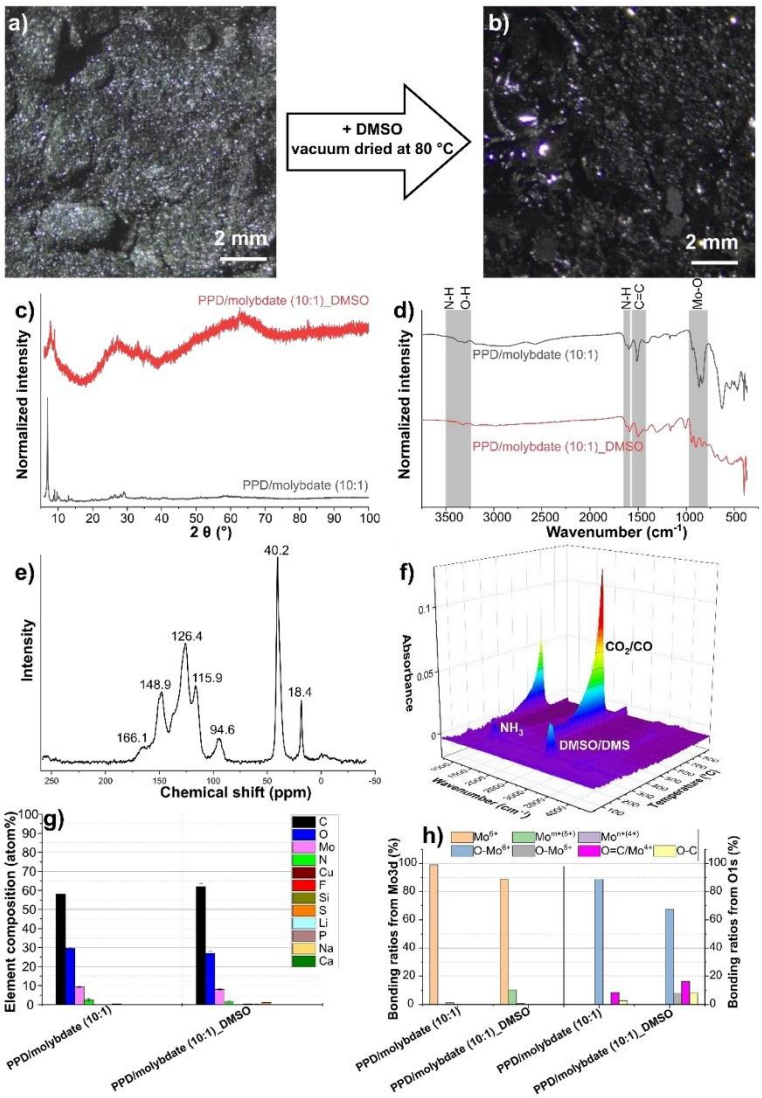

Figure S10: Investigation of the effect of DMSO. (a) Microscopic image of PPD molybdate (1:10) powder. (b) Microscopic image of PPD molybdate (10:1)_DMSO powder. (c) X-ray diffractograms of PPD/molybdate (10:1) and PPD/molybdate (10:1)_DMSO. (d) FTIR spectra of PPD/molybdate (10:1) and PPD/molybdate (10:1)_DMSO. (e) ^{13}C CP-MAS NMR spectra of PPD/molybdate (10:1)_DMSO. (f) TG-FTIR measurements of PPD/molybdate (10:1)_DMSO. (g) Element composition from XPS data for PPD/molybdate (10:1) and PPD/molybdate (10:1)_DMSO. (h) Bonding ratios determined from Mo3d peaks and O1s peaks of PPD/molybdate (10:1) and PPD/molybdate (10:1)_DMSO.

In summary, treatment with DMSO leads to solvent exchange and induces a redox reaction that partially oxidizes the PPD while simultaneously reducing DMSO and molybdenum. This shows very well how redox-active the material is when the sole treatment with DMSO induces a redox reaction.

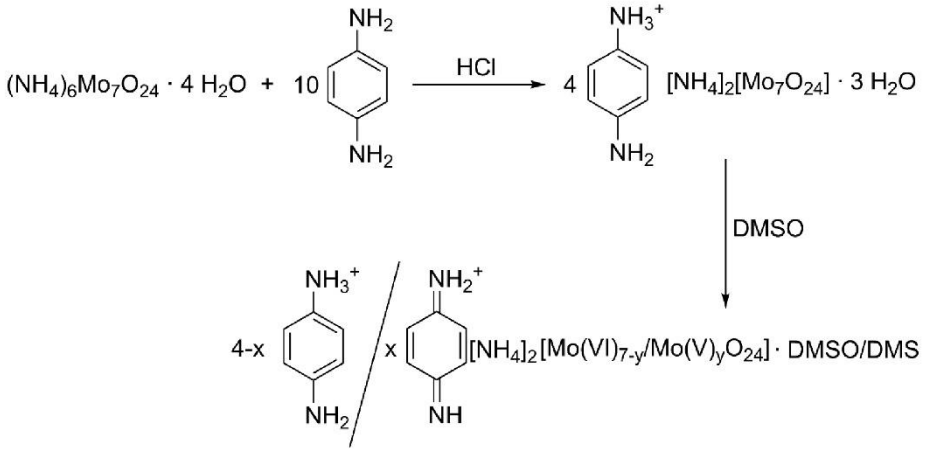

Figure S11: Reaction mechanism of PPD/molybdate (10:1) and its effect of DMSO.

Table S4: The synthesis of the PPD/molybdate precipitates with different ratios.

PPD/molybdate	Ratio (PPD : AHM)	AHM (g) (mol)	PPD (g) (mol)	HCl (M)
1	1 : 1	3.86 $3.12 \cdot 10^{-3}$	0.338 $3.13 \cdot 10^{-3}$	0.025
2	2 : 1	3.86 $3.12 \cdot 10^{-3}$	0.676 $6.25 \cdot 10^{-3}$	0.025
3	5 : 1	3.86 $3.12 \cdot 10^{-3}$	1.69 0.0156	0.025
4	9 : 1	3.86 $3.12 \cdot 10^{-3}$	3.04 0.0281	0.025
5	10 : 1	3.86 $3.12 \cdot 10^{-3}$	3.38 0.0313	0.025
6	15 : 1	3.86 $3.12 \cdot 10^{-3}$	5.07 0.0469	0.05
7	18 : 1	3.86 $3.12 \cdot 10^{-3}$	6.08 0.0562	0.05
8	20 : 1	3.86 $3.12 \cdot 10^{-3}$	6.76 0.0625	0.05
9	25 : 1	3.86 $3.12 \cdot 10^{-3}$	8.45 0.0781	0.075
10	30 : 1	3.86 $3.12 \cdot 10^{-3}$	10.14 0.0938	0.1

Table S5: The synthesis of the PPD/molybdate precipitates in the microjet reactor with different ratios.

PPD/molybdate	Ratio (PPD : AHM)	AHM (g) (mol)	PPD (g) (mol)	HCl (M)
11	1 : 1	3.86 $3.12 \cdot 10^{-3}$	0.338 $3.13 \cdot 10^{-3}$	0.025
12	2 : 1	3.86 $3.12 \cdot 10^{-3}$	0.676 $6.25 \cdot 10^{-3}$	0.025
13	5 : 1	3.86 $3.12 \cdot 10^{-3}$	1.69 0.0156	0.025
14	9 : 1	3.86 $3.12 \cdot 10^{-3}$	3.04 0.0281	0.025
15	10 : 1	3.86 $3.12 \cdot 10^{-3}$	3.38 0.0313	0.025
16	15 : 1	3.86 $3.12 \cdot 10^{-3}$	5.07 0.0469	0.05
17	18 : 1	3.86 $3.12 \cdot 10^{-3}$	6.08 0.0562	0.05
18	20 : 1	3.86 $3.12 \cdot 10^{-3}$	6.76 0.0625	0.05
19	25 : 1	3.86 $3.12 \cdot 10^{-3}$	8.45 0.0781	0.075
20	30 : 1	3.86 $3.12 \cdot 10^{-3}$	10.14 0.0938	0.1

Supporting references

(1) Upreti, S.; Ramanan, A. Structure-Directing Role of Hydrogen-Bonded Dimers of Phenylenediammonium Cations: Supramolecular Assemblies of Octamolybdate-Based Organic-Inorganic Hybrids. *Cryst. Growth Des.* **2005**, *5*, 1837–1843. https://doi.org/10.1021/cg050100m.

(2) Ohno, K.; Okimura, M.; Akai, N.; Katsumoto, Y. The Effect of Cooperative Hydrogen Bonding on the OH Stretching-Band Shift for Water Clusters Studied by Matrix-Isolation Infrared Spectroscopy and Density Functional Theory. *Phys. Chem. Chem. Phys.* **2005**, *7*, 3005–3014. https://doi.org/10.1039/b506641g.

(3) Xu, L.; Sun, Y.; Han, B.; Chang, S. Electrochemical Performances on Both Poly(Phenylenediamine) Derivatives as Anode of Lithium-Ion Batteries. *J. Electrochem. Soc.* **2019**, *166*, A1363–A1369. https://doi.org/10.1149/2.0351908jes.

3.2 Continuous Wet Chemical Synthesis of $Mo(C,N,O)_x$ as Anode Materials for Li-Ion Batteries

This chapter builds on the previous results and deals with the pyrolysis of presented inorganic-organic hybrid materials. A further class of material is presented as an anode material based on inorganic-organic hybrid precursors. The sizes and morphologies could be obtained during the pyrolysis of the hybrid precursors. Since these are important factors for electrochemical performance, as mentioned above, it is a suitable synthesis route for the production of anode materials for LIBs.

By optimizing the pyrolysis conditions such as temperature and time, mixtures of molybdenum carbides, nitrides, oxides, elemental molybdenum and mixed anionic compounds such as $Mo(C,N,O)_x$ embedded in a carbonaceous matrix could be obtained. The proportion of organic components in the hybrid precursor is also decisive for pyrolysis. The latter material, $Mo(C,N,O)_x$ embedded in a carbonaceous matrix, shows not only excess carbon but also staple defects, which leads to an improvement in electrochemical performance.

Beyond the synthetic process, the article highlights the in-depth characterization of the materials and the examination of the electrochemical lithiation of the materials.

Author Contributions:

Mana Abdirahman Mohamed: Conceptualization, materials synthesis, measurements, data analysis, writing, plotting, discussion, and manuscript revision.

Stefanie Arnold: Electrochemical measurements, writing, plotting, discussion, Raman measurements, and manuscript revision.

Oliver Janka: Discussion, analysis of the PXRD data and manuscript revision.

Antje Quade: XPS measurement, plotting, discussion, and manuscript revision.

Jörg Schmauch: Acquisition of HR-TEM and TEM images and determination of lattice plane distances.

Volker Presser: Supervision, discussion, and manuscript revision.

Guido Kickelbick: Conceptualization, supervision, project administration, discussion, and manuscript revision.

Journal of Materials Chemistry A

ROYAL SOCIETY OF CHEMISTRY

PAPER

View Article Online
View Journal | View Issue

Check for updates

Cite this: J. Mater. Chem. A, 2023, 11, 19936

Continuous wet chemical synthesis of $Mo(C,N,O)_x$ as anode materials for Li-ion batteries†

Mana Abdirahman Mohamed, ‡[a] Stefanie Arnold, ‡[bc] Oliver Janka, [a] Antje Quade, [e] Jörg Schmauch, [f] Volker Presser *[bcd] and Guido Kickelbick *[a]

Molybdenum carbides, oxides, and mixed anionic carbide–nitride–oxides $Mo(C,N,O)_x$ are potential anode materials for lithium-ion batteries. Here we present the preparation of hybrid inorganic–organic precursors by a precipitation reaction of ammonium heptamolybdate ($(NH_4)_6Mo_7O_{24}$) with *para*-phenylenediamine in a continuous wet chemical process known as a microjet reactor. The mixing ratio of the two components has a crucial influence on the chemical composition of the obtained material. Pyrolysis of the precipitated precursor compounds preserved the size and morphology of the micro- to nanometer-sized starting materials. Changes in pyrolysis conditions such as temperature and time resulted in variations of the final compositions of the products, which consisted of mixtures of $Mo(C,N,O)_x$, MoO_2, Mo_2C, Mo_2N, and Mo. We optimized the reaction conditions to obtain carbide-rich phases. When evaluated as an anode material for application in lithium-ion battery half-cells, one of the optimized materials shows a remarkably high capacity of 933 mA h g^{-1} after 500 cycles. The maximum capacity is reached after an activation process caused by various conversion reactions with lithium.

Received 6th June 2023
Accepted 6th August 2023

DOI: 10.1039/d3ta03340f

rsc.li/materials-a

1. Introduction

Due to their high energy density, long cycle life, and high working potential, rechargeable lithium-ion batteries (LIBs) dominate the current electrochemical energy storage market.[1–3] The ever-growing demand for LIBs, especially in electric vehicles, has increased the necessity for new electrode materials with improved battery performance. Graphite remains one of the most important anode materials for LIBs, with a theoretical capacity of 372 mA h g^{-1}.[4,5] Designing new anode materials with high specific capacity is becoming an increasingly important requirement for high-performance LIBs. Therefore, research is focussing on other materials with enhanced capacity. Particularly attractive are alloying or conversion-type materials.[6–9] For example, molybdenum oxides provide a theoretical capacity of 1117 mA h g^{-1} for MoO_3 [10–12] and 838 mA h g^{-1} for MoO_2 [13–15] when forming Li-rich phases during conversion reaction. Molybdenum carbides with the compositions Mo_2C or MoC_x show favorable lithium storage properties compared to pure oxides due to better electrical conductivity and excellent mechanical and chemical stability.[16] Combining the properties of molybdenum oxides and carbides could lead to promising electrode materials for LIBs.

A promising way to produce molybdenum carbides and molybdenum oxycarbides is through precursor methods. The milder reaction conditions, in combination with a versatile composition of the precursors, allow better tailoring of the size and morphology of the final product and are less energy consuming than other methods.[17] Suitable precursors can be obtained from precipitation reactions, which are subsequently pyrolyzed to the target compounds. Typical examples for this route are mixtures of various molybdates with aniline,[18] *para*-phenylenediamine,[19] 2-methylimidazole,[16] melamine,[20] or dicyandiamide.[21] Giordano *et al.* also showed that Mo_2C and Mo_2N nanoparticles could be prepared from $MoCl_5$ and urea.[22] A facile preparation method *via* self-polymerization of dopamine for Mo_2C nanoparticles supported on 3D carbon micro flowers was discovered by Huang *et al.*[23] Li *et al.* developed a new pathway for mesoporous and nanosized Mo_2C/Mo_2N heterojunctions using dopamine-molybdate coordination precursor with silica nanoparticles,[24] while mixed salt precursors consisting of a molybdenum hexamethylenetetramine complex were presented by Wang *et al.*[25]

[a]Saarland University, Inorganic Solid-State Chemistry, Campus C4 1, 66123 Saarbrücken, Germany. E-mail: guido.kickelbick@uni-saarland.de
[b]INM – Leibniz Institute for New Materials, 66123 Saarbrücken, Germany. E-mail: volker.presser@leibniz-inm.de
[c]Saarland University, Department of Materials Science and Engineering, 66123 Saarbrücken, Germany
[d]Saarene – Saarland Center for Energy Materials and Sustainability, 66123 Saarbrücken, Germany
[e]Leibniz Institute for Plasma Science and Technology, Felix-Hausdorff-Straße 2, 17489 Greifswald, Germany
[f]Physics Department, Saarland University, Campus D2.2, 66123 Saarbrücken, Germany

† Electronic supplementary information (ESI) available. See DOI: https://doi.org/10.1039/d3ta03340f

‡ Equal contributions.

A popular source for molybdenum in the precursors is ammonium heptamolybdate $(NH_4)_6Mo_7O_{24}$ (AHM), which can form inorganic–organic hybrid precipitates with various organic molecules that can be pyrolyzed to Mo_2C.[22,26] The pyrolysis conditions for converting the precursors to the carbides must be accurately controlled because of the many binary compounds in the Mo–O and Mo–C systems. Examples include orthorhombic high-temperature Mo_4O_{11},[27,28] monoclinic MoO_2,[28] orthorhombic Mo_2C[29] (ESI, Fig. S1a†), and even cubic Mo.[30,31] At around 600 °C, MoO_2, MoC, and C are in equilibrium. Molybdenum oxycarbide can be obtained at this temperature, while above 650 °C Mo_2C is the most stable phase.[32] Other molybdenum carbide products, such as cubic (ESI, Fig. S1b†) or hexagonal (ESI, Fig. S1c†) MoC_x ($x = 0.46$–0.75) can also be formed. The use of amine ligands may furthermore lead to the formation of nitrides such as Mo_2N.[22,32]

The present work uses the continuous[26,33,34] and easy-to-scale[35–37] microjet reactor synthesis to obtain nanostructured Mo-based particles. The continuous wet chemical process allows for larger production volumes while often also a better control over reaction conditions, and thus a better control over particle morphology and reproducibility are achieved. We present a systematic study on the precursor formation by the microjet method and subsequent pyrolysis of $Mo(C,N,O)_x$ materials. In a previous publication, we could show that different precursor compositions are obtained depending on the ratio between the molybdenum source and the *para*-phenylenediamin (PPD) in the reactor.[26] The resulting non-pyrolyzed materials showed different electrochemical behavior in battery applications depending on their composition. The precursors are obtained as precipitates in the microjet reaction by an exchange reaction of the ammonium ions in AHM against the protonated PPD. In our present study, we will focus on the pyrolysis of the achieved precursors and their electrochemical behavior. The influence of various parameters, such as the decomposition temperature, which affects the molybdenum carbide species, and the effect of the precursor composition was analyzed to understand the role of the carbon source during the pyrolysis. In addition, we carried out an electrochemical characterization on the obtained compounds to understand the effect of composition on electrochemical parameters.

2. Experimental section

2.1. Materials

Ammonium heptamolybdate tetrahydrate ($(NH_4)_6Mo_7O_{24}\cdot 4H_2O$, AHM; ≥99%) was purchased from Carl Roth. *para*-Phenylenediamine (PPD; 97%) was ordered from Alfa Aesar. Hydrochloric acid (HCl; 37%) was bought from Bernd Kraft GmbH. Ethanol (99% denatured with 1% petroleum ether) was received from BCD Chemie GmbH. Conductive carbon additive (Type C65) was ordered from IMERYS Graphite&Carbon. Polyvinylidene fluoride (PVdF, 99.5%), dimethyl sulfoxide (DMSO, anhydrous, ≥99.9%), and lithium hexafluorophosphate ($LiPF_6$; LP 30; 1 M in an ethylene carbonate (EC) and dimethyl carbonate (DMC) mixture in the ratio EC : DMC (1 : 1 by volume)) as electrolyte were obtained from Sigma-Aldrich. No further purification was conducted for all chemicals.

2.2. Material synthesis

The PPD/molybdate precursor synthesis is described in detail in our previous work.[26] Briefly, AHM and PPD were dissolved in water, and a 0.25–0.10 M diluted HCl solution was prepared. These solutions were the educt solution for the beaker and microjet precipitation. For the microjet experiments, two HPLC pumps (LaPrep P110 preparative HPLC pumps (VWR)) were used to deliver the solutions with a flow rate of 250 mL min^{-1} at room temperature. The reaction occurred in the microjet reactor, where the solutions were pushed at high pressure through a 300 μm diameter nozzle into the reaction chamber. Nitrogen gas was applied to remove the particles formed.[26,33] The particles were isolated by centrifugation (8000 rpm, 15 min) at the end of the precipitation. All products were washed with ethanol and dried at 80 °C. Finally, the obtained precursors were pyrolyzed under argon flow with the temperature program shown in Fig. 1.

2.3. Material characterization

Powder X-ray diffraction (PXRD) measurements were performed using a Bruker D8-A25-Advance diffractometer in a Bragg–Brentano geometry with CuK_α-radiation ($Cu\text{-}K_\alpha$, $\lambda = 154.06$ pm, 40 kV, 40 mA). PXRD was conducted with a total measurement time of 1 h and from 6–130° 2θ with a step size of 0.013°. The powder is applied to a recessed stainless steel or a silicon zero-background carrier. Rietveld analysis using Topas 5 was applied to quantify the crystalline phases in the samples.[38] The crystallographic data for the Rietveld refinements were obtained from Crystallographic Open Database (COD) and the Inorganic Crystal Structure Database (ICSD).

Scanning electron microscopy (SEM) was carried out using JEOL JSM-7000 F microscope at a working distance of 10 mm and operating at 20 kV. A small amount was placed on a sample stub covered with carbon adhesive film to prepare the samples, and then a thin gold layer was deposited *via* sputter coating.

The elemental analyses were performed on an Elementar Vario Micro cube. 1.5–2.5 mg of the substance to be analyzed is weighed out. The sample weight is determined to the nearest 0.001 mg. The powders are weighed into special tin boats, then folded into cube-shaped packets.

X-ray photoelectron spectroscopy (XPS) was conducted using an Axis Supra (Kratos Analytical) spectrometer. Survey and elemental scans were recorded using $Al\text{-}K_\alpha$ radiation with a power of 150 W and a pass energy of 160 eV and 80 eV,

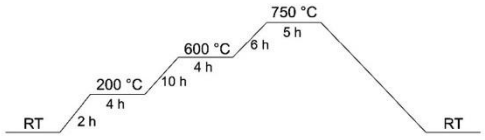

Fig. 1 Temperature program for the pyrolysis (RT: room temperature).

respectively. Concerning high-resolution measurements, 225 W at 10 eV was employed. The data was processed with CasaXPS (Casa Software, version 2.3.15). The powders were sprinkled onto the surface of a small piece (5 × 5 mm^2) of sticky carbon tape using a spatula. The flat side of the spatula was used to press the powders firmly into the tape. After removing the loose powder from the surface of the sample bar, the holder was inserted into the XPS load lock.

A Renishaw inVia Raman microscope was used to collect Raman spectra, equipped with a neodymium-doped yttrium-aluminum-garnet laser with an excitation wavelength of 532 nm and a laser power of approximately 0.05 mW at the sample surface, a 2400 mm per grating, and a 50× objective with a numerical aperture of 0.75. From each sample, five different spots were collected with five accumulations and 30 s acquisition time. Normalization of all spectra from 0–1 was performed. The powder samples were fixed onto the glass microscope slides. The spectra underwent automatic cosmic ray removal. Before and after the measurement, a silicon standard was used to calibrate the system.

Transmission electron microscopy (TEM) was performed using a JEOL JEM-2011 and a JEOL JEM-ARM 200 instrument. Previously, the sample was suspended in ethanol, assisted by ultrasonic treatment, then that suspension was deposited on carbon-coated copper grids (Plano S160-3).

3. Electrochemical characterization

3.1. Electrode materials and preparation

Working electrodes were obtained by mixing 80 mass% PPD/molybdate (1 : 1) (750 °C), PPD/molybdate (10 : 1) (750 °C), PPD/molybdate (9 : 1) (600 °C) or PPD/molybdate (10 : 1) (600 °C) powder, respectively, with 10 mass% conductive carbon additive (Type C65, IMERYS Graphite&Carbon) and 10 mass% polyvinylidene fluoride (PVdF, 99.9%, Sigma-Aldrich), dissolved in dimethyl sulfoxide (DMSO, >99.9%, anhydrous, Sigma-Aldrich), in a SpeedMixer DAC 150 SP from Hauschild. After the active material and the conductive carbon were mixed and grounded manually in a mortar, the dry powder mix was mixed at 1000 rpm for 5 min in a SpeedMixer. Then the DMSO was added dropwise to obtain a viscous paste. This paste was again mixed at 1500 rpm for 5 min following 2500 rpm for 5 min. After adding the PVdF binder solution (10 mass% PVdF in DMSO),[39,40] the last mixing step was conducted at 800 rpm for 10 min. The suspension was stirred for 12 h on a magnetic stirrer to obtain a homogeneous electrode slurry. The obtained slurries were doctor-blade cast on copper foil with a wet thickness of 200 μm. After an initial drying step of the electrodes at ambient conditions for 12 h, a further drying step at 110 °C for 12 h was conducted to remove the remaining solvent. The packing density of the electrode was adjusted by dry-pressing in the rolling machine (HR01 hot rolling machine, MTI). Afterward, discs of 12 mm diameter were punched from the coating using press-punch (EL-CELL) and applied as the working electrode (WE). The resulting electrode thickness of the dried electrodes was 45–65 μm with a material loading of 2.5 ± 1 mg cm^{-2}.

3.2. Cell preparation and electrochemical characterization

2032-type coin cells as a two-electrode system were used for electrochemical testing with an organic electrolyte. After drying all cell parts at 100 °C, the cells were assembled inside an argon-filled glovebox (MBraun Labmaster 130; O_2 and H_2O < 0.1 ppm) using a hydraulic crimper (MSK-110, MTI corp). A pressed and punched lithium metal disc (MTI Corp) of 11 mm diameter and a uniform thickness of 0.45 mm was used both as the counter electrode (CE) and a reference electrode (RE). To separate the WE and CE/RE, vacuum-dried compressed glass-fiber separator (GF/F, Whatman) discs measuring 18 mm in diameter were utilized. On the backside of each lithium counter electrode, a stainless-steel spacer/current collector was placed. The cells were filled with 150 μL of 1 M lithium hexafluoridophosphate ($LiPF_6$) in a mixture of ethylene carbonate (EC) and dimethyl carbonate (DMC) in a volume ratio of 1 : 1 (EC : DMC) as the electrolyte (LP 30, Sigma-Aldrich).

All electrochemical measurements were carried out in a climate chamber (Binder) with a constant temperature of 25 ± 1 °C. Cyclic voltammetry (CV) measurements were performed with a multi-channel potentiostat/galvanostat VMP300 (Bio-Logic Science Instrument), equipped with the EC-Lab software. All CV measurements were carried out with different scan rates of 0.10/0.25/0.50/0.75/1.00/2.50/5.00/7.50/10.00 mV s^{-1} for 5 cycles each in a potential window of 0.01–3.00 V *vs.* Li^+/Li.

The galvanostatic charge/discharge cycling with potential limitation (GCPL) was carried out in the range of 0.01–3.00 V *vs.* Li^+/Li with a specific current of 100 mA g^{-1} using an Arbin battery cycler. For the calculation of the specific current and specific capacity, the mass of active material (total hybrid material) was used for normalization. Rate performance measurements were conducted in the same potential window at different currents. The applied specific currents were 0.1, 0.2, 0.5, 1.0, 2.0, 4.0, 8.0 A g^{-1}, and (again) 0.1 A g^{-1}.

4. Results and discussion

4.1. Precipitation of precursors

Precipitation reactions for forming precursors were performed in an aqueous solution by mixing AHM as a molybdenum source with *para*-phenylenediamine (PPD). The resulting hybrid inorganic–organic precipitates were used as precursors in a subsequent pyrolysis reaction to form molybdenum carbides, oxides, oxycarbides, and nitrides (ESI, Fig. S2†). The organic components serve as carbon and nitrogen sources during thermal decomposition, while the molybdate supplies the oxygen. Details on the preparations can be found in a previous publication.[26]

Two hybrid inorganic–organic precursors can be synthesized depending on the mixing ratio of molybdate and PPD, regardless of the chosen reaction method (batch or microjet). The first precursor is formed at a low PPD ratio (1 : 1 to 5 : 1) and has the composition $[C_6H_{10}N_2]_2[Mo_8O_{26}]\cdot 6H_2O$. The second compound with the composition $[C_6H_9N_2]_4[NH_4]_2[Mo_7O_{24}]\cdot 3H_2O$ is formed at PPD to AHM ratios of 10 : 1 and higher.[26]

4.2. Pyrolysis of the precursors

The pyrolysis of the precursors was carried out by heating the precipitated products to 600 °C or 750 °C in an Ar flow. The obtained products were characterized by powder X-ray diffraction (XRD).

The formation of molybdenum carbide from the precursor during pyrolysis follows a two-step mechanism.[26,31] In the first step, MoO_3 is formed by eliminating H_2O and NH_3. In the second step, the formed molybdenum(VI)-oxide reacts with the carbon source to form carbides such as Mo_2C (eqn (1)). The ratio between MoO_3 and the carbon source is critical since the deficiency or excess of carbon leads to non-targeted side-products such as remaining oxides or elemental Mo.

The binary Mo–C phase diagram reports different molybdenum carbides with the general composition MoC_x.[41] Table 1 lists the structurally characterized modifications according to their carbon content. The highest carbon content discussed here applies to the hexagonal γ-/γ′-MoC ($x = 1$), which crystallizes dimorphically in the WC or TiP-type structure.[42] A defective cubic NaCl type structure is observed when the carbon content is lowered, between $x = 0.67$ and $x = 0.75$.[43] Between $x = 0.46$ and $x = 0.64$, a defective hexagonal NiAs type structure was reported.[44] Since these phases exhibit carbon deficiencies, they seem to be stabilized by the respective carbon content, leading to the assumption that electronic reasons play an important role.[45] For $x = 0.5$, the ordered orthorhombic phase Mo_3C is also observed. For the latter phase, however, reduced electrochemical activity has been reported.[16,46–48] Therefore, the defects in the cubic and hexagonal MoC_x phases can play a significant role in electrochemical intercalation chemistry.[49]

Besides the pure carbides MoC_x, oxycarbides $Mo(C,O)_x$, nitride carbides $Mo(C,N)_x$, and oxide nitride carbides $Mo(C,N,O)_x$ may exist. Further analytical techniques were required to determine the chemical composition. In the following paragraphs, only the description of a pure carbide is used, while the description of oxides or nitrides is used when a clear identification is possible. For example, a pure molybdenum nitride crystallizes in a tetragonal crystal structure.[50] Therefore, it is possible to distinguish this phase from the carbide phases or the molybdenum oxides.

Fig. 2a shows the diffraction data of a pyrolyzed microjet sample (750 °C) with a precursor ratio of 9 : 1 (PPD : AHM). In the Rietveld refinement, the presence of orthorhombic Mo_2C,[29,51] elemental Mo,[30,52] and carbon-deficient MoC_x [53] was observed. The latter phase can adopt a defective NiAs- or NaCl-type structure, in which not all octahedral voids are filled by carbon atoms. Due to the uncertainties regarding the elemental composition and the amount of x, the composition $MoC_{0.67}$ [53] was used to model and refine the cubic phase. In contrast, a hexagonal phase was used for $MoC_{0.5}$.[42]

The X-ray diffractograms show the presence of crystalline Mo and Mo_2C besides a phase with extensively broadened Bragg reflections. These broad reflections could be assigned to a NaCl-type structure. However, the (111) reflection is shifted to higher angles, while the (200) reflection for the same phase is shifted to lower 2θ values. Furthermore, the (200) reflection is significantly broadened compared to the (111) reflection. This behavior is known to be caused by stacking defects in, for example, metals of the Cu type (fcc).[54–57] Here, the (111) plane is a gliding plane that leads to stacking errors that can locally show the atomic arrangement of the hexagonal closed-packed (hcp) structure. To address this problem and qualitatively describe the stacking errors, the structure refinement (Fig. 2a) was carried out using two MoC_x phases, one derived from the NaCl type and the other from the NiAs type. The procedure described was also used to interpret the diffraction data of the samples described in the next paragraphs.

Starting from the different precursor systems, we investigated the influence of pyrolysis at 750 °C.[19,23] Both batch and microjet synthesized samples with PPD-AHM ratios between 1 : 1 and 30 : 1 were used. The systematic studies of the batch samples show that a ratio between AHM and PPD of at least 9 : 1 is required to form the desired MoC_x carbide phase (Fig. 2b). At ratios <9 : 1, orthorhombic Mo_2C, monoclinic MoO_2,[58] and tetragonal Mo_2N,[50] are formed in addition to elemental Mo. At higher PPD amounts, mainly MoC_x is formed with fewer amounts of Mo_2C and elemental Mo. The ratios 9 : 1 and 10 : 1 showed no impurity of elemental Mo. According to these studies, the first assumption that the organic amount in the precursor sample plays an essential role in the pyrolysis process could be verified.

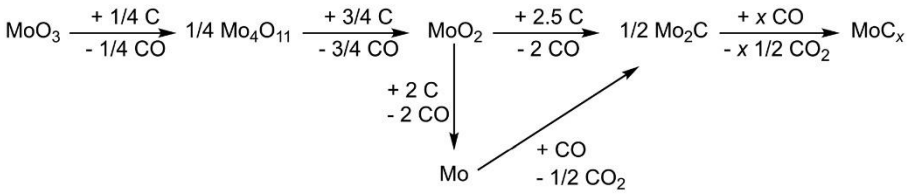

(1)

View Article Online
Journal of Materials Chemistry A Paper

Table 1 Different molybdenum carbide modifications (with increasing carbon content from left to right)

Composition	Mo_2C	$MoC_{0.46-0.64}$	$MoC_{0.67-0.75}$	γ-MoC	γ′-MoC
Space group	*Pbcn*	$P6_3/mmc$	$Fm\bar{3}m$	$P\bar{6}m2$	$P6_3/mmc$
Structure type	$Fe_2N_{0.94}$	Defective NiAs	Defective NaCl	WC	TiP
Stacking sequence	AB	AB	ABC	AA	AABB

Subsequently, analogous to the pyrolyzed PPD/molybdate precursors from batch synthesis, Rietveld analyses were performed to determine the composition of the pyrolyzed products from the microjet synthesis (Fig. 2c). These studies show a similar trend to the results from the batch synthesis. A PPD : AHM ratio of at least 9 : 1 is required to obtain an excess of MoC_x. Compared to the phase compositions of the pyrolyzed PPD/molybdate precursors from the batch synthesis, the pyrolyzed samples from the microjet synthesis tend to form less Mo_2C and Mo at high PPD contents. These observations can be explained by the different phases (with different chemical compositions) formed in the precursor syntheses, as described in our previous work.[26]

A previously reported predominance-area diagram for the carbothermic reduction of MoO_2 shows an equilibrium between MoO_2, C, and MoC_x at 600 °C.[32] In comparison, the reduction product Mo_2C is more stable above 650 °C. Metallic Mo is predominantly formed above 1060 °C with a certain CO content.[32] This leads to the assumption that the formation of MoC_x or the respective oxide nitride carbide $Mo(C,N,O)_x$ could be enhanced at 600 °C.[16]

Therefore, we also investigated the influence of temperature during pyrolysis (Fig. 2d). For this purpose, the 10 : 1 PPD/molybdate precursors were pyrolyzed at 600 °C and 750 °C, respectively. In addition, the pyrolysis time was extended to 10 hours instead of 5 hours. Rietveld analysis of the product

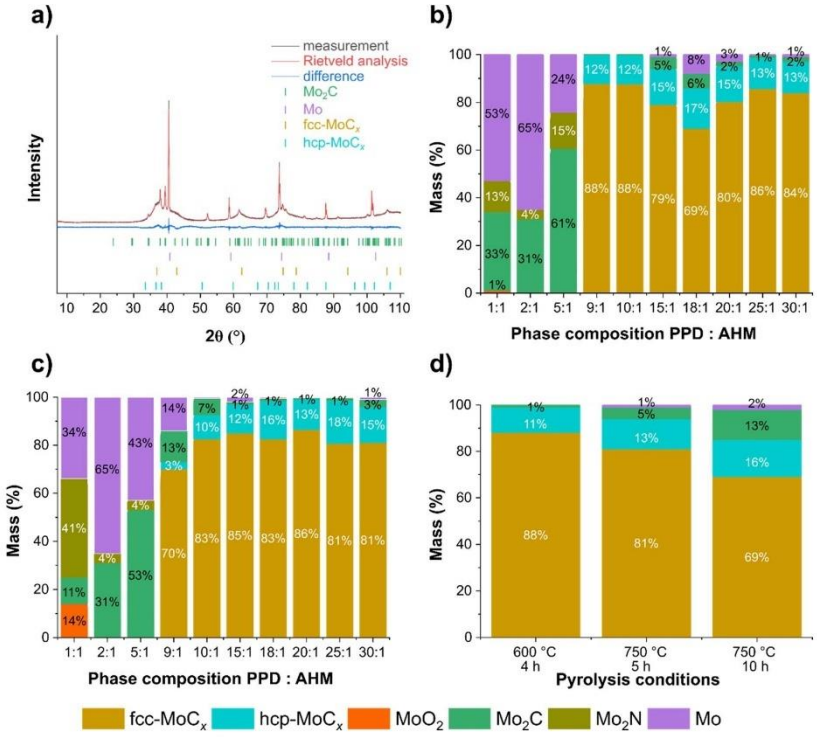

Fig. 2 (a) Structural analysis of the thermally treated PPD/molybdate precursor (9 : 1) at 750 °C: the refined phase compositions are 70(1) mass% fcc-MoC_x, 3(1) mass% hcp-MoC_x, 13(1) mass% Mo_2C and 14(1) mass% Mo. (b) Phase compositions of the pyrolyzed PPD/molybdate precursors from batch synthesis and (c) from microjet synthesis determined *via* fitting the XRD data. (d) Phase compositions of the pyrolyzed PPD/molybdate precursors (10 : 1) determined *via* fitting the XRD data.

illustrates the expected trend. Lower temperature results in an excess of the MoC_x phase without significant contamination by Mo_2C and elemental molybdenum. Increasing the pyrolysis temperature and time leads to an increase in Mo_2C and elemental molybdenum.

A possible approach to avoid the formation of elemental molybdenum could be to increase the amount of organic components. This would result in the formation of less reducing CO and thus more Mo_2C (eqn (1)). Another approach to avoid elemental molybdenum in the sample could be to lower the reaction temperature. This can be concluded from the thermodynamic studies of Zhu *et al.*[32]

Having established the compositional space by X-ray diffraction, additional measurements were employed to verify the results. Elemental analysis of the thermally treated PPD/molybdate precursors (10 : 1) (600 °C and 750 °C) shows a high carbon (21 mass% and 20 mass%, respectively) content (*ESI*, Table S1†) that can be attributed to the presence of amorphous carbon in the samples. The product particles are embedded in a carbon matrix through the pyrolysis of the precursors conducted in an argon atmosphere.[16,21,59,60]

By comparing the elemental analysis of the pyrolyzed PPD/molybdate precursors from the 1 : 1 to 30 : 1 ratios (ESI, Table S1†), it is apparent that the carbon content in the 1 : 1 to 5 : 1 ratios was not as high as that of the 9 : 1 to 30 : 1 samples. This suggests that a higher PPD content is needed to produce the desired MoC_x phases and generate a carbon matrix that hosts these particles.

The Raman spectra of the pyrolyzed precursors (10 : 1 ratio) also confirm the presence of graphitic carbon in the sample, where the characteristic D-band (1360 cm^{-1}) and G-band (1600 cm^{-1}) are observed (Fig. 3a).[61] In contrast, no D-band and G-band are visible in the Raman spectrum of pyrolyzed PPD/molybdate precursors from the 1 : 1 ratio (Fig. 3a). This observation agrees with the elemental analysis, where we noted an absence of excess carbon for samples 1 : 1 to 5 : 1. At the same time, this is the case for samples 9 : 1 to 30 : 1. Transmission electron microscopy (TEM, Fig. 3c and d) of the samples obtained from the 10 : 1 precursor further confirms that the MoC_x particles are embedded in a carbon matrix. Combining MoC_x particles embedded in carbonaceous materials creates a potential anode material with high capacity and cycling stability.[16] Finally, Raman spectra of the pyrolyzed 1 : 1 precursors (750 °C) revealed the formation of MoO_2, which is in good agreement with the above-shown results.[62,63]

Being able to produce nearly phase-pure samples of MoC_x at lower decomposition temperatures revitalized the question about the stacking problem before addressing the electrochemical performance. Fig. 3b shows a powder diffraction pattern of a PPD : AHM 9 : 1 sample decomposed at 600 °C. The diffraction pattern can be refined by contributions of cubic and hexagonal MoC_x phases, modeling the stacking faults present in the material. To further assess the postulated stacking fault interpretation, TEM investigations were conducted. The images unambiguously prove the presence of stacking faults (Fig. 3c). Lattice plane distances observed in TEM agree with the expected values from hexagonal and cubic MoC_x. The *d*-values between 0.22 nm (011) and 0.24 nm (002) correspond to hexagonal MoC_x, while the lattice plane distance of $d = 0.243$ nm agrees with the (111) distance from cubic MoC_x (Fig. 3d).

Since batch and microjet syntheses lead to similar products after decomposition, the samples prepared by microjet were used for further electrochemical studies. In addition, the studies show that lower decomposition temperatures (600 °C instead of 750 °C) are beneficial for the formation of the desired MoC_x phases and that the optimal PPD : AHM ratio for the present phases is between 9 : 1 and 10 : 1. In the syntheses, molybdenum (oxide nitride) carbides were embedded in an amorphous carbon matrix.

4.3. Selection of materials for electrochemical characterization

After the systematic studies regarding the synthesis and pyrolysis conditions, a range of samples with different phase compositions was chosen for the electrochemical investigations. Scanning electron microscopy (SEM) of the samples tested as LIB anodes was performed (Fig. 4). First, the samples with PPD : AHM ratio 1 : 1 (Fig. 4a) and 10 : 1 (Fig. 4b) pyrolyzed at 750 °C were investigated. Contrary to 1 : 1 sample the 10 : 1 exhibit severe stacking faults in the carbide phase and the carbon matrix.

Phases with stacking faults are favored in the application as LIB materials, and the results of the investigations show that lowering the pyrolysis temperature leads to an excess of them.[64] Therefore, the samples pyrolyzed at 600 °C with a PPD : AHM ratio of 9 : 1 (Fig. 4c) and 10 : 1 (Fig. 4d) were additionally examined. Although their phase composition is similar, the particles in the 9 : 1 sample are smaller, suggesting they could show better electrochemical performance.

4.4. Electrochemical characterization of pyrolyzed PPD/molybdate as LIB anode

The electrochemical performance of the four samples mentioned above was investigated in a LIB half-cell set-up with 1 M $LiPF_6$ in EC : DMC (1 : 1 by volume) electrolyte. The results are shown in Fig. 5 and 6. The active materials were wet-coated with a conductive additive and polyvinylidene fluoride binder for electrochemical characterization. Cyclic voltammetry (CV) measurements of all materials were recorded in the voltage range from 0.01 V to 3.00 V *vs.* Li^+/Li at different scan rates (0.10–10.00 mV s^{-1}; Fig. 6 and ESI, Fig. S3†).

The two systems containing the decomposed precursors with a PPD : AHM ratio of 1 : 1 and 10 : 1 (pyrolyzed at 750 °C) show similar peaks during cycling. For both hybrid systems, one clear reduction and one oxidation signal exist at potentials of around 1.1 V *vs.* Li^+/Li and 1.6 V *vs.* Li^+/Li, respectively. This mainly applies to the low scan rates up to 1.00 mV s^{-1}. When the lithiation potential decreases from 1.50 V to 0.05 V *vs.* Li^+/Li, the region where the conversion reaction occurs can be associated with the formation of amorphous Li_2O and the full reduction of Mo.[65] At high scan rates, the 10 : 1 sample pyrolyzed at 750 °C current level is reduced, and the curve slightly deviates from a pure capacitive-like behavior. This may indicate that the scan

View Article Online
Journal of Materials Chemistry A Paper

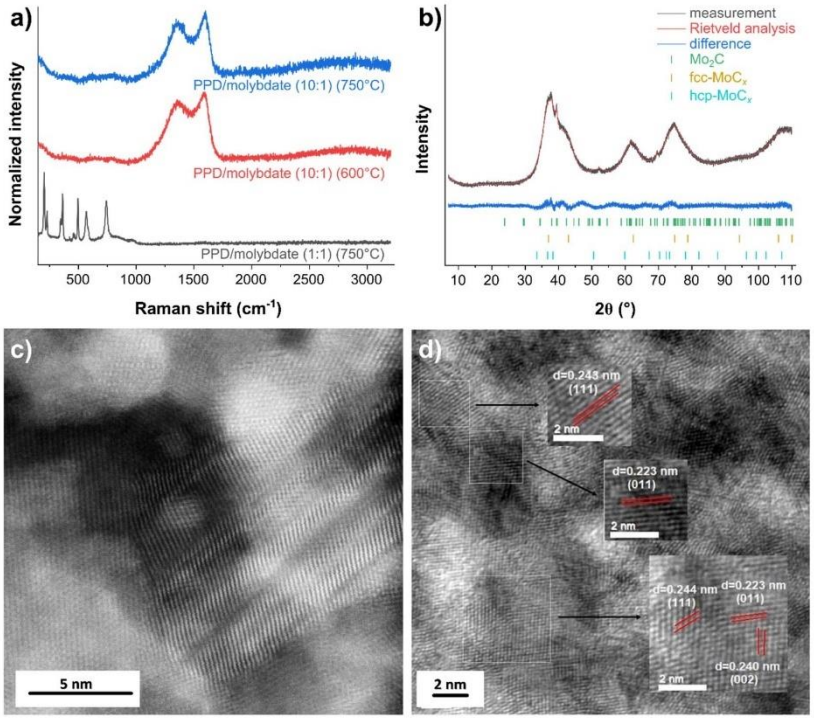

Fig. 3 (a) Raman spectra of pyrolyzed PPD/molybdate precursors measured with 532 nm laser excitation. (b) Structural analysis of the thermally treated PPD/molybdate precursor (9 : 1) at 600 °C: the refined phase compositions are 90(1) mass% fcc-MoC_x, 9(1) mass% hcp-MoC_x and 1(1) mass% Mo_2C. (c) Transmission electron micrographs of the thermally treated PPD/molybdate precursor. (d) The lattice plane distances (d-values) of selected areas.

rate is too fast for the conversion reaction process or that the electrode degrades quickly.

The two samples with a PPD : AHM ratio of 9 : 1 and 10 : 1 pyrolyzed at 600 °C exhibit similar electrochemical behaviors, with the resulting capacity for the 9 : 1 sample pyrolyzed at 600 °C being significantly higher. The first cycle displays an irreversible signal at 0.7 V *vs.* Li^+/Li, which is related to the conversion reaction and the decomposition of electrolyte and solid electrolyte interphase (SEI) formation since this signal disappears in the following cycles. MoC_x shows a pseudocapacitive behavior due to its nanocrystallinity. The high performance at high rates can be partially explained by the significant contribution of a surface-limited capacitive-like process to the charge storage.

Through a kinetic analysis composed of different cyclic voltammograms collected at different scan rates, the contribution of capacitive-like charge storage can be investigated in the so-called b-value analysis. The correlation between the scan rate (v) and the current (i) can be described by the equation $i = avb$, with the fitting parameters represented by a and b. A b-value of 0.5 suggests an ideal charge storage process limited by diffusion, typically seen in battery-like behavior. Conversely, a b-value of 1 indicates a charge storage process limited by the surface and characteristic of electrosorption/capacitive processes.[66–68] The b-value analysis performed in this work on cyclic voltammetry with scan rates between 0.1–1.0 mV s^{-1} is shown in ESI Fig. S4.† In the 9 : 1 sample that was pyrolyzed at 600 °C, the sharp lithiation/de-lithiation peak has a b-value of 0.72. In contrast, the regions at 0.50 V and 2.75 V *vs.* Li^+/Li, which are more pseudocapacitive, demonstrate slightly higher b-values of 0.79 and 0.93, respectively. In comparison, all other samples in this study obtain a slightly lower fraction of non-diffusion limited charge storage.

The distinct signals which appear from the second cycle onward at 1.4 V *vs.* Li^+/Li (oxidation) and 1.3 V *vs.* Li^+/Li (reduction) can be attributed to the conversion reactions of the associated lithiation/de-lithiation of MoC_x ($yLi^+ + MoC_x + y\ e^- \rightarrow Mo + Li_yC_x$, reaction during charging process).[47,69,70] Likewise, significantly weaker reversible redox peaks occur mainly with the 9 : 1 sample pyrolyzed at 600 °C at about 1.2 V *vs.* Li^+/Li, which are related to the partial embedding of the Li-ions into the MoC_x lattice to form Li_yMoC_x.[46,71] The following oxidation

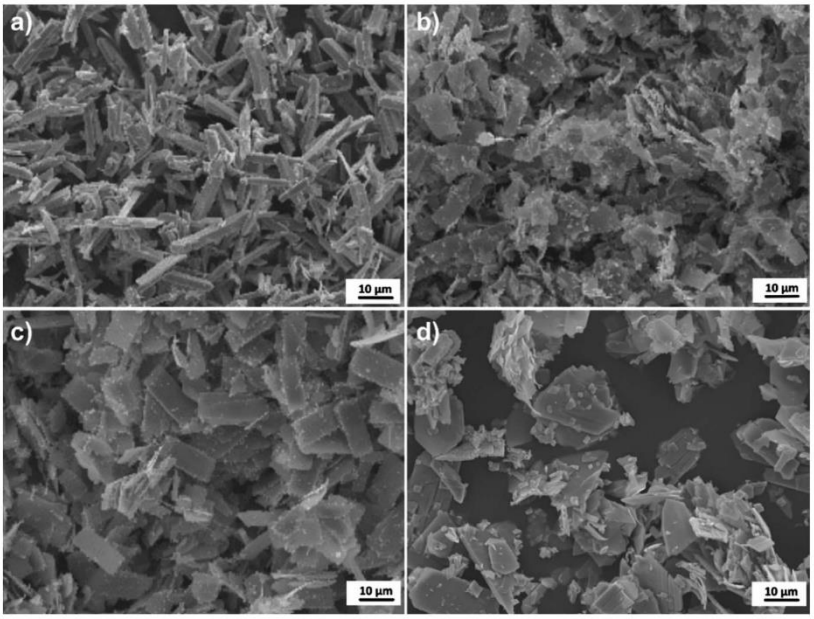

Fig. 4 Scanning electron micrographs of pyrolyzed PPD/molybdate samples (a) 1 : 1 and (b) 10 : 1 pyrolyzed at 750 °C and (c) 9 : 1 and (d) 10 : 1 pyrolyzed at 600 °C.

peak at 1.46 V *vs.* Li^+/Li can be attributed to the oxidation from Li_yMoC_x to Mo and Li_2O during Li^+ deintercalation. Mo_2C does not exhibit any electrochemical activity in the voltage range of 0.01–3.0 V *vs.* Li^+/Li, so there are no detectable reduction or oxidation signals in the cyclic voltammograms.[46]

To explore the electrochemical performance and the corresponding conversion reaction of the various pyrolyzed samples, galvanostatic charge, and discharge experiments were conducted. Typically, the galvanostatic discharge and charge profiles obtained from these experiments (Fig. 6a–d) are analyzed for further insights and confirm the observations from the CV measurements. The first discharge capacities of the precursors with the PPD : AHM ratio of 1 : 1 and 10 : 1 pyrolyzed at 750 °C electrodes occur at 87.5 mA h g^{-1} and 123.8 mA h g^{-1}, with an initial Coulombic efficiency of 44.7% and 65.6%, respectively. This capacity loss follows SEI film formation and insertion of Li^+ into the MoC_x structure. In the following cycles, one can observe a broad plateau at 1.4 V and 0.7 V *vs.* Li^+/Li in the lithiation curve, and a clear plateau at 1.4 V *vs.* Li^+/Li and a broad peak at 1.6 V *vs.* Li^+/Li in the de-lithiation curve. These two charge–discharge plateaus were ambiguously found, indicating the phase transition and conversion reaction, which agrees well with the CV study above. All the plateaus observed, which are still very pronounced in the first cycles, are significantly weakened during the first 100 cycles, which indicates a changed reaction mechanism and/or rapid aging and degradation of the cell.

In comparison, the galvanostatic charge and discharge curves of precursors with a PPD : AHM ratio of 10 : 1 at 600 °C and 9 : 1 pyrolyzed at 600 °C show a discharge capacity of 148 mA h g^{-1} and 531 mA h g^{-1} with Coulombic efficiencies of 94.4% and 54.7%, respectively. The 10 : 1 sample pyrolyzed at 600 °C does not show a substantial plateau in the individual cycles. Instead, there is a broad plateau in the lithiation cycle at around 0.9 V *vs.* Li^+/Li and in the de-lithiation of about 1.5 V *vs.* Li^+/Li. The same plateaus are also observed in a slightly more pronounced form in the 9 : 1 sample pyrolyzed at 600 °C sample, which characterizes the lithiation process of the MoC_x electrode with the associated conversion reaction. It is remarkable that at the 100th cycle, an additional plateau appears at 2.5 V *vs.* Li^+/Li, which can also be identified in the CV analysis. So there seems to be another process responsible for slowly increasing the capacity after a certain number of cycles. The observed electrochemical signatures indicate that the fundamental electrochemical process is not significantly varied by varying the precursors and the pyrolyzing temperature. We also assume that activated carbon might have contributed slightly to the capacity.

Fig. 6f demonstrates the difference in cycling stability of all different $Mo(C,N,O)_x$ embedded in carbonaceous materials at a rate of 100 mA g^{-1}. The lowest electrochemical performance is delivered by the 1 : 1 sample pyrolyzed at 750 °C, which starts with a capacity of 82 mA h g^{-1} and delivers around 104 mA h g^{-1} after 200 cycles, demonstrating a capacity gain of 25%. The

View Article Online
Journal of Materials Chemistry A Paper

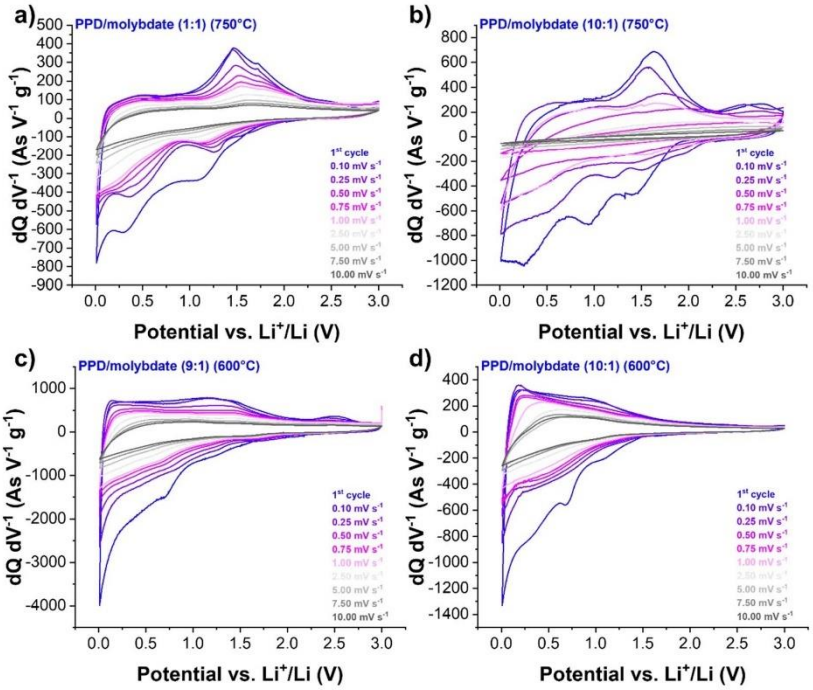

Fig. 5 Cyclic voltammograms of pyrolyzed PPD/molybdate hybrid materials (normalized to scan rate) recorded at different scan rates and a potential range between 0.01 V and 3.00 V *vs.* Li^+/Li for (a) PPD/molybdate (1 : 1) (750 °C), (b) PPD/molybdate (10 : 1) (750 °C), (c) PPD/molybdate (9 : 1) (600 °C), and (d) PPD/molybdate (10 : 1) (600 °C).

10 : 1 sample pyrolyzed at 750 °C, and the 10 : 1 sample pyrolyzed at 600 °C, offer very similar electrochemical behavior compared to the 1 : 1 sample pyrolyzed at 750 °C with de-lithiation capacities of 94 mA h g^{-1} and 154 mA h g^{-1} after 200 cycles combined with a capacity retention of 81% and 124%, respectively.

In contrast, the 9 : 1 sample pyrolyzed at 600 °C yields high electrochemical performance. The values start with an initial capacity of 531 mA h g^{-1}, showing a capacity fading for the first 50 cycles but then rising to a capacity value of 933 mA h g^{-1}, demonstrating capacity retention of 175% after 500 cycles. The presence of Mo_2C and carbon in the hybrid materials may increase the structural stability and buffer the volume changes during the conversion reaction or lithium-ion insertion/extraction, resulting in no severe capacity degradation after 200–500 cycles.[47] The hybrid material with the PPD : AHM ratio of 9 : 1 pyrolyzed at 600 °C indicates at this point that the structure obtained after pyrolysis is electrochemically active or is activated while cycling and thus represents a promising high-capacity material for application in LIBs.

These observations agree with the rate capability tests (Fig. 6e) and indicate that the hybrid material with the PPD : AHM ratio of 9 : 1 pyrolyzed at 600 °C shows volatile performance. Combined with the charge and discharge profiles, this could explain that the pre-activation or the addition in the lithiation mechanism is not achieved yet, leading to very unstable capacities during different specific currents. With significantly lower de-lithiation capacities but much more stable behavior, the precursors 1 : 1 and 10 : 1 pyrolyzed at 750 °C and the precursor 10 : 1 pyrolyzed at 600 °C delivered values of up to 144 mA h g^{-1}, 115 mA h g^{-1} and 243 mA h g^{-1} with a capacity retention of 85%, 82%, and 91%, respectively when returning to the initial current. Overall, good electrochemical performance is favored by the structural defects present in the material, which significantly improves the electrical conductivity of the electrode. Likewise, the formed nanoparticle size influences the Li insertion behavior and lithium storage capacity.[72–76] Smaller particle sizes of the intermediates allow a smaller lithium-ion diffusion distance and form a larger specific surface area, thus achieving a larger electrolyte–electrode material contact area. This effect may improve the kinetic properties of the system since short ion diffusion paths exist. Due to the conversion reactions occurring during cycling, free carbon is also formed from the initial material, which forms a carbon matrix. It can thus buffer the volume change during the lithiation/de-lithiation process while

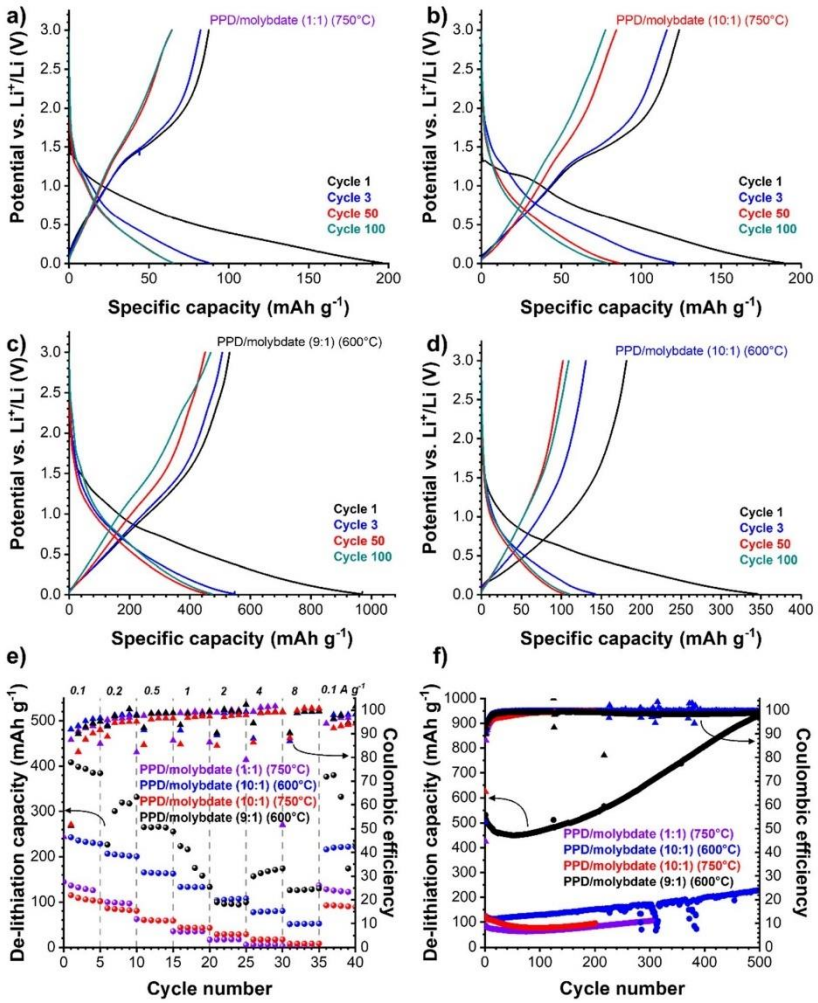

Fig. 6 Electrochemical performance of pyrolyzed PPD/molybdate hybrid materials. Galvanostatic charge and discharge profiles at an applied specific current of 100 mA g^{-1} between 0.01 V and 3.00 V *vs.* Li^+/Li (a) 1 : 1 and (b) 10 : 1 pyrolyzed at 750 °C, and (c) 9 : 1 and (d) 10 : 1 synthesized at 600 °C. Galvanostatic charge/discharge cycling electrochemical performance stability with corresponding Coulombic efficiency values at a specific current of 100 mA g^{-1} for (e) 1 : 1 and 10 : 1 pyrolyzed at 750 °C and 9 : 1 and 10 : 1 synthesized at 600 °C. Rate performance using galvanostatic charge/discharge cycling with corresponding Coulombic efficiency at different values for the specific current for (f) 1 : 1 and 10 : 1 pyrolyzed at 750 °C, and 9 : 1 and 10 : 1 synthesized at 600 °C.

reducing the aggregation of $Mo(C,N,O)_x$ particles.[77,78] The carbon formed can also be activated by the reactions to contribute to the electrochemical storage of the lithium ions. The high specific capacity of the 9 : 1 sample pyrolyzed at 600 °C can be explained by the enhanced formation of Mo^{4+} after lithiation, a reversible process without the evolution of the monoclinic MoO_2 in the 9 : 1 sample pyrolyzed at 600 °C.[79] In addition to the larger interlayer spacing, which favors faster kinetics, the oxygen vacancies also allow a larger physical space for lithium-ion storage to be obtained.[49,80]

Comparing the obtained electrochemical performances with other hybrid and composite molybdenum oxycarbides and molybdenum carbide compounds reported in the literature (Table 2), the optimized sample with the PPD : AHM ratio of 9 : 1 pyrolyzed at 600 °C can show favorable electrochemical performance values (*e.g.*, 933 mA h g^{-1} after 500 cycles at

Table 2 Summary of different electrochemical performances and characteristics of different molybdenum oxycarbides/carbide/oxide hybrid or composite materials[a]

Material	Total electrode composition	Potential *vs.* Li^+/Li/V	Electrolyte	Normalization	Capacity/ mA h g^{-1}	Specific current/ mA g^{-1}	Cycles	Ref.
Molybdenum oxide carbide nanoparticles embedded in N-doped carbon	Active material : SuperP : PVdF 7 : 2 : 1	0.01–3.00	1 M $LiPF_6$ in EC/DMC (1 : 1 by volume)	n.a.	793	100	100	Xiu *et al.*[16]
Mo_2C@C core–shell nanocrystals	Active material : acetylene black : sodium alginate 7 : 2 : 1	0.01–3.00	1 M $LiPF_6$ in EC/EMC/ DMC (1 : 1 : 1 by volume)	n.a.	1089	100	100	Xin *et al.*[85]
MoO_2–Mo_2C–C	MoO_2–Mo_2C–C : acetylene black : CMC 7 : 2 : 1	0.01–3.00	1 M $LiPF_6$ in EC/DEC (1 : 1 by volume)	n.a.	1188	100	250	Yang *et al.*[81]
Red-blood-cell-like porous Mo_2C@CNT microspheres	Active material, SuperP, PVdF 8 : 1 : 1	0.005–3.00	1 M $LiPF_6$ in EC/DMC (1 : 1 by volume)	Mo_2C@CNT	878	160	750	Yu *et al.*[86]
Reduced graphene oxide supported molybdenum carbides	Mo_2C-rGO : SuperP : PVdF 8 : 1 : 1	0.01–3.00	1 M $LiPF_6$ in EC/DMC (1 : 1 by volume)	n.a.	856	100	400	Chen *et al.*[87]
Molybdenum carbide embedded in CNFs	n.a.	0.01–3.00	1.1 M $LiPF_6$ in EC/DMC (1 : 1 by volume)	n.a.	350	500	300	Lee *et al.*[82]
Mesoporous Mo_2C–C hybrid nanospheres	Active material, carbon black, sodium alginate 6 : 2 : 2	0.01–3.00	1 M $LiPF_6$ in EC/DEC/ DMC (1 : 1 : 1 by volume)	Mo_2C and C	673	100	50	Gao *et al.*[69]
MoO_2/Mo_2CT_x heteromicrospheres	Active material, acetylene black, PVdF 8 : 1 : 1	n.a.	1 M $LiPF_6$ in EC/DMC (1 : 1 by volume + 2 wt% VC)	n.a.	780	100	160	Min *et al.*[88]
PPD/molybdate (9 : 1) (600° C) → $Mo(C,N,O)_x$@C hybrid: Conductive carbon additive: PVdF 8 : 1 : 1	**$Mo(C,N,O)_x$@C hybrid: Conductive carbon additive: PVdF 8 : 1 : 1**	**0.01–3.00**	**1 M $LiPF_6$ in EC/DMC (1 : 1 by volume)**	**Total hybrid**	**933**	**100**	**500**	**Our work**

[a] Data from literature sources that are not available are donated as "n.a.". PVdF (polyvinylidene fluoride), $LiPF_6$ (lithium hexafluoridophosphate), EC (ethylene carbonate), DMC (dimethyl carbonates), EMC (ethyl methyl carbonate, DEC (diethyl carbonate), VC (vinylene carbonate), CMC (carboxymethyl cellulose), CNT (carbon nanotubes), CNF (carbon nanofibers), rGO (reduced graphene oxide).

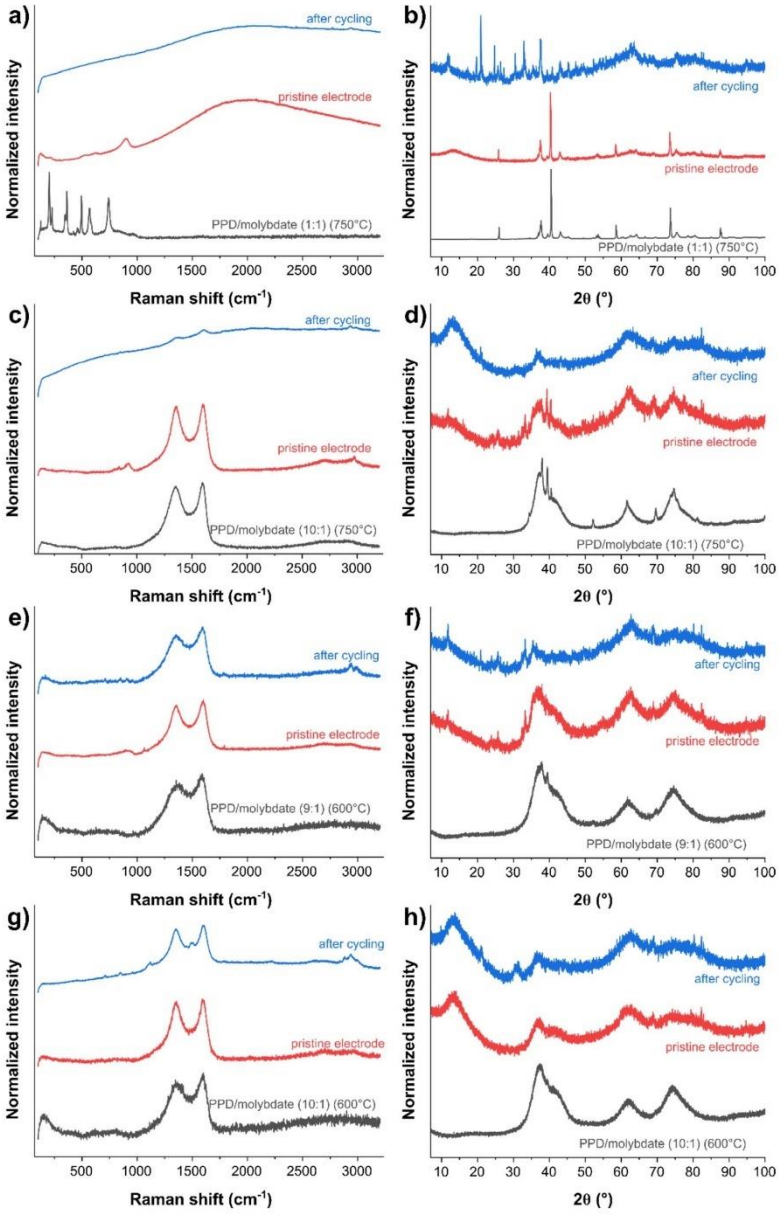

Fig. 7 Raman spectra of the hybrid materials (a) 1 : 1 and (c) 10 : 1 pyrolyzed at 750 °C, and (e) 9 : 1 and (g) 10 : 1 synthesized at 600 °C. X-ray diffractograms of the hybrid materials (b) 1 : 1 and (d) 10 : 1 pyrolyzed at 750 °C, and (f) 9 : 1 and (h) 10 : 1 synthesized at 600 °C.

100 mA h g^{-1}). The materials, optimized by a straightforward manufacturing process, can therefore keep up well with the standard of state-of-the-art literature. For example, Xiu *et al.* obtained with their molybdenum oxycarbide nanoparticles embedded in N-doped carbon a reversible capacity of 793 mA h g^{-1} only for low cycling stability (100 cycles).[16] A high

reversible capacity of 1188 mA h g^{-1} after 250 cycles at a specific current of 100 mA g^{-1} was reported by Yang *et al.* for MoO_2–Mo_2C–C microspheres.[81] Based on a one-step annealing approach, this material delivers a similar electrochemical behavior to our data. This particularly concerns the increasing capacity while cycling, probably connected with an activation process and a change of the material and reaction mechanism, even if our material shows a slightly steeper increase in capacity after the 250 cycles than shown here. With a 2.6-fold higher capacity, our optimized system impresses, for example, compared to the molybdenum carbide embedded in carbon nanofiber as a 3D flexible anode system investigated by Lee *et al.* in 2018. With superior stability and high-rate performance in LIBs, performance values of 350 mA g^{-1} could be achieved after 300 cycles at a specific current of 500 mA g^{-1}.[82] While not showing the trend of increasing capacity during cycling, Gao *et al.* mesoporous Mo_2C–C hybrid nanospheres system show slightly lower de-lithiation capacity with 673 mA h g^{-1} after 50 cycles and a cycling rate of 100 mA h g^{-1}.[69]

In summary, we see good performance with low energy consumption for synthesis and the advantages of the microjet reactor. Optimizing synthesis parameters and subsequent pyrolysis at relatively low temperatures made it possible to obtain characteristic electrochemical behavior comparable to that found in the literature for different molybdenum carbides.[47,83,84]

4.5. Post mortem characterization of pyrolyzed PPD/molybdate LIB anodes

The electrochemical properties and structure–property correlation were better understood by comparing the cycled with untreated materials using Raman spectroscopy and XRD (Fig. 7). PXRD of the PPD : AHM ratio 1 : 1 pyrolyzed at 750 °C shows no significant change, which reveals no significant structural change after electrode preparation (Fig. 7b). After cycling, the powder X-ray diffractogram changes completely and could be assigned to lithium molybdate (Li_2MoO_4; Fig. 7b), crystallizing the trigonal crystal system with space group $R\bar{3}$ ($a = 1433.0(2)$, $c = 958.4(2)$ pm).[89]

No significant changes are visible in the Raman spectra of the 10 : 1 sample pyrolyzed at 750 °C compared to its pristine electrode (Fig. 7c). The D-band and G-band are still present after cycling, but we see a strong fluorescence background. Small peaks in the spectra indicate the presence of the D-band and

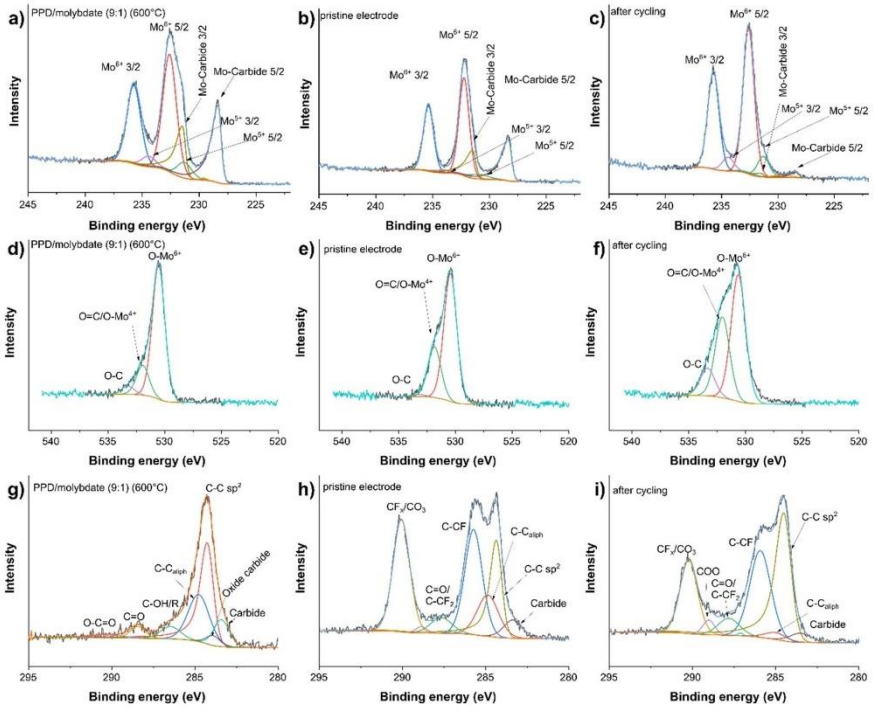

Fig. 8 Fitted XPS Mo 3d spectra of the (a) PPD/molybdate with a PPD : AHM ratio of 9 : 1 pyrolyzed at 600 °C, (b) pristine electrode, (c) electrode after cycling. Fitted XPS O 1s spectra of the (d) PPD/molybdate with a PPD : AHM ratio of 9 : 1 pyrolyzed at 600 °C, (e) pristine electrode, (f) electrode after cycling. Fitted XPS C 1s spectra, (g) PPD/molybdate with a PPD : AHM ratio of 9 : 1 pyrolyzed at 600 °C, (h) pristine electrode, and (i) electrode after cycling.

G-band (Fig. 7c). The corresponding powder X-ray diffractograms reveal a decrease in the crystallinity of the material after electrode preparation. After cycling, the amorphization of the material increases even further (Fig. 7d).

The Raman spectra of the 9 : 1 sample pyrolyzed at 600 °C, the corresponding pristine electrode, and the corresponding electrode after cycling all show the carbon-related D-band and G-band (Fig. 7e). X-ray diffractograms show an amorphization of the material after electrode preparation and cycling (Fig. 7f). The 10 : 1 samples pyrolyzed at 600 °C show similar behavior to the sample 9 : 1 pyrolyzed at 600 °C. The Raman spectra of the 10 : 1 pyrolyzed at 600 °C and the pristine electrode and the electrode after cycling show the D-band and G-band (Fig. 7g). Furthermore, a decrease in crystallinity is visible in the X-ray diffractograms (Fig. 7h). Moreover, the X-ray diffractograms of the electrodes with the ratio 10 : 1 pyrolyzed at 750 °C after cycling, and the samples 9 : 1 and 10 : 1 pyrolyzed at 600 °C show a decrease of the intensity of the reflection at ~37° 2θ, which belongs to the carbide. Nevertheless, several peaks appear in the electrode materials due to the electrode preparation, where PVdF as a binder and carbon black is involved. Furthermore, after cycling, electrolyte components can be detected.[90]

X-ray photoelectron spectroscopy (XPS) was conducted to provide information on the Mo species' oxidation states, oxygen bonding states, and carbon bonding states. Four components were used to fit the Mo 3d peaks (Fig. 8a–c). The Mo^{6+} species has the maximum binding energy (BE) with a BE of 232.6(2) eV. Mo^{5+} with a constant binding energy distance of −1.3 eV was fitted to Mo^{6+}, while Mo^{4+} with a constant binding energy distance of −3 eV was fitted to the Mo^{6+} binding energy. The Mo-carbides were fitted with a BE of 228.5(3) eV.[91] There were four components to fit the O 1s peaks (Fig. 8d–f). The signal at 530.6 eV was used for calibration, which is caused by the O–Mo^{6+} interaction. At a binding energy of 531.2 eV, the O–Mo^{5+} contribution was detected. The binding energies attributed to the O=C and O–Mo^{4+} bonds overlap at 532.0 eV, and the O–C-bond-derived contribution has a binding energy of 533.3 eV.[91] The C 1s peaks were fitted with eight components (Fig. 8g–i). The carbide carbon (Mo–C) was fitted with a binding energy of 283.4(1) eV. The oxide carbide carbon (C–Mo–O) was fitted at 283.9(1) eV. Graphitic carbon (C–C sp^2) is seen at 284.3(1) eV, and amorphous carbon (aliphatic C–C sp^3) is observed at 284.8(1) eV. The binding energies of C–OH/R were found at 286.5(1) eV and C=O at 288.4(1) eV.[92,93] Additionally, the electrode material bonding of C_x–F_y is visible, which partially overlapped. The binding energy of C–CF is 285.7 eV, the one of C=O/C–CF_2 is 287.7 eV, and the one of CF_x/CO_3 is at 290.1 eV.[94] In all cases, the precursor with the PPD : AHM ratio of 9 : 1 pyrolyzed at 600 °C electrode after cycling was compared with its pristine electrode.

The shallow signal depth of XPS of about 10 nm favors information from the interfacial/superficial SEI layer. A comparison of the Mo 3d spectra of the precursor with the PPD : AHM ratio of 9 : 1 pyrolyzed at 600 °C (Fig. 8a) with the pristine electrode (Fig. 8b) shows no significant change. The only difference is that the Mo carbide content decreases slightly while the Mo^{6+} increases slightly. A major change is visible after cycling (Fig. 8c). The content of Mo^{6+}, Mo^{5+}, and Mo^{4+} increases while the Mo-carbide decreases enormously. The O 1s spectra show a decrease in the O–Mo^{6+} content and an increase of the O=C/O–Mo^{4+} content from the precursor with the PPD : AHM ratio of 9 : 1 pyrolyzed at 600 °C (Fig. 8d) to the pristine electrode (Fig. 8e) or the electrode after cycling (Fig. 8f). In the C 1s spectra of the precursor with the PPD : AHM ratio of 9 : 1 pyrolyzed at 600 °C (Fig. 8g), both carbide (Mo–C) and oxycarbides (C–Mo–O), C=O, C–C sp^2, and aliphatic C–C sp^3 are visible. In the pristine electrode (Fig. 8h) and the electrode after cycling (Fig. 8i), CF_x appears due to the polymer binder PVdF added to the material during electrode fabrication. In addition, the peak of aliphatic C–C sp^3 increases because carbon black was also added during electrode fabrication. The increase of the signal sp^2 C–C– binding energy confirms the above assumptions that the carbon matrix increases.

The XPS data indicates a complex process occurs during the electrode preparation and cycling. The Mo-carbide peak vanishes in the Mo 3d spectra, consistent with the XRD data. A shift in the relative ratios of the O–Mo peaks indicates a reduction from O–Mo^{6+} to O–Mo^{4+}.

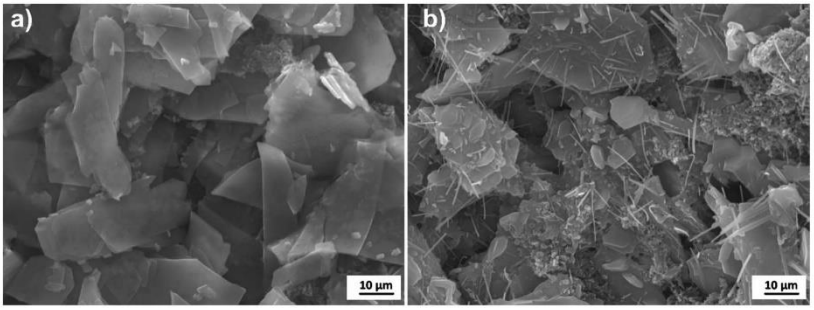

Fig. 9 Scanning electron micrographs of the PPD/molybdate with a PPD : AHM ratio of 9 : 1 pyrolyzed at 600 °C, (a) pristine electrode, and (b) electrode after cycling.

Scanning electron micrographs of the original electrode (Fig. 9a) and the electrode after cycling (Fig. 9b) were performed to confirm the assumption that two processes (decomposition of the carbide and the reduction of O–Mo^{6+}) occur during cycling leading to the formation of two products. In the pristine electrode, the initially present sheet-like morphology originating from the precursor with the PPD : AHM ratio of 9 : 1 pyrolyzed at 600 °C can be seen. In addition, a homogeneous distribution of the carbon black particles is observed. The electrode additionally shows particles with a fibrous morphology after cycling. This underlines the assumption that a lithium-ion insertion/extraction and a conversion reaction must occur during the electrochemical cycling.

5. Conclusions

In this study, we investigated the effects of synthesis conditions for synthesizing inorganic–organic hybrid materials from ammonium heptamolybdate (AHM) and *para*-phenylenediamine (PPD) by a wet chemical continuous precipitation microjet method. In the second step, these served as precursors for the pyrolytic production of molybdenum carbides, nitrides, and oxides. Our data show the crucial role of the proportions of the organic component in the hybrid precursors. The precursors with lower PPD content resulted in a mixture of Mo_2C, MoO_2, Mo_2N, and elemental Mo. These materials do not exhibit stacking defects and excess carbon, which was shown to be crucial for improving electrochemical performance. Precursors with higher PPD content led to $Mo(C,N,O)_x$ with stacking defects embedded in a carbonaceous matrix, a potential anode with high capacity and cycling stability. The electrochemical measurements showed that different morphologies and particle sizes could be obtained by different synthesis parameters and pyrolysis temperature settings, resulting in different electrochemical behaviors. For example, the precursor with a PPD : AHM ratio of 9 : 1 was pyrolyzed at 600 °C and exhibited capacities up to 933 mA h g^1 after 500 cycles. Further investigation showed that two processes, decomposition of the carbide and reduction of O–Mo^{6+} occur during cycling. We assume that lithium storage/removal and a conversion reaction occur during electrochemical cycling, resulting in an improved electrochemical performance with high cycling stability.

Author contributions

Mana Abdirahman Mohamed: materials synthesis, measurements, data analysis, writing, plotting, discussion, and manuscript revision. Stefanie Arnold: electrochemical measurements, writing, plotting, discussion, Raman measurements, and manuscript revision. Oliver Janka: discussion, analysis of the PXRD data and manuscript revision. Antje Quade: XPS measurement, plotting, discussion, and manuscript revision. Jörg Schmauch: acquisition of HR-TEM and TEM images and determination of lattice plane distances. Volker Presser: supervision, discussion, and manuscript revision. Guido Kickelbick: conceptualization, supervision, project administration, discussion, and manuscript revision.

Conflicts of interest

There are no conflicts to declare.

Acknowledgements

Instrumentation and technical assistance for this work were provided by the Service Center X-ray Diffraction, with financial support from Saarland University and German Science Foundation (project number INST 256/349-1). We thank Dr Robert Haberkorn (Saarland University) for the helpful discussion and advice regarding the Rietveld refinements. Special thanks also to Susanne Harling (Saarland University) for conducting the elemental analyses.

References

1 S. Chu and A. Majumdar, Opportunities and Challenges for a Sustainable Energy Future, *Nature*, 2012, **488**, 294–303, DOI: 10.1038/nature11475.
2 M. Weiss, R. Ruess, J. Kasnatscheew, Y. Levartovsky, N. R. Levy, P. Minnmann, L. Stolz, T. Waldmann, M. Wohlfahrt-Mehrens, D. Aurbach, M. Winter, Y. Ein-Eli and J. Janek, Fast Charging of Lithium-Ion Batteries : A Review of Materials Aspects, *Adv. Energy Mater.*, 2021, **11**, 1–37, DOI: 10.1002/aenm.202101126.
3 Y. Gao, X. I. Zhang, Q. Cheng, B. Guo and J. Yang, Classification and Review of the Charging Strategies for Commercial Lithium-Ion Batteries, *IEEE Access*, 2019, **7**, 43511–43524, DOI: 10.1109/ACCESS.2019.2906117.
4 H. Zhang, Y. Yang, D. Ren, L. Wang and X. He, Graphite as Anode Materials: Fundamental Mechanism, Recent Progress and Advances, *Energy Storage Mater.*, 2021, **36**, 147–170, DOI: 10.1016/j.ensm.2020.12.027.
5 J. Asenbauer, T. Eisenmann, M. Kuenzel, A. Kazzazi, Z. Chen and D. Bresser, The Success Story of Graphite as a Lithium-Ion Anode Material-Fundamentals, Remaining Challenges, and Recent Developments Including Silicon (Oxide) Composites, *Sustain. Energy Fuels*, 2020, **4**, 5387–5416, DOI: 10.1039/d0se00175a.
6 L. Lu, X. Han, J. Li, J. Hua and M. Ouyang, A Review on the Key Issues for Lithium-Ion Battery Management in Electric Vehicles, *J. Power Sources*, 2013, **226**, 272–288, DOI: 10.1016/j.jpowsour.2012.10.060.
7 V. Etacheri, R. Marom, R. Elazari, G. Salitra and D. Aurbach, Challenges in the Development of Advanced Li-Ion Batteries: A Review, *Energy Environ. Sci.*, 2011, **4**, 3243–3262, DOI: 10.1039/c1ee01598b.
8 A. Pan, H. B. Wu, L. Yu, T. Zhu and X. W. Lou, Synthesis of Hierarchical Three-Dimensional Vanadium Oxide Microstructures as High-Capacity Cathode Materials for Lithium-Ion Batteries, *ACS Appl. Mater. Interfaces*, 2012, **4**, 3874–3879, DOI: 10.1021/am3012593.
9 C. F. Armer, J. S. Yeoh, X. Li and A. Lowe, Electrospun Vanadium-Based Oxides as Electrode Materials, *J. Power Sources*, 2018, **395**, 414–429, DOI: 10.1016/j.jpowsour.2018.05.076.

10 S. B. Patil, Udayabhanu, B. Kishore, G. Nagaraju and J. Dupont, High Capacity MoO_3/RGO Nanocomposite Anode for Lithium Ion Batteries: An Intuition into the Conversion Mechanism of MoO_3, *New J. Chem.*, 2018, **42**, 18569–18577, DOI: 10.1039/c8nj03190h.

11 H. Zhang, L. Gao and Y. Gong, Exfoliated MoO_3 Nanosheets for High-Capacity Lithium Storage, *Electrochem. Commun.*, 2015, **52**, 67–70, DOI: 10.1016/j.elecom.2015.01.014.

12 J. Ni, G. Wang, J. Yang, D. Gao, J. Chen, L. Gao and Y. Li, Carbon Nanotube-Wired and Oxygen-Deficient MoO_3 Nanobelts with Enhanced Lithium-Storage Capability, *J. Power Sources*, 2014, **247**, 90–94, DOI: 10.1016/j.jpowsour.2013.08.068.

13 J. J. Auborn and Y. L. Barberio, Lithium Intercalation Cells Without Metallic Lithium: MoO_2/$LiCoO_2$ and WO_2/$LiCoO_2$, *J. Electrochem. Soc.*, 1987, **134**, 638, DOI: 10.1149/1.2100521.

14 A. Manthiram and C. Tsang, Synthesis of Amorphous $MoO_{2+\delta}$ and Its Electrode Performance in Lithium Batteries, *J. Electrochem. Soc.*, 1996, **143**, L143, DOI: 10.1149/1.1836955.

15 Z. Wang, J. S. Chen, T. Zhu, S. Madhavi and X. W. Lou, One-Pot Synthesis of Uniform Carbon-Coated MoO_2 Nanospheres for High-Rate Reversible Lithium Storage, *Chem. Commun.*, 2010, **46**, 6906–6908, DOI: 10.1039/c0cc01174f.

16 Z. Xiu, D. Kim, M. H. Alfaruqi, J. Song, S. Kim, P. T. Duong, V. Mathew, J. P. Baboo and J. Kim, Ultrafine Molybdenum Oxycarbide Nanoparticles Embedded in N-Doped Carbon as a Superior Anode Material for Lithium-Ion Batteries, *J. Alloys Compd.*, 2017, **696**, 143–149, DOI: 10.1016/j.jallcom.2016.11.235.

17 H. Preiss, B. Meyer and C. Olschewski, Preparation of Molybdenum and Tungsten Carbides from Solution Derived Precursors, *J. Mater. Sci.*, 1998, 713–722, DOI: 10.1023/A:1004393813199.

18 L. Liao, S. Wang, J. Xiao, X. Bian, Y. Zhang, M. D. Scanlon, X. Hu, Y. Tang, B. Liu and H. H. Girault, A Nanoporous Molybdenum Carbide Nanowire as an Electrocatalyst for Hydrogen Evolution Reaction, *Energy Environ. Sci.*, 2014, **7**, 387–392, DOI: 10.1039/c3ee42441c.

19 C. Ge, P. Jiang, W. Cui, Z. Pu, Z. Xing, A. M. Asiri, A. Y. Obaid, X. Sun and J. Tian, Shape-Controllable Synthesis of Mo_2C Nanostructures as Hydrogen Evolution Reaction Electrocatalysts with High Activity, *Electrochim. Acta*, 2014, **134**, 182–186, DOI: 10.1016/j.electacta.2014.04.113.

20 M. Pang, X. Wang, W. Xia, M. Muhler and C. Liang, Mo(VI)-Melamine Hybrid As Single-Source Precursor to Pure-Phase β-Mo_2C for the Selective Hydrogenation of Naphthalene to Tetralin, *Ind. Eng. Chem. Res.*, 2013, **52**, 4564–4571, DOI: 10.1021/ie400119d.

21 Y. Liu, G. Yu, G.-D. Li, Y. Sun, T. Asefa, W. Chen and X. Zou, Coupling Mo_2C with Nitrogen-Rich Nanocarbon Leads to Efficient Hydrogen-Evolution Electrocatalytic Sites, *Angew. Chem.*, 2015, **127**, 10902–10907, DOI: 10.1002/ange.201504376.

22 C. Giordano, C. Erpen, W. Yao and M. Antonietti, Synthesis of Mo and W Carbide and Nitride Nanoparticles via a Simple "Urea Glass" Route, *Nano Lett.*, 2008, **8**, 4659–4663, DOI: 10.1021/nl8018593.

23 Y. Huang, Q. Gong, X. Song, K. Feng, K. Nie, F. Zhao, Y. Wang, M. Zeng, J. Zhong and Y. Li, Mo_2C Nanoparticles Dispersed on Hierarchical Carbon Microflowers for Efficient Electrocatalytic Hydrogen Evolution, *ACS Nano*, 2016, **10**, 11337–11343, DOI: 10.1021/acsnano.6b06580.

24 S. Li, C. Cheng, A. Sagaltchik, P. Pachfule, C. Zhao and A. Thomas, Metal-Organic Precursor–Derived Mesoporous Carbon Spheres with Homogeneously Distributed Molybdenum Carbide/Nitride Nanoparticles for Efficient Hydrogen Evolution in Alkaline Media, *Adv. Funct. Mater.*, 2019, **29**, 1–10, DOI: 10.1002/adfm.201807419.

25 H.-M. Wang, X.-H. Wang, M.-H. Zhang, X.-Y. Du, W. Li and K.-Y. Tao, Synthesis of Bulk and Supported Molybdenum Carbide by a Single-Step Thermal Carburization Method, *Chem. Mater.*, 2007, **19**, 1801–1807, DOI: 10.1021/cm0615471.

26 M. A. Mohamed, S. Arnold, O. Janka, A. Quade, V. Presser and G. Kickelbick, Self-Activation of Inorganic-Organic Hybrids Derived through Continuous Synthesis of Polyoxomolybdate and Para-Phenylenediamine Enables Very High Lithium-Ion Storage Capacity, *ChemSusChem*, 2023, **16**, 1–15, DOI: 10.1002/cssc.202202213.

27 M. Zoller, R. Bubnova, Y. Biryukov, E. Haussühl, R. Pöttgen, O. Janka, S. Penner, C. Praty, H. Fitzek, J. Winkler, S. Filatov and H. Huppertz, Elucidating the Physical Properties of the Molybdenum Oxide Mo_4O_{11} and Its Tantalum Substituted Variant Mo2Ta2O11, *Z. Kristallogr.*, 2020, **235**, 143–155, DOI: 10.1515/zkri-2019-0073.

28 O. Glemser and G. Lutz, Über Molybdänoxyde, *Z. Anorg. Allg. Chem.*, 1950, **263**, 2–14.

29 E. Parthé and V. Sadogopan, The Structure of Dimolybdenum Carbide by Neutron Diffraction Technique, *Acta Crystallogr.*, 1963, **16**, 202–205, DOI: 10.1107/s0365110x63000487.

30 A. W. Hull, The Positions of Atoms in Metals, *Proc. Am. Inst. Electr. Eng.*, 1919, **38**, 1171–1192, DOI: 10.1109/T-AIEE.1919.4765642.

31 W.-F. Chen, C.-H. Wang, K. Sasaki, N. Marinkovic, W. Xu, J. T. Muckerman, Y. Zhu and R. R. Adzic, Highly Active and Durable Nanostructured Molybdenum Carbide Electrocatalysts for Hydrogen Production, *Energy Environ. Sci.*, 2013, **6**, 943–951, DOI: 10.1039/c2ee23891h.

32 H. Zhu, Z. Li, H. Yang and L. Luo, Carbothermic Reduction of MoO_3 for Direct Alloying Process, *J. Iron Steel Res. Int.*, 2013, **20**, 51–56, DOI: 10.1016/S1006-706X(13)60176-4.

33 C. Odenwald and G. Kickelbick, Additive-Free Continuous Synthesis of Silica and ORMOSIL Micro- and Nanoparticles Applying a Microjet Reactor, *J. Sol-Gel Sci. Technol.*, 2019, **89**, 343–353, DOI: 10.1007/s10971-018-4626-x.

34 A. Betke and G. Kickelbick, Bottom-Up, Wet Chemical Technique for the Continuous Synthesis of Inorganic Nanoparticles, *Inorganics*, 2014, **2**, 1–15, DOI: 10.3390/inorganics2010001.

35 B. Krüner, C. Odenwald, A. Tolosa, A. Schreiber, M. Aslan, G. Kickelbick and V. Presser, Carbide-Derived Carbon

Beads with Tunable Nanopores from Continuously Produced Polysilsesquioxanes for Supercapacitor Electrodes, *Sustain. Energy Fuels*, 2017, **1**, 1588–1600, DOI: 10.1039/c7se00265c.

36 B. Krüner, C. Odenwald, N. Jäckel, A. Tolosa, G. Kickelbick and V. Presser, Silicon Oxycarbide Beads from Continuously Produced Polysilsesquioxane as Stable Anode Material for Lithium-Ion Batteries, *ACS Appl. Energy Mater.*, 2018, **1**, 2961–2970, DOI: 10.1021/acsaem.8b00716.

37 B. Krüner, C. Odenwald, A. Quade, G. Kickelbick and V. Presser, Influence of Nitrogen-Doping for Carbide-Derived Carbons on the Supercapacitor Performance in an Organic Electrolyte and an Ionic Liquid, *Batter. Supercaps*, 2018, **1**, 135–148, DOI: 10.1002/batt.201800051.

38 A. X. S. Bruker and G. Karlsruhe, *Topas 5.1. General Profile and Structure Analysis Software for Powder Diffraction Data*, 2014.

39 K. Pfeifer, S. Arnold, J. Becherer, C. Das, J. Maibach, H. Ehrenberg and S. Dsoke, Can Metallic Sodium Electrodes Affect the Electrochemistry of Sodium-Ion Batteries? Reactivity Issues and Perspectives, *ChemSusChem*, 2019, **12**, 3312–3319, DOI: 10.1002/cssc.201901056.

40 M. Wang, X. Dong, I. C. Escobar and Y. T. Cheng, Lithium Ion Battery Electrodes Made Using Dimethyl Sulfoxide (DMSO) - A Green Solvent, *ACS Sustain. Chem. Eng.*, 2020, **8**, 11046–11051, DOI: 10.1021/acssuschemeng.0c02884.

41 H. W. Hugosson, O. Eriksson, L. Nordström, U. Jansson, L. Fast, A. Delin, J. M. Wills and B. Johansson, Theory of Phase Stabilities and Bonding Mechanisms in Stoichiometric and Substoichiometric Molybdenum Carbide, *J. Appl. Phys.*, 1999, **86**, 3758–3767, DOI: 10.1063/1.371284.

42 K. Kuo and G. Hägg, A New Molybdenum Carbide, *Nature*, 1952, **170**, 245–246.

43 E. Rudy and F. Benesovsky, Untersuchungen Im System Vanadin-Molybdän-Kohlenstoff Stabilisierung Des Kubischen Molybdänkarbids, *Planseeber. für Pulvermetall.*, 1962, **10**, 42–64.

44 A. Westgren and G. Phragmén, Röntgenanalyse Der Systeme Wolfram-Kohlenstoff Und Molybdän-Kohlenstoff, *Z. Anorg. Allg. Chem.*, 1926, **156**, 27–36.

45 S. T. Oyama, Preparation and Catalytic Properties of Transition Metal Carbides and Nitrides, *Catal. Today*, 1992, **15**, 179–200, DOI: 10.1016/0920-5861(92)80175-M.

46 H.-J. Zhang, K.-X. Wang, X.-Y. Wu, Y.-M. Jiang, Y.-B. Zhai, C. Wang, X. Wei and J.-S. Chen, MoO_2/Mo_2C Heteronanotubes Function as High-Performance Li-Ion Battery Electrode, *Adv. Funct. Mater.*, 2014, **24**, 3399–3404, DOI: 10.1002/adfm.201303856.

47 T. Chen, X. Yan, Z. Ma, Y. Zhang, X. Zheng and Y. Jiang, A General Method to Synthesize a MoC/C Composite Material with Potential Application as an Anodic Material in Lithium-Ion Batteries, *Ionics*, 2020, **26**, 4869–4875, DOI: 10.1007/s11581-020-03633-2.

48 L. Gurusamy, G.-J. Lee, S. Anandan, N. Liu and J. J. Wu, Fabrication of Molybdenum Oxycarbide Nanoparticles Dispersed on Nitrogen-Doped Carbon Hollow Nanotubes through Anion Exchange Mechanism for Enhanced Performance in Supercapacitor, *J. Energy Storage*, 2020, **27**, 1–13, DOI: 10.1016/j.est.2019.101122.

49 J. Zhang, L. Zhang, J. Zhang, Z. Zhang and Z. Wu, Effect of Surface/Bulk Oxygen Vacancies on the Structure and Electrochemical Performance of TiO_2 Nanoparticles, *J. Alloys Compd.*, 2015, **642**, 28–33, DOI: 10.1016/j.jallcom.2015.04.096.

50 P. Ettmayer, Das System Molybdaen-Stickstoff, *Monatsh. Chem.*, 1970, **101**, 127–140.

51 A. Norlund Christensen, A Neutron Diffraction Investigation on a Crystal of Alpha-Mo_2C, *Acta Chem. Scand.*, 1977, **31**, 509–511.

52 J. Häglund, A. Fernndez Guillermet, G. Grimvall and M. Körling, Theory of Bonding in Transition-Metal Carbides and Nitrides, *Phys. Rev. B: Condens. Matter Mater. Phys.*, 1993, **48**, 11685–11691, DOI: 10.1103/PhysRevB.48.11685.

53 E. Rudy, C. E. Brukl and S. Windisch, Constitution of Niobium (Columbium)-Molybdenum-Carbon Alloys, *Trans. Metall. Soc. AIME*, 1967, **239**, 1796–1808.

54 U. Wolf, F. Ernst, T. Muschik, M. W. Finnis and H. F. Fischmeister, The Influence of Grain Boundary Inclination on the Structure and Energy of $\sigma = 3$ Grain Boundaries in Copper, *Philos. Mag. A*, 1992, **66**, 991–1016, DOI: 10.1080/01418619208248003.

55 D. Hofmann and F. Ernst, Quantitative High-Resolution Transmission Electron Microscopy of the Incoherent Σ3 (211) Boundary in Cu, *Ultramicroscopy*, 1994, **53**, 205–221, DOI: 10.1016/0304-3991(94)90035-3.

56 G. H. Campbell, D. K. Chan, D. L. Medlin, J. E. Angelo and C. B. Carter, Dynamic Observation of the FCC to 9R Shear Transformation in a Copper $\Sigma = 3$ Incoherent Twin Boundary, *Scr. Mater.*, 1996, **35**, 837–842, DOI: 10.1016/1359-6462(96)00220-5.

57 D. L. Medlin, G. H. Campbell and C. B. Carter, Stacking Defects in the 9R Phase at an Incoherent Twin Boundary in Copper, *Acta Mater.*, 1998, **46**, 5135–5142, DOI: 10.1016/S1359-6454(98)00164-5.

58 A. A. Bolzan, B. J. Kennedy and C. J. Howard, Neutron Powder Diffraction Study of Molybdenum and Tungsten Dioxides, *Aust. J. Chem.*, 1995, **48**, 1473–1477.

59 R. Wang, J. Yang, K. Shi, B. Wang, L. Wang, G. Tian, B. Bateer, C. Tian, P. Shen and H. Fu, Single-Step Pyrolytic Preparation of Mo_2C/Graphitic Carbon Nanocomposite as Catalyst Carrier for the Direct Liquid-Feed Fuel Cells, *RSC Adv.*, 2013, **3**, 4771–4777, DOI: 10.1039/c3ra23391j.

60 Y.-Y. Chen, Y. Zhang, W.-J. Jiang, X. Zhang, Z. Dai, L.-J. Wan and J.-S. Hu, Pomegranate-like N,P-Doped Mo_2C@C Nanospheres as Highly Active Electrocatalysts for Alkaline Hydrogen Evolution, *ACS Nano*, 2016, **10**, 8851–8860, DOI: 10.1021/acsnano.6b04725.

61 A. C. Ferrari and J. Robertson, Interpretation of Raman Spectra of Disordered and Amorphous Carbon, *Phys. Rev. B*, 1999, **61**, 14095–14107, DOI: **10.1103/PhysRevB.61.14095**.
62 R. Srivastava and L. L. Chase, Raman Spectra of CrO_2 and MoO_2 Single Crystals, *Solid State Commun.*, 1972, **11**, 349–353.
63 L. Kumari, Y.-R. Ma, C.-C. Tsai, Y.-W. Lin, S. Y. Wu, K.-W. Cheng and Y. Liou, X-Ray Diffraction and Raman Scattering Studies on Large-Area Array and Nanobranched Structure of 1D MoO_2 Nanorods, *Nanotechnology*, 2007, **18**, 1–7, DOI: **10.1088/0957-4484/18/11/115717**.
64 R. Shunmugasundaram, R. S. Arumugam and J. R. Dahn, A Study of Stacking Faults and Superlattice Ordering in Some Li-Rich Layered Transition Metal Oxide Positive Electrode Materials, *J. Electrochem. Soc.*, 2016, **163**, A1394–A1400, DOI: **10.1149/2.1221607jes**.
65 J. S. Chen, Y. L. Cheah, S. Madhavi and X. W. Lou, Fast Synthesis of α-MoO_3 Nanorods with Controlled Aspect Ratios and Their Enhanced Lithium Storage Capabilities, *J. Phys. Chem. C*, 2010, **114**, 8675–8678, DOI: **10.1021/jp1017482**.
66 V. Augustyn, J. Come, M. A. Lowe, J. W. Kim, P.-L. Taberna, S. H. Tolbert, H. D. Abruña, P. Simon and B. Dunn, High-Rate Electrochemical Energy Storage through Li+ Intercalation Pseudocapacitance, *Nat. Mater.*, 2013, **12**, 518–522, DOI: **10.1038/nmat3601**.
67 S. Fleischmann, J. B. Mitchell, R. Wang, C. Zhan, D. E. Jiang, V. Presser and V. Augustyn, Pseudocapacitance: From Fundamental Understanding to High Power Energy Storage Materials, *Chem. Rev.*, 2020, **120**, 6738–6782, DOI: **10.1021/acs.chemrev.0c00170**.
68 S. Ardizzone, G. Fregonara and S. Trasatti, "Inner" and "Outer" Active Surface of RuO_2 Electrodes, *Electrochim. Acta*, 2002, **35**, 263–267, DOI: **10.1016/0013-4686(90)85068-X**.
69 Q. Gao, X. Zhao, Y. Xiao, D. Zhao and M. Cao, A Mild Route to Mesoporous Mo_2C-C Hybrid Nanospheres for High Performance Lithium-Ion Batteries, *Nanoscale*, 2014, **6**, 6151–6157, DOI: **10.1039/c3nr06678a**.
70 M. Li, S. Yu, Z. Chen, Z. Wang, F. Lv, B. Nan, Y. Zhu, Y. Shi, W. Wang, S. Wu, H. Liu, Y. Tang and Z. Lu, MoC Ultrafine Nanoparticles Confined in Porous Graphitic Carbon as Extremely Stable Anode Materials for Lithium- and Sodium-Ion Batteries, *Inorg. Chem. Front.*, 2017, **4**, 289–295, DOI: **10.1039/c6qi00465b**.
71 J. Ni, Y. Zhao, L. Li and L. Mai, Ultrathin MoO_2 Nanosheets for Superior Lithium Storage, *Nano Energy*, 2015, **11**, 129–135, DOI: **10.1016/j.nanoen.2014.10.027**.
72 C. H. Lu and S. W. Lin, Influence of the Particle Size on the Electrochemical Properties of Lithium Manganese Oxide, *J. Power Sources*, 2001, **97**(98), 458–460, DOI: **10.1016/S0378-7753(01)00637-1**.
73 I. Hwang, C. W. Lee, J. C. Kim and S. Yoon, Particle Size Effect of Ni-Rich Cathode Materials on Lithium Ion Battery Performance, *Mater. Res. Bull.*, 2012, **47**, 73–78, DOI: **10.1016/j.materresbull.2011.10.002**.
74 X. Su, Q. Wu, J. Li, X. Xiao, A. Lott, W. Lu, B. W. Sheldon and J. Wu, Silicon-Based Nanomaterials for Lithium-Ion Batteries: A Review, *Adv. Energy Mater.*, 2014, **4**, 1–23, DOI: **10.1002/aenm.201300882**.
75 I. Capone, K. Hurlbutt, A. J. Naylor, A. W. Xiao and M. Pasta, Effect of the Particle-Size Distribution on the Electrochemical Performance of a Red Phosphorus-Carbon Composite Anode for Sodium-Ion Batteries, *Energy Fuel.*, 2019, **33**, 4651–4658, DOI: **10.1021/acs.energyfuels.9b00385**.
76 H. Choi, A. R. Schuer, H. Moon, M. Kuenzel and S. Passerini, Investigating the Particle Size Effect on the Electrochemical Performance and Degradation of Cobalt-Free Lithium-Rich Layered Oxide $Li_{1.2}Ni_{0.2}Mn_{0.6}O_2$, *Electrochim. Acta*, 2022, **430**, 141047, DOI: **10.1016/j.electacta.2022.141047**.
77 R. Zhou, H. Guo, Y. Yang, Z. Wang, X. Li and Y. Zhou, N-Doped Carbon Layer Derived from Polydopamine to Improve the Electrochemical Performance of Spray-Dried Si/Graphite Composite Anode Material for Lithium Ion Batteries, *J. Alloys Compd.*, 2016, **689**, 130–137, DOI: **10.1016/j.jallcom.2016.07.315**.
78 S. Goriparti, E. Miele, F. De Angelis, E. Di Fabrizio, R. Proietti Zaccaria and C. Capiglia, Review on Recent Progress of Nanostructured Anode Materials for Li-Ion Batteries, *J. Power Sources*, 2014, **257**, 421–443, DOI: **10.1016/j.jpowsour.2013.11.103**.
79 H. S. Kim, J. B. Cook, H. Lin, J. S. Ko, S. H. Tolbert, V. Ozolins and B. Dunn, Oxygen Vacancies Enhance Pseudocapacitive Charge Storage Properties of MoO_{3-X}, *Nat. Mater.*, 2017, **16**, 454–462, DOI: **10.1038/NMAT4810**.
80 J. Qiu, C. Lai, E. Gray, S. Li, S. Qiu, E. Strounina, C. Sun, H. Zhao and S. Zhang, Blue Hydrogenated Lithium Titanate as a High-Rate Anode Material for Lithium-Ion Batteries, *J. Mater. Chem. A*, 2014, **2**, 6353–6358, DOI: **10.1039/c4ta00556b**.
81 X. Yang, Q. Li, H. Wang, J. Feng, M. Zhang, R. Yuan and Y. Chai, In-Situ Carbonization for Template-Free Synthesis of MoO_2-Mo_2C-C Microspheres as High-Performance Lithium Battery Anode, *Chem. Eng. J.*, 2018, **337**, 74–81, DOI: **10.1016/j.cej.2017.12.072**.
82 G. H. Lee, S. H. Moon, M. C. Kim, S. J. Kim, S. Choi, E. S. Kim, S. B. Han and K. W. Park, Molybdenum Carbide Embedded in Carbon Nanofiber as a 3D Flexible Anode with Superior Stability and High-Rate Performance for Li-Ion Batteries, *Ceram. Int.*, 2018, **44**, 7972–7977, DOI: **10.1016/j.ceramint.2018.01.237**.
83 M. Ihsan, H. Wang, S. R. Majid, J. Yang, S. J. Kennedy, Z. Guo and H. K. Liu, MoO_2/Mo_2C/C Spheres as Anode Materials for Lithium Ion Batteries, *Carbon*, 2016, **96**, 1200–1207, DOI: **10.1016/j.carbon.2015.10.076**.
84 Y. Zhu, S. Wang, Y. Zhong, R. Cai, L. Li and Z. Shao, Facile Synthesis of a MoO_2-Mo_2C-C Composite and Its Application as Favorable Anode Material for Lithium-Ion Batteries, *J. Power Sources*, 2016, **307**, 552–560, DOI: **10.1016/j.jpowsour.2016.01.014**.
85 H. Xin, Y. Hai, D. Li, Z. Qiu, Y. Lin, B. Yang, H. Fan and C. Zhu, Coupling Mo_2C@C Core-Shell Nanocrystals on 3D Graphene Hybrid Aerogel for High-Performance Lithium Ion Battery, *Appl. Surf. Sci.*, 2018, **441**, 69–76, DOI: **10.1016/j.apsusc.2018.01.187**.

86 B. Yu, D. Yang, Y. Hu, J. He, Y. Chen and W. He, Mo_2C Nanodots Anchored on N-Doped Porous CNT Microspheres as Electrode for Efficient Li-Ion Storage, *Small Methods*, 2019, **3**, 1–7, DOI: **10.1002/smtd.201800287**.

87 M. Chen, J. Zhang, Q. Chen, M. Qi and X. Xia, Construction of Reduced Graphene Oxide Supported Molybdenum Carbides Composite Electrode as High-Performance Anode Materials for Lithium Ion Batteries, *Mater. Res. Bull.*, 2016, **73**, 459–464, DOI: **10.1016/j.materresbull.2015.09.030**.

88 J. Min, K. Wang, J. Liu, Y. Yao, W. Wang, L. Yang, R. Zhang and M. Lei, Facile Synthesis of Uniform MoO_2/Mo_2CT_X Heteromicrospheres as High-Performance Anode Materials for Lithium-Ion Batteries, *J. Power Sources*, 2017, **363**, 392–403, DOI: **10.1016/j.jpowsour.2017.07.079**.

89 U. Kolitsch, The Crystal Structures of Phenacite-Type Li2(MoO4), and Scheelite-Type LiY(MoO4)2 and LiNd(MoO4)2, *Z. Kristallogr.*, 2001, **216**, 449–454, DOI: **10.1524/zkri.216.8.449.20358**.

90 A. Krause, O. Tkacheva, A. Omar, U. Langklotz, L. Giebeler, S. Dörfler, F. Fauth, T. Mikolajick and W. M. Weber, In Situ Raman Spectroscopy on Silicon Nanowire Anodes Integrated in Lithium Ion Batteries, *J. Electrochem. Soc.*, 2019, **166**, A5378–A5385, DOI: **10.1149/2.0541903jes**.

91 L. Liu, W. Zhang, P. Guo, K. Wang, J. Wang, H. Qian, I. Kurash, C. H. Wang, Y. W. Yang and F. Xu, A Direct Fe-O Coordination at the $FePc/MoO_x$ Interface Investigated by XPS and NEXAFS Spectroscopies, *Phys. Chem. Chem. Phys.*, 2015, **17**, 3463–3469, DOI: **10.1039/c4cp04199b**.

92 P. Delporte, F. Meunier, C. Pham-Huu, P. Vennegues, M. J. Ledoux and J. Guille, Physical Characterization of Molybdenum Oxycarbide Catalyst; TEM, XRD and XPS, *Catal. Today*, 1995, **23**, 251–267, DOI: **10.1016/0920-5861(94)00166-Y**.

93 R. Savinelli, J. Li, R. Seshadri and S. L. Scott, *Molybdenum Carbide and Oxycarbide Hydrogen Production Catalysts, in 21st North American Catalysis Society, PW-68*, San Francisco, 2009.

94 A. P. Dementjev, A. V. Eletskii, K. I. Maslakov, E. G. Rakov, V. F. Sukhoverhov and A. V. Naumkin, Fluorination of Carbon Nanostructures and Their Comparative Investigation by XPS and XAES Spectroscopy, *Fullerenes, Nanotub. Carbon Nanostruct.*, 2006, **14**, 287–296, DOI: **10.1080/15363830600663990**.

Electronic Supplementary Material (ESI) for Journal of Materials Chemistry A.

Supporting Information

Continuous Wet Chemical Synthesis of $Mo(C,N,O)_x$ as Anode Materials for Li-Ion Batteries

Mana Abdirahman Mohamed[a]+ (0000-0003-0708-7623),
Stefanie Arnold[b,c]+ (0000-0002-4954-4610),
Dr. Oliver Janka[a] (0000-0002-9480-3888),
Dr. Antje Quade[e] (0000-0003-0814-4319),
Jörg Schmauch[f],
Prof. Dr. Volker Presser[b,c,d]* (0000-0003-2181-0590),
Prof. Dr. Guido Kickelbick[a]* (0000-0001-6813-9269)

[a] Saarland University, Inorganic Solid-State Chemistry, Campus C4 1, 66123 Saarbrücken, Germany
[b] INM - Leibniz Institute for New Materials, 66123 Saarbrücken, Germany
[c] Saarland University, Department of Materials Science and Engineering, 66123 Saarbrücken, Germany
[d] Saarene - Saarland Center for Energy Materials and Sustainability, 66123 Saarbrücken, Germany
[e] Leibniz Institute for Plasma Science and Technology, Felix-Hausdorff-Straße 2, 17489 Greifswald, Germany
[f] Physics Department, Saarland University, Campus D2.2, 66123 Saarbrücken, Germany

+ equal contributions
* Corresponding authors:
GK: guido.kickelbick@uni-saarland.de
VP: volker.presser@leibniz-inm.de

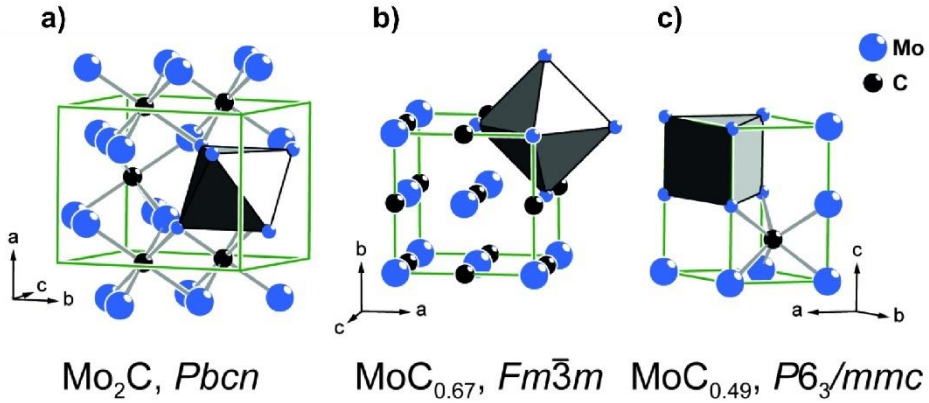

Figure S1: Crystal structures of a) orthorhombic Mo_2C,[1,2] b) cubic $MoC_{0.67}$,[3] and c) hexagonal $MoC_{0.49}$ Mo atoms are depicted in blue, C atoms in black.

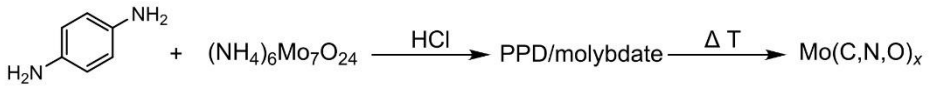

Figure S2: General reaction scheme, first step precursor precipitation followed by pyrolysis reaction.

Table S1: Elemental analysis of PPD/molybdate precursors after the pyrolysis.

	Carbon / mass%	**Hydrogen / mass%**	**Nitrogen / mass%**
Ideal Mo_2C	5.89	0	0
Ideal MoOC	9.69	0	0
Ideal Mo_2N	0	0	6.80
PPD/molybdate **(9:1) (600°C)**	20.85	0.24	0.74
PPD/molybdate **(10:1) (600°C)**	21.45	0.22	0.59
PPD/molybdate **(1:1) (750°C)**	0.38	0	2.56
PPD/molybdate **(2:1) (750°C)**	2.01	0	0.22
PPD/molybdate **(5:1) (750°C)**	3.19	0	0.14
PPD/molybdate **(9:1) (750°C)**	22.75	0	0.24
PPD/molybdate **(10:1) (750°C)**	20.02	0	0.24
PPD/molybdate **(15:1) (750°C)**	22.62	0	0.30
PPD/molybdate **(18:1) (750°C)**	23.57	0	0.20
PPD/molybdate **(20:1) (750°C)**	23.15	0	0.19
PPD/molybdate **(25:1) (750°C)**	22.86	0	0.23
PPD/molybdate **(30:1) (750°C)**	22.59	0	0.23

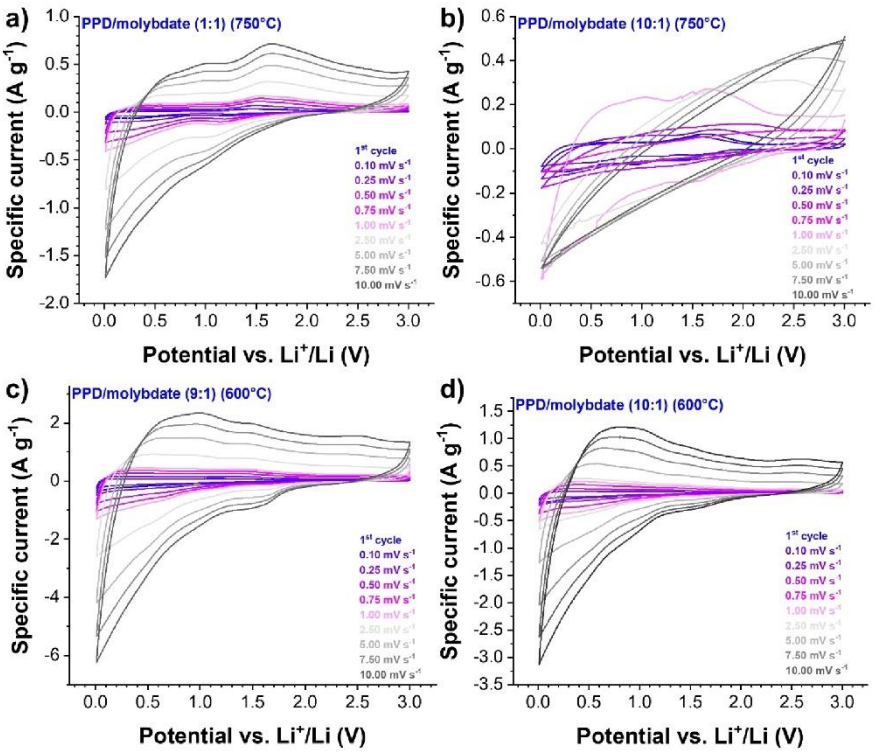

Figure S3: Electrochemical performance of pyrolyzed PPD/molybdate hybrid materials. Cyclic voltammograms at different scan rates and potential range between 0.01 V and 3.00 V vs. Li^+/Li for (a) 1:1 and (b) 10:1 pyrolyzed at 750 °C as well as (c) 9:1 and (d) 10:1 synthesized at 600 °C.

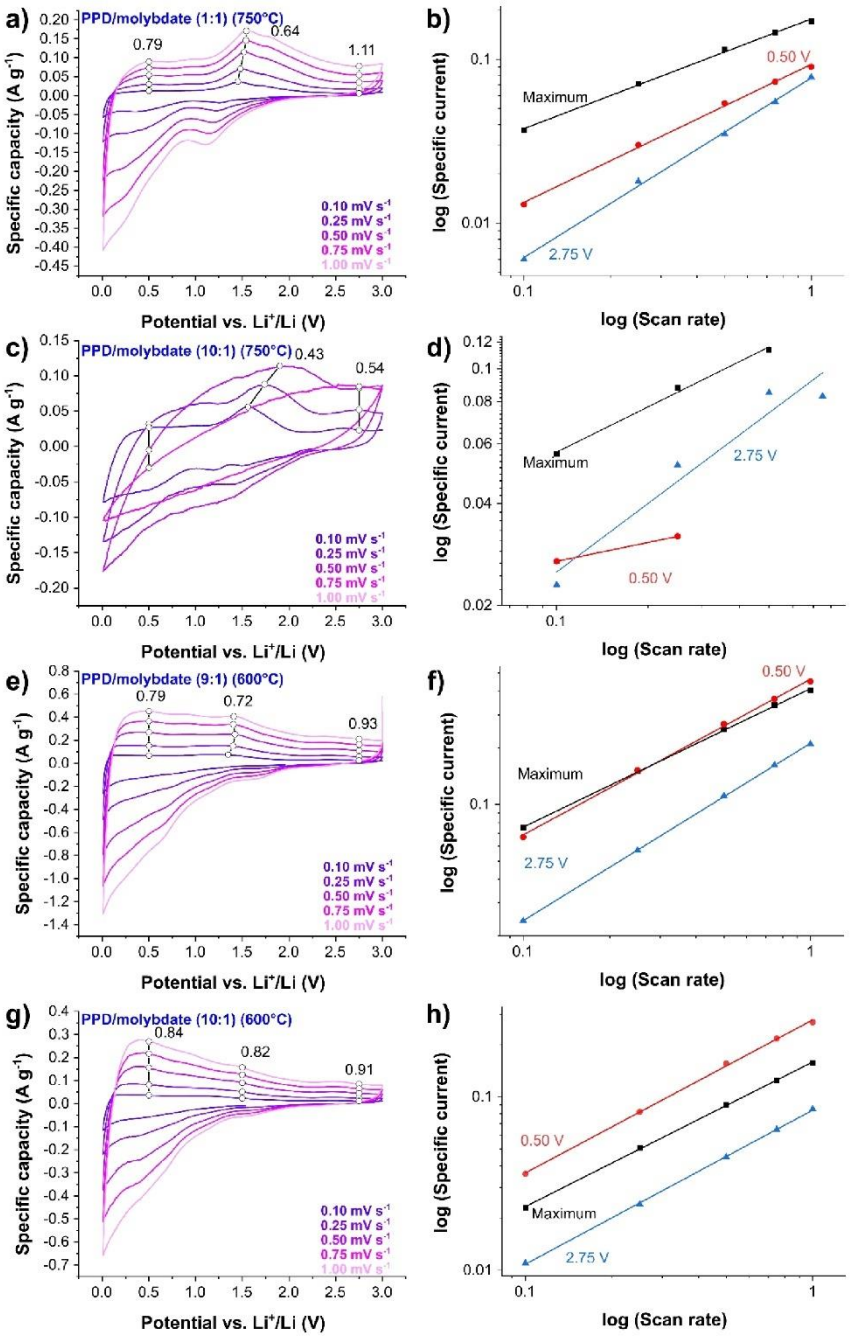

Figure S4: Cyclic voltammograms at different scan rates and kinetic fitting to calculate b-values for (a-b) PPD/molybdate (1:1) (750°C); (c-d) PPD/molybdate (10:1) (750°C); (e-f) PPD/molybdate (9:1) (600°C); (g-h) PPD/molybdate (10:1) (600°C).

Supporting References

(1) Parthé, E.; Sadogopan, V. The Structure of Dimolybdenum Carbide by Neutron Diffraction Technique. *Acta Crystallogr.* **1963**, *16*, 202–205. https://doi.org/10.1107/s0365110x63000487.

(2) Norlund Christensen, A. A Neutron Diffraction Investigation on a Crystal of Alpha-Mo_2C. *Acta Chem. Scand. Ser. A* **1977**, *31*, 509–511.

(3) 'Rudy, E. .; 'Brukl, C. E. .; 'Windisch, S. . Constitution of Niobium (Columbium)-Molybdenum-Carbon Alloys. *Trans. Metall. Soc. AIME* **1967**, *239*, 1796–1808.

3.3 Precursor-Based Syntheses of Mo(C,N,O)$_x$, Molybdenum Carbide, Nitride, and Oxide Applying a Microjet Reactor

In the last article, the influence of the carbon source on the pyrolysis reaction is investigated in more detail. Previous results showed that the carbon content is a decisive factor for pyrolysis. First, new inorganic-organic hybrid compounds are prepared using 1,8-diaminonaphthalene (1,8-DAN) or hexamethylenediamine (HMD) as organic species and in combination with ammonium heptamolybdate as inorganic species. The syntheses and optimization are carried out in line with the previous work. There is a clear trend towards the use of aromatic systems, due to their better stability compared to aliphatic systems, as well as organic species with the highest possible carbon content. These materials were also produced via simple continuous precipitation reactions in the microjet reactor.

Thus, the following composite material Mo(C,N,O)$_x$ embedded in a carbon matrix with high carbon excess is obtained. Both the produced inorganic-organic hybrid materials and the composite material Mo(C,N,O)$_x$ embedded in a carbon matrix are potential candidates as anode materials in LIBs.

In addition to the synthesis, the next article concentrates on the extensive characterization of the materials.

Author Contributions:

Mana Abdirahman Mohamed: Conceptualization, investigation, methodology, materials synthesis, measurements, data analysis, plotting, discussion, and writing—original draft.

Oliver Janka: Methodology, discussion, analysis of the PXRD data and writing—review and editing.

Susanne Harling: Investigation, assistance with preparative work, methodology and performing the elemental analyses.

Guido Kickelbick: Conceptualization, funding acquisition, project administration, resources, supervision, discussion, and writing—review and editing.

solids

MDPI

Article

Precursor-Based Syntheses of Mo(C,N,O)$_x$, Molybdenum Carbide, Nitride, and Oxide Applying a Microjet Reactor

Mana Abdirahman Mohamed [1], Oliver Janka [1], Susanne Harling [1] and Guido Kickelbick [1,2,*]

[1] Inorganic Solid-State Chemistry, Saarland University, Campus C4 1, 66123 Saarbrücken, Germany; mana.mohamed@uni-saarland.de (M.A.M.); oliver.janka@uni-saarland.de (O.J.)
[2] Saarene—Saarland Center for Energy Materials and Sustainability, 66123 Saarbrücken, Germany
* Correspondence: guido.kickelbick@uni-saarland.de

Abstract: Composite materials such as molybdenum carbides, nitrides, oxides, and mixed anionic compounds like Mo(C,N,O)$_x$ embedded in carbonaceous matrix exhibit promising potential as anode materials for lithium batteries, with a preference for fine-grained morphologies. In this study, we present a novel synthetic approach involving an inorganic–organic hybrid precursor precipitated from aqueous solutions of ammonium heptamolybdate and one of two organic species: 1,8-diaminonaphthalene (1,8-DAN) or hexamethylenediamine (HMD). The precipitation reaction can be carried out in a beaker and in a continuous process using a microjet reactor. This enables the synthesis of precursor material on the gram scale within minutes. The pyrolysis of these precursors yields mixtures of Mo(C,N,O)$_x$, MoO_2, Mo_2C, Mo_2N, and Mo, with the choice of organic compound significantly influencing the resulting phases and the excess carbon content in the pyrolyzed product. Notably, the pyrolysis process maintains the size and morphology of the micro- to nanometer-sized starting materials.

Keywords: continuous synthesis; molybdate; 1,8-diaminonapthalene; hexamethylenediamine; inorganic–organic hybrid material; pyrolysis; molybdenum oxide carbide; composite material

Citation: Abdirahman Mohamed, M.; Janka, O.; Harling, S.; Kickelbick, G. Precursor-Based Syntheses of Mo(C,N,O)$_x$, Molybdenum Carbide, Nitride, and Oxide Applying a Microjet Reactor. *Solids* **2024**, *5*, 443–459. https://doi.org/10.3390/solids5030030

Academic Editors: Andrei V. Shevelkov and Maxim N. Sokolov

Received: 8 July 2024
Revised: 15 August 2024
Accepted: 28 August 2024
Published: 4 September 2024

1. Introduction

Current lithium-ion batteries (LIBs) contain graphite as anode material, which has a relatively low capacity of 372 mA h g^{-1}. The limited capacity of intercalation materials, e.g., graphite and other types of materials, such as lithium titanate, $Li_4Ti_5O_{12}$ (LTO), can be exceeded by conversion materials, e.g., nanoparticles of transition metal oxides, e.g., Fe_2O_3, CoO, and CuO. These materials are being explored for improved battery performance [1–4].

Molybdenum oxides, showing theoretical capacities of 837 mA h g^{-1} for MoO_2 and 1117 mA h g^{-1} for MoO_3, are also potential candidates for anode materials. Molybdenum carbides like Mo_2C and MoC_x (x = 0.43–0.75) exhibit beneficial lithium storage properties relative to simple oxides because of their better chemical stability, electrical conductivity, and excellent mechanical properties [1]. The combination of the properties of molybdenum oxides and carbides has the potential to create a new class of electrode materials for LIBs [1].

Generally, the industrial production of molybdenum carbides proceeds via a powder metallurgical process, in which the molybdenum oxides are reduced to the element by applying hydrogen. Afterwards, the metal is carburized with carbon powders at very high temperatures (1500–2000 °C). This process is extremely energy intensive, and the formed Mo_2C cannot be used for application in LIBs due to the lack of the required high specific surface area. Therefore, low-temperature preparation routes are preferred for the electrochemical applications [5].

One potential method for the production of valuable materials is chemical vapor deposition (CVD), in which carbonaceous gases like CH_4, C_2H_6, and CO, along with Mo-containing precursors, are used for the deposition of the materials on various substrates.

While showing some advantages to the industrial method, still the pore structure and purity of the resulting Mo_2C are not satisfying. In addition, the equipment costs of CVD systems are quite high [5,6]. Alternative synthesis strategies include the use of molecular precursors in pyrolytic reactions at much lower temperatures than the previously mentioned techniques. More moderate reaction conditions, in addition to a diverse composition of precursors, allow a more flexible adjustment of the size and morphology of the final product, which is beneficial for the LIB application [5].

Several reports in the literature show that suitable compounds can be obtained from precipitation reactions. Subsequent pyrolytic reactions allow the preparation of the targeted compounds. In the following, several methods for the carbothermic reduction of molybdenum carbide via a precursor route are listed. Precursors as previously studied starting materials were mixtures of molybdate and 2-methylimidazole [1], aniline [7], p-phenylenediamine [8], melamine [9], and dicyandiamide [10]. A novel procedure for the synthesis of Mo_2C and Mo_2N nanoparticles was reported by Giordano et al. It was based on a process in which $MoCl_5$ was dissolved in ethanol, and urea was subsequently added to form a polymeric, glassy phase. Later, thermal treatment under nitrogen gas flow was applied, and by changing the molar ratio of metal to urea, molybdenum nitride or the respective carbide was synthesized [11]. A simple way to prepare Mo_2C nanoparticles on 3D carbon microflowers by self-polymerization of dopamine was found by Huang et al. who performed the pyrolysis under argon flow [12]. A new route for mesoporous and nanoscale Mo_2C/Mo_2N heterojunctions was designed by Li et al. using a dopamine–molybdate coordination precursor with silica nanoparticles [13]. Finally, Wang et al. found that a mixed salt precursor containing a molybdenum–hexamethylenetetramine complex could be pyrolyzed under an argon atmosphere [14].

Several phases can be obtained by such decomposition reactions, such as orthorhombic HT-Mo_4O_{11} [15,16], monoclinic MoO_2 [16], orthorhombic Mo_2C [17] (Figure 1a), and cubic Mo [18]; thus, reaction conditions have to be accurately controlled [6]. Around 873 K, MoO_2, MoC, and C exist in an equilibrium. At this point, molybdenum oxide carbide can be obtained; above 923 K, Mo_2C is the stable phase [19]. It is also possible to obtain other molybdenum carbides such as cubic (Figure 1b) or hexagonal (Figure 1c) MoC_x. Furthermore, it is also possible to obtain Mo_2N due to the use of amines in the hybrid precursors [11,19].

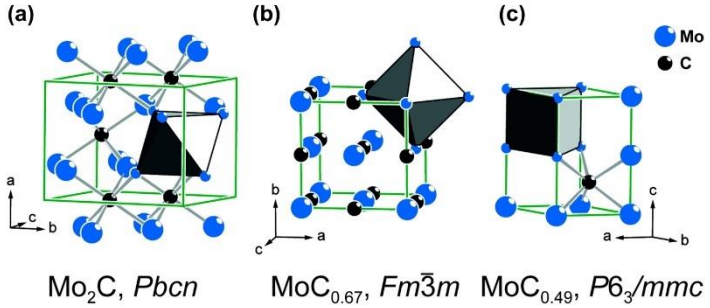

Figure 1. Crystal structures of (**a**) orthorhombic Mo_2C [17,20], (**b**) cubic $MoC_{0.67}$ [21], and (**c**) hexagonal $MoC_{0.49}$ [22]. Mo atoms are illustrated in blue, C atoms in black. The space groups are provided.

A prominent source of molybdenum in the precursors is ammonium heptamolybdate $(NH_4)_6Mo_6O_{24}$ (AHM), which often forms precipitates together with cationic organic compounds. Mo_2C can be obtained after pyrolysis of the resulting, often insoluble precipitates [11]. Another potential molybdenum source is $MoCl_5$ [11], while compounds such as H_2MoO_4 and MoO_3 are less often used due to their low solubility [5].

For the application of such materials in energy storage, the formation of nanoscopic precursors would be very attractive, especially if the precursor can be transformed into

the desired molybdenum carbide without losing the initial morphology. In addition, the large-scale production of such materials is important since relevant amounts have to be produced. In previous studies of our group, it was shown that precipitation methods, which are commonly conducted in batch processes, can be transformed into a continuous process by applying a microjet reactor [23,24]. Consequently, the possibility of a large-scale production of well-defined (nano)particles is opened up. In this procedure, two reactant solutions are fed into a reaction chamber under high pressure, which initiates the nucleation process through rapid mixing. The mixed product is removed from the mixing chamber by a gas jet, and particle growth takes place on the path to the collection container. Isolating nucleation and growth enable a high degree of control over particle properties. We have applied this method already to the formation of silicon oxide carbides species for battery applications [25–27].

Based on the work of Ge et al. [8], where Mo_2C nanoparticles are prepared by direct pyrolysis of their MoO_x/p-phenylenediamine hybrid precursors, we optimize in our previous work the synthesis to transfer this procedure to the microjet reactor [28,29]. This synthesis was further modified by changing the organic component for the presented study.

Herein, we report a systematic study on the formation of precursors and the synthesis of molybdenum carbides, nitrides, oxides, and $Mo(C,N,O)_x$ composite materials. The effects of the precursor ratio and the influence of different organic species were evaluated to further explore the role of carbon sources for pyrolysis. In our work, we mainly focus on the different amines used, the influence of the ratios used, and the resulting compounds, as well as their composition after pyrolysis.

The aim of the study was not to obtain phase-pure materials but to investigate the influence of different diamines on the final composition of the precipitated as well as the pyrolyzed compounds. This work follows on from two of our previously published papers [28,29]. There, the synthesis and pyrolysis of the precursor using paraphenylenediamine (PPD) was investigated. The present study builds on these earlier results. Using different amines, the overall influence of organic species in the synthesis of such molybdenum carbides, nitrides, oxides, and $Mo(C,N,O)_x$ composite materials is compared.

2. Materials and Methods

2.1. Materials

Ammonium heptamolybdate tetrahydrate ($(NH_4)_6Mo_7O_{24}{\cdot}4\ H_2O$, AHM; ≥99%) and hexamethylenediamine (HMD; ≥99.5%) were obtained from Carl Roth GmbH & Co. KG, Karlsruhe, Germany. 1,8-diaminonapthalene (1,8-DAN; 97%) was purchased from Alfa Aesar, Haverhill, MA, USA. Hydrochloric acid (HCl; 37%) was obtained from Bernd Kraft GmbH, Oberhausen, Germany. Ethanol (99% denatured with 1% PE) was received from BCD Chemie GmbH, Hamburg, Germany. All chemicals were used without further purification.

2.2. Syntheses—Microjet Synthesis of Precipitates

Diluted hydrochloric acid (between 0.05 and 0.6 mmol L^{-1}, solution A) and a combination of an aqueous AHM solution and an ethanolic solution of 1,8-DAN or an aqueous solution of HMD (solution B) (Tables 1 and 2) were used in the synthesis. The solutions were pumped into the reactor using two HPLC pumps (LaPrep P110 preparative HPLC pumps (VWR)) at a flow rate of 250 mL min^{-1}. In the microjet reactor, the solutions collide through a nozzle with a diameter of 300 µm and a strong mixing takes place under high pressure. The resulting particle suspensions were removed with a stream of nitrogen gas at a pressure of 8 bar [23]. Each reactant starting solution (solution A and solution B) had a volume of 1 L. Both solution jets collide at an angle of 180° to each other, while the nitrogen stream enters the reaction chamber at an angle of 90° to the nozzles and the outlet pipe is at an angle of 180° to the nitrogen stream A schematic illustration of the experimental setup is shown in Figure 2.

Table 1. The syntheses of the precursors 1,8-DAN/molybdate and the different ratios in the mixing solution.

Reaction Number	Ratio (1,8-DAN:AHM)	1,8-DAN (g) (mmol)	AHM (g) (mmol)	HCl (M)
1	1:1	0.5 3.16	3.86 3.12	0.05
2	2:1	1.0 6.32	3.86 3.12	0.05
3	5:1	1.25 7.90	1.93 1.56	0.025
4	9:1	2.33 15	1.93 1.56	0.025
5	10:1	2.5 16	1.93 1.56	0.025
6	15:1	3.75 24	1.93 1.56	0.05
7	18:1	4.375 28	1.93 1.56	0.05
8	20:1	5.16 33	1.93 1.56	0.05
9	25:1	6.09 38	1.93 1.56	0.075
10	30:1	7.34 46	1.93 1.56	0.1

Table 2. The syntheses of the precursors HMD/molybdate and the different ratios in the mixing solution.

Reaction Number	Ratio (HMD:AHM)	HMD (g) (mmol)	AHM (g) (mmol)	HCl (M)
1	1:1	0.365 3.14	3.86 3.12	0.2
2	2:1	0.725 6.24	3.86 3.12	0.2
3	5:1	1.815 16	3.86 3.12	0.3
4	9:1	3.265 28	3.86 3.12	0.3
5	10:1	3.63 31	3.86 3.12	0.3
6	15:1	5.445 47	3.86 3.12	0.3
7	18:1	6.535 56	3.86 3.12	0.4
8	20:1	7.01 60	3.86 3.12	0.4
9	25:1	9.075 78	3.86 3.12	0.6
10	30:1	10.89 97	3.86 3.12	0.6

Once synthesized in the microjet reactor, the particles were separated by centrifugation (8000 rpm, 15 min). Products were washed with ethanol and dried at 80 °C.

Finally, the precursors obtained were pyrolyzed under argon flow using the following temperature program (Figure 3).

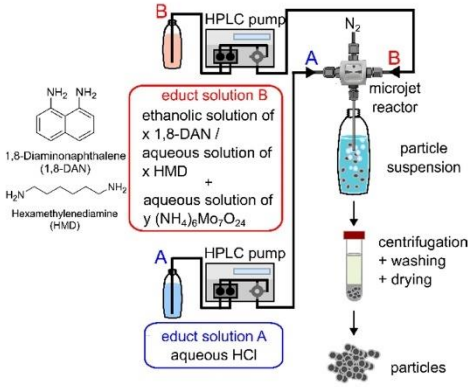

Figure 2. General reaction scheme showing the continuous wet-chemical synthesis of the products 1,8-DAN/molybdate and HMD/molybdate.

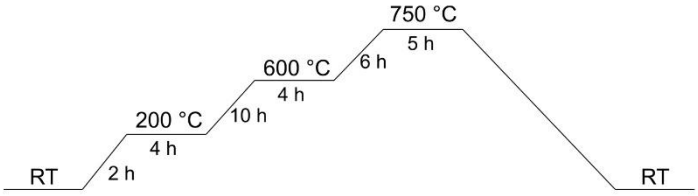

Figure 3. Temperature program for the pyrolysis.

In the 1,8-DAN/molybdate system, the pH values were between 1 and 3. The pH values in the HMD/molybdate system were between 0 and 2.

2.3. Characterization

Fourier-transform infrared spectroscopy measurements (FT-IR) of dried samples were recorded in attenuated total reflectance (ATR) mode using a Bruker Vertex 70 spectrometer (Bruker Optics GmbH & Co. KG, Ettlingen, Germany). Each spectrum was performed in the wave number range of 500–4500 cm^{-1} and by averaging 32 scans with spectral resolution of 4 cm^{-1}. The elemental analyses were conducted on an Elementar Vario Micro cube (Elementar Analysensysteme GmbH, Langenselbold, Germany). Thermogravimetric analyses (TGA) were performed on a Netzsch TG F1 Iris (NETZSCH GmbH & Co. Holding KG, Selb, Germany) under a constant flow of N_2 (40 mL min^{-1}) with a heat rate of 20 K min^{-1} and until 1173 K. During the measurements the samples were placed in an open alumina crucible. Powder X-ray diffraction (XRD) measurements were carried out on a Bruker D8-A25-Advance diffractometer (Bruker AXS GmbH & Co. KG, Karlsruhe, Germany) in a Bragg–Brentano geometry with CuK_α-radiation. The XRD patterns were performed with a total measurement time of 1 h and from 7 to 110° 2θ with a step size of 0.013°. By the Rietveld analysis, the quantitative analyses were carried out, and the sample composition could be determined by this method using TOPAS 5 [30]. The crystallographic data for the Rietveld refinement were obtained from the Crystallographic Open Database (COD) and the Inorganic Crystal Structure Database (ICSD). Following CIFs were used for Rietveld Refinement Mo_2C [17,20], Mo_2N [31], MoO_2 [32], $MoC_{0.67}$ [21], $MoC_{0.5}$ [22] and Mo [18,33]. SEM images were taken using a JEOL JSM-7000 F microscope (JEOL (Germany) GmbH, Freising, Germany) with a working distance of 10 mm and operating at 20 kV. For the sample preparation, a small amount was placed on a specimen stub covered with a carbon adhesive foil, followed by the deposition of a gold layer.

3. Results and Discussion

3.1. Synthesis/Precipitation Reaction

The first precipitation reaction that was carried out in a continuous process was mixing ammonium heptamolybdate (AHM) as a source of molybdenum with para-phenylenediamine (PPD) in acidic conditions [28]. For the presented study, the organic components were changed to study the influence of an aromatic versus a non-aromatic diamine on their capability as precipitation precursors. The studied diamines were chosen based on their high carbon content and good availability. In addition, potential differences in the precursor production and the final product formation depending on the stereochemistry of the diamines and the extent of aromaticity in the organic molecules can be compared. 1,8-Diaminonaphthalene (1,8-DAN) with a higher organic content in comparison to PPD and hexamethylenediamine (HMD) as a non-aromatic diamine were chosen. The precursors were precipitated by mixing the aqueous solution of AHM as a molybdenum source and an ethanolic solution of 1,8-DAN or an aqueous solution of HMD under acidic conditions (Figure 2). The precipitation reactions were carried out in a microjet reactor using different molar ratios between the molybdenum source and the organic compounds. Subsequently, the correlation between the formation of the molybdenum oxide carbides, carbides, oxides, and nitrides and the composition of the precipitated precursor was investigated.

The precipitation reaction was followed by a subsequent pyrolysis reaction to form molybdenum oxide carbide, carbide, oxide, and nitride (Equation (1)). The organic moieties in the species act as carbon sources during the thermal decomposition. In our approach, we exclusively used amines since other groups, such as hydroxyl, carboxyl, or phosphate groups, can introduce other atoms that can disrupt the delicate reduction equilibrium. These can cause either an excess of various molybdenum oxides or impurities such as phosphorus compounds to be obtained. Only the use of amines leads to the desired molybdenum oxide carbide.

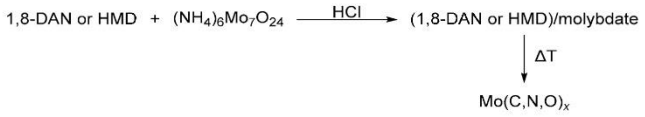

(1)

The precipitates were characterized employing Fourier-transform infrared (FT-IR) spectroscopy, elemental analysis, and thermogravimetric analysis (TGA), as well as scanning electron microscopy (SEM) and powder X-ray diffraction (PXRD).

Comparing the FT-IR spectra of all 1,8-DAN/molybdate precipitates with different ratios indicates a great similarity between these (Supporting Information, Figure S1a). In the spectra of the 1,8-DAN, a broad band in the area of 3550–3350 cm^{-1} can be attributed to the stretching vibration of the N–H group [34,35]. In the spectra of AHM at 3600–3200 cm^{-1}, a broad band indicates the presence of water [36]. These bands almost completely disappear in the 1,8-DAN/molybdate precipitates. All spectra show vibrations at 1650–1550 cm^{-1}, which are caused by the N–H deformation vibrations. In addition, C=C stretching vibrations can be detected in the range of 1500–1480 cm^{-1}. Additionally, typically, molybdate bands are present from 935 to 890 cm^{-1} (Figure 4a). These findings indicate that both organic and inorganic components are integrated in the precipitates [9,37–39]. The N–H deformation vibrations are more pronounced at the higher ratios from 10:1, which indicates a higher amine content in these samples. The vibrations of the molybdate units have the same shape both at low ratios of 1:1 and higher ratios of 10:1. This indicates that the same molybdate cluster must be present.

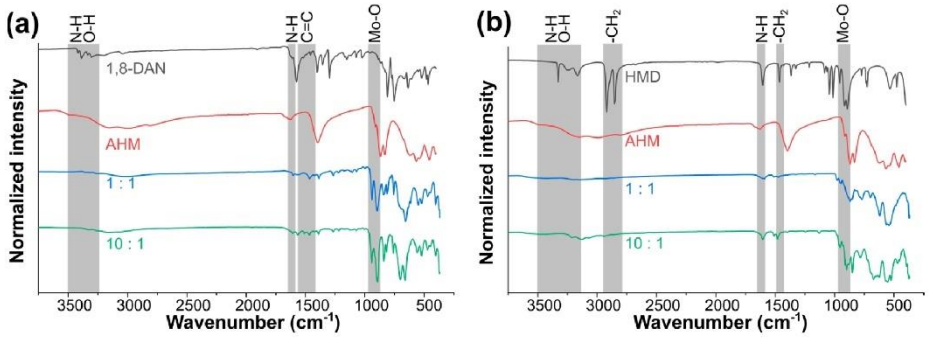

Figure 4. (**a**) IR spectra of the starting materials 1,8-DAN, AHM, and two spectra of a 1:1 and 10:1 mixture. (**b**) IR spectra of HMD/molybdate and their reactants.

In the spectra of HMD, a broad band in the range of 3550–3350 cm^{-1} can be assigned to the stretching vibration of the N–H group [34,40]. Furthermore, two bands appear at 2960–2850 cm^{-1}, belonging to the $–CH_2$ vibrations, while the AHM shows the same vibrations as stated before (vide supra). Again, these bands almost completely disappear in the products of the reaction between HMD and AHM. A comparison of the IR spectra obtained for the different HMD/molybdate ratios revealed two different types of spectra in this system depending on the ratios between the components (Supporting Information, Figure S1b), suggesting the formation of two different compounds. The vibrations at 1650–1550 cm^{-1} of the N–H deformation are visible in all spectra, as well as the $–CH_2$ deformation vibrations, which are detected in the range of 1470–1430 cm^{-1}. Finally, the characteristic bands of the molybdate units are located in the range of 935–890 cm^{-1} (Figure 4b), indicating that both starting materials are found in the precipitate [9,37–39]. There is a more significant N–H deformation oscillation at the higher ratios above 10:1, indicating a higher amine content in these compounds. At the higher ratios, the vibrations of the molybdate units show a shift to higher wavenumbers and a more pronounced peak, indicating a change in the molybdate cluster.

The chemical composition of the precipitates, especially the carbon content, is important for the pyrolytic formation of oxide carbides, carbides, oxides, and nitrides. Therefore, elemental analyses were carried out for all obtained precipitates (Supporting Information, Tables S1 and S2, and Figure S2). Based on these results, two different compositions could be determined. Similar to the results from the IR spectra, the samples with the lower 1,8-DAN content from the ratios 1:1 to 5:1 show similar compositions. This is also the case for the HMD/molybdate precipitates. However, in the latter example, there is no clear trend as the HMD ratio increases. Overall, the amount of carbon increases when more diamine is added to the AHM.

According to the experimental results described until now, the different mixing ratios show different products. Furthermore, different morphologies of the precipitates of 1,8-DAN and molybdate were observed depending on the mixing ratios (Figure 5a and Supporting Information, Figure S3). The first products with the ratio 1:1 and 2:1 show similar block-shaped morphologies. The larger amounts of 1,8-DAN (5:1 to 30:1) lead to highly anisotropic rod-shaped morphologies. Also, in the HMD/molybdate system, different morphologies were observed for the precursor precipitates (Figure 5b and Supporting Information, Figure S4). In this case, the morphologies are more irregularly shaped. The precipitates show agglomerated layered platelets.

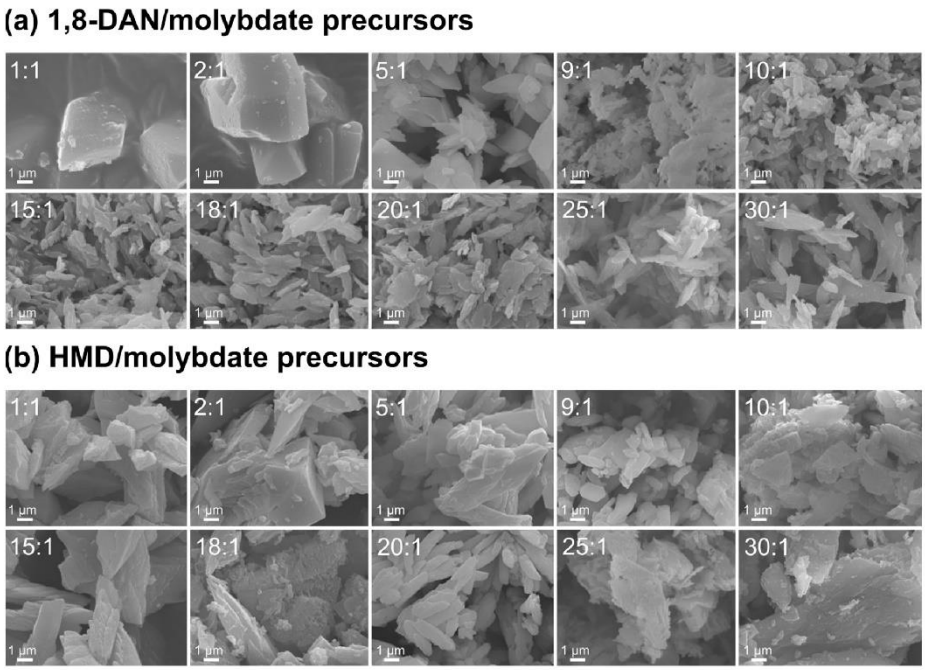

Figure 5. (**a**) SEM images of the products of 1,8-DAN/molybdate precursors with different mixing ratios. (**b**) SEM images of HMD/molybdate precursors.

Both the composition and the synthesis conditions have a strong influence on the morphologies of the precursor systems formed. Since we showed in previous studies that the morphologies of the precipitated products are preserved after pyrolysis, it is therefore possible to adjust the morphology of the pyrolyzed product by adjusting the precursor precipitation reactions. These results are consistent with our earlier findings [28,29].

All precipitates obtained are crystalline phases, as demonstrated by XRD analysis (Figure 6). Based on these measurements, our assumption that different crystalline structures are formed depending on the ratio between the components can be underlined. The diffractograms of the 1,8-DAN/molybdate, again in agreement with the results discussed above, show a transition between a lower ratio of 1,8-DAN (1:1–5:1) and a higher ratio of 1,8-DAN (9:1–30:1) (Figure 6a and Supporting Information, Figure S5a).

The diffractograms of HMD/molybdate do not show such a clear trend, similar to the results of the elemental analysis. The samples with the lower amount of HMD (1:1–5:1) again show the formation of the same compound as the diffraction patterns are similar. Increasing the amount of HMD again leads to similar diffractograms (9:1–30:1) (Supporting Information, Figure S5b). However, closer observation reveals several additional reflections in some diffractograms that could be assigned to the reflections from diffractograms with lower HMD content (1:1–5:1) (Figure 6b). These observed discrepancies most likely also explain the irregular trends in the elemental analysis. It appears that increasing the amount of HMD leads to the mixing of the lower ratio (1:1) and higher ratio (20:1) compounds.

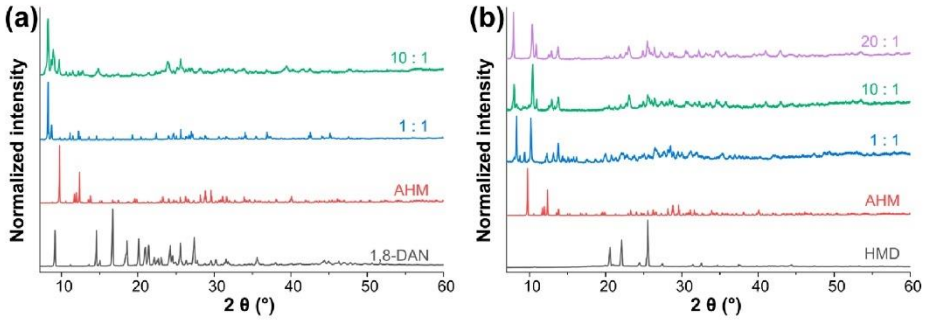

Figure 6. (**a**) XRD pattern of the starting materials 1,8-DAN, AHM, and 1,8-DAN/molybdate (1:1 and 10:1 mixture). (**b**) XRD pattern of the starting materials HMD, AHM, and HMD/molybdate (1:1, 10:1, and 20:1 mixture).

3.2. Thermal Decomposition Behavior of the Precursors

The thermogravimetric analysis (TGA) and TG-FTIR data of the 1,8-DAN/molybdate samples support the hypothesis that two different products were obtained at different ratios (Figures 7a and 8 and Supporting Information, Figure S6). The TGA curves were recorded in nitrogen atmosphere with a heating rate of 20 K min^{-1}. At lower 1,8-DAN to molybdate ratios the release of water, carbon monoxide and carbon dioxide are visible. As the amount of 1,8-DAN increases, the release of ammonia is also observed.

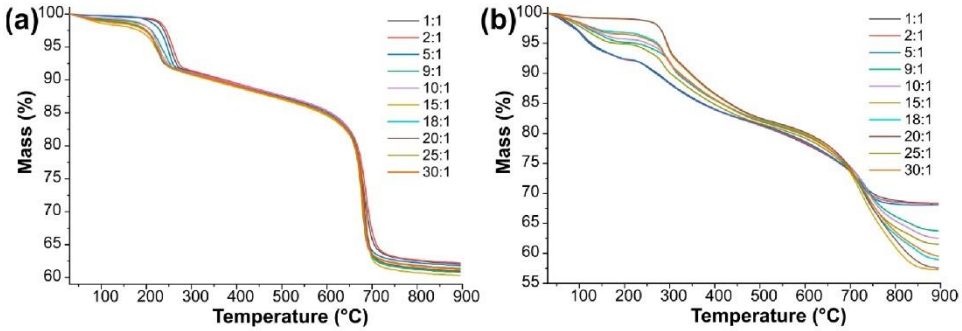

Figure 7. (**a**) Overview of TG curves of 1,8-DAN/molybdate with different ratios; heating rate: 20 K min^{-1}; gas: nitrogen. (**b**) Overview of TG curves of HMD/molybdate with different ratios; heating rate: 20 K min^{-1}; gas: nitrogen.

Furthermore, the TGA and TG-FTIR date of HMD/molybdates samples (Figures 7b and 9 and Supporting Information, Figure S7) also show the formation of two products depending on the respective reactant ratios. At lower HMD ratios, three distinct steps of mass loss are visible, which can be attributed to the loss of water, ammonia, carbon monoxide and carbon dioxide. An increase in the HMD ratio results in the release of less water, more ammonia, carbon monoxide and carbon dioxide.

These results are very similar to the trend of our previous results [28]. In all cases, an increase in the amount of diamine leads to a release of ammonia or an excess of ammonia. The previous results with the PPD/molybdate system show that in the samples with less diamine the diamine is doubly protonated, while in the samples with higher diamine the amine is monoprotonated due to the higher basicity of these samples. The samples with higher diamine also contained ammonium cations (NH_4^+) in order to achieve electroneu-

trality [28]. The release of ammonia observed in the TG-FTIR measurements underlines that the 1,8-DAN/molybdate and HMD/molybdate samples show a similar trend.

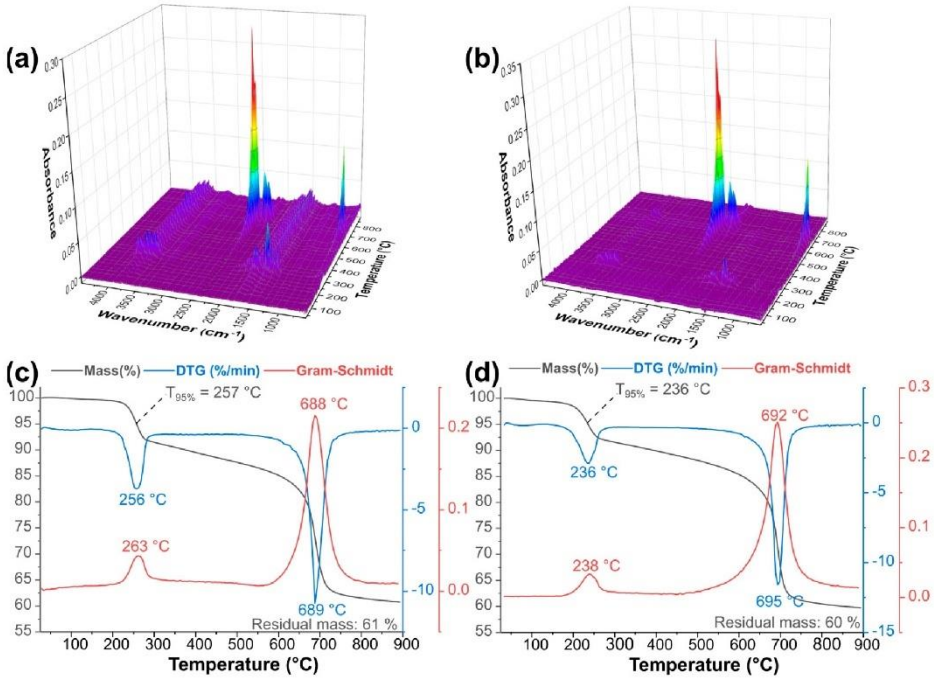

Figure 8. (**a**) TG-FTIR measurements of 1,8-DAN/molybdate (1:1), (**b**) TG-FTIR measurements of 1,8-DAN/molybdate (10:1), (**c**) thermogravimetric curve, with Gram-Schmidt and differential thermogravimetric curve of 1,8-DAN/molybdate (1:1); heating rate: 20 K min^{-1}; gas: nitrogen; (**d**) thermogravimetric curve, with Gram-Schmidt and differential thermogravimetric curve of 1,8-DAN/molybdate (10:1); heating rate: 20 K min^{-1}; gas: nitrogen.

3.3. Pyrolysis of the Precipitation Products

In analogy to our previous work [29], all precursors were heated to 1023 K in an Ar flow and allowed to remain at this temperature for 5 h. As described previously [29], a two-step mechanism takes place during pyrolysis when forming molybdenum carbide from the starting material [6]. Exemplarily, the X-ray diffraction pattern of the decomposed precursor 1,8-DAN/molybdate (1:1) and 1,8-DAN/molybdate (10:1) are presented together with the obtained fit (Figure 10a,b). The presence of orthorhombic Mo_2C [17,20] (*Pbcn*), cubic Mo [18,33] ($Fm\bar{3}m$), and also MoC_x ($Fm\bar{3}m$ or $P6_3/mmc$) [21] was observed. The latter phase is described as a defect structure of the NaCl or NiAs type, whereby not all octahedral voids are filled by carbon atoms. The formation of the respective structure types is attributed to the different carbon content. Because of the uncertainties concerning the elemental composition and thus the amount of x, the composition $MoC_{0.67}$ [21] was used to refine the structure of the NaCl type, while the composition $MoC_{0.5}$ [22] was used for the hexagonal NiAs type.

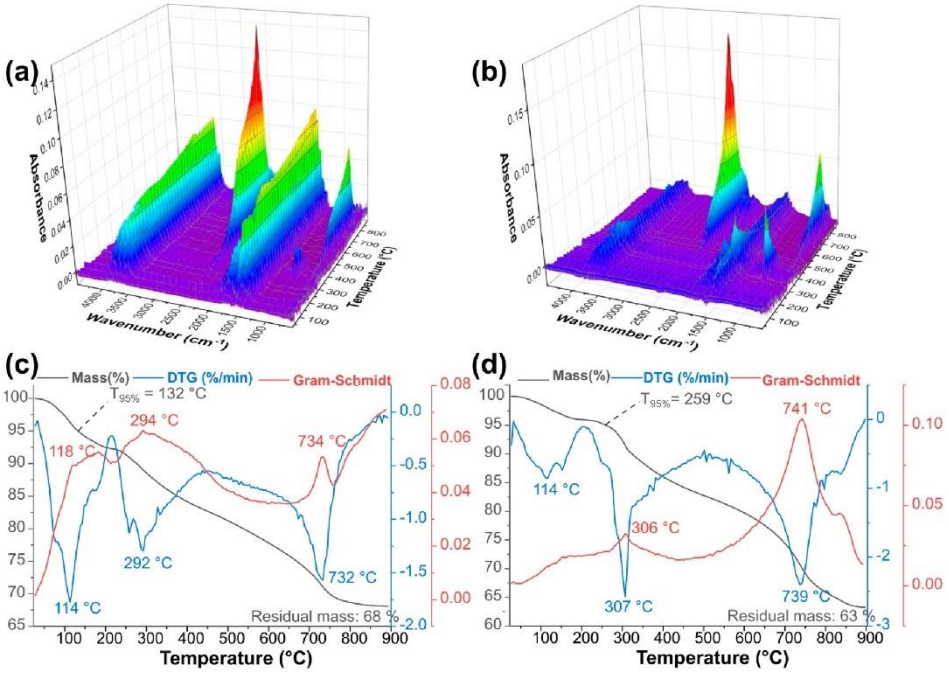

Figure 9. (**a**) TG-FTIR measurements of HMD/molybdate (1:1), (**b**) TG-FTIR measurements of HMD/molybdate (10:1), (**c**) thermogravimetric curve, with Gram-Schmidt and differential thermogravimetric curve of HMD/molybdate (1:1); heating rate: 20 K min^{-1}; gas: nitrogen; (**d**) thermogravimetric curve, with Gram-Schmidt and differential thermogravimetric curve of HMD/molybdate (10:1); heating rate: 20 K min^{-1}, gas: nitrogen.

As described in our previous work [29], stacking faults can be observed in these materials; therefore, the refinement has been conducted using the cubic as well as the hexagonal phase (Figure 10a,b) to model the different stacking periodicities. Metals adapting the Cu-type structure show a similar behavior [41–44]. Representative XRD patterns of the decomposed precursors HMD/molybdate (1:1) and HMD/molybdate (10:1) are shown together with the achieved fit (Figure 10c,d). In contrast to the XRD pattern from the 1,8-DAN/molybdate precursor systems (Figure 10a,b), the XRD pattern from the HMD/molybdate systems (Figure 10c,d) is more crystalline. There is no broad reflection attributable to MoC_x [21], and no amorphous background is visible. The structure refinement revealed the presence of orthorhombic Mo_2C [17,20] besides the presence of monoclinic MoO_2 [32], tetragonal Mo_2N [31], and cubic Mo [18,33].

The pyrolysis of the 1,8-DAN/molybdate precursor was carried out at 1023 K in accordance with our previous experiments [29]. Results from phase composition are presented in Figure 11a. In comparison to the PPD/molybdate system [29], the 1,8-DAN/molybdate precursors mainly form the MoC_x carbide phases besides small amounts of Mo_2C, emphasizing the previous assumption that the pyrolysis process depends on the carbon content in the precursor [29]. This is furthermore in line with the carbon content of PPD (67 mass% C) versus 1,8-DAN (76 mass% C).

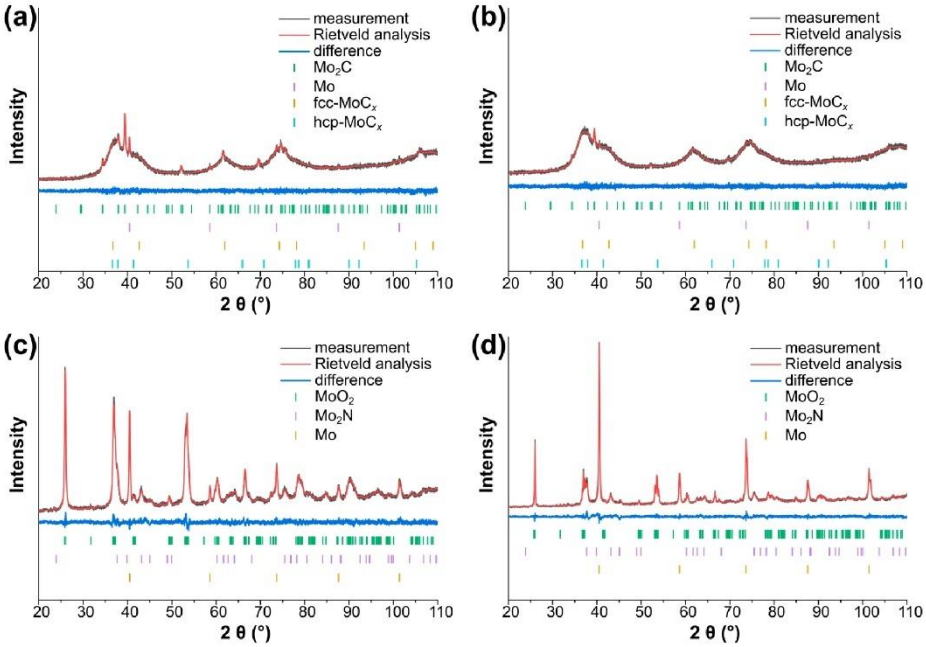

Figure 10. (**a**) Structural analysis of the thermally treated 1,8-DAN/molybdate precursor (1:1) at 1023 K: the refined phase compositions are 78(1) mass% *fcc*-MoC_x, 11(1) mass% *hcp*-MoC_x, 10(1) mass% Mo_2C, and 2(1) mass% Mo. (**b**) Structural analysis of the thermally treated 1,8-DAN/molybdate precursor (10:1) at 1023 K: the refined phase compositions are 87(1) mass% *fcc*-MoC_x, 9(1) mass% *hcp*-MoC_x, 3(1) mass% Mo_2C, and 1(1) mass% Mo. (**c**) Structural analysis of the thermally treated HMD/molybdate precursor (1:1) at 1023 K: the refined phase compositions are 69(1) mass% MoO_2, 21(1) mass% Mo_2N, and 10(1) mass% Mo. (**d**) Structural analysis of the thermally treated HMD/molybdate precursor (10:1) at 1023 K: the refined phase compositions are 39(1) mass% Mo, 33(1) mass% MoO_2, and 27(1) mass% Mo_2N.

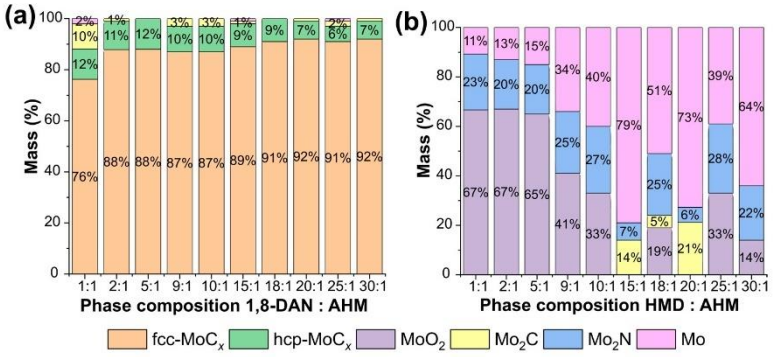

Figure 11. (**a**) Phase compositions of the pyrolyzed 1,8-DAN/molybdate precursors (different phase compositions) determined via fitting the powder X-ray diffraction data. (**b**) Phase compositions of the pyrolyzed HMD/molybdate precursors (different phase compositions) determined via fitting the powder X-ray diffraction data.

HMD/molybdate was pyrolyzed, applying the same parameters as the other two examples. Results from phase composition are presented in Figure 11b. The pyrolysis study of HMD/molybdate with the use of an aliphatic amine does not show a clear trend. In many samples, an increased amount of elemental molybdenum besides MoO_2 is found. Reasons for this divergent trend might be the lower carbon content of HMD (62 mass% C) and its aliphatic nature along with the lower stability (in comparison to aromatic amines) that do not allow for the formation of molybdenum carbide.

The elemental analysis of all pyrolyzed products of 1,8-DAN/molybdate shows a high amount of carbon (Supporting Information, Table S3). This is in contrast to the pyrolyzed samples from the PPD/molybdate system, where only the samples with higher PPD ratios showed higher carbon contents [29]. This is due to the higher carbon content introduced via 1,8-DAN. This excess carbon found in the elemental analysis furthermore indicates that amorphous carbon has to exist in the samples, especially since a high amorphous fraction and no crystalline carbon was observed in the XRD pattern discussed above. Due to an argon atmosphere pyrolysis of the precursors, the resulting particles are embedded in a carbon matrix [1,10,45,46]. Combining molybdenum oxides with carbides and carbonaceous materials creates a potential anode material. For other systems, it has been reported that this can lead to materials that exhibit high capacities along with good cycling stability [1]. The elemental analysis of the pyrolyzed products of the combination between HMD and AHM, again, shows different results. The carbon content in the sample is very low, which is based on the lower carbon content and lower stability of the aliphatic amine (Supporting Information, Table S4). This reveals that the amines decomposed more or less completely via the pyrolysis process.

Finally, SEM images were taken to compare the morphologies before and after pyrolysis. The SEM images before pyrolysis are shown above (Figure 5). In Figure 12a, the corresponding images after pyrolysis of the 1,8-DAN/molybdate precursors are depicted. It is obvious that morphology was preserved after pyrolysis. The SEM images of the HMD/molybdate precursors also indicate the preservation of the morphology after pyrolysis (Figure 12b).

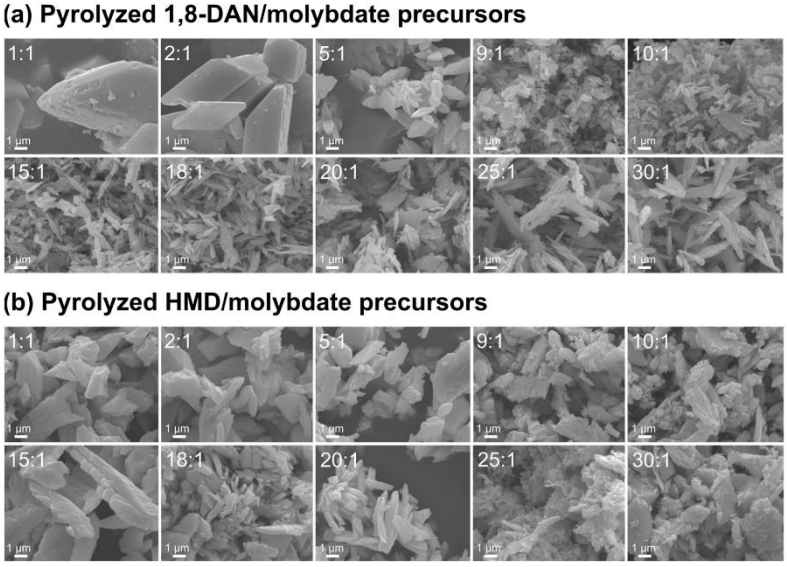

Figure 12. (**a**) SEM images of the pyrolyzed 1,8-DAN/molybdate precursor. (**b**) SEM images of the pyrolyzed HMD/molybdate precursors.

It is interesting to note that there is a great correlation between all reported experiments and our previous results with the PPD/molybdate systems [28,29]. The variation of the ratio between ammonium heptamolybdate and diamine under acidic conditions leads to the formation of two different precipitate compounds with different morphologies. In any case, increasing the diamine amount causes a higher organic content in the precipitate. The results also show the occurrence of ammonium cations with increasing diamine content, which is due to monoprotonated diamines [28]. The pyrolysis of the precursors systems PPD/molybdate [29], 1,8-DAN/molybdate, and HMD/molybdate reveals a similar trend. Pyrolysis of the PPD/molybdate system shows that at low PPD amounts, a mixture of orthorhombic Mo_2C, monoclinic MoO_2, tetragonal Mo_2N, and cubic Mo is formed, while at higher PPD amounts, mainly MoC_x with lower amounts of Mo_2C and elemental Mo is obtained [29]. Similarly to these results, the pyrolysis of the 1,8-DAN/molybdate precursors reveals the formation of MoC_x carbide phases with less impurities of Mo_2C and elemental Mo due to the higher carbon amount in all investigated ratios. Compared to the pyrolysis behavior of PPD/molybdate [29] and 1,8-DAN/molybdate precursors, the HMD/molybdate precursors show a difference. No formation of the MoC_x carbide phases is visible. At lower HMD amounts, mainly MoO_2 was obtained, while at higher HMD amounts, elemental Mo was received. Other side products were Mo_2C and Mo_2N. The low stability of the aliphatic diamine of HMD compared to the aromatic diamine of PPD and 1,8-DAN is the reason for the formation of carbon deficiency in the pyrolysis products of HMD/molybdate precursors. This behavior is also known in the literature. Varganici et al. [47] and García et al. [48] reported higher thermal stability of aromatic compounds compared to aliphatic compounds.

4. Conclusions

The aim of this study was to investigate the synthesis conditions for the preparation of inorganic–organic hybrid materials from ammonium heptamolybdate (AHM) and 1,8-daminonaphthalene (1,8-DAN) or hexamethylenediamine (HMD) utilizing a wet-chemical continuous microjet precipitation method along with subsequent pyrolytic production of molybdenum carbides/nitrides/oxides. For the first step, organic components were selected according to their structure. On the one hand, 1,8-DAN, as an aromatic amine with higher carbon content, was used. On the other hand, hexamethylenediamines, as an aliphatic amine, were utilized. The results clearly show that these differences play a key role in the pyrolysis. Pyrolytic treatment of the 1,8-DAN/molybdate hybrid precursor leads to a variety of composite materials ($Mo(C,N,O)_x$, molybdenum carbide, and molybdenum) embedded in the carbonaceous matrix. The molybdenum carbide MoC_x shows stacking defects, as seen from PXRD measurements. In contrast, the pyrolysis of the HMD/molybdate precursor does not lead to a material with an excess of carbon, which is attributed to the reduced stability and carbon content of the aliphatic amine. It was also shown that the pyrolysis of the inorganic–organic hybrid materials 1,8-DAN/molybdate as well as HMD/molybdate leads to the preservation of the morphology. In the present work, we show that the newly used amines and the newly produced hybrid materials exhibit different behavior in the pyrolysis of the composites than in our previous studies [28,29]. We also observed that different compositions are obtained. Overall, the microjet method enables the synthesis of an extremely interesting hybrid material that could potentially become a candidate as an anode material for Li-ion batteries because of its potentially high capacities and cycling stability over other carbide materials.

Supplementary Materials: The following supporting information can be downloaded at https://www.mdpi.com/article/10.3390/solids5030030/s1, Figure S1: (a) Overview of the received IR spectra of the products from reactions with different ratios of 1,8-DAN/molybdate. (b) Overview of the received IR spectra from HMD/molybdate with different ratio; Figure S2: C, H and N mass percent as a function of the ratio of precursors; Figure S3: SEM images of 1,8-DAN/molybdate precursor; Figure S4: SEM images of HMD/molybdate precursors; Figure S5: (a) Overview of the received XRD pattern of the products from reactions with different ratios of 1,8-DAN/molybdate.

(b) Overview of the received XRD pattern from HMD/molybdate with different ratio; Figure S6: TG-FTIR measurements (a) associated FTIR spectra of 1,8-DAN/molybdate (1:1) and (b) associated FTIR spectra of 1,8-DAN/molybdate (10:1); Figure S7: TG-FTIR measurements (a) associated FTIR spectra of HMD/molybdate (1:1) and (b) associated FTIR spectra of HMD/molybdate (10:1); Table S1: Elemental analysis of the precipitated products 1,8-DAN/molybdate; Table S2: Elemental analysis of the precipitated products HMD/molybdate; Table S3: Elemental analysis of 1,8-DAN/molybdate precursors after the pyrolysis; Table S4: Elemental analysis of HMD/molybdate precursors after the pyrolysis.

Author Contributions: Conceptualization, M.A.M. and G.K.; Funding acquisition, G.K.; Investigation, M.A.M. and S.H.; Methodology, M.A.M., O.J. and S.H.; Project administration, G.K.; Resources, G.K.; Supervision, G.K.; Writing—original draft, M.A.M.; Writing—review and editing, O.J. and G.K. All authors have read and agreed to the published version of the manuscript.

Funding: This research received funding from Saarland University and the German Science Foundation (INST 256/349-1 and INST 256/506-1).

Data Availability Statement: The original contributions presented in the study are included in the article/Supplementary Material. Further inquiries can be directed to the corresponding author/s.

Acknowledgments: Instrumentation and technical assistance for this work were provided by the Service Center X-ray Diffraction. We thank Jörg Schmauch for the support with scanning electron microscopy. Special thanks also to Robert Haberkorn for the helpful discussion and advice regarding the Rietveld refinements.

Conflicts of Interest: The authors declare no conflicts of interest.

References

1. Xiu, Z.; Kim, D.; Alfaruqi, M.H.; Song, J.; Kim, S.; Duong, P.T.; Mathew, V.; Baboo, J.P.; Kim, J. Ultrafine molybdenum oxycarbide nanoparticles embedded in N-doped carbon as a superior anode material for lithium-ion batteries. *J. Alloys Compd.* **2017**, *696*, 143–149. [CrossRef]
2. Lu, L.; Han, X.; Li, J.; Hua, J.; Ouyang, M. A review on the key issues for lithium-ion battery management in electric vehicles. *J. Power Sources* **2013**, *226*, 272–288. [CrossRef]
3. Etacheri, V.; Marom, R.; Elazari, R.; Salitra, G.; Aurbach, D. Challenges in the development of advanced Li-ion batteries: A review. *Energy Environ. Sci.* **2011**, *4*, 3243–3262. [CrossRef]
4. Wu, F.; Maier, J.; Yu, Y. Guidelines and trends for next-generation rechargeable lithium and lithium-ion batteries. *Chem. Soc. Rev.* **2020**, *49*, 1569–1614. [CrossRef]
5. Preiss, H.; Meyer, B.; Olschewski, C. Preparation of molybdenum and tungsten carbides from solution derived precursors. *J. Mater. Sci.* **1998**, *33*, 713–722. [CrossRef]
6. Chen, W.-F.; Wang, C.-H.; Sasaki, K.; Marinkovic, N.; Xu, W.; Muckerman, J.T.; Zhu, Y.; Adzic, R.R. Highly active and durable nanostructured molybdenum carbide electrocatalysts for hydrogen production. *Energy Environ. Sci.* **2013**, *6*, 943–951. [CrossRef]
7. Liao, L.; Wang, S.; Xiao, J.; Bian, X.; Zhang, Y.; Scanlon, M.D.; Hu, X.; Tang, Y.; Liu, B.; Girault, H.H. A nanoporous molybdenum carbide nanowire as an electrocatalyst for hydrogen evolution reaction. *Energy Environ. Sci.* **2014**, *7*, 387–392. [CrossRef]
8. Ge, C.; Jiang, P.; Cui, W.; Pu, Z.; Xing, Z.; Asiri, A.M.; Obaid, A.Y.; Sun, X.; Tian, J. Shape-controllable synthesis of Mo_2C nanostructures as hydrogen evolution reaction electrocatalysts with high activity. *Electrochim. Acta* **2014**, *134*, 182–186. [CrossRef]
9. Pang, M.; Wang, X.; Xia, W.; Muhler, M.; Liang, C. Mo(VI)-Melamine Hybrid As Single-Source Precursor to Pure-Phase β-Mo_2C for the Selective Hydrogenation of Naphthalene to Tetralin. *Ind. Eng. Chem. Res.* **2013**, *52*, 4564–4571. [CrossRef]
10. Liu, Y.; Yu, G.; Li, G.-D.; Sun, Y.; Asefa, T.; Chen, W.; Zou, X. Coupling Mo_2C with Nitrogen-Rich Nanocarbon Leads to Efficient Hydrogen-Evolution Electrocatalytic Sites. *Angew. Chem.* **2015**, *127*, 10902–10907. [CrossRef]
11. Giordano, C.; Erpen, C.; Yao, W.; Antonietti, M. Synthesis of Mo and W Carbide and Nitride Nanoparticles via a Simple "Urea Glass" Route. *Nano Lett.* **2008**, *8*, 4659–4663. [CrossRef]
12. Huang, Y.; Gong, Q.; Song, X.; Feng, K.; Nie, K.; Zhao, F.; Wang, Y.; Zeng, M.; Zhong, J.; Li, Y. Mo_2C Nanoparticles Dispersed on Hierarchical Carbon Microflowers for Efficient Electrocatalytic Hydrogen Evolution. *ACS Nano* **2016**, *10*, 11337–11343. [CrossRef] [PubMed]
13. Li, S.; Cheng, C.; Sagaltchik, A.; Pachfule, P.; Zhao, C.; Thomas, A. Metal-Organic Precursor–Derived Mesoporous Carbon Spheres with Homogeneously Distributed Molybdenum Carbide/Nitride Nanoparticles for Efficient Hydrogen Evolution in Alkaline Media. *Adv. Funct. Mater.* **2019**, *29*, 1807419. [CrossRef]
14. Wang, H.-M.; Wang, X.-H.; Zhang, M.-H.; Du, X.-Y.; Li, W.; Tao, K.-Y. Synthesis of Bulk and Supported Molybdenum Carbide by a Single-Step Thermal Carburization Method. *Chem. Mater.* **2007**, *19*, 1801–1807. [CrossRef]

15. Zoller, M.; Bubnova, R.; Biryukov, Y.; Haussühl, E.; Pöttgen, R.; Janka, O.; Penner, S.; Praty, C.; Fitzek, H.; Winkler, J.; et al. Elucidating the physical properties of the molybdenum oxide Mo_4O_{11} and its tantalum substituted variant $Mo_2Ta_2O_{11}$. *Z. Krist.-Cryst. Mater.* **2020**, *235*, 143–155. [CrossRef]
16. Glemser, O.; Lutz, G. Über Molybdänoxyde. *Z. Anorg. Allg. Chem.* **1950**, *263*, 2–14. [CrossRef]
17. Parthé, E.; Sadogopan, V. The Structure of Dimolybdenum Carbide by Neutron Diffraction Technique. *Acta Crystallogr.* **1963**, *16*, 202–205. [CrossRef]
18. Hull, A.W. The positions of atoms in metals. *Proc. Am. Inst. Electr. Eng.* **1919**, *38*, 1171–1192. [CrossRef]
19. Zhu, H.; Li, Z.; Yang, H.; Luo, L. Carbothermic Reduction of MoO_3 for Direct Alloying Process. *J. Iron Steel Res. Int.* **2013**, *20*, 51–56. [CrossRef]
20. Norlund Christensen, A. A neutron diffraction investigation on a crystal of alpha-Mo_2C. *Acta Chem. Scand. Ser. A* **1977**, *31*, 509–511. [CrossRef]
21. Rudy, E.; Brukl, C.E.; Windisch, S. Constitution of niobium (columbium)-molybdenum-carbon alloys. *Trans. Metall. Soc. AIME* **1967**, *239*, 1796–1808.
22. Kuo, K.; Hägg, G. A New Molybdenum Carbide. *Nature* **1952**, *170*, 245–246. [CrossRef]
23. Odenwald, C.; Kickelbick, G. Additive-free continuous synthesis of silica and ORMOSIL micro- and nanoparticles applying a microjet reactor. *J. Sol-Gel Sci. Technol.* **2019**, *89*, 343–353. [CrossRef]
24. Betke, A.; Kickelbick, G. Bottom-Up, Wet Chemical Technique for the Continuous Synthesis of Inorganic Nanoparticles. *Inorganics* **2014**, *2*, 1–15. [CrossRef]
25. Krüner, B.; Odenwald, C.; Tolosa, A.; Schreiber, A.; Aslan, M.; Kickelbick, G.; Presser, V. Carbide-derived carbon beads with tunable nanopores from continuously produced polysilsesquioxanes for supercapacitor electrodes. *Sustain. Energy Fuels* **2017**, *1*, 1588–1600. [CrossRef]
26. Krüner, B.; Odenwald, C.; Jäckel, N.; Tolosa, A.; Kickelbick, G.; Presser, V. Silicon Oxycarbide Beads from Continuously Produced Polysilsesquioxane as Stable Anode Material for Lithium-Ion Batteries. *ACS Appl. Energy Mater.* **2018**, *1*, 2961–2970. [CrossRef]
27. Krüner, B.; Odenwald, C.; Quade, A.; Kickelbick, G.; Presser, V. Influence of Nitrogen-Doping for Carbide-Derived Carbons on the Supercapacitor Performance in an Organic Electrolyte and an Ionic Liquid. *Batter. Supercaps* **2018**, *1*, 135–148. [CrossRef]
28. Abdirahman Mohamed, M.; Arnold, S.; Janka, O.; Quade, A.; Presser, V.; Kickelbick, G. Self-Activation of Inorganic-Organic Hybrids Derived through Continuous Synthesis of Polyoxomolybdate and para-Phenylenediamine Enables Very High Lithium-Ion Storage Capacity. *ChemSusChem* **2023**, *16*, e202202213. [CrossRef]
29. Abdirahman Mohamed, M.; Arnold, S.; Janka, O.; Quade, A.; Schmauch, J.; Presser, V.; Kickelbick, G. Continuous wet chemical synthesis of $Mo(C,N,O)_x$ as anode materials for Li-ion batteries. *J. Mater. Chem. A* **2023**, *11*, 19936–19954. [CrossRef]
30. *AXS*, Topas 5.1; General Profile and Structure Analysis Software for Powder Diffraction Data; Bruker: Karlsruhe, Germany, 2014.
31. Ettmayer, P. Das System Molybdaen-Stickstoff. *Monatshefte Chem.* **1970**, *101*, 127–140. [CrossRef]
32. Bolzan, A.A.; Kennedy, B.J.; Howard, C.J. Neutron Powder Diffraction Study of Molybdenum and Tungsten Dioxides. *Aust. J. Chem.* **1995**, *48*, 1473–1477. [CrossRef]
33. Häglund, J.; Fernndez Guillermet, A.; Grimvall, G.; Körling, M. Theory of bonding in transition-metal carbides and nitrides. *Phys. Rev. B* **1993**, *48*, 11685–11691. [CrossRef] [PubMed]
34. Cataldo, F. On the Polymerization of *P*-Phenylenediamine. *Eur. Polym. J.* **1996**, *32*, 43–50. [CrossRef]
35. Pałys, B.J.; Skompska, M.; Jackowska, K. Sensitivity of poly 1,8-diaminonaphthalene to heavy metal ions-Electrochemical and vibrational spectra studies. *J. Electroanal. Chem.* **1997**, *433*, 41–48. [CrossRef]
36. Ohno, K.; Okimura, M.; Akai, N.; Katsumoto, Y. The effect of cooperative hydrogen bonding on the OH stretching-band shift for water clusters studied by matrix-isolation infrared spectroscopy and density functional theory. *Phys. Chem. Chem. Phys.* **2005**, *7*, 3005–3014. [CrossRef]
37. Shi, Z.; Gao, B.; Mo, Q.; Shao, Z.J.; Nie, K.; Liu, B.; Zhang, H.; Wang, Y.; Zhang, Y.; Gao, Q.; et al. Organic-Inorganic-Hybrid-Derived Molybdenum Carbide Nanoladders: Impacts of Surface Oxidation for Hydrogen Evolution Reaction. *ChemNanoMat* **2018**, *4*, 194–202. [CrossRef]
38. Gao, Q.; Yang, L.; Lu, X.; Mao, J.; Zhang, Y.; Wu, Y.; Tang, Y. Synthesis, characterization and lithium-storage performance of MoO_2/carbon hybrid nanowires. *J. Mater. Chem.* **2010**, *20*, 2807–2812. [CrossRef]
39. Gao, Q.; Zhang, C.; Xie, S.; Hua, W.; Zhang, Y.; Ren, N.; Xu, H.; Tang, Y. Synthesis of Nanoporous Molybdenum Carbide Nanowires Based on Organic-Inorganic Hybrid Nanocomposites with Sub-Nanometer Periodic Structures. *Chem. Mater.* **2009**, *21*, 5560–5562. [CrossRef]
40. Kasap, E.; Özbay, A.; Özçelik, S. Infrared spectroscopic study of the Hofmann-diam-type clathrates: M(1,6-diaminohexane)$Ni(CN)_4$ C_6H_6 (M = Ni, Co or Cd). *Spectrosc. Lett.* **1997**, *30*, 491–496. [CrossRef]
41. Wolf, U.; Ernst, F.; Muschik, T.; Finnis, M.W.; Fischmeister, H.F. The influence of grain boundary inclination on the structure and energy of σ = 3 grain boundaries in copper. *Philos. Mag. A* **1992**, *66*, 991–1016. [CrossRef]
42. Hofmann, D.; Ernst, F. Quantitative high-resolution transmission electron microscopy of the incoherent Σ3 (211) boundary in Cu. *Ultramicroscopy* **1994**, *53*, 205–221. [CrossRef]
43. Campbell, G.H.; Chan, D.K.; Medlin, D.L.; Angelo, J.E.; Carter, C.B. Dynamic observation of the FCC to 9R shear transformation in a copper Σ = 3 incoherent twin boundary. *Scr. Mater.* **1996**, *35*, 837–842. [CrossRef]

44. Medlin, D.L.; Campbell, G.H.; Carter, C.B. Stacking defects in the 9R phase at an incoherent twin boundary in copper. *Acta Mater.* **1998**, *46*, 5135–5142. [CrossRef]
45. Wang, R.; Yang, J.; Shi, K.; Wang, B.; Wang, L.; Tian, G.; Bateer, B.; Tian, C.; Shen, P.; Fu, H. Single-step pyrolytic preparation of Mo_2C/graphitic carbon nanocomposite as catalyst carrier for the direct liquid-feed fuel cells. *RSC Adv.* **2013**, *3*, 4771–4777. [CrossRef]
46. Chen, Y.-Y.; Zhang, Y.; Jiang, W.-J.; Zhang, X.; Dai, Z.; Wan, L.-J.; Hu, J.-S. Pomegranate-like N,P-Doped Mo_2C@C Nanospheres as Highly Active Electrocatalysts for Alkaline Hydrogen Evolution. *ACS Nano* **2016**, *10*, 8851–8860. [CrossRef]
47. Varganici, C.D.; Rosu, D.; Barbu-Mic, C.; Rosu, L.; Popovici, D.; Hulubei, C.; Simionescu, B.C. On the thermal stability of some aromatic-aliphatic polyimides. *J. Anal. Appl. Pyrolysis* **2015**, *113*, 390–401. [CrossRef]
48. García, J.M.; Álvarez, J.C.; De La Campa, J.G.; De Abajo, J. Thermal Behavior of Aliphatic-Aromatic Poly(ether-amide)s. *J. Appl. Polym. Sci.* **1998**, *67*, 975–981. [CrossRef]

Supporting Information

Precursor-Based Syntheses of $Mo(C,N,O)_x$, Molybdenum Carbide, Nitride, and Oxide Applying a Microjet Reactor

Mana Abdirahman Mohamed [1] (0000-0003-0708-7623), Oliver Janka [1] (0000-0002-9480-3888), Susanne Harling [1] and Guido Kickelbick [1,2]* (0000-0001-6813-9269)

1 Saarland University, Inorganic Solid-State Chemistry, Campus C4 1, 66123 Saarbrücken, Germany

2 Saarene - Saarland Center for Energy Materials and Sustainability, 66123 Saarbrücken, Germany

* Corresponding author: guido.kickelbick@uni-saarland.de

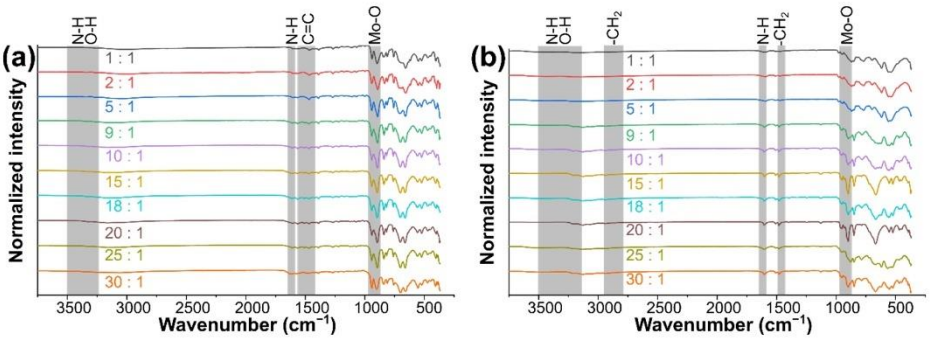

Figure S1: (a) Overview of the received IR spectra of the products from reactions with different ratios of 1,8-DAN/molybdate. (b) Overview of the received IR spectra from HMD/molybdate with different ratio.

Table S1: Elemental analysis of the precipitated products 1,8-DAN/molybdate.

Composition	C / mass%	H / mass%	N / mass%
1,8-DAN/molybdate (1:1)	26.25	2.42	6.09
1,8-DAN/molybdate (2:1)	26.39	2.42	6.09
1,8-DAN/molybdate (5:1)	26.98	2.45	6.20
1,8-DAN/molybdate (9:1)	27.18	2.44	6.21
1,8-DAN/molybdate (10:1)	27.00	2.42	6.23
1,8-DAN/molybdate (15:1)	27.16	2.35	6.17
1,8-DAN/molybdate (18:1)	27.54	2.38	6.27
1,8-DAN/molybdate (20:1)	27.70	2.39	6.32
1,8-DAN/molybdate (25:1)	28.00	2.44	6.34
1,8-DAN/molybdate (30:1)	27.82	2.54	6.25

Table S2: Elemental analysis of the precipitated products HMD/molybdate.

Composition	C / mass%	H / mass%	N / mass%
HMD/molybdate (1:1)	4.56	2.16	1.92
HMD/molybdate (2:1)	4.76	2.11	2.00
HMD/molybdate (5:1)	4.89	2.11	1.94
HMD/molybdate (9:1)	6.81	2.22	2.63
HMD/molybdate (10:1)	6.79	2.21	2.63
HMD/molybdate (15:1)	10.21	2.62	3.90
HMD/molybdate (18:1)	8.37	2.46	3.15
HMD/molybdate (20:1)	10.12	2.63	3.83
HMD/molybdate (25:1)	7.20	2.35	2.68
HMD/molybdate (30:1)	8.20	2.43	3.06

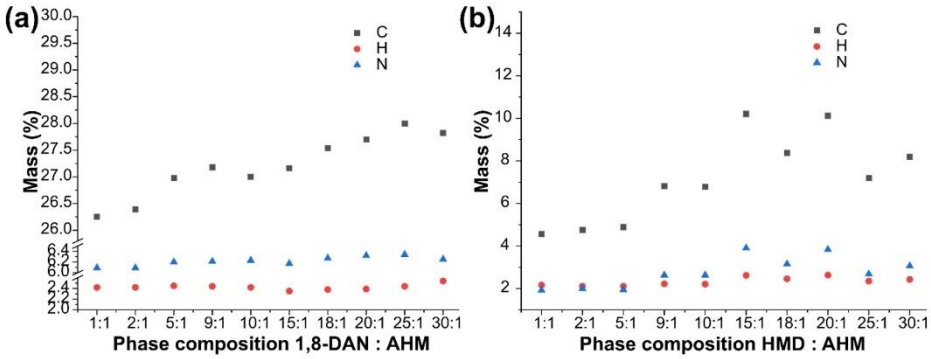

Figure S2: C, H and N mass percent as a function of the ratio of precursors.

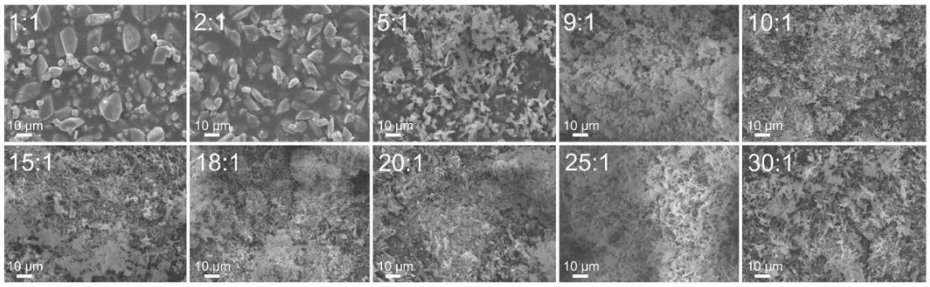

Figure S3: SEM images of 1,8-DAN/molybdate precursor.

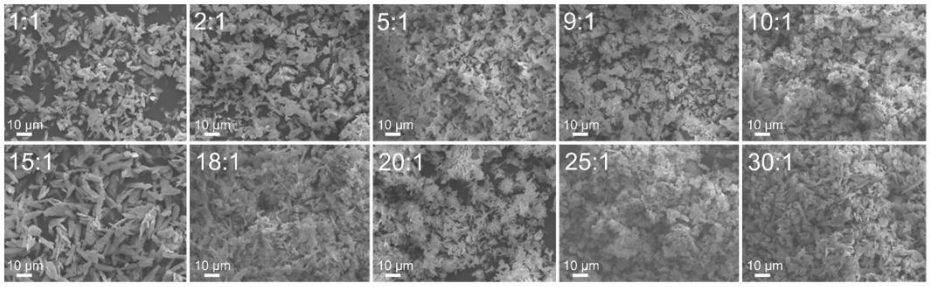

Figure S4: SEM images of HMD/molybdate precursors.

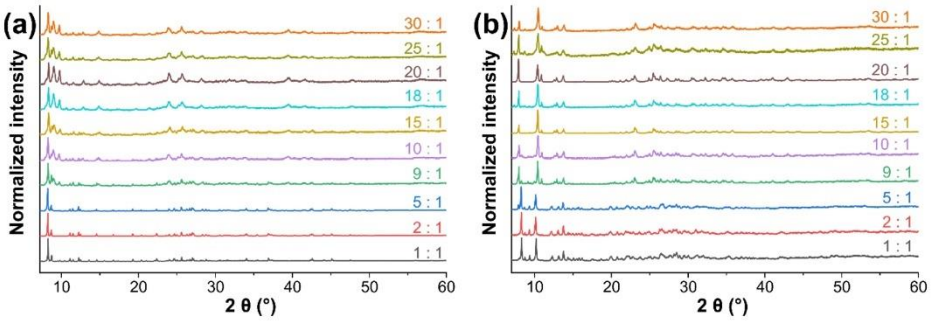

Figure S5: (a) Overview of the received XRD pattern of the products from reactions with different ratios of 1,8-DAN/molybdate. (b) Overview of the received XRD pattern from HMD/molybdate with different ratio.

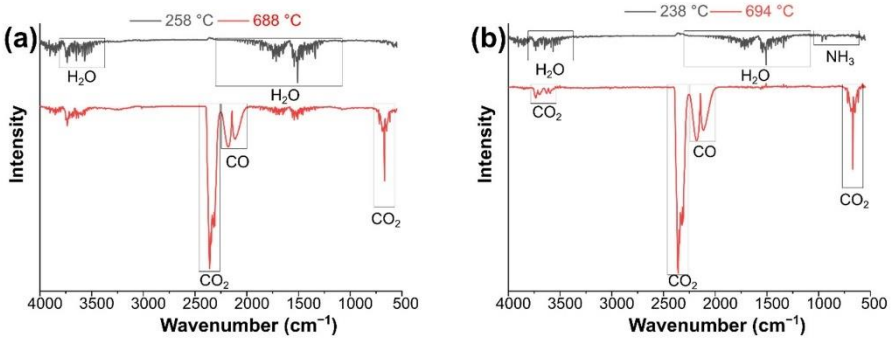

Figure S6: TG-FTIR measurements (a) associated FTIR spectra of 1,8-DAN/molybdate (1:1) and (b) associated FTIR spectra of 1,8-DAN/molybdate (10:1).

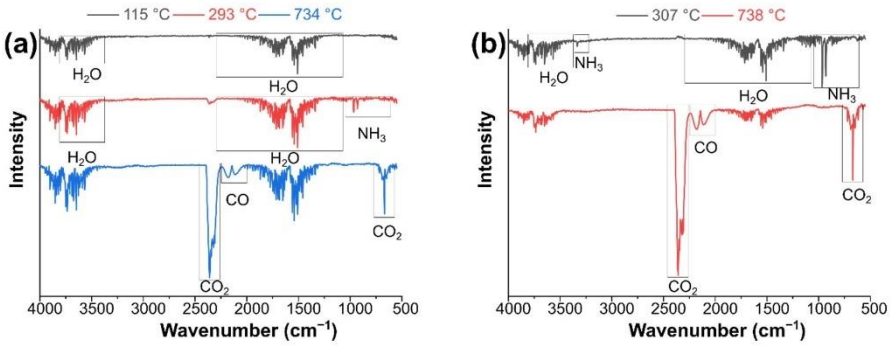

Figure S7: TG-FTIR measurements (a) associated FTIR spectra of HMD/molybdate (1:1) and (b) associated FTIR spectra of HMD/molybdate (10:1).

Table S3: Elemental analysis of 1,8-DAN/molybdate precursors after the pyrolysis.

Composition	C / mass%	H / mass%	N / mass%
Theor. Mo_2C	5.89	0	0
Theor. MoOC	9.69	0	0
Theor. Mo_2N	0	0	6.80
1,8-DAN/molybdate (1:1)	29.43	0.14	0.32
1,8-DAN/molybdate (2:1)	30.41	0.33	0.36
1,8-DAN/molybdate (5:1)	31.28	0.32	0.38
1,8-DAN/molybdate (9:1)	31.05	0.28	0.42
1,8-DAN/molybdate (10:1)	30.68	0.27	0.46
1,8-DAN/molybdate (15:1)	30.95	0.26	0.46
1,8-DAN/molybdate (18:1)	28.92	0.24	0.41
1,8-DAN/molybdate (20:1)	31.14	0.28	0.52
1,8-DAN/molybdate (25:1)	31.47	0.25	0.37
1,8-DAN/molybdate (30:1)	32.22	0.25	0.44

Table S4: Elemental analysis of HMD/molybdate precursors after the pyrolysis.

Composition	C / mass%	H / mass%	N / mass%
Theor. Mo_2C	5.89	0	0
Theor. MoOC	9.69	0	0
Theor. Mo_2N	0	0	6.80
HMD/molybdate (1:1)	0	0.15	1.33
HMD/molybdate (2:1)	0	0.13	1.31
HMD/molybdate (5:1)	0	0.14	1.32
HMD/molybdate (9:1)	0	0.12	1.40
HMD/molybdate (10:1)	0	0.14	1.54
HMD/molybdate (15:1)	1.17	0.22	0.41
HMD/molybdate (18:1)	0	0.15	1.48
HMD/molybdate (20:1)	0.58	0.20	0.51
HMD/molybdate (25:1)	0	0.16	1.52
HMD/molybdate (30:1)	0	0.16	1.30

4 Summary and Outlook

In this dissertation, a sustainable continuous wet-chemical method in a microjet reactor was used to produce inorganic-organic hybrid materials based on polyoxomolybdates and diamines. Systematic studies and detailed characterizations were carried out to optimize these materials for applications in LIBs. Furthermore, these inorganic-organic hybrid compounds were pyrolyzed and can thus be used for applications as electrode materials in LIBs.

In the first part of the work, two inorganic-organic hybrid materials were prepared using two redox-active reactants ammonium heptamolybdate (AHM) as inorganic component and para-phenylenediamine (PPD) as organic component. By varying the PPD and AHM ratios, the compound PPD/molybdate (1 : 1) with the composition $[C_6H_{10}N_2]_2[Mo_8O_{26}]\cdot 6\ H_2O$ was prepared at low PPD:AHM ratios, while the compound PPD/molybdate (10 : 1) with the composition $[C_6H_9N_2]_4[NH_4]_2[Mo_7O_{24}]\cdot 3\ H_2O$ was prepared at high PPD:AHM ratios. Both materials were tested for their electrochemical performance without further treatment. The material PPD/molybdate (10 : 1) shows remarkable electrochemical properties by conversional reaction reaching extraordinary capacities up to 1084 mA h g^{-1} at 100 mA g^{-1} after 150 cycles, which corresponds to a capacity increase of 556%. This high capacity is achieved after an induction phase. This behavior is so far unknown and can be described by several conversion reactions. Post-mortem analyses show a complete decomposition of the material and the formation of crystalline Li_2MoO_4. Furthermore, in-situ polymerization of the PPD was demonstrated by model studies comparing chemically lithiated material. This could explain the unique increase in capacity.

In the second part of this work, the previously prepared inorganic-organic hybrid materials served as precursors for composite materials including molybdenum carbides, nitrides, oxides, elemental molybdenum and mixed anionic compounds such as $Mo(C,N,O)_x$ embedded in a carbonaceous matrix. During the pyrolysis of the inorganic-organic hybrid materials, the sizes and morphologies of the materials could be preserved. The size and morphology are decisive factors for the electrochemical performance. In addition to parameters like time and temperature, the proportion of organic components in the hybrid precursor is decisive for pyrolysis. A mixture of Mo_2C, MoO_2, Mo_2N and elemental Mo without stacking faults and excess carbon was obtained from the pyrolysis of the hybrid precursors with lower PPD content. With higher PPD content in the hybrid precursor, $Mo(C,N,O)_x$ with stacking faults in a

carbonaceous matrix resulted after pyrolysis. In the anode materials for LIBs, stacking faults and excess carbon were found to be critical for improving electrochemical performance. Different electrochemical behaviors could be achieved by varying synthesis parameters such as pyrolysis temperatures and different particle sizes and morphologies. The best electrochemical performance could be achieved with the hybrid precursor with higher PPD:AHM ratio, the PPD/molybdate material (9 : 1), which was pyrolyzed at 600 °C. The material demonstrated a capacity of 933 mA h g^{-1} at 100 m A g^{-1} after 500 cycles. Post-mortem analyses show that two processes take place during cyclization. One is the decomposition of the carbide and the other is the reduction of O-Mo^{6+}. This transformation reaction results in improved electrochemical performance and high cycle stability.

In the third part of this work, the aim was to gain a better understanding of the impact of the carbon source on the pyrolysis reaction. For this purpose, two new organic species 1,8-diaminonaphthalenes (1,8-DAN) or hexamethylenediamines (HMD) were synthesized in combination with ammonium heptamolybdate as inorganic species to form inorganic-organic hybrid precursors. A comparison was made with the results from the previous work, where *para*-phenylenediamine was used as the organic species. Thus, three different organic diamines were compared, namely PPD with 6 carbons and an aromatic system, 1,8-DAN with 10 carbons and an aromatic system and HMD with 6 carbons and an aliphatic system. The findings demonstrate clearly that these differences in organic species are crucial for the pyrolysis. The pyrolysis of the 1,8/molybdate precursors results mainly in the formation of a mixture of molybdenum carbide and molybdenum with composites materials $Mo(C,N,O)_x$ embedded in the carbonaceous matrix. The latter material, $Mo(C,N,O)_x$, also exhibits staple defects. Meanwhile, pyrolysis of the HMD/molybdate precursors leads to materials without excess carbon. This is due to the low carbon content of HMD and the low stability of the aliphatic diamine compared to aromatic systems. It could also be shown here that the morphologies are retained during pyrolysis of inorganic-organic hybrid precursors.

Overall, the microjet approach proved to be a sustainable and energy-saving method for producing extremely interesting inorganic-organic hybrid materials via a simple precipitation reaction. These materials are suitable for direct use as anode materials. Furthermore, these materials are good precursors for pyrolysis reactions and can then also be regarded as anodic materials for LIBs.

Combining redox-active inorganic and organic species in a hybrid material offers a wide range of variations for future research work. In addition to POM clusters made of molybdate, POM clusters with other transition metals such as tungstate or vanadate could also be used. The variation of organic species is also diverse. In addition to the use of other redox-active diamines, the addition of further functional groups is also possible. The investigation of larger aliphatic and aromatic systems is also of interest. Other monomers that can be polymerized to electroactive polymers by electropolymerization can also be used.

In addition to the almost infinite variation possibilities of the inorganic and organic species for the synthesis of hybrid materials, the structures of the 1,8/molybdate and HMD/molybdate hybrid materials can be broken down in more detail by growing single crystals for further research work with regard to characterization, and the electrochemical performance of the 1,8/molybdate and HMD/molybdate materials can be investigated in more detail.

5 References

(1) Wu, F.; Maier, J.; Yu, Y. Guidelines and Trends for Next-Generation Rechargeable Lithium and Lithium-Ion Batteries. *Chem. Soc. Rev.* **2020**, *49*, 1569–1614. https://doi.org/10.1039/c7cs00863e.

(2) Roy, P.; Srivastava, S. K. Nanostructured Anode Materials for Lithium Ion Batteries. *J. Mater. Chem. A* **2015**, *3*, 2454–2484. https://doi.org/10.1039/c4ta04980b.

(3) Korthauer, R. *Handbuch Lithium-Ionen-Batterien*; Springer Vieweg, 2013. https://doi.org/10.1007/978-3-642-30653-2 ISBN.

(4) Jeevan, T. S. M. A.; Tadele, G.; Yizengaw, L.; Johnson, M. F. G. Review on Recent Progress of Nanostructured Anode Materials for Li-Ion Batteries. *Am. J. Anal. Chem.* **2022**, *13*, 431–448. https://doi.org/10.4236/ajac.2022.1311029.

(5) Ghiji, M.; Novozhilov, V.; Moinuddin, K.; Joseph, P.; Burch, I.; Suendermann, B.; Gamble, G. A Review of Lithium-Ion Battery Fire Suppression. *Energies* **2020**, *13*, 1–30.

(6) Goriparti, S.; Miele, E.; De Angelis, F.; Di Fabrizio, E.; Zaccaria, R. P.; Capiglia, C. Review on Recent Progress of Nanostructured Anode Materials for Li-Ion Batteries. *J. Power Sources* **2014**, *257*, 421–443. https://doi.org/10.1016/j.jpowsour.2013.11.103.

(7) Nobili, F.; Marassi, R. Fundamental Principles of Battery Electrochemistry. In *Batteries: Present and Future Energy Storage Challenges*; Wiley-VCH Verlag GmbH & Co. KGaA, 2020; pp 13–48.

(8) Mizushima, K.; Jones, P. C.; Wiseman, P. J.; Goodenough, J. B. LixCoO2 (0<x<-1): A New Cathode Material for Batteries of High Energy Density. *Mater. Res. Bull.* **1980**, *15*, 783–789. https://doi.org/10.1016/0025-5408(80)90012-4.

(9) Padhi, A. K.; Nanjundaswamy, K. S.; Goodenough, J. B. Phospho-Olivines as Positive-Electrode Materials for Rechargeable Lithium Batteries. *J. Electrochem. Soc.* **1997**, *144*, 1188–1194. https://doi.org/10.1149/1.1837571.

(10) Thackeray, M. M.; David, W. I. F.; Bruce, P. G.; Goodenough, J. B. Lithium Insertion into Manganese Spinels. *Mater. Res. Bull.* **1983**, *18*, 461–472. https://doi.org/10.1016/0025-5408(83)90138-1.

(11) Whittingham, M. S. Lithium Batteries and Cathode Materials. *Chem. Rev.* **2004**, *104*, 4271–4301. https://doi.org/10.1021/cr020731c.

(12) Liu, C.; Li, F.; Ma, L.-P.; Cheng, H.-M. Advanced Materials for Energy Storage. *Adv. Mater.* **2010**, *22*, E28–E62. https://doi.org/10.1002/adma.200903328.

(13) Palacín, M. R. Recent Advances in Rechargeable Battery Materials: A Chemist's Perspective. *Chem. Soc. Rev.* **2009**, *38*, 2565–2575. https://doi.org/10.1039/b820555h.

(14) Mahmood, N.; Tang, T.; Hou, Y. Nanostructured Anode Materials for Lithium Ion Batteries: Progress, Challenge and Perspective. *Adv. Energy Mater.* **2016**, *6*, 1–22. https://doi.org/10.1002/aenm.201600374.

(15) Winter, M.; Besenhard, J. O.; Spahr, M. E.; Novák, P. Insertion Electrode Materials for Rechargeable Lithium Batteries. *Adv. Mater.* **1998**, *10*, 725–763. https://doi.org/10.1002/(SICI)1521-4095(199807)10:10<725::AID-ADMA725>3.0.CO;2-Z.

(16) Jin, Y.; Zhu, B.; Lu, Z.; Liu, N.; Zhu, J. Challenges and Recent Progress in the Development of Si Anodes for Lithium-Ion Battery. *Adv. Energy Mater.* **2017**, *7*, 1–17. https://doi.org/10.1002/aenm.201700715.

(17) Li, W.; Sun, X.; Yu, Y. Si-, Ge-, Sn-Based Anode Materials for Lithium-Ion Batteries: From Structure Design to Electrochemical Performance. *Small Methods* **2017**, *1*, 1–22. https://doi.org/10.1002/smtd.201600037.

(18) Hong, S. Y.; Kim, Y.; Park, Y.; Choi, A.; Choi, N.-S.; Lee, K. T. Charge Carriers in Rechargeable Batteries: Na Ions vs. Li Ions. *Energy Environ. Sci.* **2013**, *6*, 2067–2081. https://doi.org/10.1039/c3ee40811f.

(19) Yu, S.-H.; Feng, X.; Zhang, N.; Seok, J.; Abruña, H. D. Understanding Conversion-Type Electrodes for Lithium Rechargeable Batteries. *Acc. Chem. Res.* **2018**, *51*, 273–281. https://doi.org/10.1021/acs.accounts.7b00487.

(20) Abraham, K. M. Directions in Secondary Lithium Battery Research and Development. *Electrochim. Acta* **1993**, *38*, 1233–1248.

(21) Ohzuku, T.; Ueda, A.; Yamamoto, N. Zero-Strain Insertion Material of Li[Li1/3Ti5/3]O4 for Rechargeable Lithium Cells. *J. Electrochem. Soc.* **1995**, *142*, 1431–1435. https://doi.org/10.1149/1.2048592.

(22) Wang, G. J.; Gao, J.; Fu, L. J.; Zhao, N. H.; Wu, Y. P.; Takamura, T. Preparation and Characteristic of Carbon-Coated Li4Ti5O12 Anode Material. *J. Power Sources* **2007**, *174*, 1109–1112. https://doi.org/10.1016/j.jpowsour.2007.06.107.

(23) Yim, C.-H.; Niketic, S.; Salem, N.; Naboka, O.; Abu-Lebdeh, Y. Towards Improving the Practical Energy Density of Li-Ion Batteries: Optimization and Evaluation of Silicon:Graphite Composites in Full Cells. *J. Electrochem. Soc.* **2017**, *164*, A6294–A6302. https://doi.org/10.1149/2.0481701jes.

(24) Okamoto, Y. Density Functional Theory Calculations of Alkali Metal (Li, Na, and K) Graphite Intercalation Compounds. *J. Phys. Chem. C* **2014**, *118*, 16–19. https://doi.org/10.1021/jp4063753.

(25) Zhang, H.; Yang, Y.; Ren, D.; Wang, L.; He, X. Graphite as Anode Materials: Fundamental Mechanism, Recent Progress and Advances. *Energy Storage Mater.* **2021**, *36*, 147–170. https://doi.org/10.1016/j.ensm.2020.12.027.

(26) Asenbauer, J.; Eisenmann, T.; Kuenzel, M.; Kazzazi, A.; Chen, Z.; Bresser, D. The Success Story of Graphite as a Lithium-Ion Anode Material-Fundamentals, Remaining Challenges, and Recent Developments Including Silicon (Oxide) Composites. *Sustain. Energy Fuels* **2020**, *4*, 5387–5416. https://doi.org/10.1039/d0se00175a.

(27) Etacheri, V.; Marom, R.; Elazari, R.; Salitra, G.; Aurbach, D. Challenges in the Development of Advanced Li-Ion Batteries: A Review. *Energy Environ. Sci.* **2011**, *4*, 3243–3262. https://doi.org/10.1039/c1ee01598b.

(28) Lu, L.; Han, X.; Li, J.; Hua, J.; Ouyang, M. A Review on the Key Issues for Lithium-Ion Battery Management in Electric Vehicles. *J. Power Sources* **2013**, *226*, 272–288. https://doi.org/10.1016/j.jpowsour.2012.10.060.

(29) Li, M.; Lu, J.; Chen, Z.; Amine, K. 30 Years of Lithium-Ion Batteries. *Adv. Mater.* **2018**, *30*, 1–24. https://doi.org/10.1002/adma.201800561.

(30) Hu, H.; Lian, L.; Ji, X.; Zhao, W.-L.; Li, H.; Chen, W.; Miras, H. N.; Song, Y.-F. Polyoxometalate (POM)-Based Battery Materials: Correlation between Dimensionality of Support Material and Energy Storage Performance. *Coord. Chem. Rev.* **2024**, *503*, 1–15. https://doi.org/10.1016/j.ccr.2023.215640.

(31) Zhang, Y.; Liu, J.; Li, S.-L.; Su, Z.-M.; Lan, Y.-Q. Polyoxometalate-Based Materials for Sustainable and Clean Energy Conversion and Storage. *EnergyChem* **2019**, *1*, 1–58. https://doi.org/10.1016/j.enchem.2019.100021.

(32) Zhang, Y.; Li, Y.; Guo, H.; Guo, Y.; Song, R. Recent Advances in Polyoxometalate-Based Materials and Their Derivatives for Electrocatalysis and Energy Storage. *Mater. Chem. Front.* **2023**, *8*, 732–768. https://doi.org/10.1039/d3qm01000g.

(33) Alemán, J.; Chadwick, A. V.; He, J.; Hess, M.; Horie, K.; Jones, R. G.; Kratochvíl, P.; Meisel, I.; Mita, I.; Moad, G.; Penczek, S.; Stepto, R. F. T. Definitions of Terms Relating to the Structure and Processing of Sols, Gels, Networks, and Inorganic-Organic Hybrid Materials (IUPAC Recommendations 2007). *Pure Appl. Chem.* **2007**, *79*, 1801–1829. https://doi.org/10.1351/pac200779101801.

(34) Gomez-Romero, P. Hybrid Organic-Inorganic Materials - in Search of Synergic Activity. *Adv. Mater.* **2001**, *13*, 163–174. https://doi.org/10.1002/1521-4095(200102)13:3<163::AID-ADMA163>3.0.CO;2-U.

(35) Dolbecq, A.; Dumas, E.; Mayer, C. R.; Mialane, P. Hybrid Organic-Inorganic Polyoxometalate Compounds: From Structural Diversity to Applications. *Chem. Rev.* **2010**, *110*, 6009–6048. https://doi.org/10.1021/cr1000578.

(36) Song, Y.-F.; Long, D.-L.; Ritchie, C.; Cronin, L. Nanoscale Polyoxometalate-Based Inorganic/Organic Hybrids. *Chem. Rec.* **2011**, *11*, 158–171. https://doi.org/10.1002/tcr.201100002.

(37) Carraro, M.; Gross, S. Hybrid Materials Based on the Embedding of Organically Modified Transition Metal Oxoclusters or Polyoxometalates into Polymers for Functional Applications: A Review. *Materials (Basel).* **2014**, *7*, 3956–3989. https://doi.org/10.3390/ma7053956.

(38) Gomez-Romero, P.; Pokhriyal, A.; Rueda-García, D.; Bengoa, L. N.; González-Gil, R. M. Hybrid Materials: A Metareview. *Chem. Mater.* **2024**, *36*, 8–27. https://doi.org/10.1021/acs.chemmater.3c01878.

(39) Sing, K. S. W.; Everett, D. H.; Haul, R. A. W.; Moscou, L.; Pierotti, R. A.; Rouquérol, J.; Siemieniewska, T. Reporting Physisorption Data for Gas/Solid Systems with Special Reference to the Determination of Surface Area and Porosity (Recommendations 1984). *Pure Appl. Chem.* **1985**, *57*, 603–619. https://doi.org/10.1351/pac198557040603.

(40) Wang, X.; Bu, X.; Feng, P. Porous Inorganic Materials Xiqing Wang, Xianhui Bu, Pingyun Feng. *Encycl. Inorg. Chem.* **2006**, 1–21. https://doi.org/10.1002/0470862106.ia282.

(41) Islam, M. S.; Mubarak, M.; Lee, H.-J. Hybrid Nanostructured Materials as Electrodes in Energy Storage Devices. *Inorganics* **2023**, *11*, 1–21. https://doi.org/10.3390/inorganics11050183.

(42) Hou, R.; Gund, G. S.; Qi, K.; Nakhanivej, P.; Liu, H.; Li, F.; Xia, B. Y.; Park, H. S. Hybridization Design of Materials and Devices for Flexible Electrochemical Energy Storage. *Energy Storage Mater.* **2019**, *19*, 212–241. https://doi.org/10.1016/j.ensm.2019.03.002.

(43) Reddy, A. L. M.; Gowda, S. R.; Shaijumon, M. M.; Ajayan, P. M. Hybrid Nanostructures for Energy Storage Applications. *Adv. Mater.* **2012**, *24*, 5045–5064. https://doi.org/10.1002/adma.201104502.

(44) Gómez-Romero, P.; Cuentas-Gallegos, K.; Lira-Cantú, M.; Casañ-Pastor, N. Hybrid Nanocomposite Materials for Energy Storage and Conversion Applications. *J. Mater. Sci.* **2005**, *40*, 1423–1428. https://doi.org/10.1007/s10853-005-0578-y.

(45) Gómez-Romero, P.; Ayyad, O.; Suárez-Guevara, J.; Muñoz-Rojas, D. Hybrid Organic-Inorganic Materials: From Child's Play to Energy Applications. *J. Solid State Electrochem.* **2010**, *14*, 1939–1945. https://doi.org/10.1007/s10008-010-1076-y.

(46) Genovese, M.; Lian, K. Polyoxometalate Modified Inorganic-Organic Nanocomposite Materials for Energy Storage Applications: A Review. *Curr. Opin. Solid State Mater. Sci.* **2015**, *19*, 126–137. https://doi.org/10.1016/j.cossms.2014.12.002.

(47) Li, F.; Xu, L. Coordination Assemblies of Polyoxomolybdate Cluster Framework: From Labile Building Blocks to Stable Functional Materials. *Dalt. Trans.* **2011**, *40*, 4024–4034. https://doi.org/10.1039/c0dt00691b.

(48) Herrmann, S.; Ritchie, C.; Streb, C. Polyoxometalate - Conductive Polymer Composites for Energy Conversion, Energy Storage and Nanostructured Sensors. *Dalt. Trans.* **2015**, *44*, 7092–7104. https://doi.org/10.1039/c4dt03763d.

(49) Yang, H.; Song, T.; Liu, L.; Devadoss, A.; Xia, F.; Han, H.; Park, H.; Sigmund, W.; Kwon, K.; Paik, U. Polyaniline/Polyoxometalate Hybrid Nanofibers as Cathode for Lithium Ion Batteries with Improved Lithium Storage Capacity. *J. Phys. Chem. C* **2013**, *117*, 17376–17381. https://doi.org/10.1021/jp401989j.

(50) Xia, S.; Li, F.; Li, X.; Cheng, F.; Sun, C.; Liu, J. J.; Guo, H. An Inorganic-Organic Hybrid Supramolecular Framework as a High-Performance Anode for Lithium-Ion Batteries. *Dalt. Trans.* **2018**, *47*, 5166–5170. https://doi.org/10.1039/c8dt00335a.

(51) Wang, H.; Hamanaka, S.; Nishimoto, Y.; Irle, S.; Yokoyama, T.; Yoshikawa, H.; Awaga, K. In Operando X-Ray Absorption Fine Structure Studies of Polyoxometalate Molecular Cluster Batteries: Polyoxometalates as Electron Sponges. *J. Am. Chem. Soc.* **2012**, *134*, 4918–4924. https://doi.org/10.1021/ja2117206.

(52) Sadakane, M.; Steckhan, E. Electrochemical Properties of Polyoxometalates as Electrocatalysts. *Chem. Rev.* **1998**, *98*, 219–237. https://doi.org/10.1021/cr960403a.

(53) Ruiz-Bilbao, E.; Fernández-Navarro, L.; Artetxe, B.; Gutiérrez-Zorrilla, J. M.; Chen, J.; Liu, T.; Atrián-Blasco, E.; Soria-Carrera, H.; Martín-Rapún, R.; Mitchell, S. G.; Ruiz-Rubio, L.; Moreno, I.; Vilas-Vilela, J. L.; Alcañiz Monge, J.; Reinoso, S.; Malcolm, D.; Vilà-Nadal, L.; Barros, Á.; Eletxigerra, U.; Aranzabe, E.; Hernaiz, M.; Aureliano, M.; Marques-da-Silva, D.; Serrano, A.; Martins, J.; Faleiro, L.; Fonseca, C.; Fraqueza, G.; Lagoa, R. *Polyoxometalates: Advances, Properties, and Applications*, 1st Editio.; Rubio, L. R., Vilas-Vilela, J. L., Artetxe, B., Gutiérrez-Zorrilla, J. M., Eds.; Jenny Stanford Publishing Pte. Ltd., 2023. https://doi.org/10.1201/9781003277446-2.

(54) Gumerova, N. I.; Rompel, A. Polyoxometalates in Solution: Speciation under Spotlight. *Chem. Soc. Rev.* **2020**, *49*, 7568–7601. https://doi.org/10.1039/d0cs00392a.

(55) Misra, A.; Kozma, K.; Streb, C.; Nyman, M. Beyond Charge Balance: Counter-Cations in Polyoxometalate Chemistry. *Angew. Chemie - Int. Ed.* **2020**, *59*, 596–612. https://doi.org/10.1002/anie.201905600.

(56) Huang, S.-C.; Lin, C.-C.; Hu, C.-W.; Liao, Y.-F.; Chen, T.-Y.; Chen, H.-Y. Vanadium-Based Polyoxometalate as Electron/Ion Sponge for Lithium-Ion Storage. *J. Power Sources* **2019**, *435*, 226702. https://doi.org/10.1016/j.jpowsour.2019.226702.

(57) Lin, C. C.; Hsu, C. T.; Liu, W.; Huang, S. C.; Lin, M. H.; Kortz, U.; Mougharbel, A. S.; Chen, T. Y.; Hu, C. W.; Lee, J. F.; Wang, C. C.; Liao, Y. F.; Li, L. J.; Li, L.; Peng, S.; Stimming, U.; Chen, H. Y. In Operando X-ray Studies of High-Performance Lithium-Ion Storage in Keplerate-Type Polyoxometalate Anodes. *ACS Appl. Mater. Interfaces* **2020**, *12*, 40296–40309. https://doi.org/10.1021/acsami.0c09344.

(58) Ueda, T. Electrochemistry of Polyoxometalates: From Fundamental Aspects to Applications. *ChemElectroChem* **2018**, *5*, 823–838. https://doi.org/10.1002/celc.201701170.

(59) Anjass, M. H.; Deisböck, M.; Greiner, S.; Fichtner, M.; Streb, C. Differentiating Molecular and Solid-State Vanadium Oxides as Active Materials in Battery Electrodes. *ChemElectroChem* **2019**, *6*, 398–403. https://doi.org/10.1002/celc.201801406.

(60) Sonoyama, N.; Suganuma, Y.; Kume, T.; Quan, Z. Lithium Intercalation Reaction into the Keggin Type Polyoxomolybdates. *J. Power Sources* **2011**, *196*, 6822–6827. https://doi.org/10.1016/j.jpowsour.2010.09.107.

(61) Wang, J.; Liu, Y.; Sha, Q.; Cao, D.; Hu, H.; Shen, T.; He, L.; Song, Y.-F. Electronic Structure Reconfiguration of Self-Supported Polyoxometalate-Based Lithium-Ion Battery Anodes for Efficient Lithium Storage. *ACS Appl. Mater. Interfaces* **2022**, *14*, 1169–1176. https://doi.org/10.1021/acsami.1c21461.

(62) Chen, J.; Symes, M. D.; Fan, S.-C.; Zheng, M.-S.; Miras, H. N.; Dong, Q.-F.; Cronin, L. High-Performance Polyoxometalate-Based Cathode Materials for Rechargeable Lithium-Ion Batteries. *Adv. Mater.* **2015**, *27*, 4649–4654. https://doi.org/10.1002/adma.201501088.

(63) Zhang, Z.; Ishikawa, S.; Kikuchi, M.; Yoshikawa, H.; Lian, Q.; Wang, H.; Ina, T.; Yoshida, A.; Sadakane, M.; Matsumoto, F.; Ueda, W. High-Performance Cathode Based on Microporous Mo-V-Bi Oxide for Li Battery and Investigation by Operando X-Ray Absorption Fine Structure. *ACS Appl. Mater. Interfaces* **2017**, *9*, 26052–26059. https://doi.org/10.1021/acsami.7b07195.

(64) Jia, X.; Wang, J.; Hu, H.; Song, Y.-F. Three-Dimensional Carbon Framework Anchored Polyoxometalate as a High-Performance Anode for Lithium-Ion Batteries. *Chem. - A Eur. J.* **2020**, *26*, 5257–5263. https://doi.org/10.1002/chem.201905764.

(65) Horn, M. R.; Singh, A.; Alomari, S.; Goberna-Ferrón, S.; Benages-Vilau, R.; Chodankar, N.; Motta, N.; Ostrikov, K.; Macleod, J.; Sonar, P.; Gomez-Romero, P.; Dubal, D. Polyoxometalates (POMs): From Electroactive Clusters to Energy Materials. *Energy Environ. Sci.* **2021**, *14*, 1652–1700. https://doi.org/10.1039/d0ee03407j.

(66) Kawasaki, N.; Wang, H.; Nakanishi, R.; Hamanaka, S.; Kitaura, R.; Shinohara, H.; Yokoyama, T.; Yoshikawa, H.; Awaga, K. Nanohybridization of Polyoxometalate Clusters and Single-Wall Carbon Nanotubes: Applications in Molecular Cluster Batteries. *Angew. Chem.* **2011**, *123*, 3533–3536. https://doi.org/10.1002/ange.201007264.

(67) Kume, K.; Kawasaki, N.; Wang, H.; Yamada, T.; Yoshikawa, H.; Awaga, K. Enhanced Capacitor Effects in Polyoxometalate/ Graphene Nanohybrid Materials: A Synergetic Approach to High Performance Energy Storage. *J. Mater. Chem. A* **2014**, *2*, 3801–3807. https://doi.org/10.1039/c3ta14569g.

(68) Ding, Y.-H.; Peng, J.; Khan, S.-U.; Yuan, Y. A New Polyoxometalate (POM)-Based Composite: Fabrication through POM-Assisted Polymerization of Dopamine and Properties as Anode Materials for High-Performance Lithium-Ion Batteries. *Chem. - A Eur. J.* **2017**, *23*, 10338–10343. https://doi.org/10.1002/chem.201700773.

(69) Ni, L.; Yang, G.; Sun, C.; Niu, G.; Wu, Z.; Chen, C.; Gong, X.; Zhou, C.; Zhao, G.; Gu, J.; Ji, W.; Huo, X.; Chen, M.; Diao, G. Self-Assembled Three-Dimensional Graphene/Polyaniline/ Polyoxometalate Hybrid as Cathode for Improved Rechargeable Lithium Ion Batteries. *Mater. Today Energy* **2017**, *6*, 53–64. https://doi.org/10.1016/j.mtener.2017.08.005.

(70) Yue, Y.; Li, Y.; Bi, Z.; Veith, G. M.; Bridges, C. A.; Guo, B.; Chen, J.; Mullins, D. R.; Surwade, S. P.; Mahurin, S. M.; Liu, H.; Paranthaman, M. P.; Dai, S. A POM–Organic Framework Anode for Li-Ion Battery. *J. Mater. Chem. A* **2015**, *3*, 22989–22995. https://doi.org/10.1039/c5ta06785e.

(71) Huang, Q.; Wei, T.; Zhang, M.; Dong, L.-Z.; Zhang, A.-M.; Li, S.-L.; Liu, W.-J.; Liu, J.; Lan, Y.-Q. A Highly Stable Polyoxometalate-Based Metal-Organic Framework with π-π Stacking for Enhancing Lithium Ion Battery Performance. *J. Mater. Chem. A* **2017**, *5*, 8477–8483. https://doi.org/10.1039/c7ta00900c.

(72) Lunkenbein, T.; Kamperman, M.; Li, Z.; Bojer, C.; Drechsler, M.; Förster, S.; Wiesner, U.; Mu, A. H. E.; Breu, J. Direct Synthesis of Inverse Hexagonally Ordered Diblock Copolymer/ Polyoxometalate Nanocomposite Films. *J. Amer* **2012**, *134*, 12685–12692.

(73) Pardiwala, A.; Kumar, S.; Jangir, R. Insights into Organic-Inorganic Hybrid Molecular Materials: Organoimido Functionalized Polyoxomolybdates. *Dalt. Trans.* **2022**, *51*, 4945–4975. https://doi.org/10.1039/d1dt04376e.

(74) Kruse, J.-H.; Langer, M.; Romanenko, I.; Trentin, I.; Hernández-Castillo, D.; González, L.; Schacher, F. H.; Streb, C. Polyoxometalate-Soft Matter Composite Materials: Design Strategies, Applications, and Future Directions. *Adv. Funct. Mater.* **2022**, *32*, 1–17. https://doi.org/10.1002/adfm.202208428.

(75) Kuznetsova, L. S.; Arlyapov, V. A.; Plekhanova, Y. V.; Tarasov, S. E.; Kharkova, A. S.; Saverina, E. A.; Reshetilov, A. N. Conductive Polymers and Their Nanocomposites: Application Features in Biosensors and Biofuel Cells. *Polymers (Basel).* **2023**, *15*, 1–51. https://doi.org/10.3390/polym15183783.

(76) Gómez-Romero, P.; Lira-Cantú, M. Hybrid Organic-Inorganic Electrodes: The Molecular Material Formed between Polypyrrole and the Phosphomolybdate Anion. *Adv. Mater.* **1997**, *9*, 144–147.

(77) Chen, Y. A Review of Polyaniline Based Materials as Anodes for Lithiumion Batteries. *IOP Conf. Ser. Mater. Sci. Eng.* **2019**, *677*, 1–7. https://doi.org/10.1088/1757-899X/677/2/022115.

(78) Li, X.-G.; Huang, M.-R.; Duan, W. Novel Multifunctional Polymers from Aromatic Diamines by Oxidative Polymerizations. *Chem. Rev.* **2002**, *102*, 2925–3030. https://doi.org/10.1021/cr010423z.

(79) Xu, L.; Sun, Y.; Han, B.; Chang, S. Electrochemical Performances on Both Poly(Phenylenediamine) Derivatives as Anode of Lithium-Ion Batteries. *J. Electrochem. Soc.* **2019**, *166*, A1363–A1369. https://doi.org/10.1149/2.0351908jes.

(80) Amer, I.; Young, D. A. Chemically Oxidative Polymerization of Aromatic Diamines: The First Use of Aluminium-Triflate as a Co-Catalyst. *Polymer (Guildf).* **2013**, *54*, 505–512. https://doi.org/10.1016/j.polymer.2012.11.078.

(81) Ciric-Marjanovic, G.; Marjanović, B.; Bober, P.; Rozlívková, Z.; Stejskal, J.; Trchová, M.; Prokeš, J. The Oxidative Polymerization of *p*-Phenylenediamine with Silver Nitrate: Toward Highly Conducting Micro/Nanostructured Silver/Conjugated Polymer Composites. *J. Polym. Sci. Part A Polym. Chem.* **2011**, *49*, 3387–3403. https://doi.org/10.1002/pola.24775.

(82) Rahman, M. A.; Won, M.-S.; Kwon, N.-H.; Yoon, J.-H.; Park, D.-S.; Shim, Y.-B. Water Sensor for a Nonaqueous Solvent with Poly(1,5-Diaminonapthalene) Nanofibers. *Anal. Chem.* **2008**, *80*, 5307–5311. https://doi.org/10.1021/ac7019392.

(83) Tagowska, M.; Pałys, B.; Mazur, M.; Skompska, M.; Jackowska, K. In Situ Deposition of Poly(1,8-Diaminonaphthalene): From Thin Films to Nanometer-Sized Structures. *Electrochim. Acta* **2005**, *50*, 2363–2370. https://doi.org/10.1016/j.electacta.2004.10.049.

(84) Wang, P.; Tian, J.; Hu, J.; Zhou, X.; Li, C. Supernormal Conversion Anode Consisting of High-Density MoS_2 Bubbles Wrapped in Thin Carbon Network by Self-Sulfuration of Polyoxometalate Complex. *ACS Nano* **2017**, *11*, 7390–7400. https://doi.org/10.1021/acsnano.7b03665.

(85) Xia, G.; Liu, D.; Zheng, F.; Yang, Y.; Su, J.; Chen, Q. Preparation of Porous MoO_2@C Nano-Octahedrons from a Polyoxometalate-Based Metal-Organic Framework for Highly Reversible Lithium Storage. *J. Mater. Chem. A* **2016**, *4*, 12434–12441. https://doi.org/10.1039/c6ta03491h.

(86) Ni, J.; Wang, G.; Yang, J.; Gao, D.; Chen, J.; Gao, L.; Li, Y. Carbon Nanotube-Wired and Oxygen-Deficient MoO_3 Nanobelts with Enhanced Lithium-Storage Capability. *J. Power Sources* **2014**, *247*, 90–94. https://doi.org/10.1016/j.jpowsour.2013.08.068.

(87) Zhang, H.; Gao, L.; Gong, Y. Exfoliated MoO_3 Nanosheets for High-Capacity Lithium Storage. *Electrochem. commun.* **2015**, *52*, 67–70. https://doi.org/10.1016/j.elecom.2015.01.014.

(88) Patil, S. B.; Udayabhanu; Kishore, B.; Nagaraju, G.; Dupont, J. High Capacity MoO_3/RGO Nanocomposite Anode for Lithium Ion Batteries: An Intuition into the Conversion Mechanism of MoO_3. *New J. Chem.* **2018**, *42*, 18569–18577. https://doi.org/10.1039/c8nj03190h.

(89) Auborn, J. J.; Barberio, Y. L. Lithium Intercalation Cells Without Metallic Lithium: MoO_2/$LiCoO_2$ and WO_2/$LiCoO_2$. *J. Electrochem. Soc.* **1987**, *134*, 638. https://doi.org/10.1149/1.2100521.

(90) Manthiram, A.; Tsang, C. Synthesis of Amorphous $MoO_{2+\delta}$ and Its Electrode Performance in Lithium Batteries. *J. Electrochem. Soc.* **1996**, *143*, L143. https://doi.org/10.1149/1.1836955.

(91) Wang, Z.; Chen, J. S.; Zhu, T.; Madhavi, S.; Lou, X. W. One-Pot Synthesis of Uniform Carbon-Coated MoO_2 Nanospheres for High-Rate Reversible Lithium Storage. *Chem. Commun.* **2010**, *46*, 6906–6908. https://doi.org/10.1039/c0cc01174f.

(92) Hu, X.; Zhang, W.; Liu, X.; Mei, Y.; Huang, Y. Nanostructured Mo-Based Electrode Materials for Electrochemical Energy Storage. *Chem. Soc. Rev.* **2015**, *44*, 2376–2404. https://doi.org/10.1039/c4cs00350k.

(93) Hashem, A. M.; Abbas, S. M.; Abdel-Ghany, A. E.; Eid, A. E.; Abdel-Khalek, A. A.; Indris, S.; Ehrenberg, H.; Mauger, A.; Julien, C. M. Blend Formed by Oxygen Deficient $MoO_{3-\delta}$ Oxides as Lithium-Insertion Compounds. *J. Alloys Compd.* **2016**, *686*, 744–752. https://doi.org/10.1016/j.jallcom.2016.06.043.

(94) Gao, Q.; Zhao, X.; Xiao, Y.; Zhao, D.; Cao, M. A Mild Route to Mesoporous Mo_2C-C Hybrid Nanospheres for High Performance Lithium-Ion Batteries. *Nanoscale* **2014**, *6*, 6151–6157. https://doi.org/10.1039/c3nr06678a.

(95) Xiu, Z.; Kim, D.; Alfaruqi, M. H.; Song, J.; Kim, S.; Duong, P. T.; Mathew, V.; Baboo, J. P.; Kim, J. Ultrafine Molybdenum Oxycarbide Nanoparticles Embedded in N-Doped Carbon as a Superior Anode Material for Lithium-Ion Batteries. *J. Alloys Compd.* **2017**, *696*, 143–149. https://doi.org/10.1016/j.jallcom.2016.11.235.

(96) Preiss, H.; Meyer, B.; Olschewski, C. Preparation of Molybdenum and Tungsten Carbides from Solution Derived Precursors. *Journal of Materials Science*. 1998, pp 713–722. https://doi.org/10.1023/A:1004393813199.

(97) Chen, W.-F.; Wang, C.-H.; Sasaki, K.; Marinkovic, N.; Xu, W.; Muckerman, J. T.; Zhu, Y.; Adzic, R. R. Highly Active and Durable Nanostructured Molybdenum Carbide Electrocatalysts for Hydrogen Production. *Energy Environ. Sci.* **2013**, *6*, 943–951. https://doi.org/10.1039/c2ee23891h.

(98) Gao, Q.; Yang, L.; Lu, X.; Mao, J.; Zhang, Y.; Wu, Y.; Tang, Y. Synthesis, Characterization and Lithium-Storage Performance of MoO_2/Carbon Hybrid Nanowires. *J. Mater. Chem.* **2010**, *20*, 2807–2812. https://doi.org/10.1039/b921001f.

(99) Liao, L.; Wang, S.; Xiao, J.; Bian, X.; Zhang, Y.; Scanlon, M. D.; Hu, X.; Tang, Y.; Liu, B.; Girault, H. H. A Nanoporous Molybdenum Carbide Nanowire as an Electrocatalyst for Hydrogen Evolution Reaction. *Energy Environ. Sci.* **2014**, *7*, 387–392. https://doi.org/10.1039/c3ee42441c.

(100) Ge, C.; Jiang, P.; Cui, W.; Pu, Z.; Xing, Z.; Asiri, A. M.; Obaid, A. Y.; Sun, X.; Tian, J. Shape-Controllable Synthesis of Mo_2C Nanostructures as Hydrogen Evolution Reaction Electrocatalysts with High Activity. *Electrochim. Acta* **2014**, *134*, 182–186. https://doi.org/10.1016/j.electacta.2014.04.113.

(101) Pang, M.; Wang, X.; Xia, W.; Muhler, M.; Liang, C. Mo(VI)-Melamine Hybrid As Single-Source Precursor to Pure-Phase β-Mo_2C for the Selective Hydrogenation of Naphthalene to Tetralin. *Ind. Eng. Chem. Res.* **2013**, *52*, 4564–4571. https://doi.org/10.1021/ie400119d.

(102) Liu, Y.; Yu, G.; Li, G.-D.; Sun, Y.; Asefa, T.; Chen, W.; Zou, X. Coupling Mo_2C with Nitrogen-Rich Nanocarbon Leads to Efficient Hydrogen-Evolution Electrocatalytic Sites. *Angew. Chemie* **2015**, *127*, 10902–10907. https://doi.org/10.1002/ange.201504376.

(103) Giordano, C.; Erpen, C.; Yao, W.; Antonietti, M. Synthesis of Mo and W Carbide and Nitride Nanoparticles via a Simple “Urea Glass” Route. *Nano Lett.* **2008**, *8*, 4659–4663. https://doi.org/10.1021/nl8018593.

(104) Di, F.; Zhou, W.; Yang, H.; Sun, C.; Geng, X.; Chen, Y.; Li, L.; Liu, Z.; An, B. Surface Modification and Functional Structure Space Design to Improve the Cycle Stability of Silicon Based Materials as Anode of Lithium Ion Batteries. *Coatings* **2021**, *11*, 1–24. https://doi.org/10.3390/coatings11091047.

(105) Zoller, M.; Bubnova, R.; Biryukov, Y.; Haussühl, E.; Pöttgen, R.; Janka, O.; Penner, S.; Praty, C.; Fitzek, H.; Winkler, J.; Filatov, S.; Huppertz, H. Elucidating the Physical Properties of the Molybdenum Oxide Mo_4O_{11} and Its Tantalum Substituted Variant $Mo_2Ta_2O_{11}$. *Zeitschrift für Krist. - Cryst. Mater.* **2020**, *235*, 143–155. https://doi.org/10.1515/zkri-2019-0073.

(106) Glemser, O.; Lutz, G. Über Molybdänoxyde. *Z. Anorg. Allg. Chem.* **1950**, *263*, 2–14.

(107) Parthé, E.; Sadogopan, V. The Structure of Dimolybdenum Carbide by Neutron Diffraction Technique. *Acta Crystallogr.* **1963**, *16*, 202–205. https://doi.org/10.1107/s0365110x63000487.

(108) Hull, A. W. The Positions of Atoms in Metals. *Proc. Am. Inst. Electr. Eng.* **1919**, *38*, 1171–1192. https://doi.org/10.1109/T-AIEE.1919.4765642.

(109) Zhu, H.; Li, Z.; Yang, H.; Luo, L. Carbothermic Reduction of MoO_3 for Direct Alloying Process. *J. Iron Steel Res. Int.* **2013**, *20*, 51–56. https://doi.org/10.1016/S1006-706X(13)60176-4.

(110) Abdirahman Mohamed, M.; Arnold, S.; Janka, O.; Quade, A.; Schmauch, J.; Presser, V.; Kickelbick, G. Continuous Wet Chemical Synthesis of $Mo(C,N,O)_x$ as Anode Materials for Li-Ion Batteries. *J. Mater. Chem. A* **2023**, *11*, 19936–19954. https://doi.org/10.1039/d3ta03340f.

(111) Hugosson, H. W.; Eriksson, O.; Nordström, L.; Jansson, U.; Fast, L.; Delin, A.; Wills, J. M.; Johansson, B. Theory of Phase Stabilities and Bonding Mechanisms in Stoichiometric and Substoichiometric Molybdenum Carbide. *J. Appl. Phys.* **1999**, *86*, 3758–3767. https://doi.org/10.1063/1.371284.

(112) Kuo, K.; Hägg, G. A New Molybdenum Carbide. *Nature* **1952**, *170*, 245–246.

(113) Rudy, E.; Benesovsky, F. Untersuchungen Im System Vanadin-Molybdän-Kohlenstoff Stabilisierung Des Kubischen Molybdänkarbids. *Planseeber. Pulvermetall.* **1962**, *10*, 42–64.

(114) Westgren, A.; Phragmén, G. Röntgenanalyse Der Systeme Wolfram-Kohlenstoff Und Molybdän-Kohlenstoff. *Z. Anorg. Allg. Chem.* **1926**, *156*, 27–36.

(115) Oyama, S. T. Preparation and Catalytic Properties of Transition Metal Carbides and Nitrides. *Catal. Today* **1992**, *15*, 179–200. https://doi.org/10.1007/s00104-013-2551-7.

(116) Epicier, T.; Dubois, J.; Esnouf, C.; Fantozzi, G.; Convert, P. Neutron Powder Diffraction Studies of Transition Metal Hemicarbides M2C1-x-I. Motivation for a Study on W_2C and Mo_2C and Experimental Background for an in Situ Investigation at Elevated Temperature. *Acta Metall.* **1988**, *36*, 1891–1901. https://doi.org/10.1016/0001-6160(88)90293-3.

(117) Zhang, H.-J.; Wang, K.-X.; Wu, X.-Y.; Jiang, Y.-M.; Zhai, Y.-B.; Wang, C.; Wei, X.; Chen, J.-S. MoO_2/Mo_2C Heteronanotubes Function as High-Performance Li-Ion Battery Electrode. *Adv. Funct. Mater.* **2014**, *24*, 3399–3404. https://doi.org/10.1002/adfm.201303856.

(118) Chen, T.; Yan, X.; Ma, Z.; Zhang, Y.; Zheng, X.; Jiang, Y. A General Method to Synthesize a MoC/C Composite Material with Potential Application as an Anodic Material in Lithium-Ion Batteries. *Ionics (Kiel).* **2020**, *26*, 4869–4875. https://doi.org/10.1007/s11581-020-03633-2.

(119) Gurusamy, L.; Lee, G.-J.; Anandan, S.; Liu, N.; Wu, J. J. Fabrication of Molybdenum Oxycarbide Nanoparticles Dispersed on Nitrogen-Doped Carbon Hollow Nanotubes through Anion Exchange Mechanism for Enhanced Performance in Supercapacitor. *J. Energy Storage* **2020**, *27*, 1–13. https://doi.org/10.1016/j.est.2019.101122.

(120) Zhang, J.; Zhang, L.; Zhang, J.; Zhang, Z.; Wu, Z. Effect of Surface/Bulk Oxygen Vacancies on the Structure and Electrochemical Performance of TiO_2 Nanoparticles. *J. Alloys Compd.* **2015**, *642*, 28–33. https://doi.org/10.1016/j.jallcom.2015.04.096.

(121) *Inorganic Nanoparticles: Synthesis, Application, and Perspectives*; Altavilla, C., Ciliberto, E., Eds.; CRC Press by Tailor & Francis Group, 2011.

(122) Tu, W.; Liu, H. Continuous Synthesis of Colloidal Metal Nanoclusters by Microwave Irradiation. *Chem. Mater.* **2000**, *12*, 564–567. https://doi.org/10.1021/cm990637l.

(123) Okuyama, K.; Lenggoro, W. I. Preparation of Nanoparticles via Spray Route. *Chem. Eng. Sci.* **2003**, *58*, 537–547. https://doi.org/10.1016/S0009-2509(02)00578-X.

(124) Auffan, M.; Rose, J.; Bottero, J. Y.; Lowry, G. V.; Jolivet, J. P.; Wiesner, M. R. Towards a Definition of Inorganic Nanoparticles from an Environmental, Health and Safety Perspective. *Nat. Nanotechnol.* **2009**, *4*, 634–641. https://doi.org/10.1038/nnano.2009.242.

(125) Ealias, A. M.; Saravanakumar, M. P. A Review on the Classification, Characterisation, Synthesis of Nanoparticles and Their Application. *IOP Conf. Ser. Mater. Sci. Eng.* **2017**, *263* (3). https://doi.org/10.1088/1757-899X/263/3/032019.

(126) Jun, Y.; Choi, J.; Cheon, J. Formkontrolle von Halbleiter- Und Metalloxid-Nanokristallen Durch Nichthydrolytische Kolloidverfahren. *Angew. Chemie* **2006**, *118*, 3492–3517. https://doi.org/10.1002/ange.200503821.

(127) Khan, I.; Saeed, K.; Khan, I. Nanoparticles: Properties, Applications and Toxicities. *Arab. J. Chem.* **2019**, *12*, 908–931. https://doi.org/10.1016/j.arabjc.2017.05.011.

(128) Burda, C.; Chen, X.; Narayanan, R.; El-Sayed, M. A. Chemistry and Properties of Nanocrystals of Different Shapes. *Chem. Rev.* **2005**, *105*, 1025–1102. https://doi.org/10.1021/cr030063a.

(129) Roduner, E. Size Matters : Why Nanomaterials Are Different. *Chem. Soc. Rev.* **2006**, *35*, 583–592. https://doi.org/10.1039/b502142c.

(130) Kumar, D. S.; Kumar, B. J.; Mahesh, H. M. *Chapter 3 - Quantum Nanostructures (QDs): An Overview*; Bhagyaraj, S. M., Oluwafemi, O. S., Kalarikkal, N., Thomas, S., Eds.; Elsevier Ltd.; Woodhead Publishing, 2018. https://doi.org/10.1016/B978-0-08-101975-7.00003-8.

(131) Mohamed, W. A. A.; Abd El-Gawad, H.; Mekkey, S.; Galal, H.; Handal, H.; Mousa, H.; Labib, A. Quantum Dots Synthetization and Future Prospect Applications. *Nanotechnol. Rev.* **2021**, *10*, 1926–1940. https://doi.org/10.1515/ntrev-2021-0118.

(132) Lai, S. L.; Guo, J. Y.; Petrova, V.; Ramanath, G.; Allen, L. H. Size-Dependent Melting Properties of Small Tin Particles: Nanocalorimetric Measurements. *Phys. Rev. Lett.* **1996**, *77*, 99–102. https://doi.org/10.1103/PhysRevLett.104.189601.

(133) Murray, C. B.; Norris, D. J.; Bawendi, M. G. Synthesis and Characterization of Nearly Monodisperse CdE (E = S, Se, Te) Semiconductor Nanocrystallites. *J. Am. Chem. Soc.* **1993**, *115*, 8706–8715. https://doi.org/10.1021/ja00072a025.

(134) Zhao, C. X.; He, L.; Qiao, S. Z.; Middelberg, A. P. J. Nanoparticle Synthesis in Microreactors. *Chem. Eng. Sci.* **2011**, *66*, 1463–1479. https://doi.org/10.1016/j.ces.2010.08.039.

(135) Lieser, K. H. Steps in Precipitation Reactions. *Angew. Chemie - Int. Ed.* **1969**, *8*, 188–202.

(136) Thanh, N. T. K.; Maclean, N.; Mahiddine, S. Mechanisms of Nucleation and Growth of Nanoparticles in Solution. *Chem. Rev.* **2014**, *114*, 7610–7630. https://doi.org/10.1021/cr400544s.

(137) Polte, J. Fundamental Growth Principles of Colloidal Metal Nanoparticles - a New Perspective. *CrystEngComm* **2015**, *17*, 6809–6830. https://doi.org/10.1039/c5ce01014d.

(138) Gautam, A.; Komal, P.; Gautam, P.; Sharma, A.; Kumar, N.; Jung, J. P. Recent Trends in Noble Metal Nanoparticles for Colorimetric Chemical Sensing and Micro-Electronic Packaging Applications. *Metals (Basel).* **2021**, *11*, 1–21. https://doi.org/10.3390/met11020329.

(139) LaMer, V. K.; Dinegar, R. H. Theory, Production and Mechanism of Formation of Monodispersed Hydrosols. *J. Am. Chem. Soc.* **1950**, *72*, 4847–4854. https://doi.org/10.1097/00007611-192203000-00016.

(140) LaMer, V. K. Nucleation in Phase Transitions. *Ind. Eng. Chem.* **1952**, *44*, 1270–1277. https://doi.org/10.1021/ie50510a027.

(141) Khan, R.; Rehman, A.; Hayat, A.; Andreescu, S. Magnetic Particles-Based Analytical Platforms for Food Safety Monitoring. *Magnetochemistry* **2019**, *5*, 1–20. https://doi.org/10.3390/magnetochemistry5040063.

(142) Karpinski, P. H.; Wey, J. S. Precipitation Processes. In *Handbook of Industrial Crystallization*; Myerson, A. S., Ed.; Butterworth-Heinemann, 2002; pp 141–160.

(143) Schwarzer, H.-C.; Peukert, W. Experimental Investigation into the Influence of Mixing on Nanoparticle Precipitation. *Chem. Eng. Technol.* **2002**, *25*, 657–661. https://doi.org/10.1002/1521-4125(200206)25:6<657::AID-CEAT657>3.0.CO;2-5.

(144) Glasgow, W.; Fellows, B.; Qi, B.; Darroudi, T.; Kitchens, C.; Ye, L.; Crawford, T. M.; Mefford, O. T. Continuous Synthesis of Iron Oxide (Fe_3O_4) Nanoparticles via Thermal Decomposition. *Particuology* **2016**, *26*, 47–53. https://doi.org/10.1016/j.partic.2015.09.011.

(145) Gutierrez, L.; Gomez, L.; Irusta, S.; Arruebo, M.; Santamaria, J. Comparative Study of the Synthesis of Silica Nanoparticles in Micromixer-Microreactor and Batch Reactor Systems. *Chem. Eng. J.* **2011**, *171*, 674–683. https://doi.org/10.1016/j.cej.2011.05.019.

(146) Sui, J.; Yan, J.; Liu, D.; Wang, K.; Luo, G. Continuous Synthesis of Nanocrystals via Flow Chemistry Technology. *Small* **2020**, *16*, 1–23. https://doi.org/10.1002/smll.201902828.

(147) Wegner, K.; Pratsinis, S. E. Aerosol Flame Reactors for the Synthesis of Nanoparticles. *KONA Powder Part. J.* **2000**, *18*, 170–182. https://doi.org/10.1016/S0032-5910(02)00077-3.

(148) Gutsch, A.; Kraemer, M.; Michael, G.; Muehlenweg, H.; Pridoehl, M.; Zimmermann, G. Gas-Phase Production of Nanoparticles. *KONA Powder Part. J.* **2002**, *20*, 24–37.

(149) Swihart, M. T. Vapor-Phase Synthesis of Nanoparticles. *Curr. Opin. Colloid Interface Sciene* **2003**, *8*, 127–133. https://doi.org/10.1016/S1359-0294.

(150) Wegner, K.; Pratsinis, S. E. Gas-Phase Synthesis of Nanoparticles: Scale-up and Design of Flame Reactors. *Powder Technol.* **2005**, *150*, 117–122. https://doi.org/10.1016/j.powtec.2004.11.022.

(151) Park, H. K.; Park, K. Y. Control of Particle Morphology and Size in Vapor-Phase Synthesis of Titania, Silica and Alumina Nanoparticles. *KONA Powder Part. J.* **2015**, *32*, 85–101. https://doi.org/10.14356/kona.2015018.

(152) Hiemer, J.; Clausing, A.; Schwarz, T.; Stöwe, K. MicroJet Reactor Technology: An Automated, Continuous Approach for Nanoparticle Syntheses. *Chem. Eng. Technol.* **2019**, *42*, 2018–2027. https://doi.org/10.1002/ceat.201900083.

(153) Lin, X. Z.; Terepka, A. D.; Yang, H. Synthesis of Silver Nanoparticles in a Continuous Flow Tubular Microreactor. *Nano Lett.* **2004**, *4*, 2227–2232. https://doi.org/10.1021/nl0485859.

(154) Falk, L.; Commenge, J. Performance Comparison of Micromixers. *Chem. Eng. Sci.* **2010**, *65*, 405–411. https://doi.org/10.1016/j.ces.2009.05.045.

(155) Lohse, S. E.; Eller, J. R.; Sivapalan, S. T.; Plews, M. R.; Murphy, C. J. A Simple Millifluidic Benchtop Reactor System for the High-Throughput Synthesis and Functionalization of Gold Nanoparticles with Different Sizes and Shapes. *ACS Nano* **2013**, *7*, 4135–4150.

(156) Wang, K.; Lu, Y.; Luo, G. Strategy for Scaling-up of a Microsieve Dispersion Reactor. *Chem. Eng. Technol.* **2014**, *37*, 2116–2122. https://doi.org/10.1002/ceat.201400296.

(157) Baumgartner, L. M.; Coley, C. W.; Reizman, B. J.; Gao, K. W.; Jensen, K. F. Optimum Catalyst Selection over Continuous and Discrete Process Variables with a Single Droplet Microfluidic Reaction Platform. *React. Chem. Eng.* **2018**, *3*, 301–311. https://doi.org/10.1039/c8re00032h.

(158) Lignos, I.; Maceiczyk, R.; DeMello, A. J. Microfluidic Technology: Uncovering the Mechanisms of Nanocrystal Nucleation and Growth. *Acc. Chem. Res.* **2017**, *50*, 1248–1257. https://doi.org/10.1021/acs.accounts.7b00088.

(159) McMullen, J. P.; Jensen, K. F. Rapid Determination of Reaction Kinetics with an Automated Microfluidic System. *Org. Process Res. Dev.* **2011**, *15*, 398–407. https://doi.org/10.1021/op100300p.

(160) Shestopalov, I.; Tice, J. D.; Ismagilov, R. F. Multi-Step Synthesis of Nanoparticles Performed on Millisecond Time Scale in a Microfluidic Droplet-Based System. *Lab Chip* **2004**, *4*, 316–321. https://doi.org/10.1039/b403378g.

(161) Nakamura, H.; Yamaguchi, Y.; Miyazaki, M.; Maeda, H. Preparation of CdSe Nanocrystals in a Micro-Flow-Reactor. *Chem. Commun.* **2002**, 2844–2845.

(162) Ju, J.; Zeng, C.; Zhang, L.; Xu, N. Continuous Synthesis of Zeolite NaA in a Microchannel Reactor. *Chem. Eng. J.* **2006**, *116*, 115–121. https://doi.org/10.1016/j.cej.2005.11.006.

(163) Boleininger, J.; Kurz, A.; Reuss, V.; Sönnichsen, C. Microfluidic Continuous Flow Synthesis of Rod-Shaped Gold and Silver Nanocrystals. *Phys. Chem. Chem. Phys.* **2006**, *8*, 3824–3827. https://doi.org/10.1039/b604666e.

(164) Yen, B. K. H.; Stott, N. E.; Jensen, K. F.; Bawendi, M. G. A Continuous-Flow Microcapillary Reactor for the Preparation of a Size Series of CdSe Nanocrystals. *Adv. Mater.* **2003**, *15*, 1858–1862. https://doi.org/10.1002/adma.200305162.

(165) Günther, A.; Khan, S. A.; Thalmann, M.; Trachsel, F.; Jensen, K. F. Transport and Reaction in Microscale Segmented Gas-Liquid Flow. *Lab Chip* **2004**, *4*, 278–286. https://doi.org/10.1039/b403982c.

(166) Cai, S.; Jin, Y.; Lin, Y.; He, Y.; Zhang, P.; Ge, Z.; Yang, W. Micromixing within Microfluidic Devices: Fundamentals, Design, and Fabrication. *Biomicrofluidics* **2023**, *17* (6). https://doi.org/10.1063/5.0178396.

(167) Gradl, J.; Schwarzer, H. C.; Schwertfirm, F.; Manhart, M.; Peukert, W. Precipitation of Nanoparticles in a T-Mixer: Coupling the Particle Population Dynamics with Hydrodynamics through Direct Numerical Simulation. *Chem. Eng. Process. Process Intensif.* **2006**, *45* (10), 908–916. https://doi.org/10.1016/j.cep.2005.11.012.

(168) Marchisio, D. L.; Rivautella, L.; Barresi, A. A. Design and Scale-Up of Chemical Reactors for Nanoparticle Precipitation. *AICHE J.* **2015**, *61*, 857–866. https://doi.org/10.1002/aic.10786.

(169) Lince, F.; Marchisio, D. L.; Barresi, A. A. A Comparative Study for Nanoparticle Production with Passive Mixers via Solvent-Displacement: Use of CFD Models for Optimization and Design. *Chem. Eng. Process. Process Intensif.* **2011**, *50*, 356–368. https://doi.org/10.1016/j.cep.2011.02.015.

(170) Penth, B. Method and Device for Carrying out Chemical and Physical Processes. Patent WO 00/61275, 2002.

(171) Penth, B. Kontinuierliche Produktion in Mikroreaktoren. German Patent DE102006004350 A1, 2007.

(172) Betke, A.; Kickelbick, G. Bottom-Up, Wet Chemical Technique for the Continuous Synthesis of Inorganic Nanoparticles. *Inorganics* **2014**, *2*, 1–15. https://doi.org/10.3390/inorganics2010001.

(173) Krüner, B.; Odenwald, C.; Tolosa, A.; Schreiber, A.; Aslan, M.; Kickelbick, G.; Presser, V. Carbide-Derived Carbon Beads with Tunable Nanopores from Continuously Produced Polysilsesquioxanes for Supercapacitor Electrodes. *Sustain. Energy Fuels* **2017**, *1*, 1588–1600. https://doi.org/10.1039/c7se00265c.

(174) Wille, C.; Gabski, H. P.; Haller, T.; Kim, H.; Unverdorben, L.; Winter, R. Synthesis of Pigments in a Three-Stage Microreactor Pilotplant-an Experimental Technical Report. *Chem. Eng. J.* **2004**, *101*, 179–185. https://doi.org/10.1016/j.cej.2003.11.007.

(175) Rüfer, A.; Räuchle, K.; Krahl, F.; Reschetilowski, W. Kontinuierliche Darstellung von Bariumsulfat-Nanopartikeln Im MicroJet-Reaktor. *Chemie-Ingenieur-Technik* **2009**, *81*, 1949–1954. https://doi.org/10.1002/cite.200900108.

(176) Dittert, B.; Gavrilović, A.; Schwarz, S.; Angerer, P.; Steiner, H.; Schöftner, R. Phase Content Controlled TiO_2 Nanoparticles Using the MicroJetReactor Technology. *J. Eur. Ceram. Soc.* **2011**, *31*, 2475–2480. https://doi.org/10.1016/j.jeurceramsoc.2011.01.015.

(177) Beyer, S.; Xie, L.; Gräfe, S.; Vogel, V.; Dietrich, K.; Wiehe, A.; Albrecht, V.; Mäntele, W.; Wacker, M. G. Bridging Laboratory and Large Scale Production: Preparation and in Vitro-Evaluation of Photosensitizer-Loaded Nanocarrier Devices for Targeted Drug Delivery. *Pharm. Res.* **2015**, *32*, 1714–1726. https://doi.org/10.1007/s11095-014-1569-y.

(178) Reichelt, L.; Bertau, M. Production of Ferrihydrite and Schwertmannite Using a Microjet Mixer Device. *Chem. Eng. Res. Des.* **2015**, *98*, 70–80. https://doi.org/10.1016/j.cherd.2015.04.008.

(179) Türeli, A. E. Nanoparticle Preparation Process Using Novel Microjet Reactor Technology for Enhancing Dissolution Rates of Poorly Water Soluble Drugs, Johannes Gutenberg-Universität in Mainz, 2015.

(180) Günday Türeli, N.; Türeli, A. E.; Schneider, M. Counter-Ion Complexes for Enhanced Drug Loading in Nanocarriers: Proof-of-Concept and Beyond. *Int. J. Pharm.* **2016**, *511*, 994–1001. https://doi.org/10.1016/j.ijpharm.2016.08.004.

(181) Günday Türeli, N.; Türeli, A. E.; Schneider, M. Optimization of Ciprofloxacin Complex Loaded PLGA Nanoparticles for Pulmonary Treatment of Cystic Fibrosis Infections: Design of Experiments Approach. *Int. J. Pharm.* **2016**, *515*, 343–351. https://doi.org/10.1016/j.ijpharm.2016.10.025.

(182) Volk, C.; Kratz, N.; Werner, J. Synthese Und Herstellung von Hochreinen Yttriumvanadat-Keramiken Für Optische Anwendungen. *Keramische Zeitschrift* **2017**, *69*, 156–159. https://doi.org/10.1007/bf03400332.

(183) Lohmann-Richters, F. P.; Odenwald, C.; Kickelbick, G.; Abel, B.; Varga. Facile and Scalable Synthesis of Sub-Micrometer Electrolyte Particles for Solid Acid Fuel Cells. *RSC Adv.* **2018**, *8*, 21806–21815. https://doi.org/10.1039/c8ra03293a.

(184) Krüner, B.; Odenwald, C.; Jäckel, N.; Tolosa, A.; Kickelbick, G.; Presser, V. Silicon Oxycarbide Beads from Continuously Produced Polysilsesquioxane as Stable Anode Material for Lithium-Ion Batteries. *ACS Appl. Energy Mater.* **2018**, *1*, 2961–2970. https://doi.org/10.1021/acsaem.8b00716.

(185) Krüner, B.; Odenwald, C.; Quade, A.; Kickelbick, G.; Presser, V. Influence of Nitrogen-Doping for Carbide-Derived Carbons on the Supercapacitor Performance in an Organic Electrolyte and an Ionic Liquid. *Batter. Supercaps* **2018**, *1*, 135–148. https://doi.org/10.1002/batt.201800051.

(186) Odenwald, C.; Kickelbick, G. Additive-Free Continuous Synthesis of Silica and ORMOSIL Micro- and Nanoparticles Applying a Microjet Reactor. *J. Sol-Gel Sci. Technol.* **2018**, *89*, 343–353. https://doi.org/10.1007/s10971-018-4626-x.

(187) Odenwald, C. Continuous and Wet-Chemical Synthesis of Micro- and Nanoparticles in a Microreactor, Universität des Saarlandes in Saarbrücken, 2020.

(188) Modl, T.; Lynn, N.; Schmitz-Stöwe, S.; Schwarz, T.; Stöwe, K. Development of an Impinging Jet Microreactor Synthesis Process for Surfactant-free Pt-Nanoparticles as PEMFC Catalyst Component. *ChemCatChem* **2024**, *16*, 1–9. https://doi.org/10.1002/cctc.202400768.

(189) Abdirahman Mohamed, M.; Arnold, S.; Janka, O.; Quade, A.; Presser, V.; Kickelbick, G. Self-Activation of Inorganic-Organic Hybrids Derived through Continuous Synthesis of Polyoxomolybdate and Para-Phenylenediamine Enables Very High Lithium-Ion Storage Capacity. *ChemSusChem* **2023**, *16*, 1–15. https://doi.org/10.1002/cssc.202202213.

(190) Abdirahman Mohamed, M.; Janka, O.; Harling, S.; Kickelbick, G. Precursor-Based Syntheses of Mo(C,N,O)x, Molybdenum Carbide, Nitride, and Oxide Applying a Microjet Reactor. *Solids* **2024**, *5*, 443–459. https://doi.org/10.3390/solids5030030.

(191) Reynolds, O. XXIX. An Experimental Investigation of the Circumstances Which Determine Whether the Motion of Water Shall Be Direct or Sinuous, and of the Law of Resistance in Parallel Channels. *Philos. Trans. R. Soc. London* **1883**, *174*, 935–982. https://doi.org/10.1098/rstl.1883.0029.

(192) Erbacher, C.; Bessoth, F. G.; Busch, M.; Verpoorte, E.; Manz, A. Towards Integrated Continuous-Flow Chemical Reactors. *Mikrochim. Acta* **1999**, *131* (1–2), 19–24. https://doi.org/10.1007/s006040050004.

(193) Wong, S. H.; Ward, M. C. L.; Wharton, C. W. Micro T-Mixer as a Rapid Mixing Micromixer. *Sensors Actuators, B Chem.* **2004**, *100*, 359–379. https://doi.org/10.1016/j.snb.2004.02.008.

(194) Fani, A.; Camarri, S.; Salvetti, M. V. Investigation of the Steady Engulfment Regime in a Three-Dimensional T-Mixer. *Phys. Fluids* **2013**, *25* (6). https://doi.org/10.1063/1.4809591.

(195) Novopashin, S.; Muriel, A. Is the Critical Reynolds Number Universal? *J. Exp. Theor. Phys.* **2002**, *95*, 306–309.

(196) Pohl, B.; Özyilmaz, N.; Brenner, G.; Peuker, U. A. Charakterisierung Einer Konischen Geometrie Für Einen Ultraschalldurchflussreaktor. *Chemie Ing. Tech.* **2009**, *81*, 1613–1622. https://doi.org/10.1002/cite.200900077.

(197) Jähnisch, K.; Hessel, V.; Löwe, H.; Baerns, M. Chemistry in Microstructured Reactors. *Angew. Chemie - Int. Ed.* **2004**, *43*, 406–446. https://doi.org/10.1002/anie.200300577.

(198) Schikarski, T.; Trzenschiok, H.; Peukert, W.; Avila, M. Inflow Boundary Conditions Determine T-Mixer Efficiency. *React. Chem. Eng.* **2019**, *4* (3), 559–568. https://doi.org/10.1039/c8re00208h.

(199) Duschman, S. The Rate of the Reaction between Iodic and Hydriodic Acids. *J. Phys. Chem.* **1904**, *8*, 453–482.

(200) Fournier, M.-C.; Falk, L.; Villermaux, J. A New Parallel Competing Reaction System for Assessing Micromixing Efficiency - Experimental Approach. *Chem. Eng. Sci.* **1996**, *51*, 5053–5064. https://doi.org/10.1016/0009-2509(96)00270-9.

(201) Fournier, M.-C.; Falk, L.; Villermaux, J. A New Parallel Competing Reaction System for Assessing Micromixing Efficiency - Determination of Micromixing Time by a Simple Mixing Model. *Chem. Eng. Sci.* **1996**, *51*, 5187–5192.

(202) Commenge, J.-M.; Falk, L. Villermaux-Dushman Protocol for Experimental Characterization of Micromixers. *Chem. Eng. Process.* **2011**, *50*, 979–990. https://doi.org/10.1016/j.cep.2011.06.006.

(203) Wenzel, D.; Nolte, K.; Górak, A. Reactive Mixing in Rotating Packed Beds: On the Packing's Role and Mixing Modeling. *Chem. Eng. Process. - Process Intensif.* **2019**, *143*, 1–9. https://doi.org/10.1016/j.cep.2019.107596.

(204) Guichardon, P.; Falk, L.; Villermaux, J. Characterisation of Micromixing Efficiency by the Iodide-Iodate Reaction System. Part II: Kinetic Study. *Chem. Eng. Sci.* **2000**, *55*, 4245–4253. https://doi.org/10.1016/S0009-2509(00)00069-5.

(205) Kölbl, A.; Desplantes, V.; Grundemann, L.; Scholl, S. Kinetic Investigation of the Dushman Reaction at Concentrations Relevant to Mixing Studies in Stirred Tank Reactors. *Chem. Eng. Sci.* **2013**, *93*, 47–54. https://doi.org/10.1016/j.ces.2013.01.067.

(206) Baccar, N.; Kieffer, R.; Charcosset, C. Characterization of Mixing in a Hollow Fiber Membrane Contactor by the Iodide-Iodate Method: Numerical Simulations and Experiments. *Chem. Eng. J.* **2009**, *148*, 517–524. https://doi.org/10.1016/j.cej.2008.12.020.

(207) Guichardon, P.; Falk, L. Characterisation of Micromixing Efficiency by the Iodide-Iodate Reaction System. Part I: Experimental Procedure. *Chem. Eng. Sci.* **2000**, *55* (19), 4233–4243. https://doi.org/10.1016/S0009-2509(00)00068-3.

(208) Manzano Martínez, A. N.; Jansen, R.; Walker, K.; Assirelli, M.; van der Schaaf, J. Experimental and Modeling Study on Meso- and Micromixing in the Rotor–Stator Spinning Disk Reactor. *Chem. Eng. Res. Des.* **2021**, *173*, 279–288. https://doi.org/10.1016/j.cherd.2021.07.012.